AD-A183 450   OBJECTIVE ANALYSIS AND PREDICTION TECHNIQUES(U) SASC   1/3
              TECHNOLOGIES INC LEXINGTON MA   A M GERLACH 30 NOV 86
   SCITNTIFIC-12 AFGL-TR-87-0013 F19620-82-C-0023

UNCLASSIFIED   F/G 4/2   NL
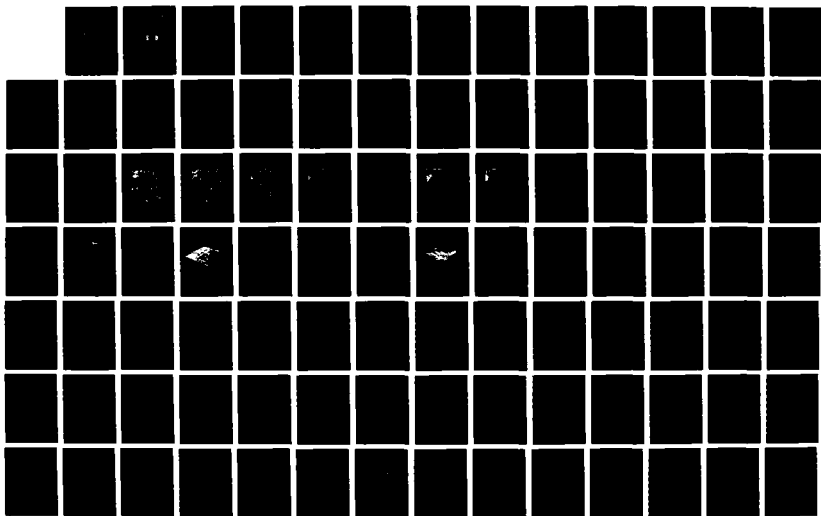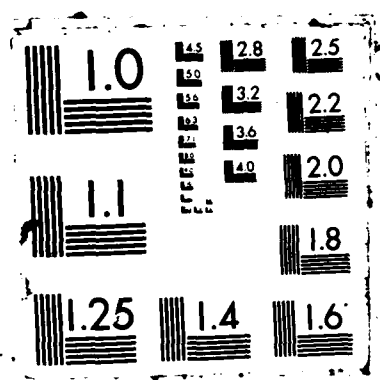
AFGL-TR-87-0013

DTIC FILE COPY

OBJECTIVE ANALYSIS AND PREDICTION TECHNIQUES - FINAL REPORT

Alan M. Gerlach (ed.)

AD-A183 450

DTIC
SELECTED
AUG 1 2 1987
D

SASC Technologies, Inc.
109 Massachusetts Avenue
Lexington, MA 02173

November 30, 1986

Scientific Report No. 12

Approved for public release; distribution unlimited

AIR FORCE GEOPHYSICS LABORATORY
AIR FORCE SYSTEMS COMMAND
UNITED STATES AIR FORCE
HANSCOM AFB, MASSACHUSETTS 01731

This technical report has been reviewed and is approved for publication.

ALLAN J. BUSSEY
Contract Manager

FOR THE COMMANDER
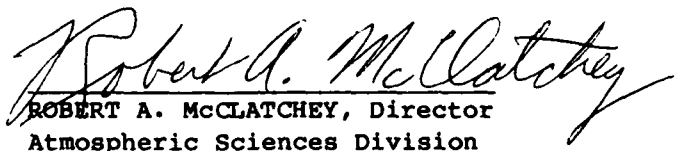
ROBERT A. McCLATCHEY, Director
Atmospheric Sciences Division

This report has been reviewed by the ESD Public Affairs Office (PA) and is releasable to the National Technical Information Service (NTIS).

Qualified requestors may obtain additional copies from the Defense Technical Information Center. All others should apply to the National Technical Information Service.

If your address has changed, or if you wish to be removed from the mailing list, or if the addressee is no longer employed by your organization, please notify AFGL/DAA, Hanscom AFB, MA 01731. This will assist us in maintaining a current mailing list.

AD-A183450

REPORT DOCUMENTATION PAGE

1a. REPORT SECURITY CLASSIFICATION UNCLASSIFIED	1b. RESTRICTIVE MARKINGS
2a. SECURITY CLASSIFICATION AUTHORITY	3. DISTRIBUTION/AVAILABILITY OF REPORT Approved for public release; distribution unlimited
2b. DECLASSIFICATION/DOWNGRADING SCHEDULE	

4. PERFORMING ORGANIZATION REPORT NUMBER(S)	5. MONITORING ORGANIZATION REPORT NUMBER(S) AFGL-TR-87-0013

6a. NAME OF PERFORMING ORGANIZATION SASC Technologies, Inc.	6b. OFFICE SYMBOL (If applicable)	7a. NAME OF MONITORING ORGANIZATION Air Force Geophysics Laboratory
6c. ADDRESS (City, State and ZIP Code) 109 Massachusetts Avenue Lexington, MA 02137		7b. ADDRESS (City, State and ZIP Code) Hanscom AFB, MA 01731 Monitor/LY/ Allan J. Bussey

8a. NAME OF FUNDING/SPONSORING ORGANIZATION Air Force Geophysics Laboratory	8b. OFFICE SYMBOL (If applicable) LY	9. PROCUREMENT INSTRUMENT IDENTIFICATION NUMBER Contract No. F19628-82-C-0023

8c. ADDRESS (City, State and ZIP Code) Hanscom AFB, MA 01731	10. SOURCE OF FUNDING NOS.			
	PROGRAM ELEMENT NO. 62101F	PROJECT NO. 6670	TASK NO. 00	WORK UNIT NO. AC

11. TITLE (Include Security Classification) Objective Analysis and Prediction Techniques - Final Report

12. PERSONAL AUTHOR(S)
Gerlach, Alan M. (ed.)

13a. TYPE OF REPORT Scientific Rpt. 12	13b. TIME COVERED FROM 85/12/1 TO 86/11/30	14. DATE OF REPORT (Yr., Mo., Day) 86/11/30	15. PAGE COUNT 268

16. SUPPLEMENTARY NOTATION

17. COSATI CODES			18. SUBJECT TERMS (Continue on reverse if necessary and identify by block number)
FIELD	GROUP	SUB. GR.	Objective analysis Interactive forecasting
0401			Initialization Mesocyclone detection/classification
0402			VAS data processing Satellite cloud analysis

19. ABSTRACT (Continue on reverse if necessary and identify by block number)

Part One reports on research performed in 1986 in numerical weather prediction, mesoscale forecasting, boundary layer meteorology, radar meteorology, satellite meteorology, and design climatology. Part Two provides five-year surveys of research activities in those technical areas.

20. DISTRIBUTION/AVAILABILITY OF ABSTRACT UNCLASSIFIED/UNLIMITED ☒ SAME AS RPT. ☐ DTIC USERS ☐	21. ABSTRACT SECURITY CLASSIFICATION UNCLASSIFIED
22a. NAME OF RESPONSIBLE INDIVIDUAL Allan J. Bussey	22b. TELEPHONE NUMBER (Include Area Code) (617) 377-2977	22c. OFFICE SYMBOL LY

DD FORM 1473, 83 APR   EDITION OF 1 JAN 73 IS OBSOLETE.

FOREWORD

This is the Final Report under Contract F19628-82-C-0023 with the Atmospheric Sciences Division, Air Force Geophysics Laboratory. The contract work performance period extended from November 25, 1981 to November 24, 1986.

This report consists of two parts: Part One details the results and status of research performed by SASC Technologies, Inc. during 1986; Part Two provides five-year overviews of research activities in the six discrete technical areas called for in the contract. These technical areas are:

Numerical Weather Prediction
Mesoscale Forecasting
Boundary Layer Meteorology
Radar Meteorology
Satellite Meteorology
Climatology

Personnel associated with these areas at any time during the contract, in alphabetical order, were:

Numerical Weather Prediction – Joan-Marie Freni, B.A.
Isidore M. Halberstam, Ph.D.
Chris Johnson, B.S.
Donald C. Norquist, M.S.
Shu-Lin Tung, M.S.

Mesoscale Forecasting – Russell C. Dengel, B.S.
Charles F. Ivaldi, Jr., B.S.
Michael E. Niedzielski, B.S.
Lisa G. Phillips, B.S.
Randy Schechter, M.S.
James H. Willand

Boundary Layer Meteorology – Joan-Marie Freni, B.A.
Clyde L. Lawrance
Leo F. Rockwood
Joan M. Ward, A.B.
James H. Willand

Radar Meteorology – Steven B. Alejandro, M.S.
Chen-Hung Chang, M.S.
Neil Day
Paul R. Desrochers, M.S.

Ralph J. Donaldson, Jr., S.M.
Dagmar Rapp Egerton, B.S.
Alison L. Godfrey, B.S.
F. Ian Harris, Ph.D.
James L. Lagesse, B.A.
Thomas C. Liu
Donald C. Rich, Jr.
Frank H. Ruggiero, M.S.
Glenn R. Smythe, M.S.
James G. Wieler, M.S.

Satellite Meteorology –   Gary B. Gustafson, B.S.
Robert G. Hallowell, B.S.
Charles F. Ivaldi, Jr. B.S.
Marc S. Jorrens
Pao-Huo Kuo
Barry A. Mareiro
Michael E. Niedzielski, B.S.
John M. Powers, B.A.
D. Keith Roberts
Randy Schechter, M.S.

Climatology –   Albert R. Boehm, M.S.
Arthur J. Kantor, M.Ed.
James H. Willand

Principal Investigator was Alan M. Gerlach, Ph.D.

Reports were prepared by the scientists, engineers, and mathematicians identified in the Table of Contents. SASC Technologies, Inc. is generally referred to in the report as STX.

The following technical reports were issued under the contract:

Scientific Report No. 1
    Norquist, D. C., and C. Johnson, 1982: Spectral Characteristics of the Global Moisture Distribution and Their Importance in Objective Analysis of Moisture for NWP Models. AFGL-TR-82-0190, ADA120397.

Scientific Report No. 2
    Gerlach, A. M., ed., 1982: Objective Analysis and Prediction Techniques. AFGL-TR-82-0394, ADA131465.

Scientific Report No. 3
    Gerlach, A. M., ed., 1983: Objective Analysis and Prediction Techniques - 1983. AFGL-TR-83-0333, ADA142441.

Scientific Report No. 4
    Halberstam, I., C. Johnson, D. C. Norquist, and S.-L. Tung, 1984: Two Methods of Global Data Assimilation. AFGL-TR-84-0260, ADA155981.

Scientific Report No. 5
    Smythe, G. R., and F. I. Harris, 1984: Sub-Cloud Layer Motions from Radar Data Using Correlation Techniques. AFGL-TR-84-0272, ADA156477.

Scientific Report No. 6
     Wieler, J. G., 1984: Real-Time Automated Detection of Mesocyclones and
Tornado Vortex Signatures. AFGL-TR-84-0282, ADA154968.

Scientific Report No. 7
     Norquist, D. C., 1984: Users Guide for Optimum Interpolation Method of
Global Data Assimilation. AFGL-TR-84-0290, ADA155929.

Scientific Report No. 8
     Gerlach, A. M., ed., 1984: Objective Analysis and Prediction
Techniques - 1984. AFGL-TR-84-0328, ADA160377.

Scientific Report No. 9
     Tung, S.-L., 1985: Users Guide for Normal Mode Objective Analysis of
Global Data Assimilation. AFGL-TR-85-0042, ADA160373.

Scientific Report No. 10
     Gerlach, A. M., ed., 1985: Objective Analysis and Prediction
Techniques - 1985. AFGL-TR-86-0002, ADA169746.

Scientific Report No. 11
     Norquist, D. C., 1986: Alternative Forms of Moisture Information in
4-D Assimilation. AFGL-TR-86-0194. ADA179792

Scientific Report No. 12
     Gerlach, A. M., ed., 1986: Objective Analysis and Prediction
Techniques - Final Report. AFGL-TR-87-0013.

     Journal articles and AFGL technical reports reporting research
performed under the contract are listed in the references and bibliographies
following the appropriate sections of the report.
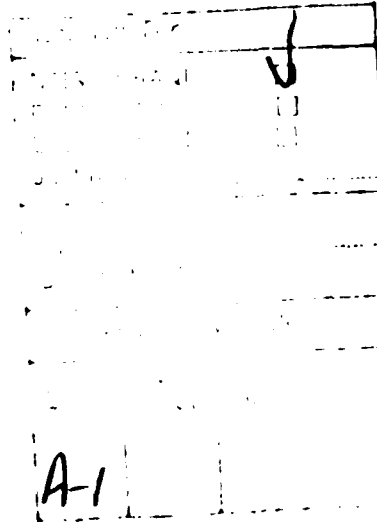
TABLE OF CONTENTS

PART ONE

PART ONE

I. NUMERICAL WEATHER PREDICTION

A. Experimentation and Initial Testing with the Relocatable Limited-Area Model (RLAM)

1. Introduction

The Relocatable Limited-Area Model (RLAM), first mentioned in Gerlach (1984) and again in Gerlach (1985), has become a vehicle for experimentation and testing. That is not to say that the RLAM can be deemed complete. However, sufficient progress has been made to permit testing many combinations of numerical procedures with but one set of physical parameterizations. In addition, the Air Force Global Weather Central Relocatable Window Model (RWM), at present a copy of the National Meteorological Center (NMC) Quasi-Lagrangian Nested-Grid Model (QNGM) (Mathur, 1983), was brought on-line and was tested in tandem with the RLAM. Whenever possible, forecasts from both models were compared with contemporaneous forecasts from AFGL's Global Spectral Model (GSM). This use of the GSM as a standard does not necessarily assume its fitness as a forecasting tool, but it should, because of the similarity between models, guarantee the reasonableness of the RLAM and RWM forecasts.

The physical parameterizations for the RLAM are currently the same as those for the RWM and contain a Kuo-type moist convective process, dry convective adjustment, and a simple parameterized boundary layer flux of momentum and temperature. Precipitation from the Kuo convection and from the large-scale adjustments is gathered at each grid location for 12 h and saved on file. Unlike the RWM, the physical processes have been separated to allow selective activation of each process.

2. The Selections

The various configurations of the RLAM are determined by choices offered to the user in the form of a NAMELIST input or edit symbols. The initial conditions are given by a list of variables describing the location,

resolution, and dimensions of the domain, while others determine mapping and boundary thickness and whether both full fields and boundary information are to be furnished. Most of these parameters have already been explained in Gerlach (1985).

The RLAM itself allows a choice of time stepping routines, horizontal differencing, grid staggering, boundary conditions, smoothing, diffusion, and physics. Each of these choices is described separately.

a. Time Differencing

At present, the RLAM is able to perform either a leap-frog centered time differencing or a differencing scheme based on the work of Brown and Campana (1978). Both are able to add a time filter. The Brown–Campana scheme involves averaging the pressure gradient force over several time steps. By doing so, the numerical prediction scheme stays stable for large time steps. To demonstrate how the RLAM generalized the scheme to make it applicable to both leap-frog and Brown–Campana time stepping, we need to look at the following set of equations:

$$\frac{\theta_*^{n+1} - \theta^{n-1}}{2\Delta t} = f(u_*^n,\ v_*^n,\ \theta_*^n)$$

$$\phi_*^{n+1} = g(\theta_*^{n+1})$$

$$p_s^{n+1} - p_s^{n-1} = 2\Delta t\ D(u_*^n,\ v_*^n) \tag{1}$$

$$\frac{u_*^{n+1} - u^{n-1}}{2\Delta t} = F(u_*^n, v_*^n) + \alpha(\phi_*^{n+1} + RT_*^{n+1}\ \ln p_{s*}^{n+1} + \phi^{n-1} + RT^{n-1}\ \ln p_s^{n-1})$$
$$+ (1-2\alpha)[\phi_*^n + RT_*^n\ \ln p_{s*}^n]$$

where u and v are the east-west and north-south wind velocity components, ϕ is the geopotential, θ is potential temperature, p_s is surface pressure, Δt is the time increment, T is temperature, and R is the universal gas constant for dry air. The asterisk implies interim values, while the superscript indicates time step. The weight α lies between 0

and 1/2. Eqs. (1) are coupled with an Asselin (1972) filter of the form

$$A^n = b(A_\star^{n+1} + A^{n-1}) + (1 - 2b)A_\star^n \qquad (2)$$

where A represents any variable and b is the time weight which lies
somewhere between 0 and 1/2. When α is set to 0, Eqs. (1) become the
classical leap-frog scheme. If b is also set to 0, the scheme will be
unfiltered and can lead to a separation of solutions between odd and even
time steps with the introduction of a computational mode. When $\alpha \neq 0$,
the Brown-Campana scheme is invoked with an allowance for larger time
steps. In practice, the leap-frog scheme was run only at time steps of 5
min or less, while Brown-Campana time steps were as large as 20 min without
much loss in accuracy.

An implicit scheme was also added to the selection of temporal
differencing. The implicit scheme is based on work done by McGregor et al.
(1978), Robert (1982), and Robert et al. (1985). The method involves
averaging all linear terms between the forecast time step and the previous
time step. The pressure gradient terms are also separated into linear and
non-linear portions, with the linear portion averaged in time. By
substituting into the continuity equation from the momentum and
thermodynamic equations, one can reduce the set of equations to a single
elliptic matrix equation involving temperature at the forecast time. To
solve this equation, we have to reduce the matrix to a two-dimensional
system and then treat the elliptic equation. Because the coefficient of the
undifferentiated term is variable in x and y, there is no direct method of
solving the elliptic equation. There is, however, quite a selection of
elliptic solvers either by iterative procedures, "shooting" methods, or
relaxation techniques; these were investigated as to efficiency and
accuracy. A two-step relaxation technique seemed to converge quickest.
There is also a very real problem in dealing with the boundaries, especially
since the "known" right-hand side of the equation contains higher-order
derivatives. In fact, some terms require as high as a third-order
derivative to be evaluated in x and y. Such high-order derivatives are very
difficult to approximate near boundaries and great care must be exercised in
choosing a suitable numerical representation. In practice, extra boundary
rows were added to allow for the higher-order derivatives. Though the

3

implicit scheme is an option of the RLAM, it has not been successfully tested.

b. Horizontal Differencing and Grid Staggering

For horizontal differencing, the RLAM offers a choice of second- or fourth-order schemes as well as a fourth-order compact (fc) scheme. Also, the grid can be staggered to allow for various horizontal configurations of the variables. Thus for first-order horizontal derivatives, the generalized differencing formulation for both second- and fourth-order accuracy appears as:

$$f'_{j+\alpha} = [a(f_{j+1} - f_j) + b(f_j - f_{j-1}) + c(f_{j+2} - f_{j-1}) + d(f_{j+1} - f_{j-2})]\Delta^{-1}; \quad (3)$$

where α is any value between $+1/2$ and $-1/2$, $a = (1 - 6c + 2\alpha)/2$, $b = (1 - 6d - 2\alpha)/2$, $c = (6\alpha^2 - \alpha - 2)/24$, and $d = (6\alpha^2 + \alpha - 2)/24$ for fourth-order accuracy, while $c = d = 0$ for second-order accuracy. Technically, Eq. (3) can be applied to any staggering of grid points with α defining the distance of one grid from the other. For instance, the Arakawa c-grid sets off the u-grid one-half mesh to the right of the primary grid and the v-grid one-half mesh above the primary grid. In the notation of Eq. (3), this is represented as $\alpha = 1/2$ and $\Delta = \Delta x$ for the u-grid and $\Delta = \Delta y$ for the v-grid. For second-order differencing of any variable, say p, about the u-grid, we get for second-order

$$a = 1, \ b = 0, \text{ and } \frac{\partial p}{\partial x}\left((j + \frac{1}{2})\Delta x\right) \simeq (p_{j+1} - p_j)/\Delta x;$$

for fourth-order we get

$$a = 9/8, \ b = 0, \ c = -1/24, \ d = 0,$$

$$\frac{\partial p}{\partial x}\left((j + 1/2)\Delta x\right) = 9/8\left(\frac{p_{j+1} - p_j}{\Delta x}\right) - 1/8\left(\frac{p_{j+2} - p_{j-1}}{3\Delta x}\right).$$

The same would apply to the v-grid with respect to y-derivatives. For derivatives of u about the primary grid, we set $\alpha = -1/2$ and then, for second-order, $a = 0$, $b = 1$, yielding $\frac{\partial u}{\partial x}\left[(j - \frac{1}{2})\Delta x\right] \simeq (u_j - u_{j-1})/\Delta x$.

Again, the same will apply in the y-direction. Unstaggered grids are

4

created by setting $\alpha = 0$. For that case $a = b = 1/2$ for second-order accuracy and the derivative of any variable f then is

$$\frac{\partial f}{\partial x} (j\Delta x) = (f_{j+1} - f_{j-1})/2\Delta x,$$

which is a centered differencing, known to be of second-order accuracy. For fourth-order, the parameters become

$$a = b = 3/4, \ c = d = -1/12 \text{ and } \frac{\partial f}{\partial x} (j\Delta x) \approx \frac{4}{3} \frac{(f_{j+1} - f_{j-1})}{2\Delta x} - \frac{1}{3} \frac{(f_{j+2} - f_{j-2})}{4\Delta x},$$

which, again, is the canonical form of fourth-order differencing. Other forms of staggering are possible and, although not very practical, values of α other than $-1/2$, 0, or $1/2$ can be used.

The staggered grids present a companion problem in the calculation of the vertical velocity $\dot{\sigma}$. Because vertical advection exists for all variables, it is necessary to determine a value of $\dot{\sigma}$ for all grids. Normally, one could assume that $\dot{\sigma}$ can be determined for the primary grid and averaged to determine values for the offset grids. But this presents problems near the boundaries. Assume that the u-grid is offset one-half grid space from the p-grid (primary grid). The sequence of variables is then p_0, u_0 (which are both boundary values) p_1, u_1, p_2, u_2 ...., p_{J-2}, u_{J-2}, p_{J-1}, u_{J-1}, p_J, u_J (where the J subscript also implies boundary values). To determine $\dot{\sigma}_{J-1}$ on the p-grid we evaluate the term $\dfrac{\partial p_s u}{\partial x}$ as

$(\dfrac{(p_{s_J} + p_{s_{J-1}})}{2} u_{J-1} - \dfrac{(p_{s_{J-1}} + p_{s_{J-2}})}{2} u_{J-2})(\Delta x)^{-1}$. To determine $\dot{\sigma}_{J-1}$ on the u-grid would then require an average of $\dot{\sigma}_J$ and $\dot{\sigma}_{J-1}$ from the p-grid. But $\dot{\sigma}_J$ is not available because it would require an average of p_{s_J} and $p_{s_{J+1}}$, which does not exist. A possible solution would be to carry an extra row of p_s in every direction as boundary points, but this is impractical. Another alternative is to assume some value of $\dot{\sigma}$ at the boundaries (e.g., zero), but that would lead to instabilities. Instead, RLAM recomputes a separate $\dot{\sigma}$ for each grid by changing the numerical approximation of the derivative of the products. Thus the same expression (i.e., $\dfrac{\partial p_s u}{\partial x}$) would be computed

as $[\dfrac{(u_J + u_{J-1})}{2} p_{s_J} - \dfrac{(u_{J-1} + u_{J-2})}{2} p_{s_{J-1}}](\Delta x)^{-1}$, which allows for $\dot{\sigma}_{J-1}$ on the u-grid. The same would apply for the expression $\dfrac{\partial p_s v}{\partial y}$ with respect to the v-grid. In the RLAM, provision is made to calculate different sets of $\dot{\sigma}$ for

5

each grid defined by the staggering.

The fc scheme does not contain an explicit form of the derivative. Instead, the fourth-order accuracy comes from averaging derivatives such that

$$(f'_{j+1} + 4f'_j + f'_{j-1})/6 = (f_{j+1} - f_{j-1})/2\Delta. \tag{4}$$

This can only be solved by inverting a tri-diagonal matrix containing the known values of f at all the interior points plus some value of the derivatives at the boundaries. At first, the RLAM attempted to insert actual values of the derivative calculated from the spectral coefficients at the boundaries. But this led to severe instabilities; so boundary derivatives estimated by Adam (1977) were substituted. Since little improvement resulted from using his higher-order estimate, his simpler second-order estimates were chosen. This condition is given by

$$1/2 (f'_1 + f'_2) = (f_2 - f_1)\Delta^{-1}$$

$$\tag{5}$$

$$1/2(f'_J + f'_{J-1}) = (f_J - f_{J-1})\Delta^{-1}$$

where the indices 1, 2, J-1, and J refer to the boundaries or to their adjacent points, respectively. The conditions (Eq. (5)) close the set of equations and allow calculation of the derivatives for all terms. The equations in matrix form are

$$A B = C$$

with

$$A = \begin{pmatrix} 1 & 1 & 0 & 0 & . & . & . & . & . & 0 \\ 1 & 4 & 1 & 0 & 0 & 0 & 0 & . & . & 0 \\ 0 & 1 & 4 & 1 & 0 & 0 & 0 & 0 & . & 0 \\ . & . & . & . & . & . & . & . & . & . \\ . & . & . & . & . & . & . & 1 & 4 & 1 \\ 0 & 0 & 0 & 0 & 0 & 0 & 0 & 0 & 1 & 1 \end{pmatrix} \qquad B = \begin{pmatrix} f'_1 \\ f'_2 \\ f'_3 \\ . \\ . \\ . \\ f'_{J-1} \\ f'_J \end{pmatrix} \tag{6}$$

6

and

$$
\mathbf{C} = \mathbf{A}^{-1}
\begin{pmatrix}
2 \, (f_2 - f_1) \\
3 \, (f_3 - f_1) \\
3 \, (f_4 - f_2) \\
\cdot \\
\cdot \\
\cdot \\
\cdot \\
\cdot \\
3 \, (f_J - f_{J-2}) \\
2 \, (f_J - f_{J-1})
\end{pmatrix}
$$

A is a constant matrix and need be inverted only once in the course of a forecast, making solution of **C** a relatively simple task.

There are other horizontal differencing schemes available, such as cubic splines or regional spectral models, but these have not been incorporated into the RLAM, nor has any provision been made for their eventual inclusion.

c. Smoothing and Diffusion

The RLAM, like almost all regional models, is faced with the need to control instabilities generated at the boundaries. There is also a need to represent sub-grid scale processes that tend to dissipate and diffuse some of the energy of the atmosphere. Both of these requirements can be met with some sort of smoothing or diffusion or both. Perkey and Kreitzberg (1976) (P-K) recommend both smoothing and diffusion with varying frequencies and intensities for the interior and the boundaries of their sponge boundary. The QNGM of Mathur (1983) also distinguishes between the boundary and the interior by supplying separate diffusion coefficients. The RLAM allows for either a QNGM-type second-order or a P-K-type fourth-order diffusion with up to four specifications of the diffusion coefficient, dependent on location. P-K use second-order at the boundaries, with a gradual drop in the diffusion coefficient value from the boundary to the interior. The QNGM has only two values for the second-order diffusion: one for several boundary rows and

one for the interior. In the RLAM, the thickness of the boundary can be specified and the four coefficients correspond to the outermost row (always second-order), boundary rows, transition row, and interior. For the QWGM the first and second coefficients are equal to each other, as are the third and fourth. A generalized subroutine allows for calculation of the diffusion term for either second- or fourth-order. First, a constant B is set to an appropriate value and the coefficient k is derived as $k = B(\Delta x)^n (2\Delta t)^{-1}$, where n is 2 for second-order and 4 for fourth-order. The diffusion term is then calculated from

$$d_f = k(\Delta x)^{-n} \sum_{j=0}^{n_g} \sum_{i=-j}^{j} (-1)^{(i+1)} (-1)^{(n_g+1)} (A_{i+j+1} - 2A_{i+j} + A_{i+j-1}) \quad (7)$$

where $n_g = (n-2)/2$ and A is any variable. If we are dealing with second-order, $n_g = 0$ and both sums give rise to only one term. For fourth-order, there are four terms which add up to

$$A_{i+2} - 4A_{i+1} + 6A_i - 4A_{i-1} + A_{i-2}.$$

The smoothing operator found in the RLAM is based on the smoother-desmoother described by Shapiro (1970) and mentioned by P-K. The operator smooths the variables and then undoes the smoothing for lower wave numbers, damping only the high frequency noise. Thus, if the smoothing weight is c_1, and the desmoother is c_2, we have

$$\bar{A}^{c_1} = A_i + c_1(A_{i-1} + A_{i+1} - 2A_i)$$

$$(8)$$

$$\bar{A}^{c_1,c_2} = \bar{A}_i^{c_1} + c_2(\bar{A}_{i-1}^{c_1} + \bar{A}_{i+1}^{c_1} - 2\bar{A}_i^{c_1}).$$

Usually, c_1 and c_2 are oppositely signed to produce the desired effect of only damping the high-frequency modes. The operator Eq. (8) can be applied to the boundary separately from the interior. In fact, P-K recommend more frequent smoothing of their sponge boundaries than of the

8

interior in order to control boundary-induced instabilities. The RLAM allows a choice of frequencies of smoothing both the interior and boundaries. It also allows for higher-order smoothing performed by repetition of the lower-order smoothing. In practice, when specialized boundaries have been invoked (such as the sponge), boundary smoothing frequencies have normally exceeded interior smoothing frequencies. For directly inserted boundaries, however, interior and exterior frequencies were generally set equal to each other.

d. Boundary Conditions

Lateral boundary conditions are always a sore point in regional modelling. They are a necessary evil that can lead to frustrating instabilities or computational modes that render the forecasts either inaccurate or unreasonable. The RLAM has been tested with primarily two types of boundary conditions: a sponge boundary described by P-K and a directly inserted boundary. A "porous" sponge boundary also described by P-K was also tested at first, but since the porous sponge does not interact with any outside data, it was not considered a desirable alternative to the other two. Choosing a boundary condition, however, is not as simple as choosing a second- or fourth-order scheme. Specific boundary conditions require specific data which must be prepared beforehand. It would be convenient if a universal set of boundary data were available from which specific subsets could be fashioned as needed, but such does not exist and it is doubtful whether it can feasibly exist.

The current boundary conditions are derived by cubic interpolation, as described in Gerlach (1985). They consist of actual values at the outermost rows for the directly inserted boundary, or of tendencies along five boundary rows for the sponge boundary. The sponge boundary gradually blends the tendencies from the RLAM with those from the GSM. The outermost boundary row contours the tendencies of the GSM only, while the innermost boundary row contains only the RLAM tendencies. In between, the tendencies are a combination of the two with weights geared to stress the RLAM tendencies closer to the interior and to stress the GSM closer to the exterior.

The fc scheme requires special handling of the boundaries, as mentioned

above. When derivatives were saved explicitly and inserted at the boundaries, their values were saved along with the field variables and interpolated for the appropriate time step. The Adam boundary condition had no such requirement, and the original variables were all that were necessary to close the system of equations. For the implicit scheme, it is also necessary to supply derivatives at the boundaries, and again the possibility of using either explicit derivatives (which was attempted) or an Adam-type approximation should be explored. Other forms of boundary conditions were also investigated, including a radiation scheme as proposed by Orlanski (1976) and Miller and Thorpe (1981) and NMC's boundary conditions for its Limited-area Fine-mesh model (LFM) (Newell and Deaven, 1981). Neither of these, however, has been sufficiently tested.

3. Comparisons

The RLAM has been tested against forecasts made by the AFGL GSM and the RWM. The latter is a research model discussed by Mathur (1983) that features a pseudo-Lagrangian advective scheme. The physics in the RWM has been applied to the RLAM and consists of bulk aerodynamic surface fluxes, a Kuo convective scheme, and large-scale precipitation. The programs for the RWM with proper documentation were obtained from AFGWC, where attempts are being made to modify the QNGM for employment as an operational regional window model. There were some minor changes made on the RWM as received, to permit comparisons with the RLAM. These consisted of:

1. A correction of the RWM mapping routine to account for the change of longitude on either side of the pole on a polar stereographic projection.

2. An adjustment to the calculation of the domain for a mercator projection to be commensurate with the RLAM. The RWM always draws the domain rectangle at the equator and translates it to the desired latitude, whereas the RLAM draws the rectangle at the desired latitude.

3. A correction in the Kuo convection, which in calculating the saturation mixing ratio from a stored table of values allowed the interpolation to run off the table when the atmosphere was cold and dry.

4. An adjustment for a similar problem in locating the lifting-condensation level (LCL). When the LCL was located below the first layer, the Kuo convection scheme still attempted to interpolate between the first layer and a non-existent zero layer, leading to undefined quantities.

Because the input and output files of the RWM are different from those of the RLAM, translation codes were developed to process RWM fields into RLAM fields and vice-versa. The RWM came with data from 10 November 1985, whereas the RLAM fields are started from spectral data from the GSM. Most of the GSM fields that served as initial data for the RLAM were derived from FGGE III-A data from 4 February 1979. Both the RWM and RLAM allow optional vertical resolution, but the respective data sets are of different resolution and would require some vertical interpolation. However, no vertical interpolation scheme has been implemented for the RLAM. Hence a 10-level RLAM with σ-structure similar to the 10-level RWM was run after initialization from RWM-supplied data, while the RWM was structured after the 12-level RLAM and GSM when it was initialized from the GSM data.

Inter-model comparisons were made, rather than comparisons against real data, because during the development stage it is only necessary to test the reasonableness rather than the accuracy of the forecasts. Since much of the structure of the RLAM and the GSM is the same and initial and boundary conditions are provided by the latter, their forecasts should be fairly similar. Once the model has been perfected, its accuracy should be tested against real data.

Fig. 1 shows the RMS difference for a 24 h forecast between the GSM and the RLAM at all 12 σ-layers for u, v, and T. Two RLAM runs are depicted--one with fourth-order differencing, the other with second-order differencing. Both had Brown-Campana time differencing, sponge boundaries, and contained physics. The second-order differencing was smoothed every nine time steps (3 h) and its boundaries every three time steps. The fourth-order differencing was smoothed every second time step (40 min) and its boundaries every time step. The increased smoothing was necessary to maintain stability in the fourth-order. To allow for fourth-order differencing everywhere, an extra boundary row was inserted on all four sides, so that the sponge boundary kept external tendencies on two rather than one external row. The results point up only minor differences between

11
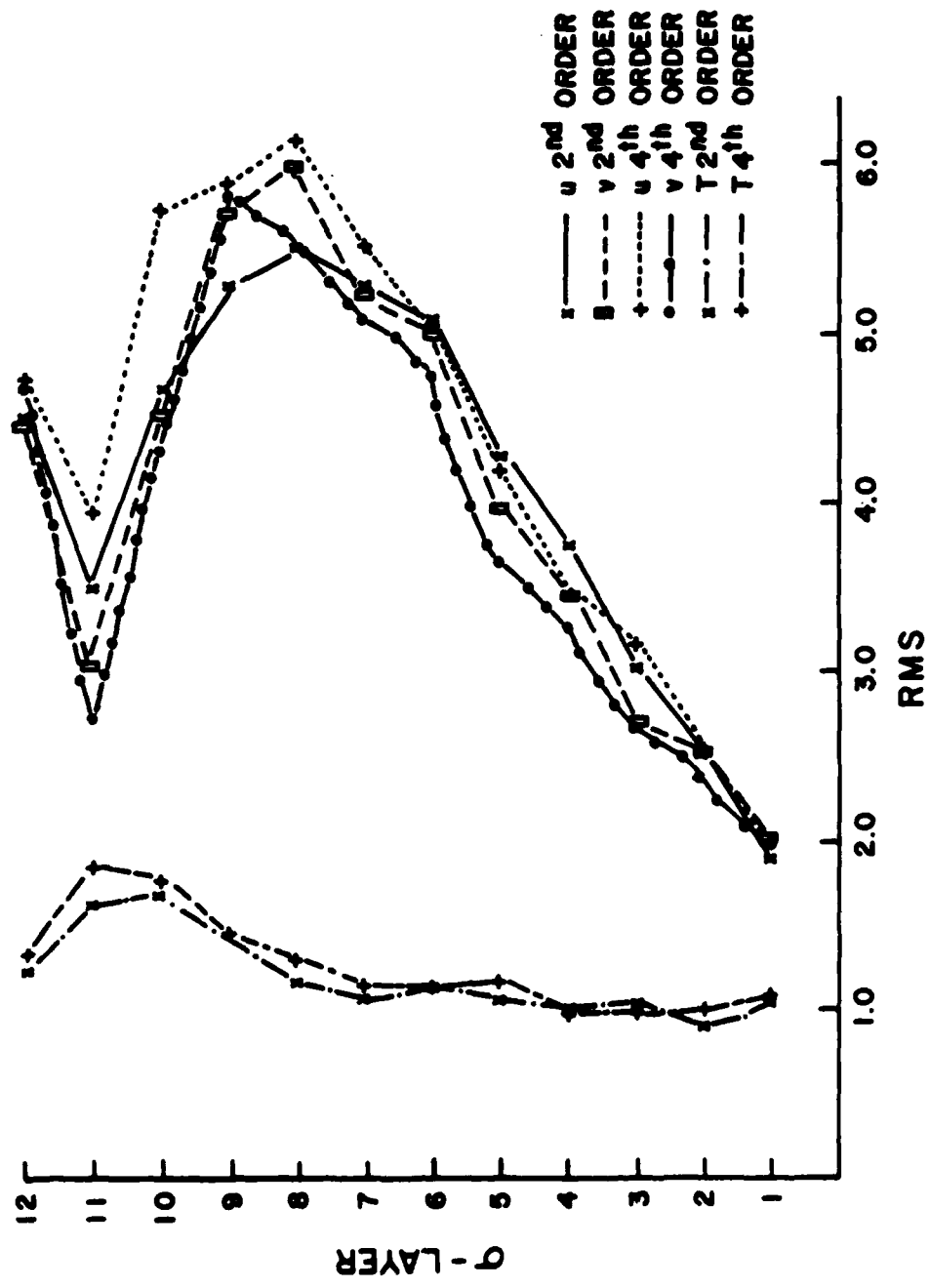
Fig. 1 RMS Differences between 24 h Forecasts of u, v, and T for All 12 σ-layers of the GSM and Forecasts of the RLAM Run with Brown-Campana Time Differencing, Sponge Boundaries, and Physical Parameterizations

(One set is for the RLAM using second-order spatial differencing with smoothing every three time steps along the boundary and every nine time steps for the entire field. The other set is for RLAM using fourth-order regular spatial differencing with smoothing each time step at the boundaries and every other time step for the entire field.)

the differencing schemes, as one would anticipate, with RMS differences in velocity reaching no more than 6 m s^{-1} in the vicinity of the tropopause and no more than about 1.5°C in temperature in the stratosphere. When physics was omitted, the RMS differences were not substantially larger, except at the surface, where the lack of surface friction or heat flux caused substantial differences between the GSM and the RLAM. Part of the reason for the inability of the physical parmeterizations to affect the upper layers is the lack of vertical diffusion in any of the models. If vertical diffusion were present, one could expect to see the effects of physical parameterization, especially the planetary boundary layer physics, percolate up to all layers. The comparison in Fig. 1 was for a mercator projection centered at 15° S, 225° E (135° W) with full mesh (Δx ~ 5° longitude) and 26x21 grid points. Fig. 2 is the same as Fig. 1 except that the domain is on a Lambert conformal mapping centered at 41° N, 270° E, (90° W) and there is no physics added to the model. The effect of physical parameterizations at the lowest layer is quite obvious especially with regard to temperature. The velocity RMS values peak at a lower layer, probably due to the lower wintertime tropopause in the northern latitudes. There also seems to be less of a zonal-meridional wind velocity difference in the mercator projection, probably due, again, to the stronger zonal jets in the mid-latitudes.

Table 1 shows an assortment of configurations of the RLAM and their respective RMS differences with the GSM. This is by no means an exhaustive list, even with the limited number of tested options available. All runs were performed without diffusion, with Brown-Campana time stepping, on an unstaggered grid with full mesh spacing, and 12 vertical layers. The RMS statistics show a wide range of agreement and disagreement with the GSM. Especially noteworthy are the large differences engendered by the fc scheme probably due to the frequent smoothing introduced in order to maintain stability. The other configurations yield essentially the same forecasts, except for the first layer where the absence of physics, as already noted, causes a departure from the GSM.

The RWM comparisons were not entirely successful. Part of the problem of comparing the RLAM with the RWM is their different treatment of the boundaries. The RWM applies heavy diffusion to the first five boundary rows, whereas the RLAM can apply diffusion optionally. When dealing with

13
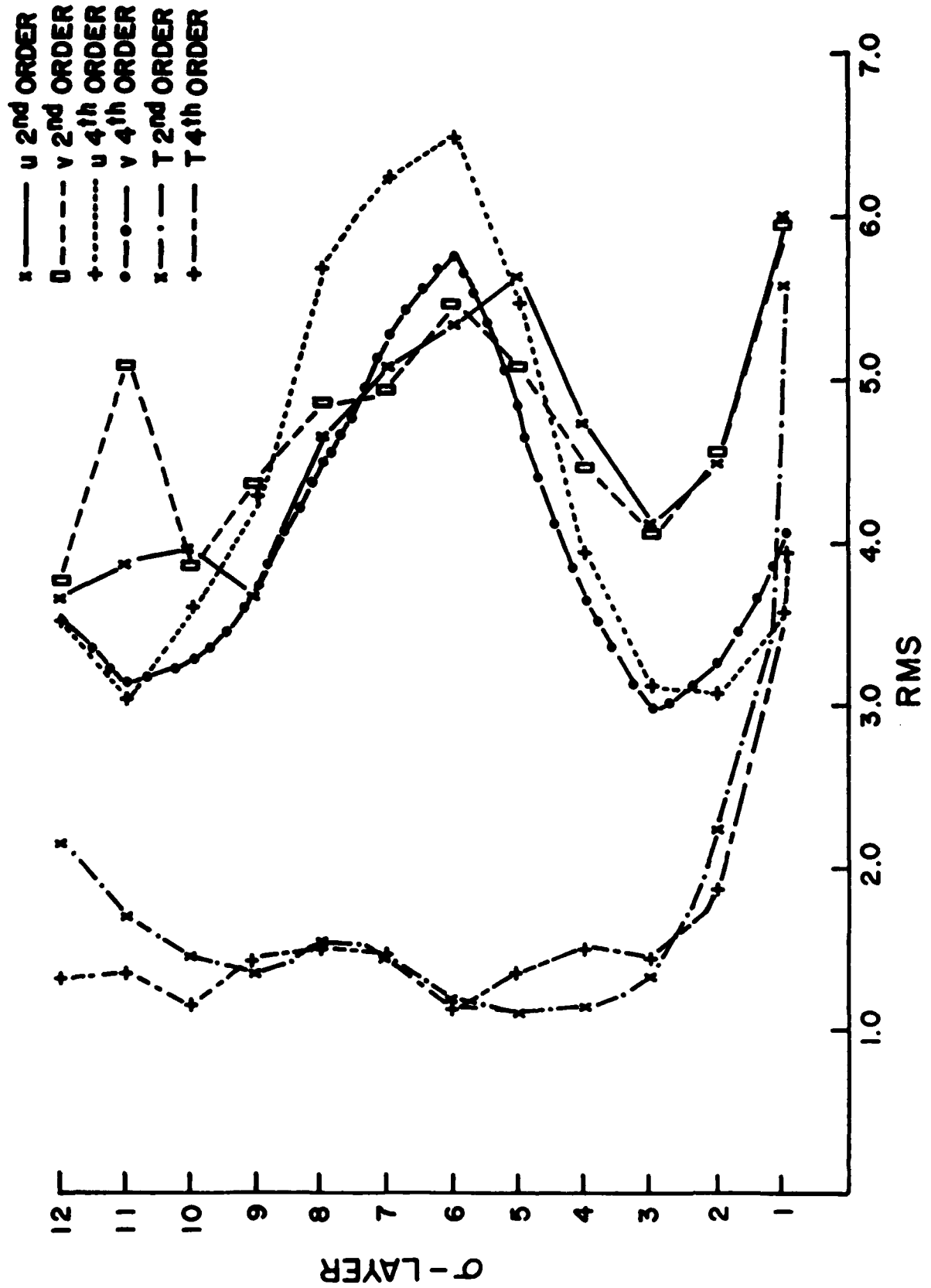
Fig. 2 Same as Fig. 1, except for Different Geographic Location, Different Mapping, and the RLAM Contains No Physics

14

Table 1. RMS Comparisons between RLAM and AFGL GSM

For temperature (T: °C), wind velocity components (u, v; m s^{-1}), and specific humidity (q; g kg^{-1}), and surface pressure (p$_s$; mb) at σ-layer 4 (approx. 550 mb) and σ-layer 1 (approx. 950 mb) for a 24 h forecast from 4 February 1979.

Map projection	Lambert	Lambert	Lambert	Mercator	Mercator	Mercator	Mercator	Mercator	Mercator	Mercator	Mercator
Physics	No	No	No	No	Yes	Yes	No	No	Yes	No	No
Boundary type	Inserted	Sponge	Inserted	Inserted	Inserted	Sponge	Inserted	Sponge	Sponge	Inserted	Sponge
Order of differencing	2	2	4	2	2	2	4	4	4	4 compact	4 compact
Smoothing every _ time steps (20 min)	9	9	1	3	3	3	1	2	2	1	1
Boundary smoothing every _ time steps	3	3	1	3	3	9	1	1	1	1	1
RMS values: T_4	1.16	1.16	1.50	1.14	1.11	1.01	1.04	1.03	1.00	1.62	1.64
u_4	4.21	4.74	3.91	3.90	3.97	3.70	3.37	3.46	3.46	8.86	10.84
v_4	3.93	4.43	3.65	3.52	3.63	3.46	3.24	3.31	3.35	13.03	10.84
q_4	0.47	0.52	0.40	0.88	0.87	0.85	0.90	0.87	0.89	1.17	1.15
T_1	4.38	5.58	3.88	2.64	1.11	1.05	2.11	1.75	1.10	2.24	2.29
u_1	4.94	5.90	3.57	4.26	2.31	1.95	3.76	3.79	2.13	9.05	10.09
v_1	4.60	5.93	4.02	3.35	2.15	2.04	3.00	3.06	2.00	8.84	7.53
q_1	2.54	2.69	2.44	2.10	1.97	1.86	1.84	1.62	1.78	2.07	2.05
P_s	5.53	5.74	5.26	7.81	8.34	4.52	5.54	5.97	5.86	11.05	10.74

26x21 grid points, removing five points from each side leaves an interior that is only one-third of the boundary, forcing the RWM to strongly damp most of the field. To rectify this situation, the domain was expanded to 39x33, resulting in an interior that is about equal to the boundary and giving the RWM room to breathe, as it were. The ideal comparison would require supplying the same grid for the RLAM and then evaluating its performance in the interior with respect to the interior of the RWM. But the RLAM requires a great deal more space than the RWM and, although 39x33 can still fit in the computer, running a larger-size program strains the computer resources at AFGL. Several attempts to run the RLAM on a 39x33 grid were not successful except for second-order differencing on a half-mesh. The smaller grid size, however, required a smaller time step even for the Brown-Campana scheme. The only successful comparisons, then, are between 26x21 grids of RLAM with the interior of a 39x33 grid of the RWM, where the data for both have been gleaned from the RWM 30 November 1985 file.

Table 2 compares the σ structure of the GSM with the RWM. Notice that not only the number of σ layers but also the configuration of the layers are different, with the RWM distributing its layers more evenly, while the GSM increases its resolution in the boundary layer and at the tropopause. Fig. 3 shows the RMS differences between the RWM and the RLAM for a 24 h forecast from RWM data. The RLAM forecast was second-order, insert boundary, with physics. The differences are close to those in Fig. 1 with somewhat higher differences near the surface. On the whole, however, the two differ by about as much as the GSM from the RLAM.

Fig. 4(a) shows difference contours between temperature T at σ-layer 1 forecast by the RLAM with second-order differencing, sponge boundary conditions, and no physics, and T forecast by the GSM. Fig. 4(b) is the same plot except for the RLAM with physics. There are noticeable differences between the two because of the planetary boundary conditions, especially near the lateral boundaries, where data from the GSM interact with the RLAM. Fig. 5(a) shows the contours from a RLAM 24 h forecast of temperature at σ-layer 4 with a directly inserted boundary, regular fourth-order differencing, and without physics or diffusion but with smoothing at every time step. Fig. 5(b) is the same but for fc differencing and 4Δ smoothing at each time step. Although similarities between the two forecasts exist, the more intense smoothing of the fc has an obvious result, especially in the interior.

16

Table 2.   σ-structures for the 12-layer AFGL GSM and the 10-layer RWM

GSM		RWM	
layer	**σ**	**layer**	**σ**
1	.962326	1	.975
2	.961960	2	.925
3	.724074	3	.850
4	.573831	4	.698
5	.436433	5	.498
6	.337003	6	.362
7	.274729	7	.287
8	.224668	8	.211
9	.174573	9	.136
10	.124400	10	.040
11	.073986		
12	.020747		
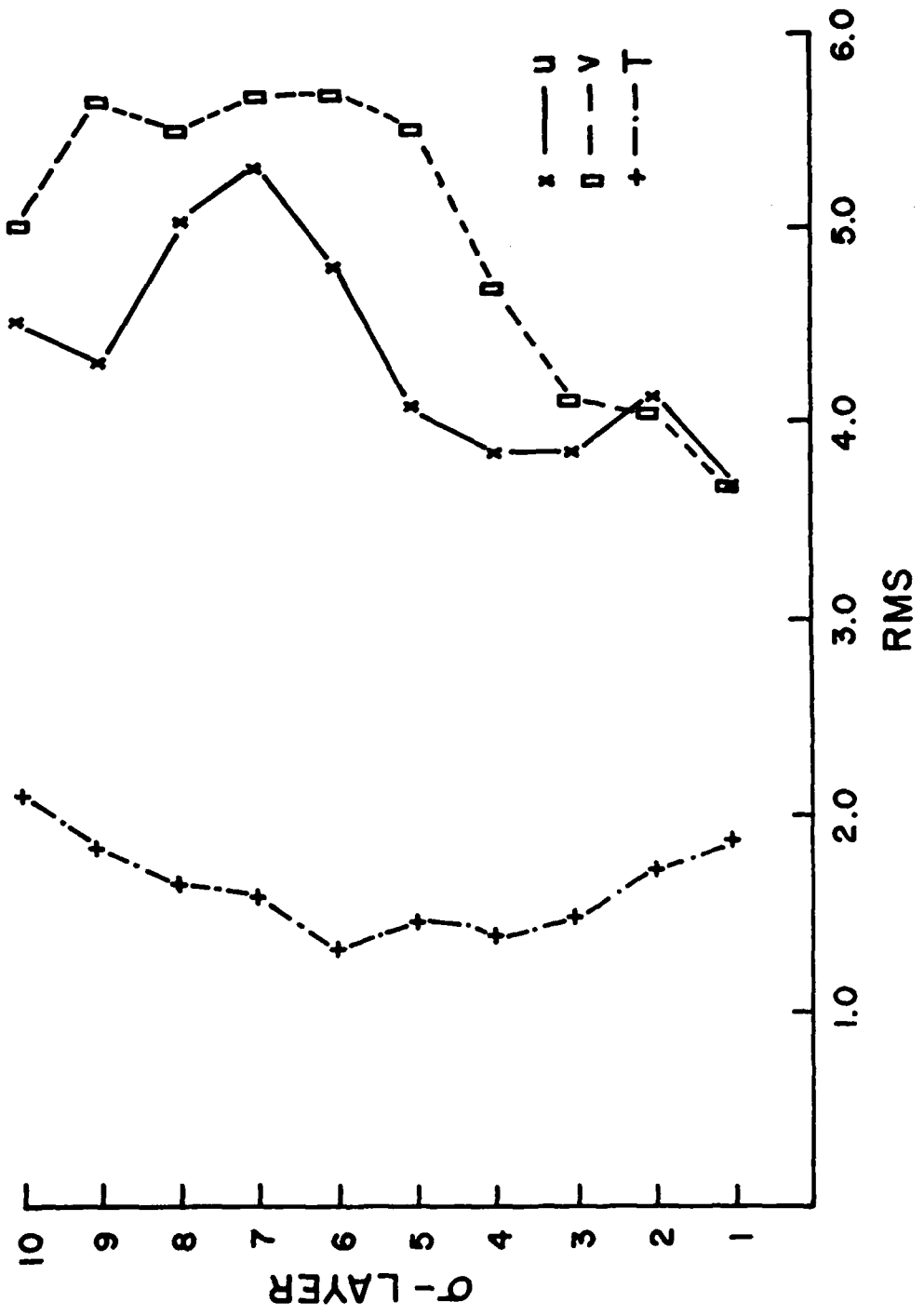
Fig. 3 RMS Differences between 24 h Forecasts of u, v, and T for All 10 σ-layers of the RMS and Forecasts of the RLAM Run with Brown-Campana Time Differencing, Directly-inserted Boundaries, Physical Parameterizations, Second-order Spatial Differencing, and Smoothing Every Third Time Step at the Boundaries and Every Nine for the Entire Field
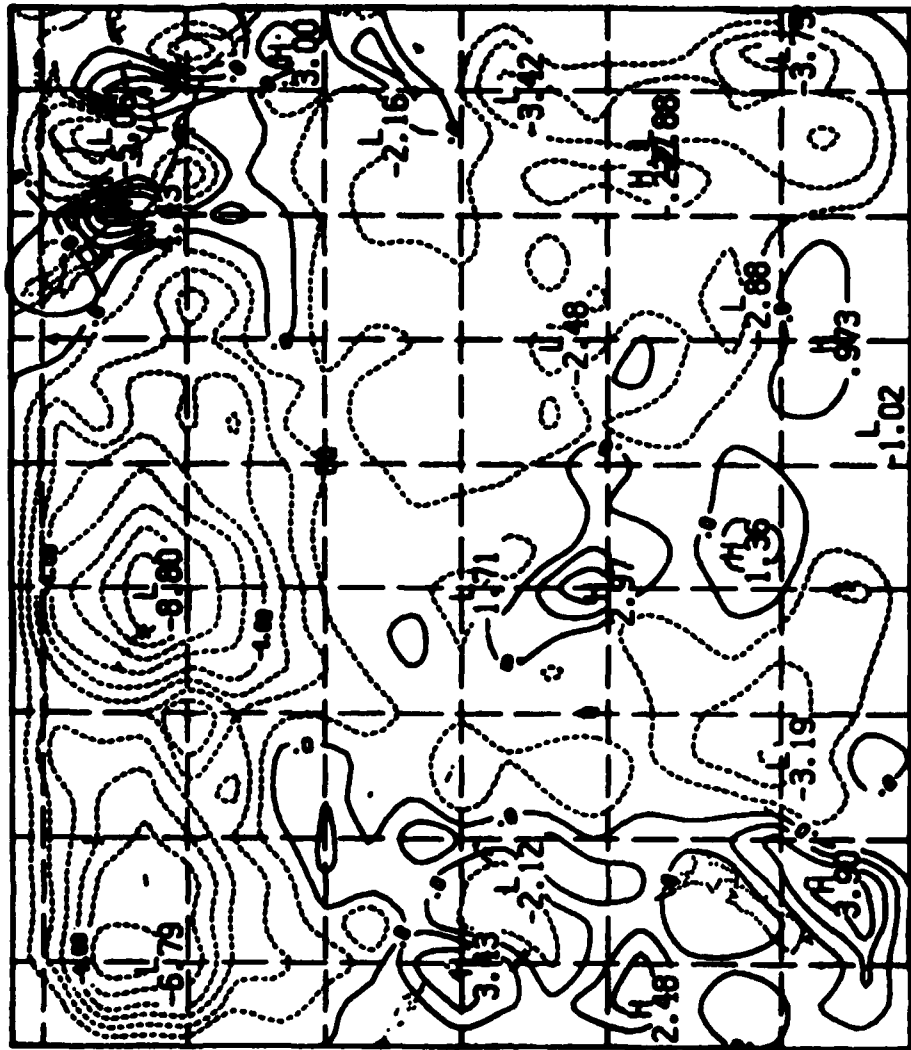
Fig. 4(a) Difference Contours of 24 h Forecast of T (1°C intervals) at σ-layer 1 Made with the RLAM Using Second-order Spatial Differencing with Smoothing at Three and Nine Time Steps, Sponge Boundaries, and No Physical Parameterizations vs. Forecast Made with the GSM

(Solid lines indicate positive values; broken lines indicate negative values.)
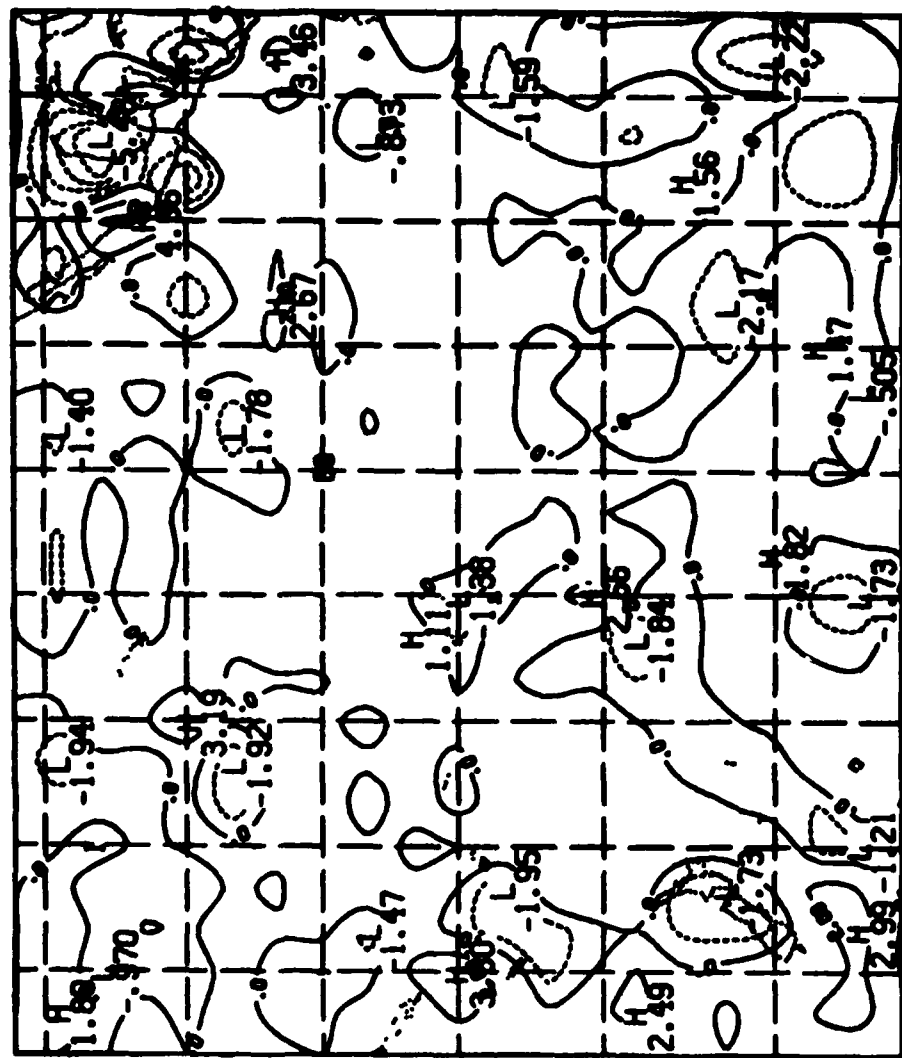
Fig. 4(b) Difference Contours of 24 h Forecast of T (1°C intervals) at σ-layer 1 Made with the RLAM Using Second-order Spatial Differencing with Smoothing at Three and Nine Time Steps, Sponge Boundaries, and Physical Parameterizations vs. Forecast Made with the GSM (Solid lines indicate positive values; broken lines indicate negative values.)
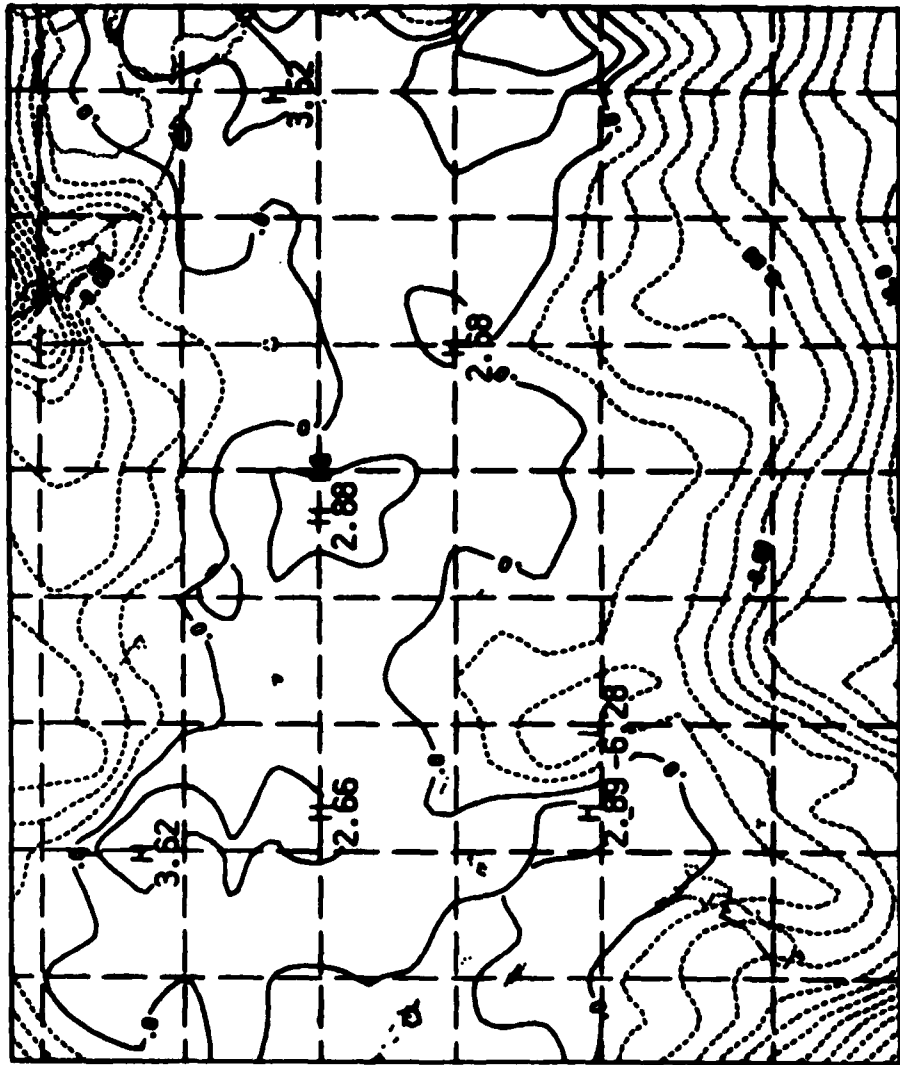
Fig. 5(a) Contours of 24 h Forecast of T at σ-layer 4 RLAM without Physics, with Directly-inserted Boundaries, Brown-Campana Temporal Scheme, and Fourth-order Regular Spatial Differencing and 2Δ Smoothing-desmoothing Every Time Step

21
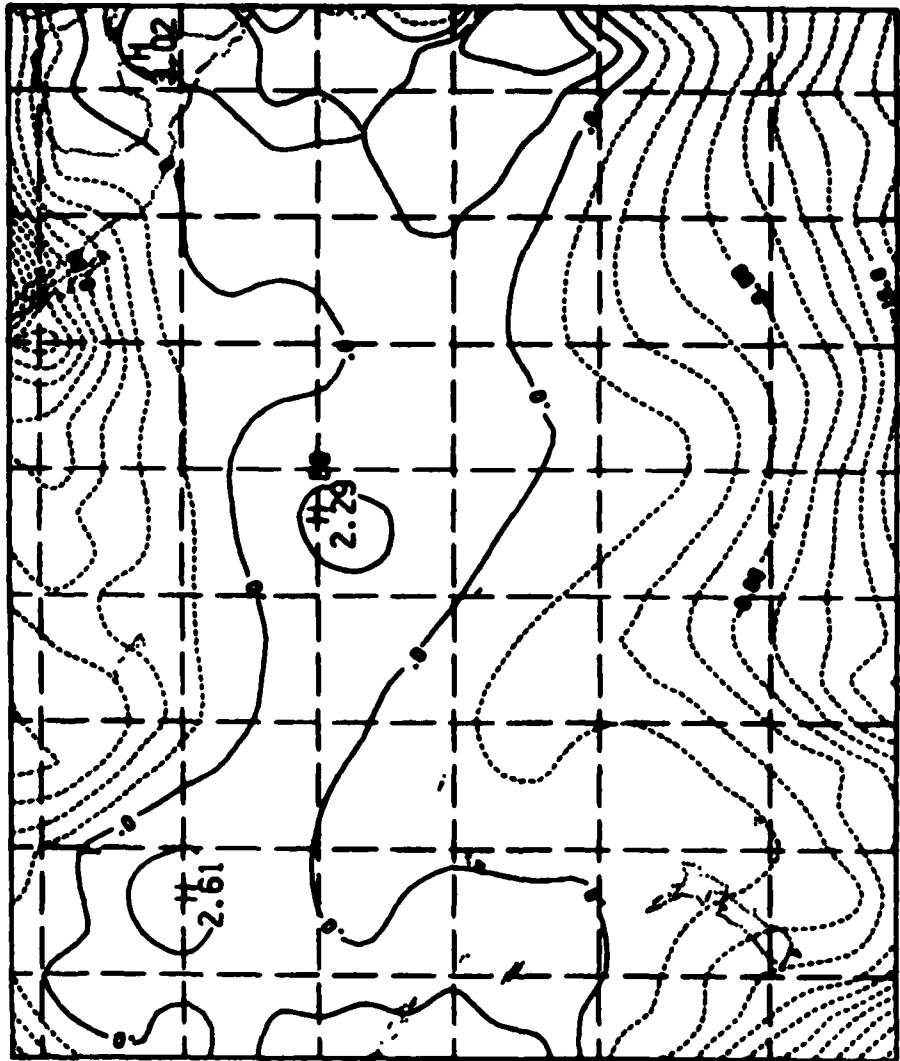
Fig. 5(b) Contours of 24 h Forecast of T at σ-layer 4 from RLAM without Physics, with Directly-inserted Boundaries, Brown-Campana Temporal Scheme, and Fourth-order Compact Spatial Differencing and 4% Smoothing-desmoothing Each Time Step

Fig. 6(a) is the T field for the RWM at its layer 4 after 24 h. The field is for the mercator projection and is the interior portion of the original 39x33 grid size. Fig. 6(b) is the RLAM 24 h T forecast for the same region and σ-layer but the domain was originally a 26x21 grid size and covered only the area displayed. The horizontal differencing was second-order, physics was included, and smoothing was performed over the entire field every three time steps. The boundary data were inserted at each time step and were gleaned from the same database as the RWM. The RWM derives its boundary values by computing 6 h tendencies from observed data and applying the tendency to each time step. Thus the boundary values applied to the 26x21 RLAM were not related to the RWM data at those grid points. Still, as Figs. 6(a)-(b) demonstrate, the two models produced temperature fields that were quite close. It is suspected that if RWM-produced data were employed as boundary data for the 26x21 RLAM, a greater correlation would exist.

4. Summary and Conclusion

The RLAM has been developed to the point where it can be run with a selection of differencing schemes and resolutions. Most of the current testing has included comparisons with the AFGL GSM and the RWM. Several of the options available under the RLAM are still not viable even if they remain stable for 24 h; e.g., the fc spatial differencing which requires a great deal of smoothing. Various temporal schemes are available, such as leap-frog and a Brown-Campana pressure averaging procedure, while an implicit scheme is available but not yet perfected. A physical package identical to the one on the RWM has been added to the RLAM and seems to function well, producing boundary layer fluxes and moist convection and precipitation. These compare well with the RWM for the same dates and locations but do not give exactly the same results even for the physical parameters that are the same in both the RLAM and RWM.

Lateral boundary conditions are very important to the RLAM as they are to most regional models. The RLAM offers a choice of several types of boundary conditions, but each requires a separate type of data input. The sponge boundary requires five rows of tenden¹·-- om the GSM, whereas the porous sponge requires none. The directly inserted boundaries require only
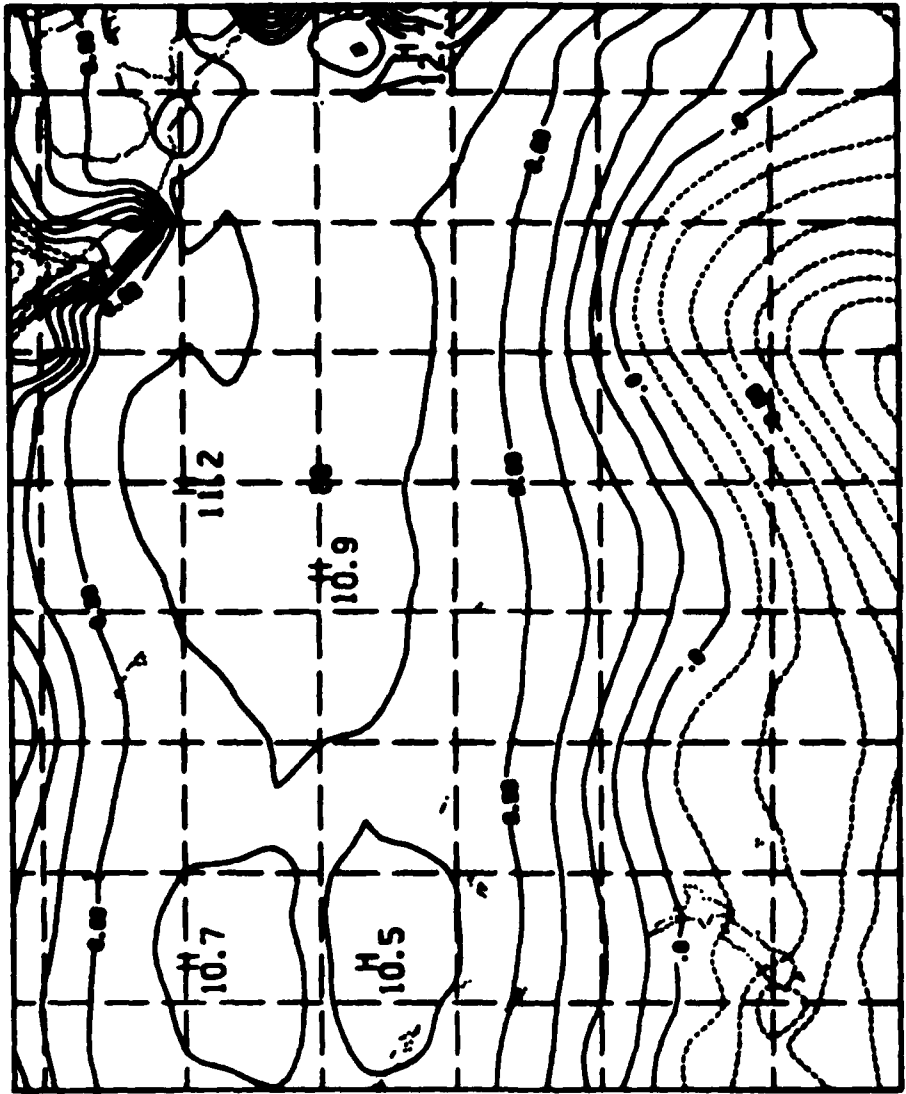
Fig. 6(a) Contours of 24 h Forecast of T at RMM σ-layer 4 from the RMM Using a Larger Domain (39x39 grid points)
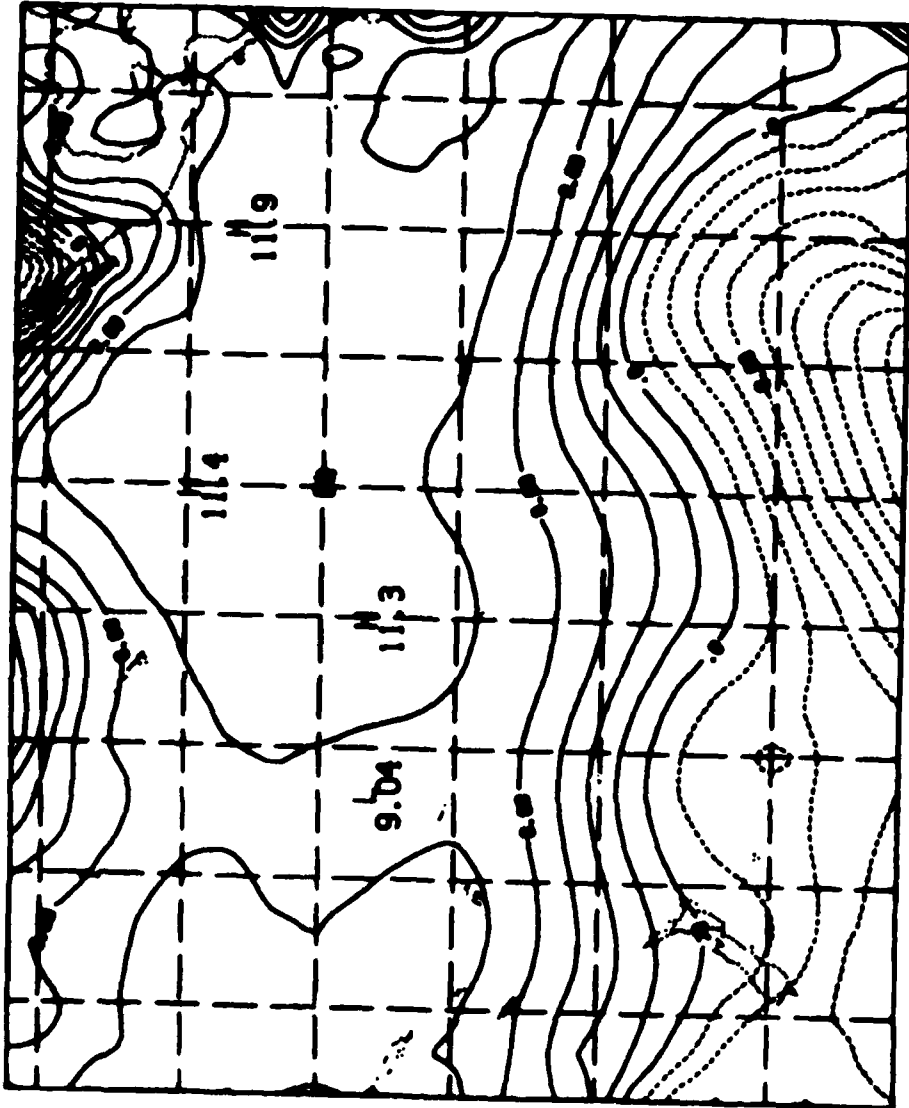
Fig. 6(b) Contours of 24 h Forecast of T at RAM σ-layer 4 from the RLAM with
Directly-inserted Boundaries, Second-order Differencing with Smoothing of Entire Field Every
Three Time Steps, Brown-Campana Temporal Differencing, and Physical Parameterizations

(The RLAM domain is exactly as depicted (26x21 grid points).)

one row of actual values for second-order differencing but two rows of
values for fourth-order regular differencing. For fc differencing, it is
possible to supply derivatives at the boundaries. The Orlanski (1976)
radiation boundary, although not fully operational, requires either no
exterior data or, at most, one row of GSM tendencies. On the other hand,
the LFM boundaries require several rows of actual data. This assortment of
data requirements diminishes the effectiveness of the RLAM in allowing
options for boundary conditions. Therefore a generalized procedure file was
devised to produce exactly the right type of boundary data for most of the
boundary conditions available. The procedure, however, is machine-dependent
and works only in a CDC/NOS 2 environment.

The RLAM can serve as a convenient vehicle for testing various
numerical and physical approximations and parameterizations for different
synoptic situations. It has the versatility needed to implement countless
numerical experiments. It is, however, by no means complete; many more
options can and should be added to the RLAM to make it a truly effective
research tool. Also, much more testing and streamlining should be performed
to insure that its components are indeed functioning properly.

5. References

Adam, Y., 1977: Highly accurate, compact, implicit methods and
boundary conditions. J. Comp. Physics, 24, 10-22.

Asselin, R. A., 1972: Frequency filter for time integrations. Mon.
Wea. Rev., 100, 487-490.

Brown, H. A., and K. A. Campana, 1978: An economical time differencing
system for numerical weather prediction. Mon. Wea. Rev., 106, 1025-1036.

Gerlach, A. M., ed., 1984: Objective Analysis and Prediction
Techniques - 1984. AFGL-TR-84-0328, Contract F19628-82-C-0023, Systems and
Applied Sciences Corp., ADA160377.

Gerlach, A. M., ed., 1985: Objective Analysis and Prediction
Techniques - 1985. AFGL-TR-86-0002, Contract F19628-82-C-0023, SASC
Technologies, Inc., ADA169746.

Mathur, M. B., 1983: A quasi-Lagrangian regional model designed for
operational weather prediction. Mon. Wea. Rev., 111, 2087-2098.

McGregor, J. L., T. M. Leslie, and D. J. Gauntlett, 1978: The ANMRC limited-area model: consolidated formulation and operational results. Mon. Wea. Rev., 106, 427-438.

Miller, M. J., and A. J. Thorpe, 1981: Radiation conditions for the lateral boundaries of limited-area numerical models. Quart. J. Roy. Met. Soc., 107, 615-628.

Newell, J. E., and D. G. Deaven, 1981: The LFM-II Model, 1980. NOAA Tech. Memo, NWS NMC 66, 20 pp. [Available from Environmental Science Information Center (D822) NOAA, 6009 Executive Boulevard, Rockville, MD 20852]

Orlanski, I., 1976: A simple boundary condition for unbounded hyperbolic flows. J. Comp. Phys., 21, 251-269.

Perkey, D. J., and C. W. Kreitzberg, 1976: A time-dependent lateral boundary scheme for limited-area primitive equation models. Mon. Wea. Rev., 104, 744-755.

Robert, A. J., 1982: A semi-Lagrangian and semi-implicit numerical integration scheme for the primitive meteorological equations. J. Meteor. Soc. Japan, 60, 319-325.

Robert, A. J., T. L. Yee, and H. Ritchie, 1985: A semi-Lagrangian and semi-implicit numerical integration scheme for multi-level atmospheric models. Mon. Wea. Rev., 113, 388-394.

Shapiro, R., 1970: Smoothing, filtering, and boundary effects. Rev. Geophys. Space Phys., 8, 359-387.

II. MESOSCALE FORECASTING

A. An Error Analysis of LFM Forecasts Using the FOUS 60-78 Bulletins

Research performed and its results are described and summarized in a
paper with the above title appearing in the preprint volume for the Eleventh
Conference on Weather Forecasting and Analysis held in Kansas City, MO, on
June 17-30, 1986, sponsored by the American Meteorological Society.

Reference

Schechter, R., 1986: An error analysis of LFM forecasts using the FOUS
60-78 bulletins. Preprints, Eleventh Conference on Weather Forecasting and
Analysis, Kansas City, MO; AMS, Boston, 67-71.

III. BOUNDARY LAYER METEOROLOGY

A. Refractive Index Study

In 1986 AFGL continued to investigate tactical tropospheric scatter
radio links in support of an Air Force Electronic Systems Division study.
By analyzing data archived onto magnetic tape from refractometers mounted on
small aircraft and flown at varying altitudes, the refractive index
structure C_N2 can be derived.

Two refractometers mounted under opposite wings of a Cessna 172
aircraft were flown over Chatham, MA in a series of test flights in
September 1985. Data from these flights formed the basis for STX
computerized processing and analysis efforts.

The sampled data in voltage form were fed to software developed for the
AFGL mainframe CDC Cyber 860. These programs converted the voltages to the
frequency domain by means of Fast Fourier Transforms. The spectral
amplitudes and phase were adjusted to corrected values by a frequency gain
calibration array using interpolation. This was done to remove the effects
of prewhitening filters located in the refractometers. The spectral data
were saved for input to VAX-resident analytical routines. The Cyber
programs produced diverse estimates of C_N2 using data from several
frequency bands.

To use VAX software the saved data were formatted and then streamed
from the Cyber to the VAX over the AFGL hyperchannel. Software was devised
to arrange these data into records of 512 values each, alternating records
of each of the two refractive index channels recorded. Headings were added
to provide such information as type of data channel recorded, air speed,
number of records at each level of flight, etc.

After the data were prepared in proper format, the Iterative Signal
Processor (ISP) software system on VAX was invoked. A specific set of
routines (NTQ) written in ISP language and designed to facilitate analysis
of sampled voltages was used. Fig. 1 shows results obtained from using the
first eight data records from each of the two refractometers flown in level
flight over Chatham on 25 September 1985. The data were detrended to remove
the linear trend and DC bias, as shown. The power spectrum average using
Fast Fourier Transforms was achieved for each refractometer channel and then

29

```
ISP>GET 'NTQNEW'
ISP>ASN 'ISP002'
File title is
TITL=CHAT
File record size is
$LEN=        512
Sampling interval is
$SI =   1.562500E-02
Air speed is
$VA =    51.4800
Number of channels is
$NCH=          2
ISP>DTR '002D',8,0
Channel Number is
    =           1
Linear Trend is
    =   6.734220E-06
DC Offset is
    =  -2.962133E-02
Channel Number is
    =           2
Linear Trend is
    =   1.201702E-05
DC Offset is
    =  -7.776964E-02
ISP>PHI N
ISP>PHI T
ISP>AVGF N
ISP>AVGF T
ISP>CXSQ N
```

```
    C N^2 ESTIMATES FROM BAND AVERAGES
   BAND    PTS        K           C N^2

     1     26      0.20596     0.364921E-02
     2     25      0.59500     0.246288E-02
     3     26      0.98404     0.288377E-02
     4     25      1.37307     0.302188E-02
     5     26      1.76211     0.330281E-02
     6     25      2.15115     0.278832E-02
     7     26      2.54019     0.313724E-02
     8     25      2.92922     0.283402E-02
     9     26      3.31826     0.219733E-02
    10     26      3.71493     0.293145E-02
ISP>CXSQ T
```

```
    C T^2 ESTIMATES FROM BAND AVERAGES
   BAND    PTS        K           C T^2

     1     26      0.20596     0.852716E-02
     2     25      0.59500     0.533270E-02
     3     26      0.98404     0.710136E-02
     4     25      1.37307     0.609964E-02
     5     26      1.76211     0.328672E-02
     6     25      2.15115     0.203087E-02
     7     26      2.54019     0.157009E-02
     8     25      2.92922     0.594566E-03
     9     26      3.31826     0.339282E-03
    10     26      3.71493     0.208498E-03
```

Fig. 1 Refractive Index Structure Functions from Two Refractometers (N, T)
Flown over Chatham, MA

gathered into ten linearly spaced bands. The wavenumber averages, power spectrum averages, and distribution of points were saved for follow-up calculation. C_N2 estimates from the computed band-averaged spectral data were derived using the 5/3 law

$$C_N2 = 4 \phi_N(K)\underline{K}^{5/3}$$

where $\underline{K}$ is the averaged wavenumber and $\phi(\underline{K})$ is the spectral value associated with the wavenumber obtained by averaging over the spectral values in the band. The second channel, labeled "T" in Fig. 1, was intended to be used for temperature but in this case is used to input the second refractive index channel "N_2".

The computed magnitude squared coherence and phase in degrees of the two channels are shown in Fig. 2. Raw data cospectra from the two refractometers indicate that for wavenumbers less than .2 there is reasonably good coherence and the phase spectra between signals indicate they are in phase. Above .2 the coherence is poor and the phase erratic. These results are not unexpected for two sensors flown in a turbulent medium, since .2 wavenumber represents about 80 ft and the sensors are mounted 15 ft apart. One would expect coherence only when the wavelength is greater than four times the sensor separation or about 60 ft and would expect it to decay for shorter wavelengths.

B. Surface Layer Windflow Model

AFGL meteorologists have been developing a computer model to predict the toxic hazard corridors that would result from an accidental chemical release at an Air Force installation. WADOCT (Windflow and Diffusion Over Complex Terrain) combines a surface layer windflow model with a Gaussian puff diffusion model. Most of 1986 was devoted to developing and checking out the two parts of the model separately, with STX primarily concerned with the windflow portion.

Terrain data describing the environs of the Vandenberg AFB, CA shuttle and missile launch facilities were acquired. Wind and temperature data collected from ten instrumented towers located at Vandenberg also were received. STX devised software to produce contour plots and a three-dimensional display of the terrain (Figs. 3 and 4) to assist

31
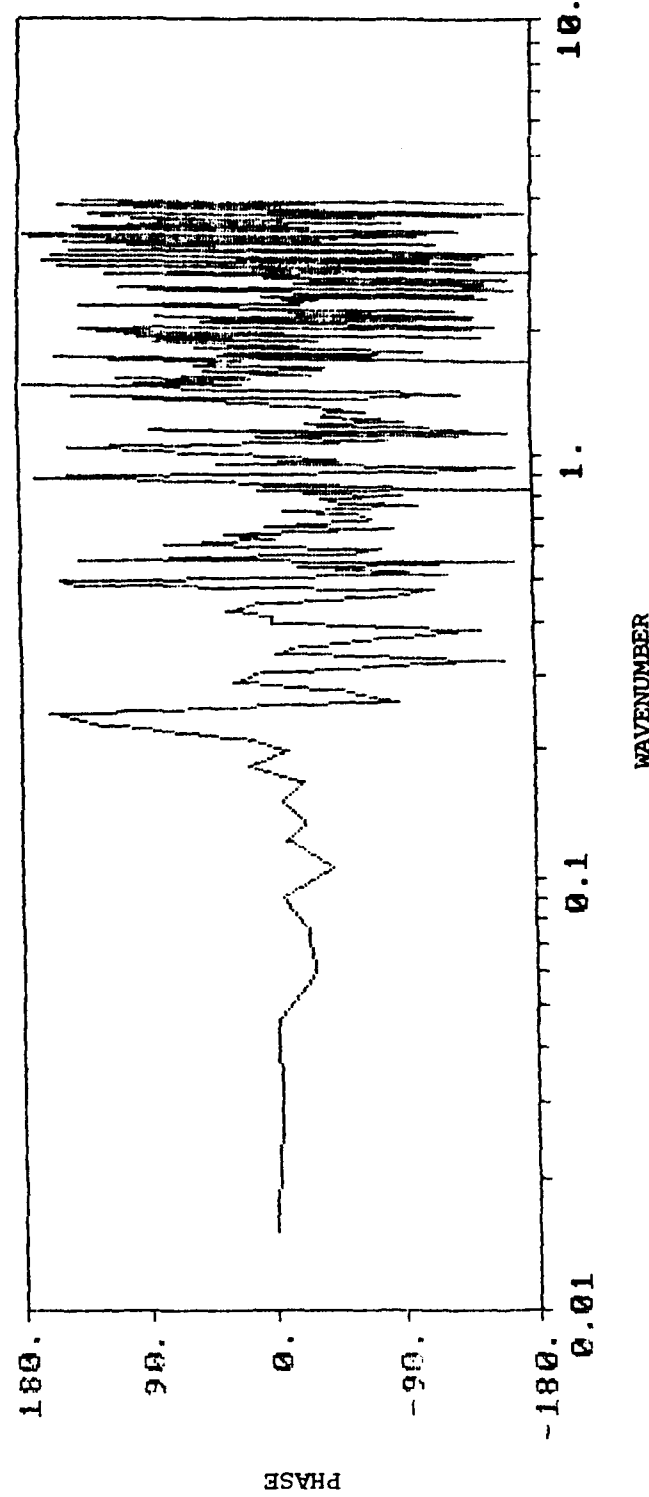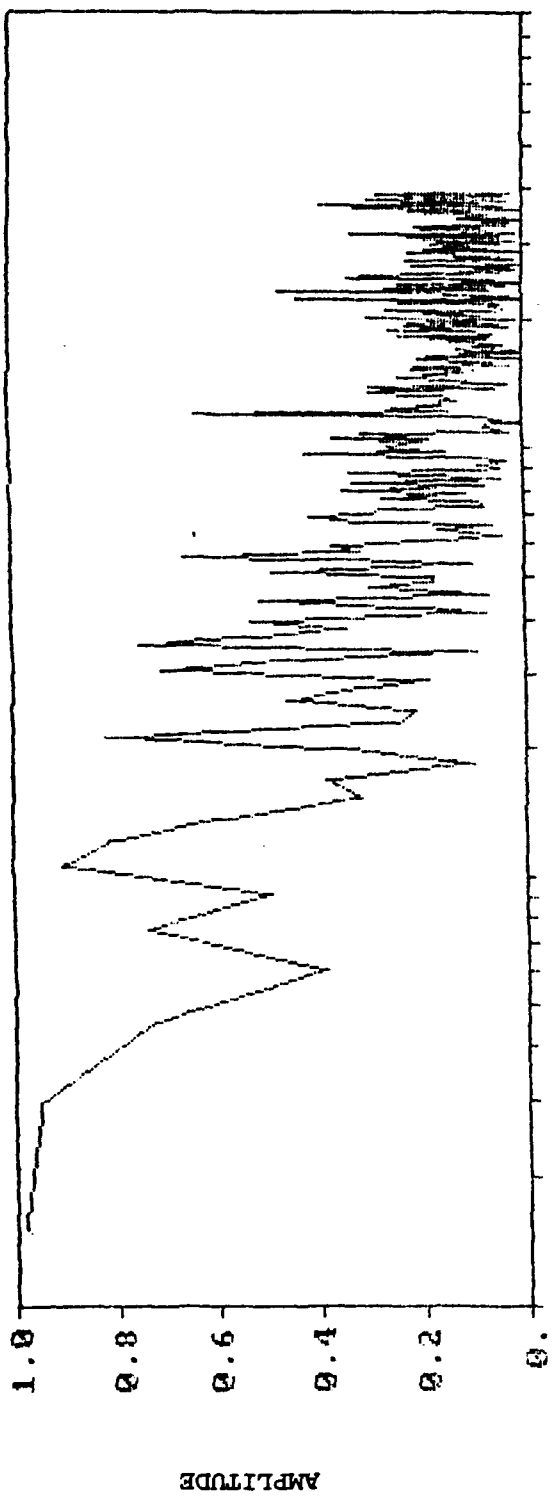
Fig. 2 Refractive Index Cross Correlation Spectra from Two Refractometers Flown at Chatham, MA. on 25 September 1985
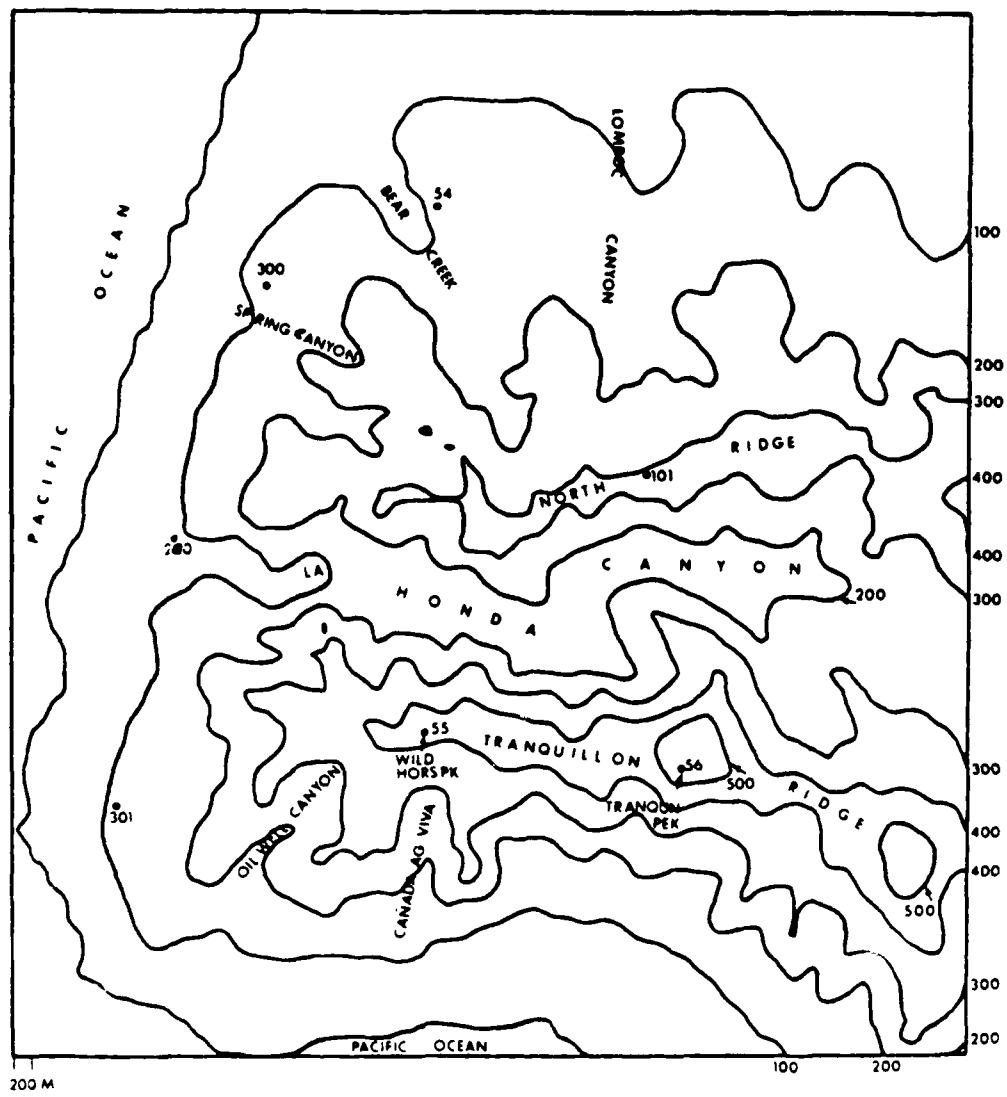
Fig. 3 Contours of South Vandenberg AFB Showing Instrumented Tower Locations

33
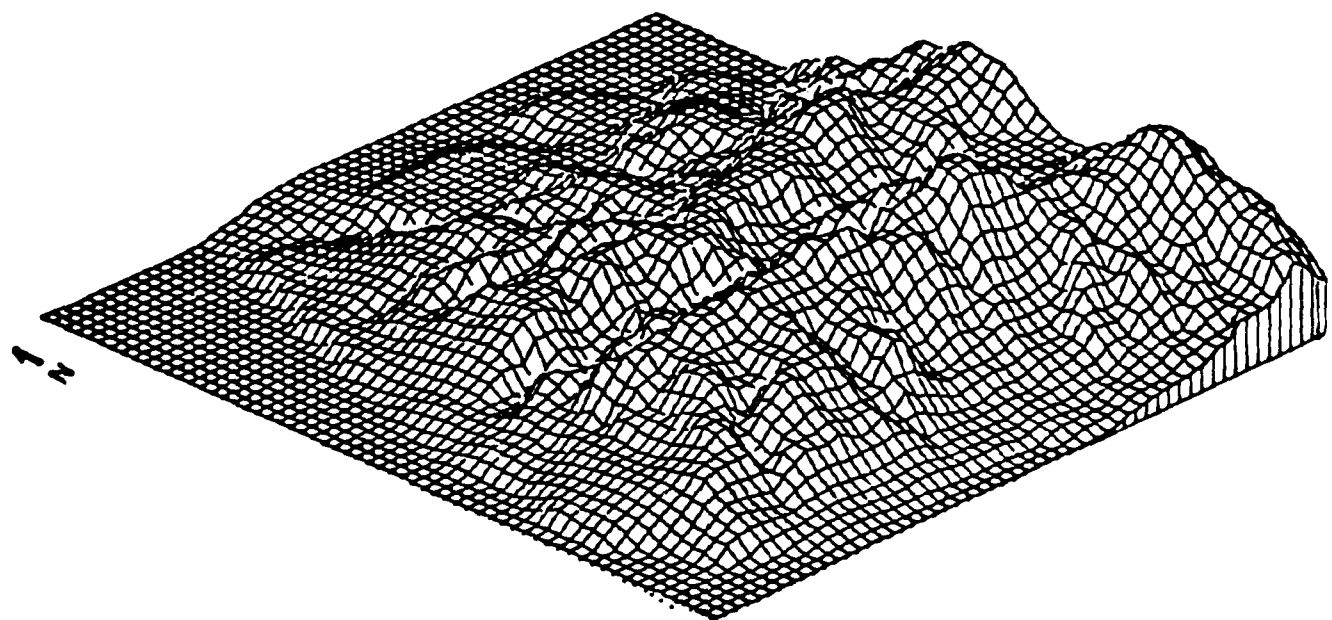
Fig. 4 3-D Display of Vandenberg AFB Terrain Generated by Windflow Model Utility Program

researchers in understanding the complexity of the boundary layer in this mountainous coastal region.

The windflow model performs a variational analysis of surface layer winds in the x-y plane to induce an initial wind field to conform to constraints of topography, buoyancy forces, advection of momentum, and conservation of mass. The driving equations for this system attempt to minimize a volume integral relating momentum advection to buoyancy forces. When the minimum value is attained, the system is said to be in quasi-steady balance between the constraints (Lanicci and Weber, 1986). The resultant windfield over the terrain is output to a Houston plotter either in the form of wind vectors (Fig. 5) or in standard wind plot notation, and can be shown in either form on the Zenith Z-100 microcomputer screen. Wind vector data and the wind profile exponent derived by the model are archived for further study.

An area 11.2 km in the east-west direction and 12.2 km in the north-south direction covering the South Vandenberg launch complex was selected from the Vandenberg data. This produced a model domain array of 56x61 using a 200 m horizontal grid spacing. The model that had been tested in 1985 using the relatively simple, flat terrain of Ft. Polk, LA with only a single meteorological input, was modified for the Vandenberg study to accept either a single climatological input or multiple observational inputs derived from tower sensors. The latter option then uses an objective analysis scheme to derive non-homogeneous initial conditions for input to the model.

Tower data tapes recorded at 60, 15, and 5 min intervals were archived onto the AFGL Cyber 860 mainframe computer. From this database, eight cases of 15 min data and two cases of 60 min data were chosen. Seven towers located in the selected model domain were used for the study. Root mean square error (RMSE) statistics were compiled by first removing the data from one tower at a time and predicting wind values by using the other six. The experiment then proceeded by removing towers two at a time, then three at a time, etc., until every combination of towers had been removed and the results verified with each prediction. A total of 127 runs of the model was made for each of the ten cases selected. The results showed that the windflow model, using a mean vector wind input, produced better verification than the multiple tower input objective analysis scheme.

35

DX = 200. METER

5.0 M/SEC
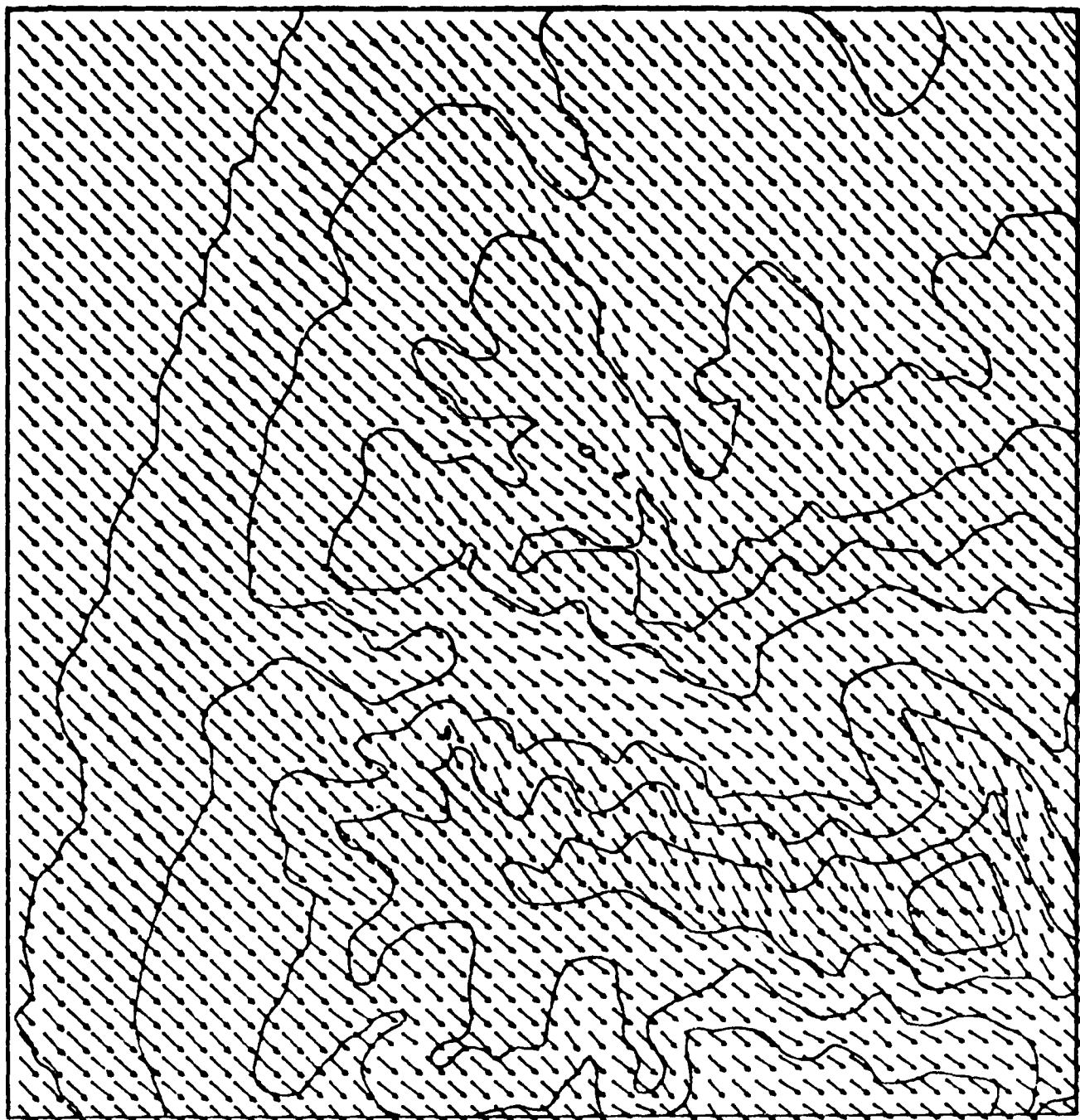
LOWER LEFT GRIDPOINT OF PLOT
IS GRIDPOINT (1, 10) OF VAN.DAT

Fig. 5   Sample Windflow Model and Contour Program Output

36

The statistics also showed that the RMSE's of the model were rarely better than the standard deviation of the mean vector wind. Further examination of verification statistics at individual towers revealed that two of the towers, located in the high terrain of Tranquillon Ridge, were in a wind regime different from that of the lower-lying towers in nearly half the cases, thus negating superior model performance at the other five towers.

The Air Force weather detachment at Ft. Devens, MA became interested in the AFGL windflow model as a tool to be used in providing weather support for Army paradrop operations. Accordingly, STX developed a simplified version of the AFGL windflow model for use in weather operations. Terrain data for east central Massachusetts were reduced to a domain file containing a 44x69 array with 200 m horizontal grid spacing. A further reduction to a 21x21 array covering only the drop zone at Ft. Devens was provided as well (Fig. 6). The model was set to use a single input of wind, temperature, and cloud cover to initialize it. The model and two utility plotting programs were confined to one floppy disk for use on a Z-100 computer available at Ft. Devens. Working with airfield forecasters led to devising simpler interactions with model operators. Calculations previously lost after the model run were archived and then retrieved automatically under software control as inputs to resultant wind field and power-law profile displays (Figs. 7 and 8). The profile estimation of wind speed from the surface to 300 ft, the upper limit of the profile program, was especially of interest to those involved in the parachute drops.

Preliminary results indicate that for predominant wind directions (southerly to northwesterly), significant terrain effects on the wind field are dominant at speeds below 5 to 8 kt; at higher speeds the model produces uniform flow conditions. Air Force forecasters at Ft. Devens showed great enthusiasm for the model as a useful tool to support low level tactical aviation and paradrop operations.

Reference

Lanicci, J. M., and H. Weber, 1986: Evaluation of a surface-layer windflow model for complex terrain using meteorological tower data from Vandenberg AFB, CA. Preprints, Fifth Joint Conference on Applications of Air Pollution Meteorology, Chapel Hill, NC; AMS, Boston, 265-268.
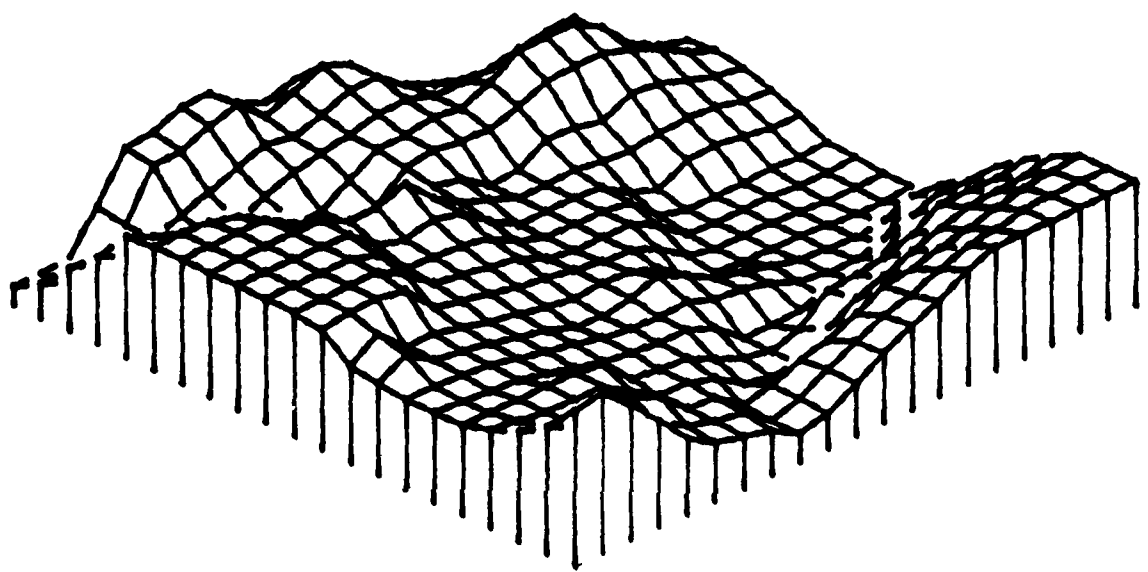
Fig. 6   3-D Display of Turner Dropzone Terrain at Ft. Devens, MA Generated
by Windflow Model Utility Program
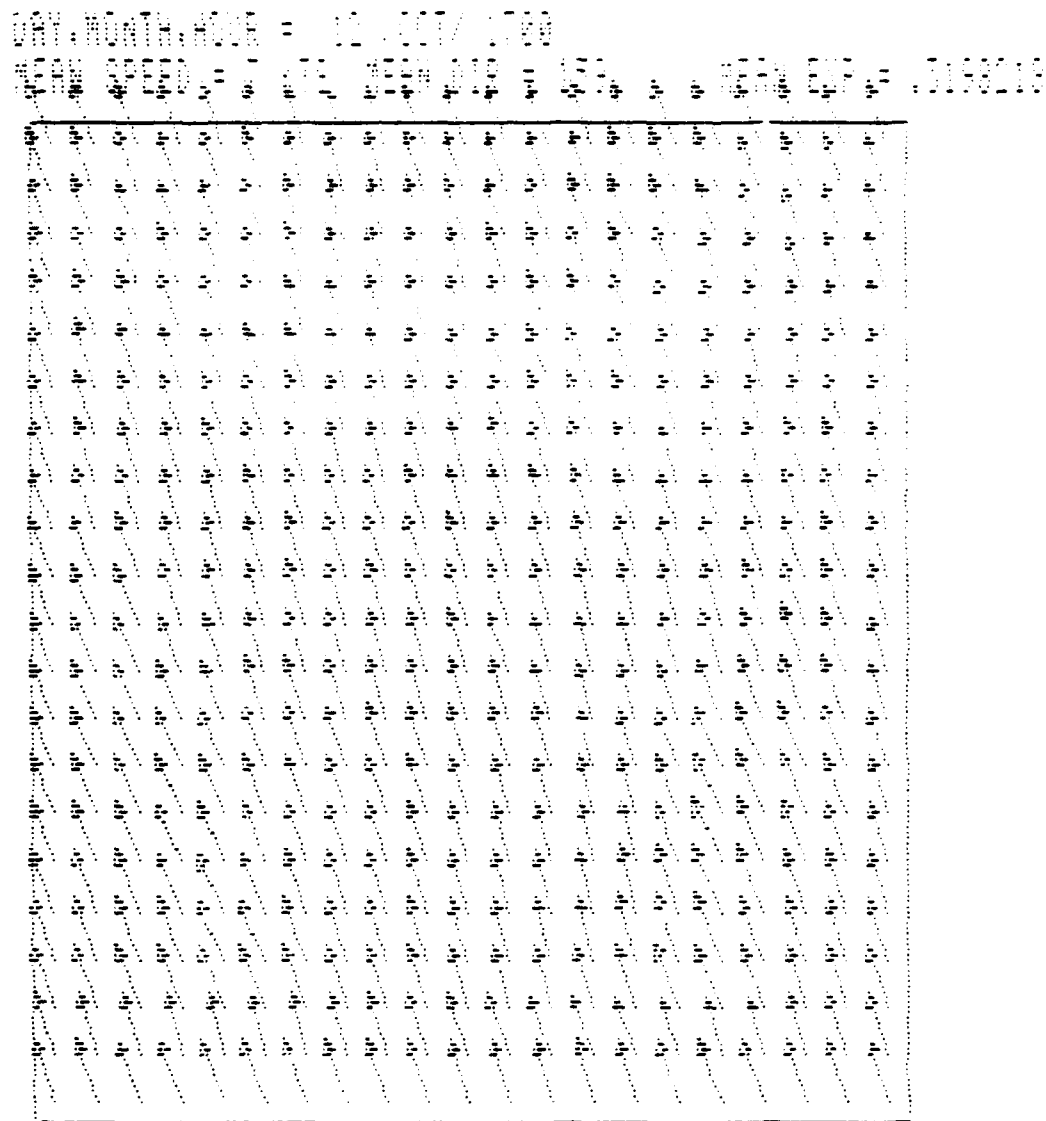
Fig. 7   Hardcopy of Z-100 Model Output of Windfield over Dropzone at Ft. Devens
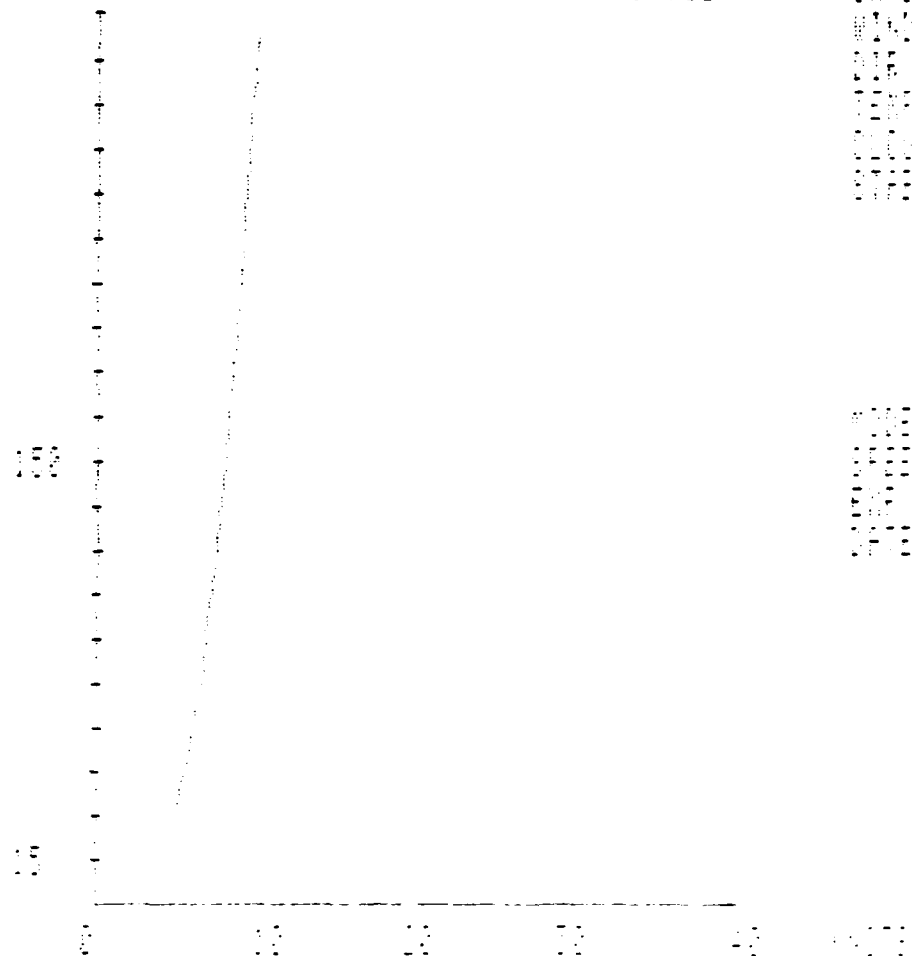
Fig. 8 Model Wind Speed Profile over Ft. Devens Dropzone

(Input and output conditions displayed to right of plot.)

C. AFGL Weather Test Facility

STX has been responsible for maintaining and operating the AFGL Weather Test Facility at Otis Air National Guard Base near Falmouth, MA. In addition to daily site and instrumentation maintenance and repair, special field activities were also undertaken.

Two Present Weather Identification systems were installed for subsequent test and evaluation. They are a VR-301 manufactured by HSS, Inc., Bedford, MA and a LEDWI (Light Emitting Diode Weather Identifier) produced by Scientific Technologies, Inc., Gaithersburg, MD. The HSS, Inc. VR-301 identifies type and intensity of precipitation and measures visibility. The LEDWI identifies type, intensity, and accumulation of precipitation but does not measure visibility.

Data from these instruments were acquired during periods of inclement weather, together with human visual observations and data recorded by three types of rain gauges, transmissometers, forward scatter visibility meters, temperature-dewpoint sets, and wind speed/direction sets.

A recently installed atmospheric temperature profiler developed by Ophir Corp., Lakewood, CA is a passive sounding system for obtaining a vertical temperature profile from the surface to approximately 15,000 ft. It consists of a radiometer, various infrared filters for measuring IR radiation at different wavelengths, a moving head to sense at different wavelengths, a moving head to sense at different angles of elevation, and a computer to control the sensing head and to process the data. Radiosonde balloon flights were conducted to obtain direct temperature measurements for evaluation of the Ophir system.

The AFGL/WTF data acquisition system (MAWS) was badly damaged by a near-miss lightning strike. The system was repaired although, because of its age, some components were impossible to acquire. Work was begun to assemble a replacement data acquisition capability based on two Zenith 248 computers.

IV. RADAR METEOROLOGY

A. Detection of Synoptic-Scale Wind Anomalies

1. Introduction

Wind field analysis through use of a single Doppler radar was first suggested by Probert-Jones (1960). He observed the component of motion of snow along his radar beam at two different azimuth angles and deduced the wind speed and direction appropriate to both azimuths. The VAD (Velocity Azimuth Display) scan was offered by Lhermitte and Atlas (1961). It is a simple and efficient technique for systematic estimation of wind speed and direction when suitably reflective wind tracers surround the radar. In the VAD mode, the radar antenna is set into a conical scan about a vertical axis, at a fairly low elevation angle in order to prevent excessive contribution to the Doppler velocity measurements by precipitation fall speeds. These measurements, recorded at a particular range during a complete 360° scan in azimuth, provide information on the wind field along the VAD scanning circle at a height given by range and elevation angle.

Both Probert-Jones and Lhermitte and Atlas recognized the underlying assumption in their techniques of a horizontally uniform wind vector throughout the area of observation. Eventually the uniformity assumption was replaced by a less restrictive linearity. Browning and Wexler (1968) extended the VAD technique to a consideration of non-uniform wind fields that vary linearly in the horizontal plane. A linear wind field is also a necessary assumption in the generalized VVP method (Volume Velocity Processing) developed by Waldteufel and Corbin (1979).

Passarelli (1983), summarizing his critique of single-Doppler techniques, deplored the inadequacy of the linearity assumption. Inspired by his commentary, Donaldson and Harris (1984) examined some of the features of Doppler VAD patterns synthesized in a curved wind field, as well as in a linear field with gradients. Their results helped to clarify some earlier Doppler radar observations of a hurricane (Donaldson et al., 1978), in which the assumption of a linear wind field would have been inappropriate. In the current study, we consider all four first-order derivatives of wind speed and direction and develop methods for recovery of these derivatives, to whatever extent possible, from observed Doppler VAD patterns.

42

2. First Derivatives of the Wind Field

The analysis is limited to first-order spatial derivatives of wind velocity in a horizontal plane. The derivatives are expressed in natural coordinates referred to the streamlines. In the natural coordinate system the s-axis is tangent to a streamline with s increasing downwind, the n-axis is normal to a streamline with n increasing to the left of the wind vector, and V is wind speed at the origin of the natural coordinate axes. A change in wind direction is denoted by the angle ψ, which is positive toward the n-axis. Both speed and direction may vary along either of the coordinate axes, and so there are four independent first-order derivatives: $\partial V/\partial s$ (downwind shear), $\partial V/\partial n$ (crosswind shear), $V \partial\psi/\partial s$ (curvature), and $V \partial\psi/\partial n$ (diffluence).

It is well known (e.g., Petterssen, 1956) that the kinematic properties of a wind field are given by sums and differences of its first-order derivatives. Expressed in natural coordinates, the kinematic properties are

Divergence	$= \partial V/\partial s + V \partial\psi/\partial n$	(1)
Stretching Deformation	$= \partial V/\partial s - V \partial\psi/\partial n$	(2)
Shearing Deformation	$= V \partial\psi/\partial s + \partial V/\partial n$	(3)
Vorticity	$= V \partial\psi/\partial s - \partial V/\partial n$.	(4)

The first three of these kinematic properties may be calculated from the Doppler VAD patterns. Caton (1963) showed that divergence is the net horizontal outflow integrated throughout the radar scanning circle divided by its radius. Browning and Wexler (1968) showed how the two components of deformation can be determined from the amplitude and phase of the second-order Fourier harmonic of the Doppler VAD pattern, assuming that the wind field derivatives can be considered as integral means throughout the radar scanning circle. Their assumption is correct when wind direction is constant within the area scanned by the radar, because in that special circumstance the remaining partial derivatives $\partial V/\partial s$ and $\partial V/\partial n$ of the wind may be expressed as total derivatives dV/dx and dV/dy of a geographically fixed coordinate system centered at the radar, with wind direction aligned with the x-axis. However, when wind direction varies considerably, special treatment of the VAD pattern is required for adequate diagnosis of the four wind field derivatives.

43

It is convenient to reference the radar observations of Doppler velocity, defined as the scalar component of wind velocity along the radar beam, to a polar coordinate system with origin at the radar, and position defined by range r and azimuth angle α. Following geographical convention, and postulating for the moment a mean westerly wind in temperate latitudes, we align the coordinate system so that the wind across the radar site is moving toward $\alpha = 90°$ and the orthogonal direction to the left of the wind is $\alpha = 0°$. Stated in Cartesian coordinates, these directions are along the x-axis and y-axis, respectively. For the sake of simplicity in exposition we assume that radar elevation angles and vertical motions are sufficiently small so that their neglect introduces errors of negligible importance in comparison with contributions from other sources. An estimated correction for contamination by vertical motions could be introduced, if necessary.

Fig. 1 depicts each of the first derivatives, combined with uniform translation from left to right, in the context of the radar scanning circle. The radius of the radar scanning circle is r, and F and R represent distances to the centers of diffluence and curvature, respectively. Initially, we shall examine the Doppler VAD patterns specific to each one of the wind fields illustrated in Fig. 1. In later sections various combinations of the wind field derivatives and their resultant VAD patterns will be studied, including the general case in which all four derivatives are present.

a. Downwind Shear

Fig. 2 illustrates the geometry of the radar scanning circle (dashed) of radius r observing a wind field with both downwind and crosswind shear. The wind speed at the radar site is V_o. In the case of downwind shear, the wind speed increases from a minimum of $V_o(1 - d)$ at distance r upwind from the radar to $V_o(1 + d)$ at distance r downwind from the radar. Accordingly, the shear is $V_o \, d/r$. The dimensionless parameter d, defined as the fractional increase in wind speed from radar site downwind to the VAD scanning circle, is an index of the relative magnitude of shear-induced asymmetry in the resultant Doppler VAD pattern.

44
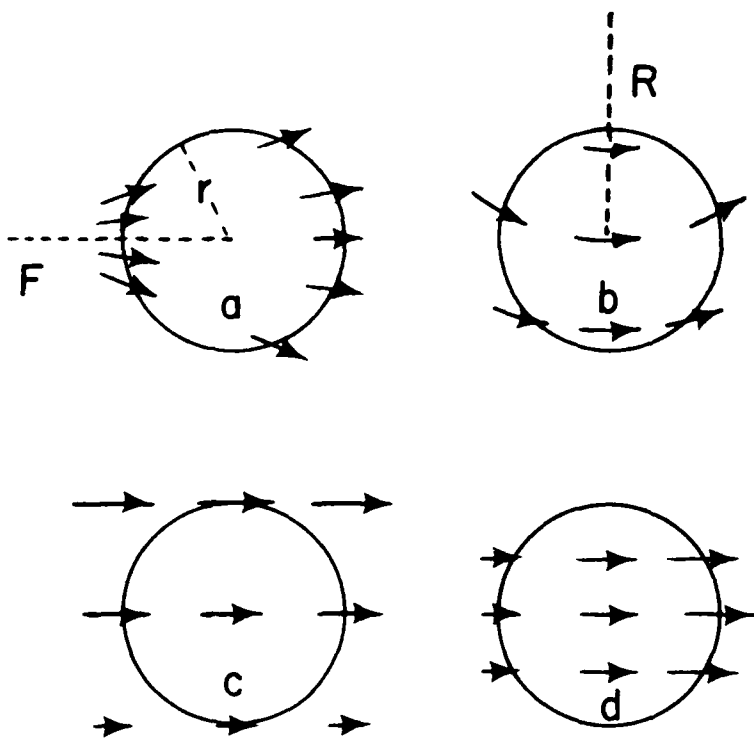
Fig. 1 Schematic Depiction of the Four First Derivatives of the Wind
Field: (a) Diffluence, (b) Curvature, (c) Crosswind Shear, (d) Downwind
Shear; Superimposed on Radar Scanning Circles of Radius r

(Bold arrows represent wind vectors.) (From Donaldson and Ruggiero, 1986)

45
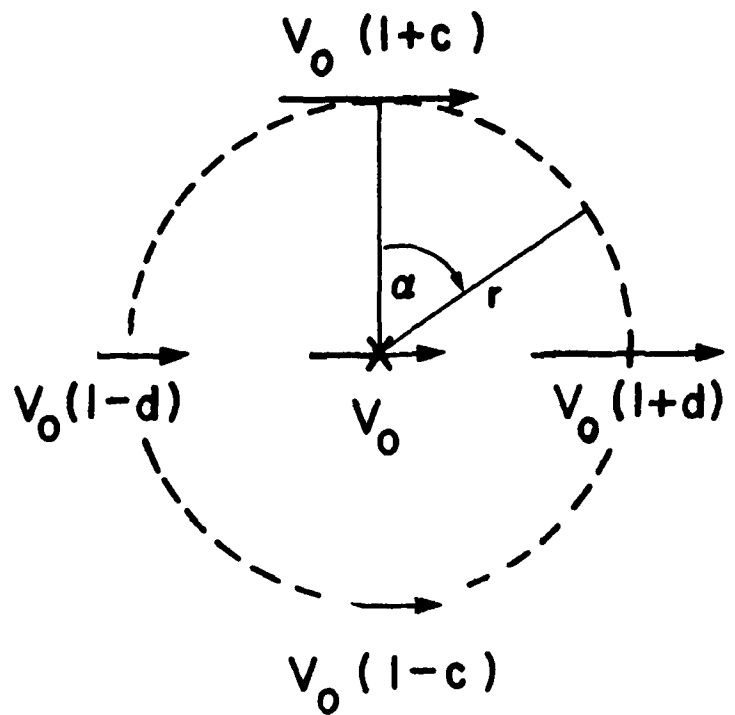
Fig. 2 Schematic Depiction of Linear Wind Field Model with Both Downwind and Crosswind Shear

(Arrows represent wind vectors; dashed line is radar scanning circle of radius r and azimuth angle α.) (From Donaldson and Harris, 1984)

At any point on the radar scanning circle, this wind field has a speed of·

$$V(\alpha) = V_0 \, (1 + d \sin \alpha) \tag{5}$$

and a uniform direction toward $\alpha = 90°$. Accordingly, the Doppler velocity V_D, the component of wind along the radar beam, is

$$V_D(\alpha) = V(\alpha)\sin \alpha = V_0 \, (\sin \alpha + d \sin^2 \alpha). \tag{6}$$

Downwind shear is easily recognized in a VAD pattern by a difference in magnitude of the maximum and minimum values of Doppler velocity. These extrema occur at $\alpha = 90°$ and $270°$, respectively, for the simple case of downwind shear expressed in Eq. (6), yielding a straightforward method for evaluation of d:

$$d = [V_D \, (\text{max}) + V_D \, (\text{min})]/[V_D \, (\text{max}) - V_D \, (\text{min})]. \tag{7}$$

Reference to Eqs. (1) and (2) shows that a uniform wind direction, in which $\partial\psi/\partial n = 0$, requires that downwind shear $(\partial V/\partial s)$ be identical to both divergence and to stretching deformation.

b. Crosswind Shear

The wind speed at any point on the radar scanning circle for the case of pure crosswind shear, with uniform wind direction toward $\alpha = 90°$, is

$$V(\alpha) = V_0 \, (1 + c \cos \alpha). \tag{8}$$

The shear toward the left of the wind direction is $V_0 \, c/r$, where c is the dimensionless parameter of crosswind shear and is defined as the fractional increase in wind speed over a distance r normal and to the left of wind direction. Under these conditions the Doppler velocity measured by the radar is

$$V_D(\alpha) = V(\alpha) \sin \alpha = V_0 \, (\sin \alpha + c \sin \alpha \cos \alpha). \tag{9}$$

47

The most prominent effect of crosswind shear on the Doppler VAD pattern is a deviation from diametric opposition of the locations of the maximum and minimum Doppler velocities. Unfortunately, the cause of this effect is not distinctive, because later discussion will demonstrate that a curved wind field produces a pattern rather similar in appearance. Fig. 3 illustrates this deviation, which is measured by the angle δ_D on the downwind side of the pattern, and δ_u on the upwind side. (The ϵ angles will be discussed later in the section on diffluence.) If crosswind shear is the only wind field derivative, $\delta_D = \delta_u$, and these angles may be determined by differentiation of Eq. (9) with respect to α to find the angular locations of the Doppler velocity extrema, which have a complementary relationship to the two identical δ angles. This process yields

$$\sin \delta = [(1 + 8c^2)^{1/2} - 1]/4c \tag{10}$$

and can also be expressed more compactly as

$$c = \sin \delta/\cos 2\delta. \tag{11}$$

Note that c and δ have the same sign in Eqs. (10) and (11), and therefore the Doppler velocity extrema are displaced toward the direction of positive crosswind shear.

The crosswind shear appears as $\partial V/\partial n$ in Eqs. (3) and (4). If wind direction is uniform, $\partial \psi/\partial s = 0$ in these equations, forcing an identity of the crosswind shear with shearing deformation and with the negative of vorticity.

c. Curvature

When streamline direction varies owing to curvature and/or diffluence, the natural coordinate system of the streamlines rotates throughout the wind field with respect to the fixed coordinate system of the radar scanning circle. Consequently, the natural derivatives in the right side of Eqs. (1) to (4) are decoupled from the linear derivatives involved in the Fourier analysis of Browning and Wexler (1968), and interpretation of the VAD pattern requires an additional level of analysis.

48
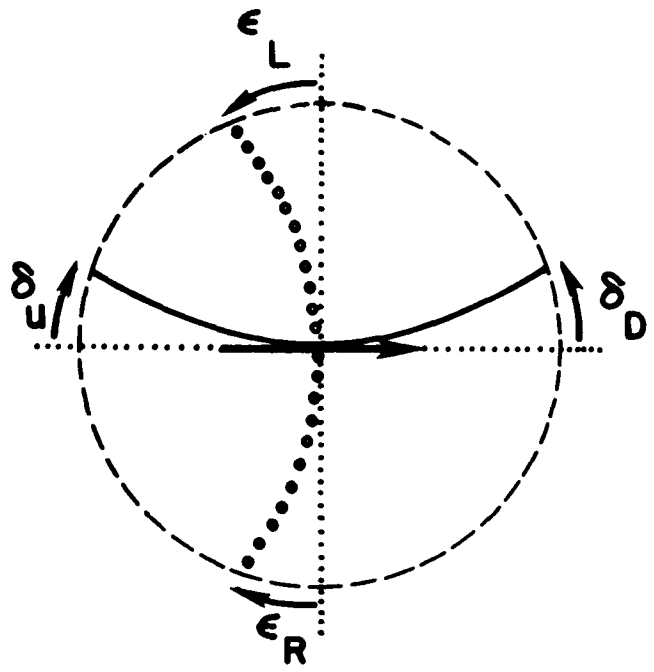
Fig. 3   Illustration Defining the Angles δ_D, δ_u, ϵ_L, and ϵ_R

(Dashed line is radar scanning circle; dotted lines indicate directions along and normal to wind vector (heavy arrow) at the radar; solid line is locus of minimum or maximum Doppler velocity; small circles show locus of zero Doppler velocity.)

49

An exact solution is possible for relating the coordinate systems of the radar and multi-directional streamlines if it can be assumed that the sole cause of the variability in wind direction is either curvature, or diffluence, but not both. We shall first consider curvature, following much of the discussion of Donaldson and Harris (1984).

It is assumed that curvature is inversely proportional to distance from a center of curvature that has a fixed position relative to the radar location. This assumption of variable curvature but fixed center of curvature has two distinct advantages: It provides a realistic wind field, with non-intersecting streamlines, and it defines geometric relationships between the wind field and the radar scanning circle that enable calculation of Doppler velocities by straightforward trigonometric manipulation.

The geometry of a radar scanning a curved wind field is portrayed in Fig. 4. (Ignore for the moment distances F and k and angle γ; these will enter our discussion of diffluence in the next section.) The distance r is the radius of the radar scanning circle and R is distance from radar to center of curvature of the wind field. The radar scanning angle α is oriented so that the center of curvature is in the direction $\alpha = 0°$. The wind direction at the radar site is toward $\alpha = 90°$, appropriate to cyclonic curvature in the Northern Hemisphere. The variable h is the distance from center of curvature to any point on the radar scanning circle. This point is also located by the angle β measured from the line R joining the center of curvature and the radar. The angle β is positive for the downwind semicircle, where $0° < \alpha < 180°$. Our analysis requires the assumption that $r < R$, and this is easily granted because r is under human control. The wind speed V_0 is assumed uniform throughout this model.

The curved wind field can be expressed in Cartesian coordinates as the vector sum of components u and v, where u is directed along $\beta = 90°$ and v along $\beta = 180°$. Inspection of Fig. 4 readily shows that $u = V_0 \cos \beta$ and $v = V_0 \sin \beta$. The radar can detect motion only along its beam. Accordingly, at any location on the radar scanning circle the Doppler velocity V_D is given by wind components along the direction α. Therefore,

$$V_D(\alpha) = u \sin \alpha + v \cos \alpha = V_0(\sin \alpha \cos \beta + \cos \alpha \sin \beta). \qquad (12)$$

50
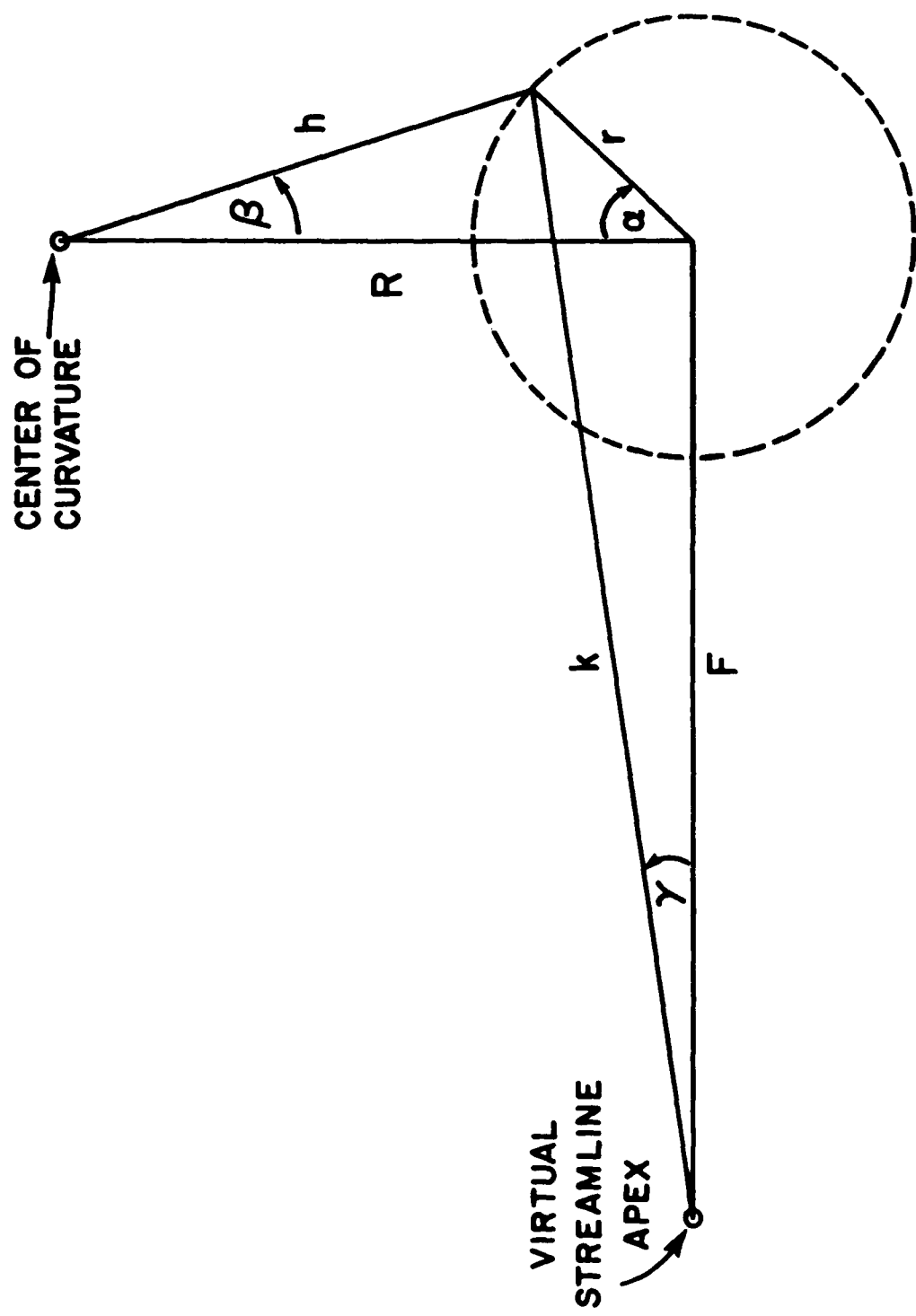
Fig. 4 Portrayal of Geometric Relationships Required for Specification of Curvature and Diffluence and Their Doppler Velocities

(Dashed curve is radar scanning circle of radius r, with α as the azimuth angle of any arbitrary point on this circle. R and h, with inclusive angle β, are distances from center of wind field curvature to radar and to the arbitrary point on the radar scanning circle, respectively. F and k, with inclusive angle γ, are distances from virtual streamline apex to radar and to the same arbitrary point, respectively.)

Through trigonometric solution of the right triangle in Fig. 4 that has h as hypotenuse and β as one of its angles, and after some algebraic manipulation, we find that $h = R\rho^{1/2}$, so that Eq. (12) can be expressed simply as a function of radar scanning angle α and a dimensionless parameter r/R relating the radii of radar scanning circle and curvature:

$$V_D(\alpha) = \rho^{-1/2}V_0 \sin \alpha, \qquad (13)$$

where $\rho = 1 + (r/R)^2 - 2(r/R) \cos \alpha$. Note that $V_0 \sin \alpha$ in Eq. (13) is the VAD pattern of a uniform linear wind directed toward $\alpha = 90°$, so the factor $\rho^{-1/2}$ is the modification of the VAD effected by curvature of the wind field.

The increment of direction per unit distance along a streamline $(\partial\psi/\partial s)$ for a circularly curved wind field is the inverse of the radius of curvature. Consequently, the curvature term appearing in Eqs. (3) and (4) is evaluated in our model wind field as $V_0/h = V_0/R\rho^{1/2}$ at any point on the radar scanning circle. The curvature term at the radar site, where $r = 0$ and ρ reduces to unity, is simply V_0/R.

The effect of curvature on the Doppler VAD pattern is qualitatively similar to the effect of crosswind shear: The maximum and minimum Doppler velocities are displaced toward the center of curvature. The effect is illustrated by the δ angles of Fig. 3. If curvature is the only wind field derivative, the upwind and downwind δ angles are equal and may be determined by differentiation of Eq. (13) with respect to α. An alternative and simpler method for calculation of δ starts with the reflection that the extrema in the VAD pattern of a curved wind field without speed gradients occur at the two angles where the wind direction is aligned with the radar beam. Therefore, the angular locations of the extrema are obtained by setting $V_D = \pm V_0$ in Eq. (13) and solving for α. The solution is $\cos \alpha = r/R$, and since δ is complementary with the angular location of a maximum or minimum in the VAD pattern,

$$r/R = \sin \delta. \qquad (14)$$

52

d. Diffluence

Diffluence, like curvature, is characterized by non-uniform wind direction. Unlike curvature, the diffluent directional shift is along a line normal to a streamline. Heretofore, the quantitative measurement of diffluence by a single Doppler radar has not been considered, although Baynton et al. (1977) showed that the presence of diffluence is very easily recognized in a Doppler VAD pattern by an asymmetric locus of zero Doppler velocity. Since the zero-Doppler locus indicates wind directions normal to the radar beam, any deviation of the two branches of this locus from opposition at the same range reveals a cross-flow difference in wind direction at the corresponding height.

A field of constant diffluence within a horizontal plane is not a realistic possibility, because streamline continuity would be compromised. Consequently, we have selected a diffluence model in which linear streamlines radiate from a fictitious virtual streamline apex. The diffluent wind vectors are sketched in Fig. 1(a), and geometrical relationships of the virtual streamline apex with the radar scanning circle are depicted in Fig. 4. The distance from streamline apex to radar is F, and to any point on the radar scanning circle is k. The angle between the F and k lines is γ, considered positive in the counter-clockwise direction. The coordinates r and α of the radar scanning circle are identical to the case for curvature, with coordinate axes aligned so that wind direction at the radar site is toward $\alpha = 90°$.

An expression for a purely diffluent wind field and its Doppler velocity measured by a radar in VAD scanning mode can be generated in a manner analogous to the derivation employed in the previous section for a purely curved wind field. The diffluent wind field can be expressed in Cartesian coordinates as the vector sum of components u and v, where u is directed along $\gamma = 0°$ and v along $\gamma = 90°$. In the absence of shear the wind speed has a uniform value V_o, and with wind direction dependent only on diffluence, Fig. 4 shows that $u = V_o \cos \gamma$ and $v = V_o \sin \gamma$. Since the radar detects motion only along its beam, the Doppler velocity V_D at any point on the radar scanning circle is given by wind components along the beam direction α. Therefore,

53

$$V_D(\alpha) = u \sin \alpha + v \cos \alpha = V_0(\sin \alpha \cos \gamma + \cos \alpha \sin \gamma). \qquad (15)$$

Substitution for γ in Eq. (15) may be accomplished by trigonometric solution of the right triangle in Fig. 4 that has k as hypotenuse and γ as one of its angles. It is helpful to express $k = F\phi^{1/2}$, where $\phi = 1 + (r/F)^2 + 2(r/F)\sin \alpha$. By means of these manipulations, Eq. (15) may be expressed as a function of radar scanning angle α and a dimensionless parameter r/F relating radius of the radar scanning circle r to the distance F from radar to the virtual streamline apex:

$$V_D(\alpha) = \phi^{-1/2} V_0(\sin \alpha + r/F). \qquad (16)$$

Note that Eq. (16) reduces to the VAD pattern of a uniform linear wind directed toward $\alpha = 90°$ when F is infinitely distant, indicating a condition of zero diffluence. Also, for a confluent, or negatively diffluent, wind field the virtual streamline apex would be downwind or to the right of the radar in Fig. 4, and F would be considered negative.

The diffluence term in Eqs. (1) and (2), $V\partial\psi/\partial n$, may be evaluated in either of two ways. More basically, we observe that our wind field model, having no derivatives higher than first order, requires that $\partial\psi/\partial n$ be constant along any curve normal to a streamline. Therefore we can easily integrate ψ from 0 to ψ_1. The corresponding integration for n is a circular arc length with angle ψ_1 and radius equal to distance k on Fig. 4 from any given point on the radar scanning circle to the virtual streamline apex. Accordingly, the diffluence term is $V_0\psi_1/\psi_1 k = \phi^{-1/2}V_0/F$, recalling that $k = F\phi^{1/2}$. At the radar site ϕ reduces to unity and the diffluence term is simply V_0/F.

The other method for evaluating diffluence is calculation of divergence under the condition of uniform wind speed V_0, which requires $\partial V/\partial s = 0$ in Eq. (1). We can do this by calculating the net outflow from a small area of width Δs with curved sides everywhere normal to the diffluent wind field and subtending an angle ψ_1. In our diffluent wind field model we set the radius of one curved side as k and the other (downwind) side as $k + \Delta s$. In this way we relate the calculation of divergence to radar parameters, because k terminates at any arbitrary point on the radar scanning circle. The inflow to this curved area is

$V_o k\psi_1$ and outflow is $V_o(k + \Delta s)\psi_1$, with no flow across the narrow sides of width Δs because these sides are oriented along the direction of flow. The size of the area in question is an infinitesimal increment larger than $k\psi_1\Delta s$. Consequently the divergence, and also the diffluence, is $[V_o(k + \Delta s)\psi_1 - V_o k\psi_1]/k\psi_1\Delta s = V_o/k = \phi^{-1/2}V_o/F$, which is identical to the previous calculation.

The easily recognizable signature of diffluence in the Doppler VAD pattern is a departure from opposition of the locus of zero Doppler velocity on either side of the mean wind vector, as illustrated in Fig. 3 by the angles c_L and c_R. Subscripts L and R denote the deviation from normal to the mean wind on its left and right sides, respectively. Diffluence is indicated by skewing upwind of the zero Doppler locus, as depicted in Fig. 3. A skewing downwind of the zero Doppler locus would indicate confluence, in which case the ϵ angles would be considered negative by our convention. In the absence of curvature, the two c angles are equal, regardless of the presence or absence of crosswind and/or downwind shear.

The c angles may be easily evaluated by solving Eq. (16) for α_o, the zero-crossing angles of the radar scan. For all values of $(r/F) < 1$, $\phi > 0$ and the solution is $\sin \alpha_o + r/F = 0$. From our definition of c as portrayed in Fig. 3, $c_L = -\alpha_{o_L}$ and $c_R = \alpha_{o_R} - \pi$. Consequently $\sin \epsilon = -\sin \alpha_o$ and

$$r/F = \sin \epsilon. \tag{17}$$

This is a useful relationship for achieving a quick evaluation of the sign and magnitude of diffluence from a cursory examination of the Doppler VAD pattern, because the Doppler velocity changes most rapidly with radar scanning angle at a zero crossing. On this account the zero crossing angle is least likely to be affected by small-scale perturbations in the wind field.

3. Combinations of the Wind Field Derivatives

Our analysis of the separate and individual effects of each of the four wind field derivatives on the Doppler VAD pattern has been instructive, at least for us, and perhaps interesting as well to the reader. However, it is not at all realistic, because it would be a most unusual wind field that contained only one of the derivatives. More than likely, we suspect, natural wind fields are characterized by all of the first derivatives, as well as higher-order contributions.

Therefore, we now expand our discussion to a brief consideration of several combinations of pairs of the first derivatives acting in concert. Then in the next section we examine the realistic situation wherein all four of the first derivatives are simultaneously present.

a. Crosswind Shear and Downwind Shear

The speed of the wind field with both shears is given by the product of the shear factors in Eqs. (5) and (8):

$$V(\alpha) = V_0(1 + c \cos \alpha)(1 + d \sin \alpha), \tag{18}$$

and with a uniform wind direction toward $\alpha = 90°$, the Doppler velocity is

$$V_D(\alpha) = V(\alpha)\sin \alpha = V_0 \sin \alpha(1 + c \cos \alpha)(1 + d \sin \alpha). \tag{19}$$

Along the mean wind vector $\alpha = 90°$ (downwind) and $270°$ (upwind), $\cos \alpha = 0$, and Eq. (19) reduces to Eq. (6). Therefore, the presence of crosswind shear does not affect the calculation of downwind shear along the axis of mean wind. If Eq. (7) is used for calculation of d, $V_D(\alpha = 90°)$ must be substituted for $V_D(\text{max})$ and $V_D(\alpha = 270°)$ for $V_D(\text{min})$. This is necessary because the presence of crosswind shear skews the maximum and minimum Doppler velocities toward the shear direction by angles δ_D and δ_u, respectively. These angles may be found by differentiation of Eq. (19) with respect to α. The solution is complex, not explicit, and not applicable to natural wind fields with variable wind directions. In

general, however, the effect of positive downwind shear is a reduction of δ_D (the higher-speed side) and a larger increase in δ_u (the lower-speed side).

b. Crosswind Shear and Diffluence

The Doppler velocity of a wind field featuring only diffluence and crosswind shear is given by Eq. (16) for diffluence alone multiplied by the variation in wind speed, $(1 + c \cos \alpha)$ from Eq. (8), appropriate for crosswind shear:

$$V_D(\alpha) = \phi^{-1/2} V_o (\sin \alpha + r/F)(1 + c \cos \alpha). \tag{20}$$

The c angles, indicating departure of the locations of zero Doppler velocity from normal to the mean wind vector, are identical to the case for diffluence alone, provided only that $c < 1$ as well as $r/F < 1$. This can be appreciated through comparison of Eq. (20) with Eq. (16) and noting that in both equations $V_D(\alpha) = 0$ only when $\sin \alpha_o + r/F = 0$. Therefore the presence of crosswind shear has no effect on the measurement of diffluence.

The reverse is not true. Diffluence does affect the angles δ_D and δ_u that measure the skew of the maximum and minimum Doppler velocities toward the shear direction. Differentiation of Eq. (20) with respect to α locates these angles. The solutions are complex and implicit, of only narrow mathematical interest, and will not be pursued here. In general, however, the effect of positive diffluence is an increase of δ_D (downwind side) and a nearly equal decrease of δ_u (upwind side).

c. Curvature and Crosswind Shear

Donaldson and Harris (1984) examined the interesting combination of curvature and crosswind shear, in which both derivatives are readily recognized by a δ signature in the VAD pattern, as given by Eq. (10) or Eq. (11) and Eq. (14), and both derivatives contribute to the shearing deformation. This earlier analysis, with slightly different notation, is reproduced here.

In combination with curvature, the crosswind shear has a variable direction because it is normal to the curved streamlines and directed toward the center of curvature. However, the wind vector and its Doppler velocity may be defined through the geometry of Fig. 4. The wind speed at any point on the VAD circle is a linear function of $h = R\rho^{1/2}$, the distance from center of wind field curvature to an arbitrary location observed by the radar. The speed function may be determined by assigning $V = V_0$ at the radar and noting, through Eq. (8), that $V(h) = V_0(1 + c)$ for $\alpha = 0°$; and at this point on the radar scanning circle Fig. 4 shows that $r = R - h$. Accordingly

$$V(h) = V_0[1 + c(R-h)/r] = V_0[1 + c(r/R)^{-1}(1 - \rho^{1/2})].\qquad(21)$$

The direction of the wind field is identical to the case of pure curvature, so the Doppler velocity of the curvature-crosswind shear combination is similar to Eq. (13), but with $V(h)$ substituted for V_0:

$$V_D(\alpha) = \rho^{-1/2}V_0[1 + c(r/R)^{-1}(1 - \rho^{1/2})]\sin\alpha.\qquad(22)$$

Differentiation of Eq. (22) with respect to α yields a complex expression relating c, r/R, and δ, namely

$$c = \frac{(r/R)[(r/R)\hat{\rho}^{-1}\cos^2\delta - \sin\delta]}{\sin\delta - \hat{\rho}^{1/2}\sin\delta - (r/R)\hat{\rho}^{-1}\cos^2\delta},\qquad(23)$$

where $\hat{\rho}$ is ρ evaluated at $\alpha = \hat{\alpha}$. The VAD function for this situation is symmetric about the line joining the center of wind field curvature and the radar location, so $\delta_u = \delta_D$ and a single value of δ is appropriate in dealing with Eq. (23).

A remarkable simplification of Eq. (22) occurs in the case of solid rotation, wherein rotational speed increases linearly with distance from the center of curvature. If the radar scanning circle is entirely within the region of solid rotation (e.g., within the area bounded by the eye wall of a hurricane), we may write $V_0/R = V_0(1 + c)/(R-r)$, which reduces to

58

$$c \text{ (solid rotation)} = -r/R. \tag{24}$$

Substitution of this relationship into Eq. (22) reduces its bracketed factor to $\rho^{1/2}$, finally leaving $V_D(\alpha) = V_o \sin \alpha$. Within solid rotation, the effects on Doppler velocity of curvature and crosswind shear cancel exactly, and the resultant VAD pattern is identical to that observed with pure translation.

Potential vortex flow, with wind speed inversely proportional to distance from a cyclone center, is another regime of special interest. This type of flow may be a better approximation to a hurricane wind field, beyond the ring of maximum wind speed, than is a linear crosswind shear.

In potential vortex flow the product of wind speed around a circulation center and distance from this center is constant. Consulting Fig. 4, then, we see that the wind speed at any point on the radar scanning circle is

$$V(\alpha) = V_o R/h = V_o \rho^{-1/2}, \tag{25}$$

where, as before, V_o is wind speed at the radar location. The Doppler velocity, with wind field direction identical to the case of pure curvature, is given by Eq. (13) with wind speed function Eq. (25) substituted for the constant speed V_o of Eq. (13):

$$V_D(\alpha) = \rho^{-1/2} V_o \rho^{-1/2} \sin \alpha = \rho^{-1} V_o \sin \alpha. \tag{26}$$

Differentiation of Eq. (26) with respect to α reveals, as expected, considerably greater deviation of the Doppler velocity extrema from the mean wind vector, than in the simple relationship Eq. (14) for curvature with uniform wind speed:

$$\sin \delta = 2(r/R)/[1 + (r/R)^2]. \tag{27}$$

Several possible methods have been examined for distinguishing curvature from crosswind shear, despite the similarity in their signatures on the Doppler VAD pattern. In principle, these methods show promise in a wind field comprised entirely of translation and first derivatives, especially in cases with moderate to large va. es of both curvature and

crosswind shear. Any success with these methods would provide heretofore inaccessible information on vorticity, which is curvature minus crosswind shear. In practice, however, observed natural wind fields contain higher order derivatives and small-scale perturbations that tend to mask the somewhat subtle differences in these two first derivatives.

4. An Approximation for the Combination of All Four Wind Field Derivatives

When both curvature and diffluence are present the simple trigonometric relationships of Fig. 4 for either curvature or diffluence alone are not valid. The lines F and R joining the radar location with virtual streamline apex and center of curvature, respectively, are no longer straight, and the angles γ and β are no longer defined in terms of right triangles. Also, these two angles are interdependent. An exact solution for the wind field and its Doppler velocity could not be derived. Therefore, approximations were sought relating β and γ to radar parameters.

We felt, after due considerations, that

$$\sin \beta \simeq (k-F)/h \text{ and } \sin \gamma \simeq (R-h)/k] \tag{28}$$

are reasonable approximations, retaining the definitions for $h = R\rho^{1/2}$ and $k = F\phi^{1/2}$ used in the earlier analysis of single derivatives, with ρ as before equal to $1 + (r/R)^2 - 2(r/R)\cos \alpha$ and $\phi = 1 + (r/F)^2 + 2(r/F)\sin \alpha$. Each approximation converges to its exact independent form as the other term vanishes. That is, $(k - F) \rightarrow r \sin \alpha$ as $F \rightarrow \infty$ and $(R - h) \rightarrow r \cos \alpha$ as $R \rightarrow \infty$.

The angles β and γ indicate the changes in wind direction owing to curvature and diffluence, respectively. When both of these derivatives are present, but with no shear, the Doppler velocity of the VAD pattern is

$$V_D(\alpha) = V_0 \sin(\alpha + \beta + \gamma), \tag{29}$$

where, as before, V_0 is wind speed at the radar site. Having confidence in the approximations of Eq. (28), we substitute them in Eq. (29) and eventually obtain an expression for the Doppler velocity with both curvature and diffluence present, but with no shear, in terms of the radar coordinates

60

r and α and the dimensionless parameters r/R and r/F of curvature and diffluence:

$$V_D(\alpha) \simeq V_0\sin\{\alpha + \sin^{-1}[(r/R)(r/F)^{-1}(\phi^{1/2} - 1)p^{-1/2}]+$$

(30)

$$\sin^{-1}[(r/F)(r/R)^{-1}(1 - \rho^{1/2})\phi^{-1/2}]\}.$$

The next step in the problem is approximation of the two shears when there is both curvature and diffluence. Consider first downwind shear. Along the curved streamline that crosses the radar location, an expression is required for streamline length from radar to scanning circle. The product of downwind shear $V_0 d/r$ and the length of this curved streamline segment defines the wind speed at the points where this central streamline intersects the radar scanning circle. Finally, a general expression is required for wind speed at any point on the radar scanning circle, reducible to the simple expression $V(\alpha) = V_0(1 + d \sin \alpha)$ for linear, parallel streamlines as both curvature and diffluence approach zero.

The distance along a curved streamline from radar location to scanning circle is somewhat greater than the radius r of the scanning circle. We shall evaluate whether neglect of this incremental distance is a valid approximation. All points along the central streamline (i.e., the curved streamline passing over the radar site) are at distance R from the center of curvature of the wind field. The length h in Fig. 4 also defines the distance from any point on the radar scanning circle to the center of curvature. Accordingly, at the intersection of the central streamline and the radar scanning circle $R = h$. In general $h = R\rho^{1/2}$, so at this intersection $\rho^{1/2} = 1 = \rho = 1 + (r/R)^2 - 2(r/R) \cos \alpha$. This can be true only where $r/R = 2 \cos \alpha$. From the geometry of Fig. 4, $\cos \beta = (R - r \cos \alpha)/h = 1 - (r/R) \cos \alpha$ at this intersection, where we can substitute $r/2R$ for $\cos \alpha$. Therefore $\cos \beta = 1 - (r/R)^2/2$ at this point. The distance of the curved streamline from radar to scanning circle is $R\beta = r(r/R)^{-1} \cos^{-1}[1 - (r/R)^2/2]$. At the fairly large value of $r/R = 0.5$, $R\beta = 1.01 r$; and even at the limiting value of $r/R = 1$, $R\beta < 1.05 r$. Consequently, the approximation of r for streamline distance from radar to scanning circle is acceptable for all permissible values of r/R.

61

By a similar argument, r is a suitable approximation, throughout all permissible values of r/F, for distance from the radar location to the intersection of the radar scanning circle with the streamline-normal curve for diffluent streamlines.

The next order of business is a reasonable approximation for distance downwind from radar location to any point on the radar scanning circle, and distance crosswind (in the left direction) to this same arbitrary point. From Fig. 4 it appears that k - F approximates well the downwind distance, and R - h is a good approximation for the crosswind distance. As the foregoing discussion demonstrated, the length of these straight lines depicted in Fig. 4 is not appreciably less than the curved streamline or streamline-normal. Also, since $k - F \rightarrow r \sin \alpha$ as $F \rightarrow \infty$ and $R - h \rightarrow r \cos \alpha$ as $R \rightarrow \infty$, these approximations merge smoothly toward the linear values wherein curvature and diffluence approach zero.

It is now possible to express wind speed at any point on the radar scanning circle in terms of radar coordinates and the dimensionless parameters of the wind field derivatives. The increase in wind speed from radar to scanning circle is the appropriate shear multiplied by the appropriate distance. Accordingly,

$$\text{downwind } V(\alpha) \simeq V_0 + (V_0 d/r)(k - F). \tag{31}$$

Similarly,

$$\text{crosswind } V(\alpha) \simeq V_0 + V_0(c/r)(R - h). \tag{32}$$

Now, because the downwind and crosswind shears are orthogonal, the wind speed at any point on the radar scanning circle is given by wind speed at the radar multiplied by the product of the two shear-dependent factors implicit in Eqs. (31) and (32). Also, substitution of $R\rho^{1/2}$ for h and $F\phi^{1/2}$ for k reduces all variables to radar coordinates and parameters of the wind field derivatives. Finally, substitution of the resultant speed function for V_0 in Eq. (30) provides a general approximation for Doppler velocity when all four wind field derivatives are present. The final expression is

$$V_D(\alpha) \simeq V_0[1 + c(r/R)^{-1}(1 - \rho^{1/2})].[1 + d(r/F)^{-1}(\phi^{1/2} - 1)] \ .$$

$$\sin\{\alpha + \sin^{-1}[(r/R)(r/F)^{-1}(\phi^{1/2} - 1)\rho^{-1/2}] +$$

$$\sin^{-1}[(r/F)(r/R)^{-1}(1 - \rho^{1/2})\phi^{-1/2}]\}. \tag{33}$$

It is necessary to demonstrate that Eq. (33) reduces to one of the exact forms Eq. (13) or Eq. (16) when either diffluence or curvature is not present and there is no shear, or to Eq. (19) when both curvature and diffluence are absent but both shears are present. With zero diffluence, $r/F = 0$ and $\phi^{1/2} = 1$. Simple substitution of these values in Eq. (33) would result in 0/0 in two of its factors. In order to avoid this indeterminacy, basic considerations are required. Recall that $\phi = 1 + (r/F)^2 + 2(r/F) \sin \alpha$. As diffluence approaches zero, F approaches very large values, at which $\phi \simeq 1 + 2(r/F)\sin \alpha$, $\phi^{1/2} \simeq 1 + (r/F)\sin \alpha$, and $(r/F)^{-1}(\phi^{1/2} - 1) \simeq \sin \alpha$. Similarly, as curvature approaches zero and R approaches very large values, $(r/R)^{-1}(1 - \rho^{1/2}) \simeq \cos \alpha$. Therefore, for zero diffluence but finite curvature, the directional factor $\sin \{---\}$ in Eq. (33) reduces to $\sin\{\alpha + \sin^{-1}[(r/R)\rho^{-1/2}\sin \alpha]\}$, and through a trigonometric identity this can be written in a form equivalent to Eq. (12) and eventually simplified to Eq. (13). Through a similar process it can be demonstrated that, with zero curvature but finite diffluence, the directional factor $\sin\{---\}$ in Eq. (33) reduces to $\sin\{\alpha + \sin^{-1}[(r/F)\phi^{-1/2}\cos \alpha]\}$ and eventually simplifies to Eq. (16). When both curvature and diffluence are zero the directional factor reduces all the way down to $\sin \alpha$ and the speed factors are greatly simplified, also. As a result of these simplifications, there are the following exact solutions for the special cases of zero diffluence and/or curvature:

With zero diffluence,

$$V_D(\alpha) = V_0[1 + c(r/R)^{-1}(1 - \rho^{1/2})].[1 + d \sin \alpha] \ . \ \rho^{1/2} \sin \alpha. \tag{34}$$

With zero curvature,

$$V_D(\alpha) = V_0[1 + c \cos \alpha].[1 + d(r/F)^{-1}(\phi^{1/2} - 1)].\phi^{1/2}(\sin \alpha + r/F). \tag{35}$$

With neither curvature nor diffluence,

$$V_D(\alpha) = V_0[1 + c \cos \alpha].[1 + d \sin \alpha] \sin \alpha. \tag{19}$$

It is satisfying to note that Eq. (34) with $d = 0$ is identical to Eq. (22),

which was derived along an approach somewhat different from the reasoning behind Eq. (34).

The validity of the general approximation Eq. (33) may be tested for any arbitrary combination of the dimensionless parameters (c, d, r/R, r/F) of the four wind field derivatives (crosswind shear, downwind shear, curvature, and diffluence). The method of testing first requires synthesis of the Doppler velocity function $V_D(\alpha)$ for a complete VAD circle by insertion of the arbitrary parameter values in Eq. (33). The next step is a Fourier analysis of the synthesized $V_D(\alpha)$ function, using the method developed by Browning and Wexler (1968). The Fourier coefficients of zeroth, first, and second order are a_0, a_1 and b_1, and a_2 and b_2, respectively. In performing this analysis care is taken to assure that the wind vector at the radar location is directed toward $\alpha = 90°$. With this precaution, b_1 estimates the mean wind speed around the VAD scanning circle and $a_1 = 0$ or very nearly so. Divergence is given by a_0/r, stretching deformation by $-2a_2/r$, and shearing deformation by $2b_2/r$. (The negative sign for the coefficient in stretching deformation is a result of our clockwise rotation of radar scanning angle α.) We can now insert these Fourier estimates in the basic wind field relationships Eqs. (1), (2), and (3), multiply all terms by r, and divide all terms by V_0, using b_1 as an estimate for V_0, to obtain

$$a_0/b_1 = d + r/F, \tag{36}$$
$$-2a_2/b_1 = d - r/F, \text{ and} \tag{37}$$
$$2b_2/b_1 = (r/R) + c. \tag{38}$$

The final step in the testing program is a comparison of the left sides of Eqs. (36) to (38), obtained by Fourier analysis, with the appropriate combinations of the arbitrarily selected wind field parameters on the right sides. Results of testing over a wide universe of parameter values indicated errors of less than five percent for r/R = 0.6 or less and for r/F and d of opposite sign.

Whenever curvature and/or diffluence are present, the Fourier coefficients are underestimated. These errors tend to cancel in the ratio of coefficients on the left sides of Eqs. (36) to (38). However, wind speed, as estimated by b_1, may be greatly underestimated; by 20 percent

64

or more, for example, with r/R = 0.8. On the other hand, the mean magnitude of the two extrema of Doppler velocity $V_m = [V_D(max) - V_D(min)]/2$ usually considerably overestimates wind speed in the presence of curvature and/or diffluence. Consequently, it was found empirically that the best estimate of wind speed is $(b_1 V_m)^{1/2}$. Within our universe of parameter value calculations, $(b_1 V_m)^{1/2}$ averaged only one percent high, and more than 80 percent of $(b_1 V_m)^{1/2}$ values were in error by three percent or less.

5. Application to Hurricane Diagnosis

The techniques developed in the foregoing discussion are very well adapted to estimating the wind field derivatives in hurricanes and may aid in detection of changes in hurricane intensity before evidence of such trends becomes apparent through local wind speed measurements. In application, the coordinate axes are aligned with the observed wind direction so that $\alpha = 90°$ is mean downwind, and the Fourier harmonics are calculated. The sum and difference of Eqs. (36) and (37) provide Fourier estimates of the parameters of downwind shear and diffluence. Also, the eye locations of threatening hurricanes are usually frequently monitored by aircraft and/or satellite, so an estimate is usually available for R, the distance from radar to circulation center. If we assume curvature is inversely proportional to R, we can solve Eq. (38) for the parameter of crosswind shear. Accordingly,

$$d_f = (a_0 - 2a_2)/2b_1, \tag{39}$$

$$(r/F)_f = (a_0 + 2a_2)/2b_1, \text{ and} \tag{40}$$

$$c_f = 2b_2/b_1 - r/R, \tag{41}$$

where the subscript f denotes wind field derivatives estimated from the Fourier coefficients.

The above equations were used to examine the trend of the wind field in Hurricane Gloria in its 1985 passage through New England. Hurricane Gloria was under surveillance by the AFGL 10 cm Doppler radar at Sudbury, MA for

more than nine hours during the morning and afternoon of 27 September 1985.
For 3.3 h the coverage of Doppler velocities within a horizontal plane
around the radar site was sufficient to provide information for calculation
of the wind field derivatives. At the beginning of this period (1059 EST)
the eye of Gloria entered Long Island and by noon had crossed Long Island
Sound into Connecticut. The radar observations were comprised of a series
of volumetric scans, each of 7.3 min duration. Each scan consisted of a
series of stepped elevation angles, with each elevation covering a complete
circle of azimuths as the radar antenna continuously rotated about a
vertical axis. The wind field was examined through VAD patterns that were
constructed from data at r = 40 km and elevation angles of 1.0° and 2.2°,
giving heights above radar of 800 m and 1500 m. There were several
relatively small data gaps, owing to insufficient reflectivity, in some of
the VAD patterns. These data gaps were filled using a least-squares
polynomial interpolation fitted to a function incorporating the first three
Fourier harmonics. Data suitable for Fourier analysis at the lower height
of 800 m occurred during a 3.3 h period from 1059 to 1416 EST, as distance
of the hurricane center from the radar decreased from 251 km at first
landfall to 103 km when in central Massachusetts. At the 1500 m altitude,
only about two hours of data were available, from 1107 to 1318 EST. Fig. 5
portrays, for both altitudes, the variation in wind speed using
$(b_1 V_m)^{1/2}$ as best estimate, and Fourier-derived estimates of the
downwind shear, diffluence, and crosswind shear obtained by multiplying the
dimensionless parameters of Eqs. (39) to (41) by b_1/r.

It seems remarkable that lower-level wind speed increased by only 15
percent during a major decrease of 60 percent in distance to the hurricane.
Wind speed actually decreased slightly after 1340 EST. The negative sign of
crosswind shear at the lower altitude throughout the observational period is
also surprising, especially the large drop to very low values after 1340
EST, because the normal hurricane wind profile has increasing speed toward
the eye, with a maximum usually in the eye wall. It is important to note
that these observations started at the time of first landfall of the eye on
Long Island, and very likely they signal a progressive but not necessarily
gradual decay of the hurricane circulation. Recall that the assumption made
in deriving crosswind shear in Eq. (41) was that curvature is inversely
proportional to distance from a circulation center. If circulation
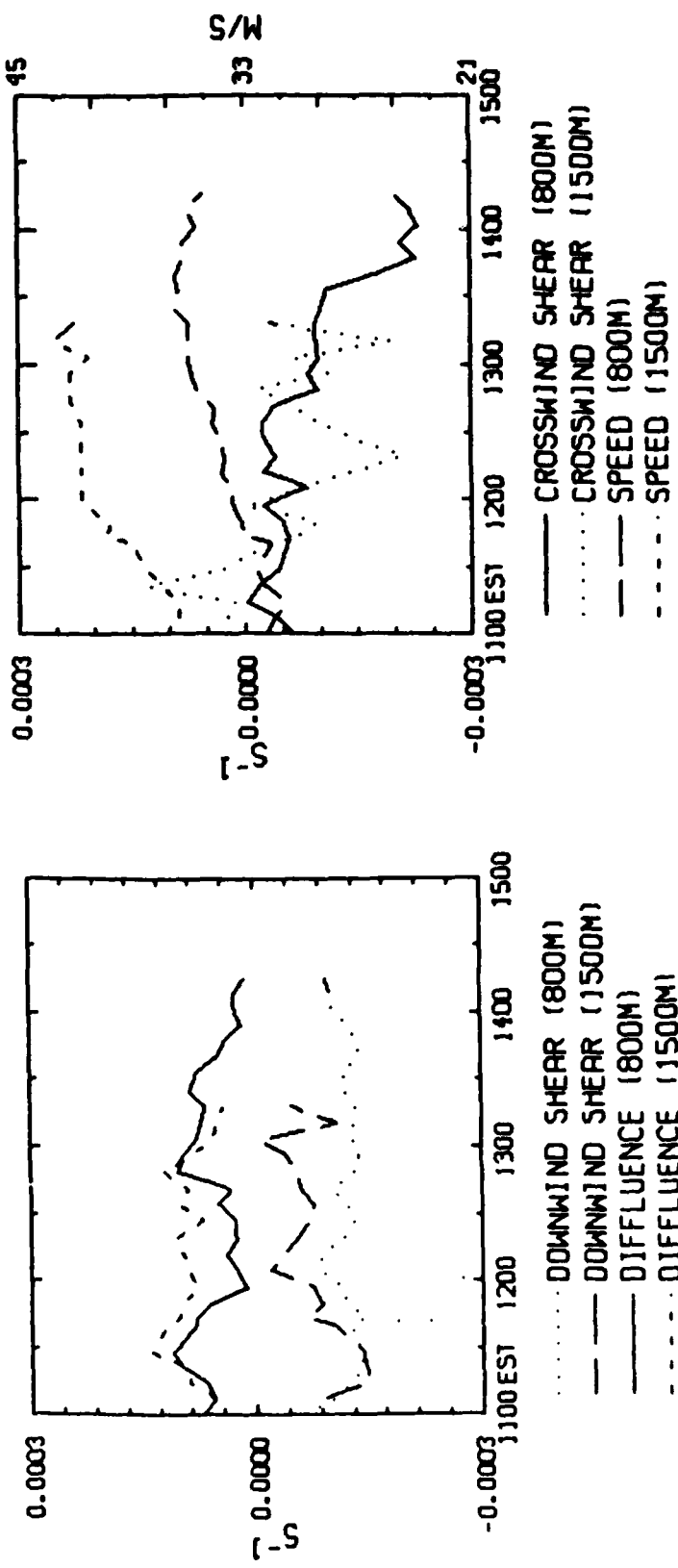
Fig. 5 Downwind Shear, Diffluence, Crosswind Shear, and Wind Speed Plotted as Function of Time at Heights of 800 m and 1500 m

(From Donaldson and Ruggiero, 1986)

67

deteriorates outward from the eye, the curvature term is diminished and Eq. (41) gives a corresponding underestimate of the crosswind shear. This hypothesis is supported by the velocity structure around the pressure center of Hurricane Gloria after 1400 EST, when it entered the unambiguous velocity range of the radar. Very little, if any, evidence of a rotating circulation was detectable.

Topography is another contributing cause to the negative values of crosswind shear. In the crosswind direction, the ground is higher and rougher toward the hurricane than opposite to it. Also, hourly mesoscale surface maps prepared by Roland Boucher of AFGL show higher wind speeds at stations farther from the hurricane than those nearer it, in the vicinity of our 40 km radius of radar observations. Crosswind shears at 1500 m also averaged negative, but with less magnitude than at 800 m; very likely an indication of less topographic influence at the higher altitude. However, the growth toward a regime of large negative values of crosswind shear at 1500 m occurred at least half an hour before this trend was apparent at 800 m, suggesting a downward deterioration of circulation within the hurricane. Also wind speeds at the higher level began to flatten as early as 1200 EST while speeds at the lower level were still rising slightly as the hurricane neared.

The downwind shears are all negative, indicating wind speed decrease owing to surface frictional loss. The average value of downwind shear at 800 m is -12×10^{-5} s^{-1}. At 1500 m the negative downwind shears average about half the magnitude of the corresponding values at 800 m, indicating, as expected, less frictional loss at the higher altitude. The diffluence values are all positive at both altitudes. At 800 m the average value of diffluence was about half the mean magnitude of downwind shear, but at 1500 m diffluence exceeded downwind shear magnitude on the average. There are interesting fluctuations in diffluence, however, which suggest a periodicity that is not apparent in the trend of downwind shear.

Two classes of difficulty may interfere with this technique for diagnosis of a hurricane or similarly configured extra-tropical storm. If there is reason to question the accuracy of Eqs. (39) through (41) because the curvature parameter is too large (e.g., r/R > 0.5) it is a simple adjustment to conduct observations with a somewhat smaller value of r, the radius of the radar scanning circle. On the other hand, if it is desired to

68

maintain the greater sensitivity to the wind field derivatives provided by a
large value of r, or if diffluence and downwind shear are not of opposite
sign, it is possible to refine the Fourier-calculated wind field derivative
parameters by entering them in the general approximation Eq. (33),
re-calculating the Fourier coefficients, and re-calculating the parameters
by Eqs. (39) through (41). It was not necessary to do this iteration for
analysis of Hurricane Gloria, so no experience has been obtained on the
number of steps required to achieve suitable accuracy. We expect, however,
that one step would be sufficient for practical purposes.

The other difficulty is more fundamental: There may not be sufficient
precipitation in all quarters around the radar to provide the data needed
for a Fourier analysis. In this event, sparse-data techniques may be
possible. If a zero-Doppler locus appears on both sides of the radar,
diffluence may be estimated by measuring $\bar{c}$ and applying Eq. (17). If both
the maximum and minimum values of Doppler velocity appear, their values can
provide an estimate of d through Eq. (7) and their angular locations give
$\bar{\delta}$. If r/R can be estimated from outside information, it can be combined
with $\bar{\delta}$ to give a rough estimate of c through Eq. (23). A 30° running mean
has been used to estimate these sparse-data indices in natural wind fields,
which, for our purposes, are always contaminated by higher than first-order
derivatives and localized perturbations. We feel that the accuracy obtained
with a 30° running mean is quite acceptable for estimating $\bar{c}$ and $V_D(max)$
and $V_D(min)$; but errors of 10° or more may occur in estimating $\bar{\delta}$, owing
to the slight variation of Doppler velocity with radar scanning angle near a
maximum or minimum. Also, the presence of downwind shear alters the
validity of Eq. (23). Nevertheless, if there are insufficient data to

calculate the shearing deformation the $\bar{\delta}$ measurement is better than
nothing, and would seem worthwhile to accomplish, particularly for values
of $\bar{\delta}$ considerably in excess of its expected error. It should also be
noted that the sparse-data calculation of downwind shear Eq. (7) is
generally an underestimate and can be erratic. However, if $\bar{\delta} + \bar{c} \leq 30°$,
the underestimate averages only seven percent, with a maximum error of ten
percent.

To summarize, the foregoing techniques for recovery of wind field
derivatives provide a means for monitoring the intensity of hurricanes and

other circularly configured storms at distances remote from the radar site. The application to forecasting is promising. The observation, through Eq. (41), of $c_f = 0$ at landfall and trending negative indicated decay of both circulation and wind speed well before confirmation by other, more direct, radar measurements. After implementation of the NEXRAD system, these techniques should be especially useful in assessing the threat to coastal areas by offshore hurricanes and intense extra-tropical storms.

6. Summary

The four first-order spatial derivatives of a wind field are curvature, diffluence, downwind shear, and crosswind shear. These derivatives are most conveniently expressed in natural coordinates referred to the streamlines. Divergence, vorticity, stretching deformation, and shearing deformation are comprised of sums and differences of pairs of the wind field derivatives. All of the properties except vorticity may be calculated by Fourier analysis of the Doppler velocity function measured by a radar scanning a complete circle in azimuth at constant range, following the VAD analysis technique proposed by Browning and Wexler (1968). The recovery of each of the wind field derivatives, however, is not a straightforward proposition, and this question was explored in depth.

Simple models of each wind field derivative in turn were considered with a Doppler radar scanning in the VAD mode inserted into the wind field, in order to synthesize characteristic Doppler velocity functions of radar scanning angle. To preserve streamline integrity the models for curvature and diffluence do not have constant values throughout the wind field. Instead, the model for curvature is related to radar coordinates by a center of streamline curvature in a fixed location with respect to the radar. A novel approach was used to model diffluence, by postulating a virtual (but fictitious) streamline apex at a fixed distance upwind from the radar for diffluence or downwind for confluence. The synthesized Doppler velocity functions for each of the wind field derivatives reveal unique signatures for diffluence and downwind shear, but qualitatively similar signatures for curvature and crosswind shear.

The scope of the discussion was expanded to a consideration of the Doppler velocity function produced by several pairs of the wind field

70

derivatives acting together. These exercises do not reflect realistic wind fields, because of the assumption that two of the derivatives are absent. They are, however, instructional for revealing trends in signature interaction. In particular, the Doppler velocity pattern for a radar scanning entirely within a radius of solid rotational flow is indistinguishable from the sinusoidal pattern in uniform linear flow.

For the natural, realistic situation wherein all four wind field derivatives are present, an exact solution could not be found for the resultant Doppler velocity function. However, a suitable approximation was derived, which reduced to an exact solution when either curvature or diffluence, or both, were eliminated. The validity of the approximation was tested over a wide-ranging set of parameter values of the four derivatives. For each set a Doppler velocity function was synthesized and then analyzed for the Fourier harmonics, which were then compared with the appropriate sums and differences of the derivatives. Results of the test showed that errors in recovery of the wind field derivatives were less than five percent except for unusual cases with diffluence and downwind shear not of opposite sign, or fairly high values of curvature for which distance from radar to center of curvature is less than twice the radius of the radar scanning circle. The test also revealed a substantial underestimate of wind speed by the magnitude of the first Fourier harmonic whenever diffluence and/or curvature were present. However, the square root of the product of this first harmonic and mean magnitude of the Doppler velocity extrema significantly reduced the error to a few percent. Consequently, there is confidence in most cases for the recovery from natural wind fields of downwind shear, diffluence, and the sum of curvature and crosswind shear, as well as wind speed. Moreover, if unacceptable errors are suspected, means are available for checking and correction.

Several methods have been examined for distinguishing curvature from crosswind shear. The methods appear promising in synthetic wind field models with no local perturbations or derivatives higher than first order. For natural wind fields, more development is required to define the efficacy, if any, of these techniques. Nevertheless, the sum of curvature and crosswind shear, as given by shearing deformation or by sparse-data signature, shows great promise for remote and early detection of trends in hurricane intensity, in combination with outside information on the location

71

of the circulation center. For example, during measurements conducted in New England in Hurricane Gloria (1985), the sum of curvature and crosswind shear showed decay after landfall of both circulation and maximum wind speed around the eye region nearly three hours before confirmation by other, more direct radar measurements. This type of diagnosis, conducted at a radar located on a coast, should be helpful in providing advance warning of the threat by destructive offshore cyclones.

7. References

Baynton, H. W., R. J. Serafin, C. L. Frush, G. R. Gray, P. V. Hobbs, R. A. Houze, Jr., and J. D. Locatelli, 1977: Real-time wind measurements in extra-tropical cyclones by means of Doppler radar. J. Appl. Meteor., 16, 1022-1028.

Browning, K. A., and R. Wexler, 1968: The determination of kinematic properties of a wind field using Doppler radar. J. Appl. Meteor., 7, 105-113.

Caton, P. G. F., 1963: Wind measurement by Doppler radar. Meteor. Mag., 92, 213-222.

Donaldson, R. J., Jr., and F. I. Harris, 1984: Detection of wind field curvature and wind speed gradients by a single Doppler radar. Preprints, 22nd Conference on Radar Meteorology, Zurich; AMS, Boston, 514-519.

Donaldson, R. J., Jr., and F. H. Ruggiero, 1986: Wind field derivatives in Hurricane Gloria estimated by Doppler radar. Preprints, Joint Sessions (Vol. 3), 23rd Conference on Radar Meteorology and Conference on Cloud Physics, Snowmass, CO; AMS, Boston, JP236-JP239.

Donaldson, R. J., Jr., M. J. Kraus, and R. J. Boucher, 1978: Doppler velocities in rain bands of Hurricane Belle. Preprints, 18th Conference on Radar Meteorology, Atlanta; AMS, Boston, 181-184.

Lhermitte, R. M., and D. Atlas, 1961: Precipitation motion by pulse Doppler. Proceedings, Ninth Weather Radar Conference, Kansas City; AMS, Boston, 218-223.

Passarelli, R. E., Jr., 1983: Wind field estimation by single Doppler radar techniques. Preprints, 21st Conference on Radar Meteorology, Edmonton; AMS, Boston, 526-529.

Petterssen, S., 1956: Weather Analysis and Forecasting, Volume I. Second Edition, McGraw-Hill, 428 pp.

Probert-Jones, J. R., 1960: Meteorological use of pulsed Doppler radar. _Nature_, _186_, 271-273.

Waldteufel, P., and H. Corbin, 1979: On the analysis of single-Doppler radar data. _J. Appl. Meteor._, _18_, 532-542.

B. Three-Dimensional Cloud and Precipitation Mapping

1. Introduction

AFGL has been developing nowcasting techniques for locating cloud and precipitation as guidance for use in satellite-to-ground communication links. As one phase of this program, STX has developed analysis techniques that characterize cloud/precipitation in terms that readily lend themselves to forecasting procedures. In this section various analysis procedures that have been explored and/or implemented are discussed and the rationale for selection or rejection is presented. Particular attention is given to type and degree of data preprocessing required for effective analysis.

The basic premise is that any cloud/precipitation analysis/prediction system will have as input timely digital radar reflectivity data and satellite visible and infrared imagery. These data may be used separately or together. This report focuses on the use of radar data since they have better time resolution for the 0 to 30 min nowcast problem. However, all of the analysis software that has been developed will operate on data from either source.

2. Data Preprocessing

a. Radar Data Coordinate Transformation

The raw data received from satellites and radars are in quite different coordinate systems. The radar collects its data in a three-dimensional spherical framework, along radials emanating from the radar itself. Data from the GOES satellite are organized in a distorted framework on a single plane, the distortion being caused by the oblique viewing angle of the satellite sensors. It is therefore essential that the data from these systems be converted to a common grid if they are to be used together in a system. A rectangular Cartesian grid centered on the radar was

selected, since it lends itself most easily to manipulation and display on the scales being considered, i.e., less than 500 km.

Development of software to convert radar data to Cartesian coordinates was assigned to STX; the satellite data conversion problem was addressed by AFGL. STX implemented two software packages, both based on the Mohr and Vaughan (1979) interpolation algorithm. One is slow and relatively cumbersome but readily available, having been developed at the National Center for Atmospheric Research (NCAR); the second, developed by STX, is real time, more efficient, and tailored to the AFGL hardware configuration and the needs of the project. The first package was adopted to allow the generation of data sets to be used for testing in other phases of this effort while the real time software was being developed concurrently.

The Mohr and Vaughan (1979) interpolation algorithm can be divided into two sections: preprocessing, and data ingestion and interpolation. In the preprocessing phase the user defines a rectangular 256x256 point Cartesian coordinate system onto which interpolated values will be placed. For each grid point, the spherical coordinates (range, azimuth, and elevation) are computed. These are then sorted and subsequently stored on disk in the form of level files. Each file contains the spherical and Cartesian coordinates for all grid points between two consecutive elevation scans of the radar. Thus, as the data from a particular elevation scan are read from the processor during the ingestion and interpolation phase, only two files need to be searched for data placement as opposed to the entire Cartesian volume. Also, because the spherical coordinates are known for each grid point it is unnecessary to compute the Cartesian coordinates for each data point, as is the case for most conventional interpolation techniques. This results in a substantial saving in terms of number and complexity of calculations. Once calculations are completed in all level files the resultant interpolated data are sorted into the horizontal planes of the rectangular framework and then output to disk. Both the NCAR and STX packages process data in this manner.

The NCAR software is a generalized package that accepts data from a variety of radar processors, converts the data to Cartesian coordinate systems, generates a variety of one-, two-, and three-dimensional displays, performs statistical analyses, allows data manipulations, and performs multiple Doppler radar data synthesis. Although not in real time, its

implementation provides analysis and display capabilities not previously available at AFGL. Its capabilities are documented in Mohr and Vaughan (1979). Software was developed by STX to rewrite the AFGL data to the format required for the interpolation routines. In addition, interactive software was written and incorporated as an integral part of this processing program to interface the output with the Adage 3000 image processor, the display device used by the Air Force. Data may be interpolated onto at most a 128x128 grid, the dimension, resolution, and location of which are specifiable by the user. These interpolated data are stored in Adage memory and then archived on the VAX disk in the common data format outlined in the RAPID System Development report (pp. 99-111, below). For larger images, it is very easy to process subsections of the radar data, then merge the images in the Adage and ultimately store the merged image on the VAX 11/750 disk.

Despite use of very efficient bilinear or nearest point interpolation techniques as the radar data are ingested, real time interpolations are not attainable with the NCAR software because it was not designed for real time operations. Therefore it was necessary for STX to develop a new software package based on the same algorithm but with streamlined data flow and adapted to AFGL data and processing equipment. It was decided that real time interpolation should be performed on the PE3242, with the resultant Cartesian fields being shipped to the VAX 11/750 for subsequent analysis. This was made possible by enhancing PE3242 capabilities through acquisition of additional memory and a large disk with an intelligent controller, and establishing an ETHERNET link between the PE3242 and the VAX 11/750. One of the ports for the AFGL Doppler processor was connected to the PE3242, permitting transmittal of mean Doppler velocity and radar reflectivity data and housekeeping data for further processing. The data transfer rate between processor and computer is close to 50 kbytes per sec or 15 mbytes per 5 min volume of data. Because the PE3242 has more memory, is faster, and has more disk storage capability than the VAX 11/750, it appeared reasonable to accomplish real time interpolation on the PE3242 and then transfer the interpolated data to the VAX via the ETHERNET.

STX designed and implemented a software package on the PE3242 that performs real time interpolation of radar data based on the Mohr and Vaughn (1979) algorithm. The software for data transfer from the PE3242 to the VAX 11/750 was designed but not implemented. The entire software package was

written in FORTRAN for ease in implementation and debugging. Debugging in a non-real time environment has been completed.

b. Evolution/Vertical Advection Considerations

It is now necessary to address the question -- what is the minimum scale that we can hope to address in a forecast mode? To answer this question one must consider the temporal and spatial scales of the meteorological phenomena being observed and of the collected data. It is well known that there are significant convective cells with scales of 2 to 5 km and lifetimes of 6 to 30 min (Foote and Mohr, 1979). However, the data have temporal resolution of no better than 5 min and spatial resolution as poor as 3 km or more at long ranges. As a consequence it is not reasonable to expect to be able to track individual convective elements. Using an approach designed to track small convective cells, Harris and Petrocchi (1984) concluded that automated tracking of these features was unreliable, because of the vertical motion and evolution of the precipitation.

As an illustration of the effects of vertical advection and evolution but on a larger scale than addressed by Harris and Petrocchi, the 32 dBz contours at 5 km above sea level are plotted in Fig. 1 for four successive scans separated by 6 min for Hurricane Gloria, 7 September 1985. The original data were collected every 300 m in range, 0.6 deg in azimuth, and 0.8 to 2.2 deg in elevation and then were interpolated to a Cartesian grid with 2 km horizontal resolution using bilinear interpolation. The contours in this figure were extracted from the interpolated data by the Freeman chain code technique outlined below. Note the degree of small scale detail in these contours and the degree of evolution that occurs amongst these sets. It should be quite obvious that working with these contours alone will not allow us to generate reasonably detailed forecasts. One approach would be to consider a three-dimensional analysis/forecast approach that would allow some assessment of vertical advection but probably not of growth. Another approach would be to derive a more conservative field, possibly through vertical integration or through some compositing of the reflectivity data.

The significantly simpler approach of deriving a more conservative field was adopted. The radar data were composited in a manner much like

76
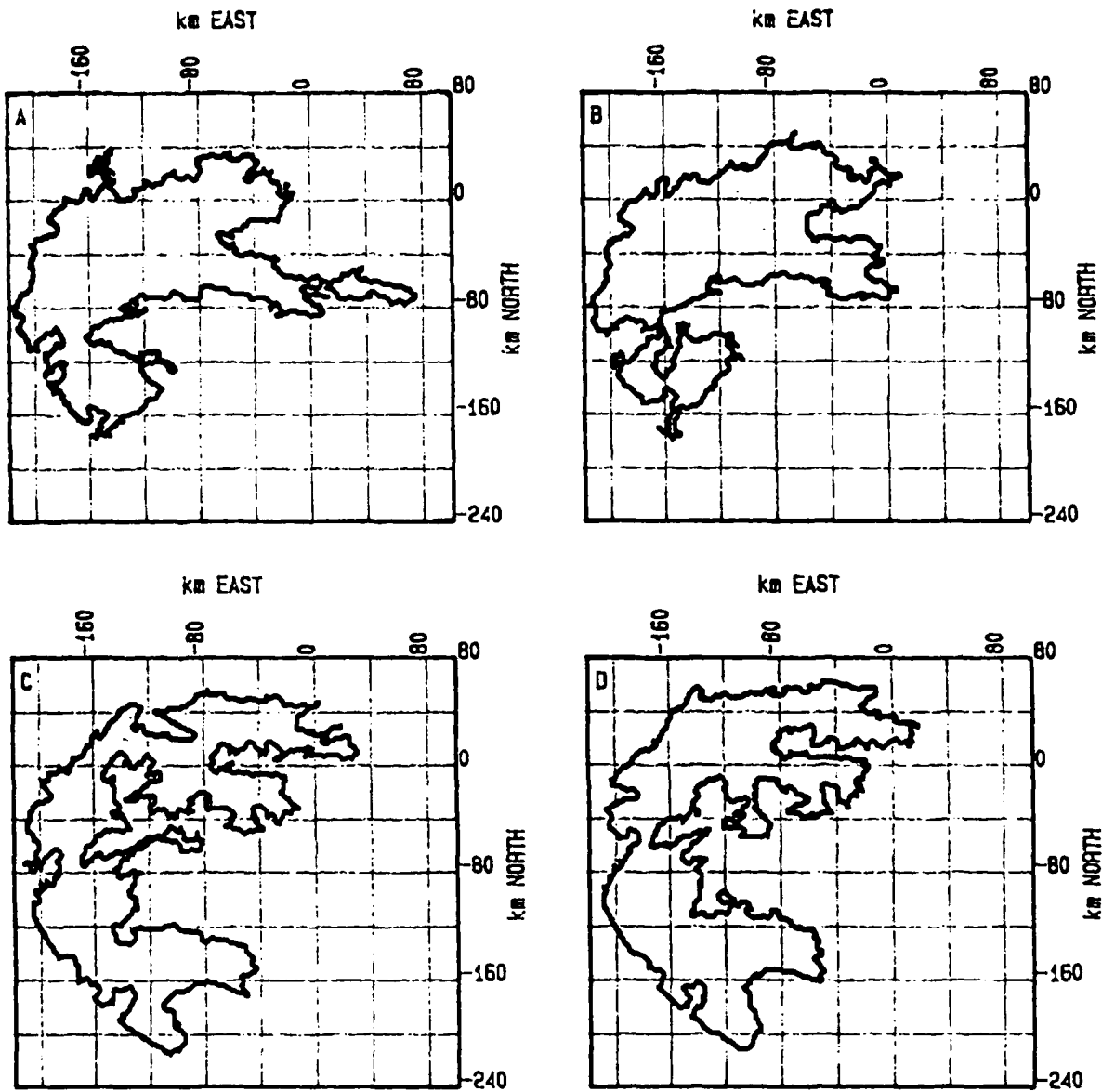
Fig. 1   Radar Reflectivity 32 dBz Contour

(Contour is for 5 km height as measured by AFGL/LYR 10 cm radar at (A) 1052 EST, (B) 1058 EST, (C) 1114 EST, and (D) 1121 EST on 27 September 1985.)

that used in the NEXRAD system; namely, by retaining the maximum reflectivity
factor throughout the depth of the observations above a horizontal grid
point. This resulted in the contours in Fig. 2, which correspond to those in
Fig. 1. Note the vastly improved degree of conservation amongst these plots
as contrasted to those of Fig. 1. There is still a significant amount of
fine-scale structure which is, of course, not nearly as conservative.
Reduction of some of this structure will be discussed next.

c. Data Filtering

Once the data have been transformed into Cartesian space and any desired
composition for integration has been performed, it is still necessary to
preprocess the data further to remove noise, smooth boundaries, and eliminate
small scale features. This involves passing filters of different types and
shapes across the data. Several that have been implemented will now be
discussed. For a more complete description of filters and their effects see
Pratt (1984).

1´. Median Filtering

The first step in this smoothing process is to apply a median filter,
sometimes as often as two to three times in succession, primarily for noise
suppression. In general, a filter of some specified geometric shape (window)
but with an odd number of elements is passed across the entire image. As it
is applied to the data, the filter replaces the center value of the window.
Some of the more commonly used window shapes for a median filter are shown in
Fig. 3. The windows used in the RAPID system are the 3x3 box to remove noise
spikes often seen in radar data and the 1x5 line to eliminate missing scan
lines often occurring in satellite imagery.

```
                         X            X

        X X X            X            X

        X X X          XXXXX          X

        X X X            X            X

                         X            X
```

Fig. 3 Windows Commonly Used with Median Filters
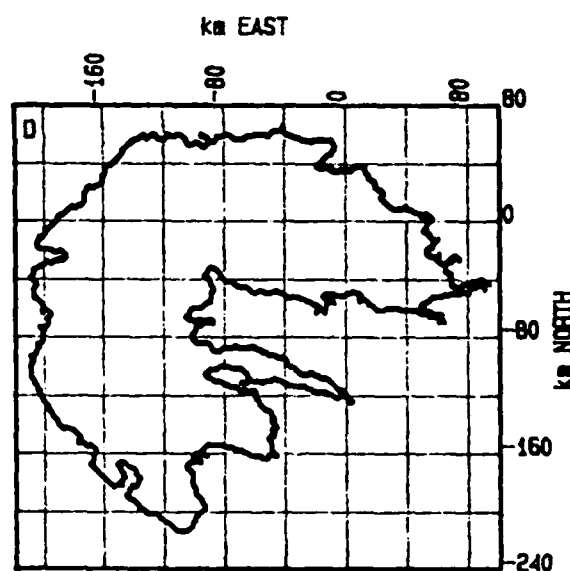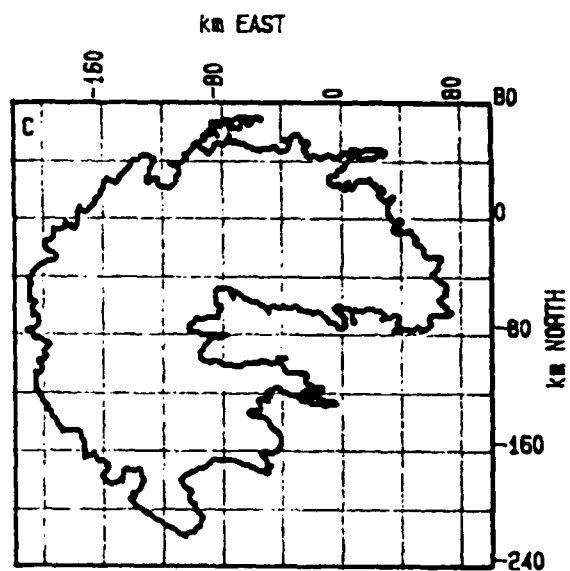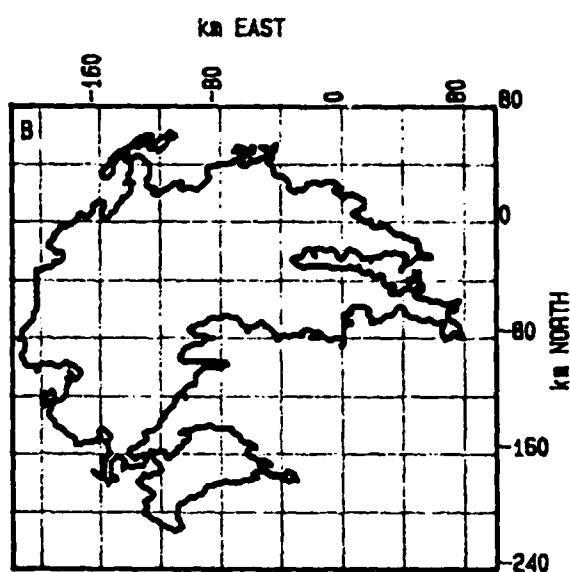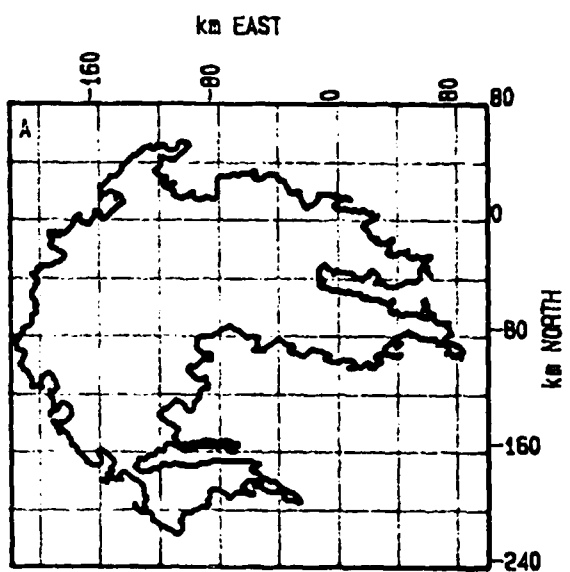
Fig. 2 Same as Fig. 1 but for Composited Reflectivity Factor

Although median filtering is highly effective for noise suppression, it also affects "good" data. Pratt (1978) states that in general, regions that are unchanged by a single pass of the median filter will remain unchanged in subsequent passes. Thus, generally only edges will be affected by median filtering, since edges are where the signals display the greatest change. This is illustrated by Fig. 4.

```
                      X X X
           Filter =   X X X
                      X X X
```

Original Feature	1 Pass with Filter	2 Passes with Filter
0 0 0 0 0 0	0 0 0 0 0 0	0 0 0 0 0 0
0 1 0 0 0 1	0 0 0 0 0 1	0 0 0 0 0 1
1 1 1 0 1 1	1 1 1 0 1 1	1 1 1 1 1 1
1 1 1 0 1 1	1 1 1 1 1 1	1 1 1 1 1 1
1 1 1 1 1 1	1 1 1 1 1 1	1 1 1 1 1 1
1 1 1 1 1 1	1 1 1 1 1 1	1 1 1 1 1 1

Fig. 4 Effect of Application of 3x3 Median Filter on Image Values

In a two-dimensional filter such as the 3x3 box filter, edges are generally preserved but thin lines are destroyed and corners are clipped. The application of a plus-shaped filter would preserve horizontal and vertical lines and corners but diagonally oriented lines or corners would still be lost. In other words, small-scale (relative to size of filter) perturbations of a feature will be smoothed by a median filter, as seen in this figure, which is exactly the result desired for noise reduction. The problem with a median filter is that its response function is basically unknown, so that there is uncertainty as to how the filter is affecting the size spectra of the data structure. However, if the filter is applied judiciously, it is thought that the effects will be minimal on the scales being addressed in this problem. This remains to be verified.

2´. Lowpass Filtering

Another filter used to smooth edges is the lowpass filter. The purpose of a lowpass filter is the same as that of a median filter; i.e., to

preserve low signals and suppress relatively high ones. The key difference
between the two types of filter lies in the fact that a lowpass filter is an
averaging filter and thus replaces the center value of the filtering window
with the average of its neighbors, not the median. Thus, the lowpass filter
has more of a blurring effect on the data. The filter is applied to the
data by multiplying the values in the window by the corresponding filter
values, adding the products, and multiplying by normalization factors. The
value in the center of the window is replaced by this average value if it is
greater than the average. Typical filters are presented in Fig. 5.

$$\frac{1}{9} * \begin{vmatrix} 1 & 1 & 1 \\ 1 & 1 & 1 \\ 1 & 1 & 1 \end{vmatrix} \qquad \frac{1}{16} * \begin{vmatrix} 1 & 2 & 1 \\ 2 & 4 & 2 \\ 1 & 2 & 1 \end{vmatrix} \qquad \frac{1}{48} * \begin{vmatrix} 0 & 1 & 2 & 1 & 0 \\ 1 & 2 & 4 & 2 & 1 \\ 2 & 4 & 8 & 4 & 2 \\ 1 & 2 & 4 & 2 & 1 \\ 0 & 1 & 2 & 1 & 0 \end{vmatrix}$$

Fig. 5   Commonly Used Lowpass Filters

The form of the lowpass filter that has been adopted is

$$\frac{1}{16} * \begin{vmatrix} 0 & 0 & 1 & 0 & 0 \\ 0 & 1 & 2 & 1 & 0 \\ 1 & 2 & 0 & 2 & 1 \\ 0 & 1 & 2 & 1 & 0 \\ 0 & 0 & 1 & 0 & 0 \end{vmatrix} \quad .$$

There are several reasons why this particular filter was selected. A
larger (more than 3x3) filter was required for smoothing considerations but
the filter size also had to be kept as small as possible for efficiency.
Also, the filtering is done in the image processor which cannot easily
handle division. Therefore, operations are greatly facilitated if a power
of two is used as the divisor, which reduces the division to a shift-left
operation. (An integer divided by 16 is equivalent to a shift-left by 4
bits.)

This filter is generally applied to the data once, so as to minimize
overfiltering. This lowpass filter has been applied to the data represented
in Fig. 2 and the resultant contour is presented in Fig. 6.

81
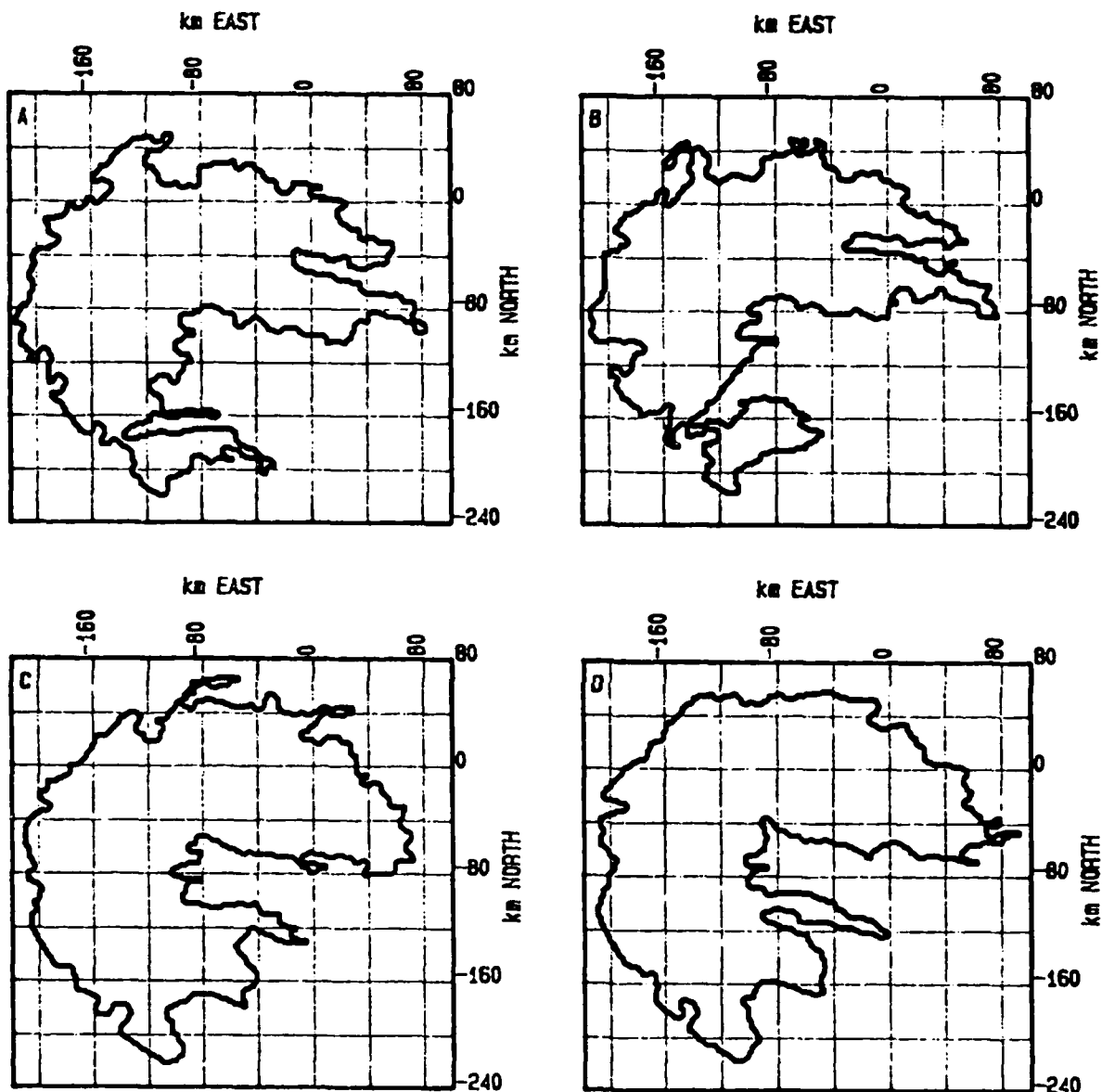
Fig. 6   Same as Fig. 2 but After Lowpass Filter Has Been Applied

d. Resolution Degradation

Filtering data effectively degrades their resolution to a scale
somewhat larger than the grid resolution. Another technique for resolution
degradation is simply to throw out every cther data point. While this is a
less controlled method of degradation than using a well designed filter, it
has the distinct advantage that the number of data points to be used for
subsequent processing is reduced by a factor of four, which obviously
facilitates processing. This step would only be required if the data had
originally been interpolated onto too fine a grid. This is the current
practice since "too fine" has yet to be determined. Fig. 7 shows the
contour of Fig. 6 after resolution degradation.

e. Feature Editing

Many times there will be a multitude of small features because of the
presence of ground clutter or small precipitation elements. Since these
should not or cannot be tracked, methods were sougnt to eliminate such
regions. Thus a technique similar to that used to extract the feature of
interest once the data are properly cleaned up has been implemented.

For a given threshold value T, a value equal to or less than that to be
used for feature extraction, the image is scanned until a region is found
having valu-s greater than or equal to T. If the boundary size of the
region is smaller than some predetermined value (for a 256x256 image with 2
km resolution, 50 appears to work well), then the region is considered to be
a contaminant or a feature too small to be retained and is eliminated. This
is done by filling in the entire region with a value of T - 1. The search
then continues, until all undesirable regions have been found and filled in
with a new lower value. At this point only the regions containing the
features to be tracked remain in the image with data values equal to or
greater than that threshold. The image is now ready for the extraction of
the features.

3. Data Representations

There are several ways to represent the data and derive characteristics
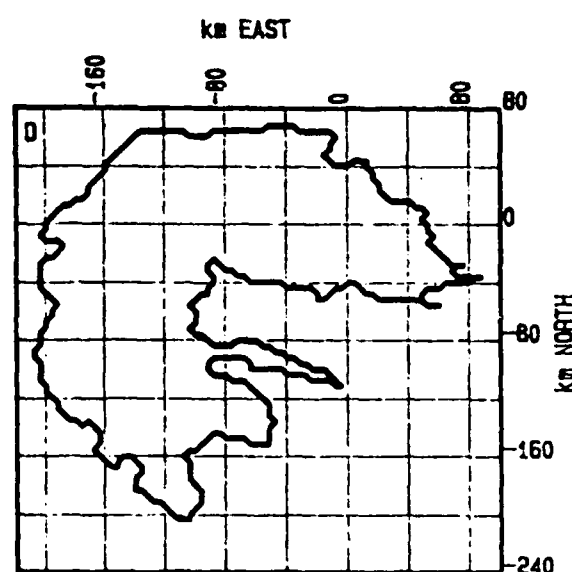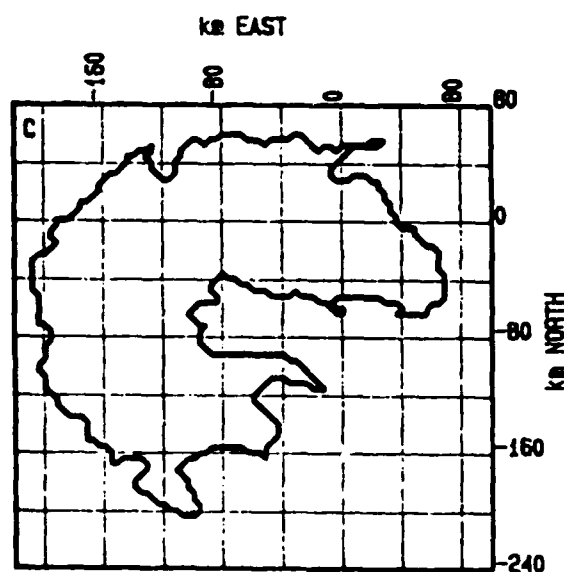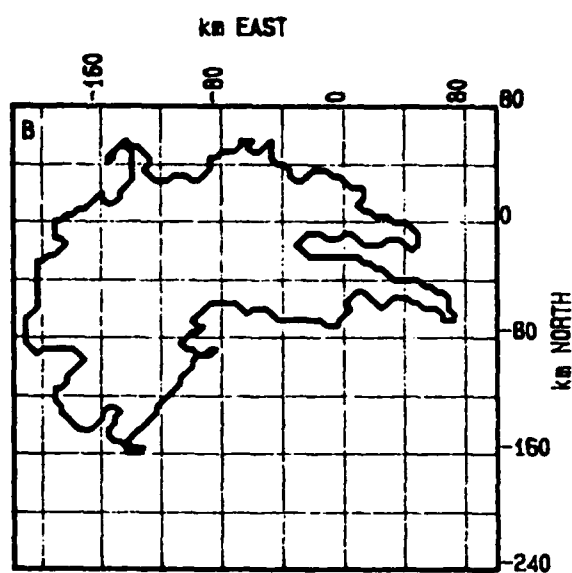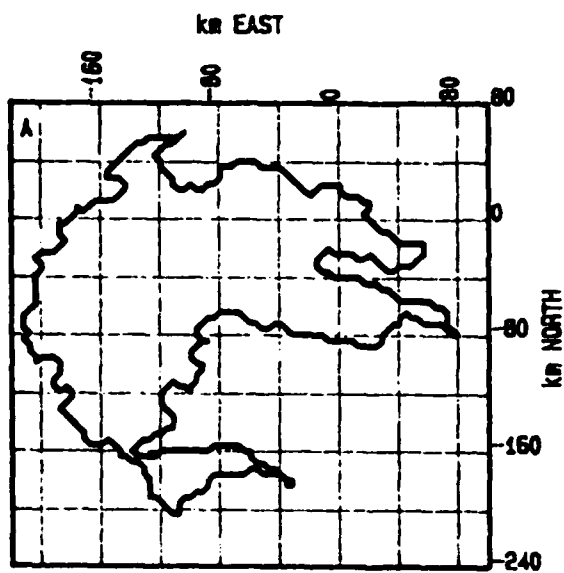
Fig. 7   Same as Fig. 6 but After Degradation of Resolution from 2 km to 4 km

that could then be used for predictions. We will now outline those that have been considered and will present reasons for pursuing or not pursuing each. It is assumed that data are available in rectangular Cartesian coordinates and, if necessary, are available at a multitude of layers through the troposphere.

a. All Data Values

This would be the brute force approach and would involve monitoring and predicting the values of the data fields everywhere within the processing realm. Three-dimensional advection and propagation would need to be assessed in order that reasonable results might be obtained. This would be a mammoth undertaking involving much more computing capability than is available. The results would be much more detailed than is required for solving the current problem. Also the probability of attaining an accurate forecast is thought to be small, because of the complexity of the problem. Even if the amount of data to be processed were reduced to a couple of planes of degraded resolution data the problem would still be complex and probably intractable.

b. Binary Data Sets

If one were to threshold the data such that data with values below the threshold were given a value of 0 and those above a value of 1, processing would be simplified. However, one would be left with a rather large data set that would still require rather complex analysis procedures. Also, there is little to be gained over the more compact and more easily handled contour representation to be examined next.

c. Boundary Extraction

A method for contour extraction was developed that employs the Freeman chain code. The image data we are working with, satellite or radar, are generally described by an array of values in Cartesian space that reflect some unit of measure (e.g., temperature in an IR image). A contour value is selected that will encompass the region of interest so that all values

85

within the contour are greater than those outside. The binary data set previously discussed would be sufficient for this analysis.

The picture is scanned in a left to right, top to bottom manner until a point on the boundary of the region is located. This is then referred to as the starting point or origin of the contour. From this point the boundary of the region is found by keeping the region within the boundary always to the left of the path being followed while searching for the next nearest neighbor to the most recently located boundary point. The directional code presented in Fig. 8 is used to represent the path to the nearest neighbor for each boundary point.
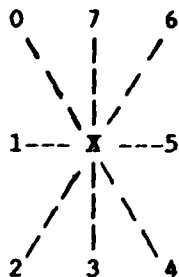
Fig. 8 8-directional Freeman Chain Code

The code leading to the nearest neighbor for each newly located boundary point is saved in an array; the origin and final length of the code are saved also. Taken together, these three elements will completely describe the boundary of any closed region. As an example, consider the rectangle (region marked by *'s) in Fig. 9.

```
  0   1   2   3   4   5   6   7   8
0 +---+---+---+---+---+---+---+---+
  |   |   |   |   |   |   |   |   |
1 +---*---*---*---*---*---*---+---+
  |   |   |   |   |   |   |   |   |
2 +---*---*---*---*---*---*---+---+
  |   |   |   |   |   |   |   |   |
3 +---*---*---*---*---*---*---+---+
  |   |   |   |   |   |   |   |   |
4 +---*---*---*---*---*---*---+---+
  |   |   |   |   |   |   |   |   |
5 +---+---+---+---+---+---+---+---+
```
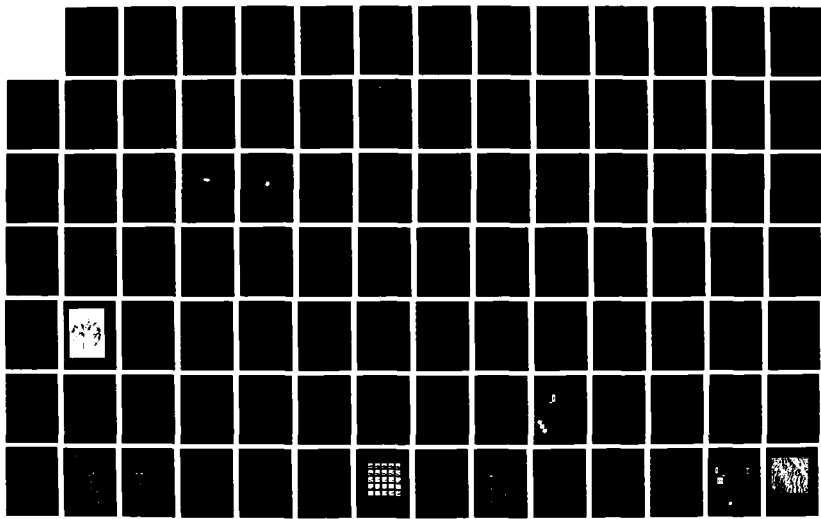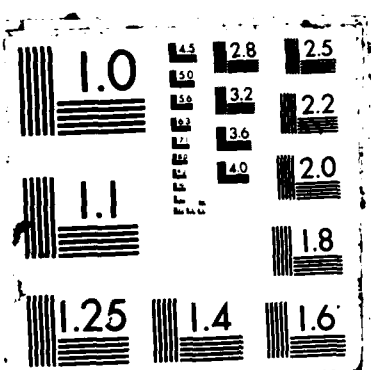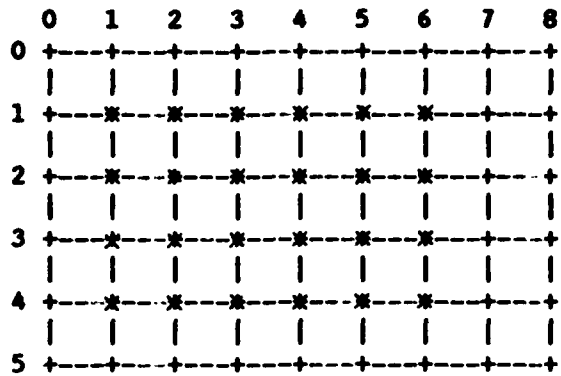
Fig. 9 Region to be Contoured Denoted by * Plotted in Cartesian Space
(Coordinates are labelled to left and across top of figure.)

This rectangle would be completely described by knowing that:

1) the origin is (1, 1);

2) the length of the code stored in an array is 16; and

3) the array contains as its elements

{ 3, 3, 3, 5, 5, 5, 5, 5, 7, 7, 7, 1, 1, 1, 1, 1 }.

4. Feature Motion

a. Cartesian Framework

One of the proposed algorithms uses the concept of orthogonal vectors
to boundary points for mapping one boundary to a second one. The Freeman
chain code is used to generate a sequence of orthogonal vectors for the set
of boundary points using the pairs of previous and next chain codes of each
point to give a resultant orthogonal vector. Each orthogonal vector is then
extended from its origin on the first boundary until it intersects the
second boundary. This intersection point is mapped to the vector origin.

For example, given a boundary point where the direction leading to it
is a 1, and the direction to the next neighbor is 3, the direction of a
vector perpendicular to the angle between the point and its two neighbors
can be determined to be 0 or 4. Once vectors for all points along one
boundary have been found, the first contour is aligned with the second
contour by means of minimizing the areal difference between the two images
or by overlaying the areal centers.

Theoretically this system appears quite feasible, and in some types of mapping, such as with strictly convex contours, will be quite effective. For IR or radar data, however, the algorithm has been found to be not very useful, because of the general overall "curviness" of the contours involved as well as the smaller irregularities along the boundaries. One of the major difficulties is the multitude of vectors that cross one another, as shown in Fig. 10. Averaging or thinning of the orthogonal vectors tends to alleviate but not eliminate the problem of crossovers. Another difficulty is the slowness of operating on such a large set of data points (average of 300 points on a boundary).

b. Freeman Chain Code

1'. Matching Straight Line Segments

One of the algorithms showing great promise in mapping and tracking is one that involves breaking up contours into straight lines and then matching these straight line segments for successive scans. A matching algorithm has been developed that uses this idea of line segments to break the data down and simplify them before performing some kind of matching. Classification of the data in this manner reduces the number of data points with which we need to work from about 300 to 15 to 25.

To break up the chain code (i.e., classify it piece-wise), a means of classification was developed. The method currently employed is a segmentation of the chain code into a sequence of straight or pseudo-straight lines. Two techniques have been tested for this type of classification. Both methods are based on Freeman's definitions of what constitutes a line in chain code. The first requires strict adherence to his three rules while the second reduces his criteria to the first rule. For details as to Freeman's rules and how they have been implemented see Appendix A.

Once straight line segments are identified in chain codes for two successive data fields, a process of matching segments from the first field with those from the second is applied. Details of this matching process are contained in Appendix B.
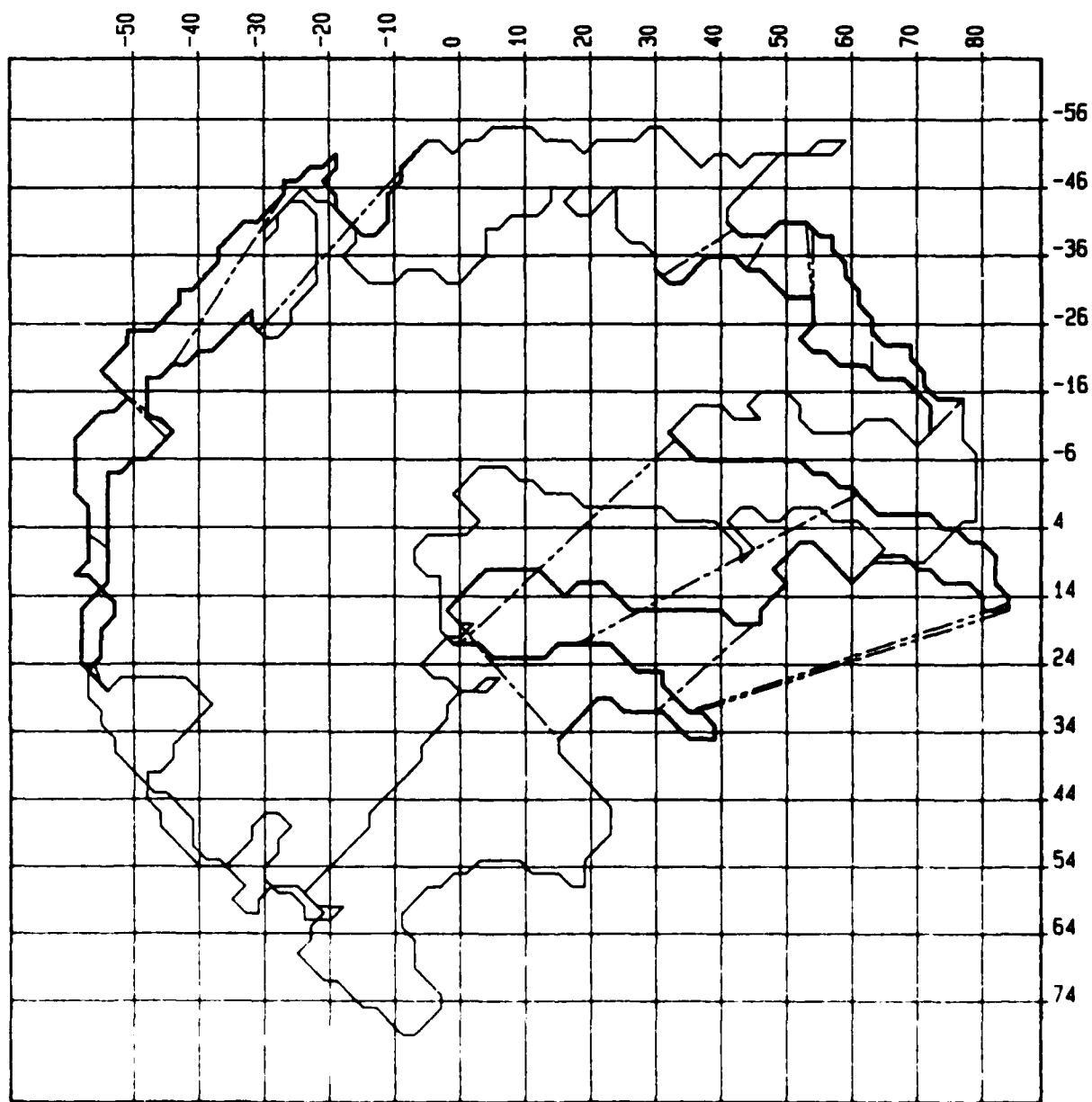
Fig. 10 Example of Orthogonal Vector Technique of Motion Estimation

(Dark contour is reflectivity contour for 1052 EST; light contour is for 1058 EST. Dashed lines are selected lines drawn orthogonally from earlier contour to later one.)

2´. Curve Fitting Chain Code Segments

The goal is to take segments of the chain code for one data field regardless of shape and to find the best match in the code for the next time. This technique therefore focuses on looking for identical shapes, which is a major part of pattern recognition. The assumption in this technique is that during advection and evolution, contour segments retain their shapes. Quite obviously this will not always be the case. However, this issue will be addressed further a little later. In this technique the chain code for the first data set is divided into segments of specified length, usually 10 to 25 percent of the total number of codes. This segment is then compared with every possible segment of identical length in the second data set. For each comparison, the mean difference and the mean square of the differences are computed regardless of location in space. An example of one such computation is contained in Fig. 11 where these two parameters are plotted vs. starting segment number for the second data field. From this figure there is a very obvious minimum of the mean squares of the differences at segment 157 where there is also a minimum of the mean and in fact a crossover of the mean curve from positive to negative. Not all attempts at curve matching produced such neat results. In some cases, because of considerable evolution, no match was possible. However, in all cases where the fit looked reasonable to the eye and mind, the best fit appeared to be that identified with the minimum mean square. By applying a maximum acceptable value for the minimum mean square, one was able to focus in on those regions of best fit. This is the criterion used for the presentation in Fig. 12.

c. Motion Determination

Both matching techniques outlined above have as products old and new positions of line segments. For each segment the following can be determined:

* Absolute location
* Length.

90
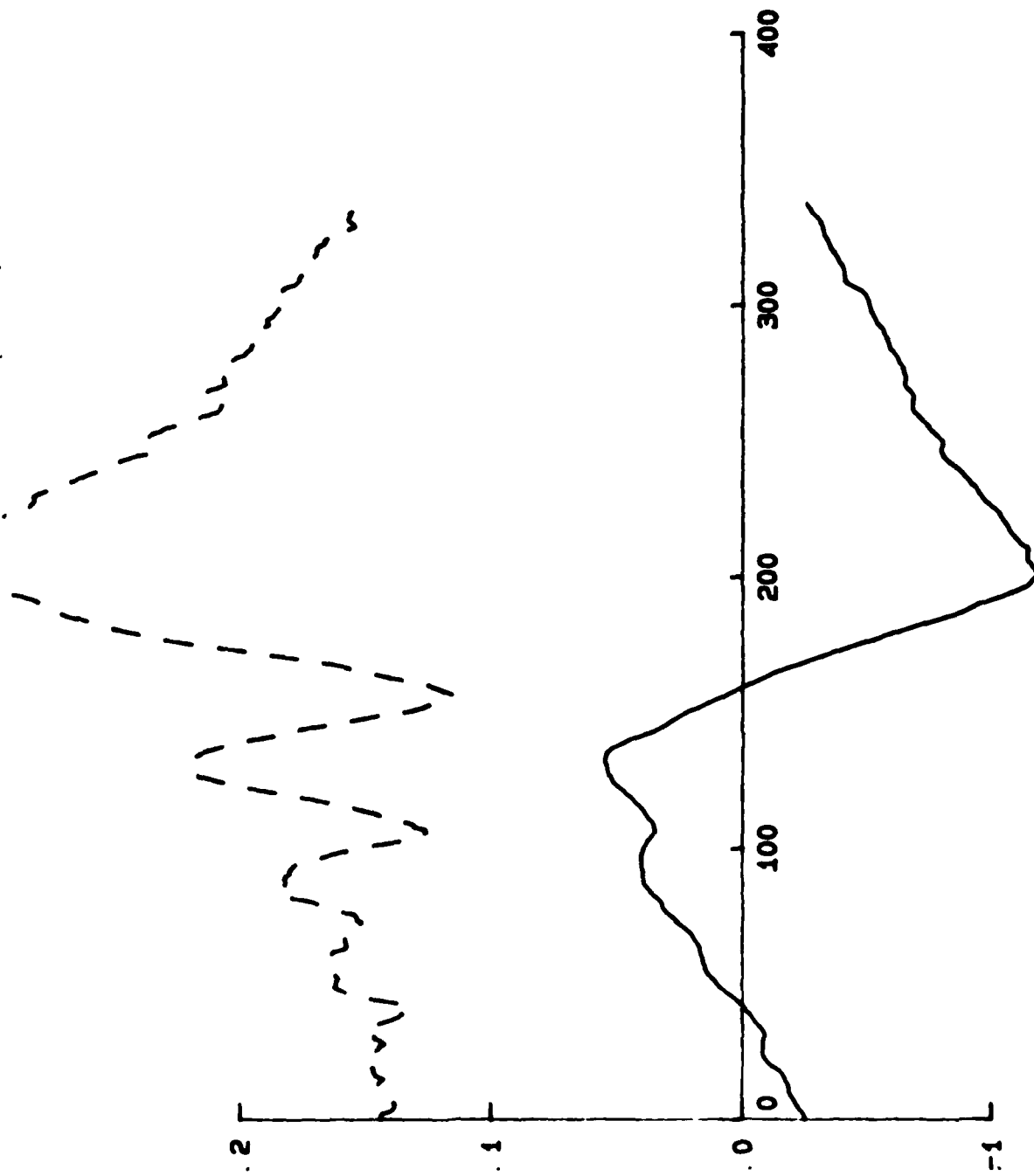
Fig. 11 Mean Differences (solid line) and Standard Deviations (dashed line) for Fit of Selected Segment from Data for 1114 EST (Fig. 7(C) with All Possible Segments in Data for 1121 EST (Fig. 7(D))

(Abscissa is starting element number for each segment of second contour.)

91
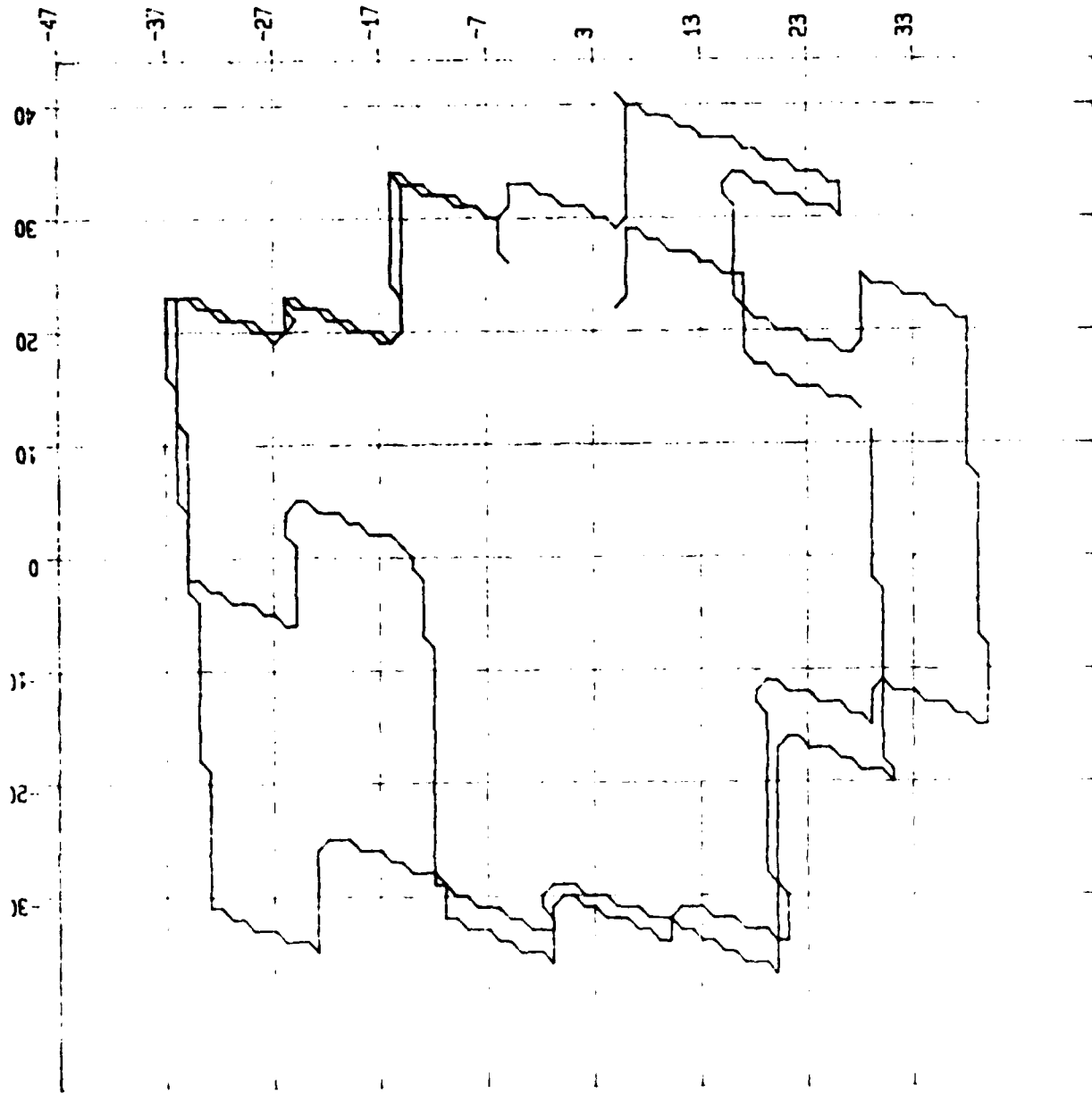
Fig. 12 Example of Best Fit of Segments for Two Successive IR Scans

(Light plot is later contour; dark segments are for earlier contour and are located where they best fit later contour.)

92

From these characteristics, one can then determine:

* Absolute motion of the segments
* Relative motion of the segments to assess evolution
* Global motion of the feature.

These attributes will be used by AFGL radar meteorologists in developing techniques for nowcasting precipitation locations.

5. References

Dudani, S. A., 1976: Region extraction using boundary following. In Pattern Recognition and Artificial Intelligence, C. H. Chen, ed., Academic Press, pp. 216-232.

Harris, F. I., and P. J. Petrocchi, 1984: Automated Cell Detection as a Mesocyclone Precursor Tool. AFGL-TR-84-0266, Air Force Geophysics Laboratory, Hanscom AFB, MA, ADA154952.

Mohr, C. G., and R. Vaughan, 1979: An economical procedure for Cartesian interpolation and display of reflectivity factor data in three-dimensional space. J. Appl. Meteor., 18, 661-670.

Pratt, William K., 1978: Digital Image Processing. Wiley-Interscience.

Wu, Lo-De, 1982: On the chain code of a line. IEEE Trans. on Pat. Anal. and Mach. Intel., Vol. PAMI-4, #3, 347-353.

Appendix A - Straight Line Segmentation of Chain Code

Two techniques for determining whether a chain code sequence is a straight line will be presented. The first method employs Freeman's definition for the chain code of a line. He stated that in order for a chain code to be a line it must meet the following criteria:

1) At most two basic directions are present and these can only differ by 1 modulo 8;
2) One of these values always occurs singly;
3) Successive occurrences of the principal direction occurring singly are as uniformly spaced as possible.

Wu (1982) provides the algorithm presented in Fig. A-1 for determining whether a given string of code represents a line according to the criteria suggested by Freeman.

Another more relaxed method for determining straight lines in the chain code employs only the first of Freeman's criteria; i.e., that the chain code will describe a line if the chain contains no more than two directions and these directions differ by 1 modulo 8.

The chain code (C) for a contour is broken into a series of sequential, connected line segments by iteratively applying one of the above algorithms to each point of the chain code, decreasing the length of the chain until a valid line is found beginning at that element, and then noting this maximum length and the primary direction of the line for each starting element of the code. For the rectangular region denoted in Fig. 9, the maximum line lengths found for each element of the code would be stored in an array MAXLEN as (length, direction) given C = (3, 3, 3, 5, 5, 5, 5, 5, 7, 7, 7, 1, 1, 1, 1, 1)

MAXLEN [0] = 3, 3
MAXLEN [1] = 2, 3
MAXLEN [2] = 1, 3
MAXLEN [3] = 5, 5
MAXLEN [4] = 4, 5
MAXLEN [5] = 3, 5
MAXLEN [6] = 2, 5
MAXLEN [7] = 1, 5
MAXLEN [8] = 3, 7

Input string $C = c_1 c_2 c_3 \ldots c_a$

How many different symbols in it?   > 2 (left)   1 (right)   2 (down)

Do these two symbols only differ by one?   No

Yes

Does one of them occur singly?   No

Yes

Does the symbol occurring singly appear only once?   Yes

No

REJECT
Not chain code line

Compute k_1, n_1, n_2, $\ldots, n_p$, k_2.
k_1, is position where symbol occurring singly is first present.
n_1, n_2, n_3, $\ldots$ are lengths of successive symbols occurring singly.
k_2 is length between last symbol and last symbol occurring singly.

PASS
Chain code of line

Compute $M = \max(n_1, n_2, \ldots)$

$k_1 <= M$ and $k_2 <= M$?   No

Yes

Form new string C:
if $k_1 = M$ and $k_2 = M$, $C = k_1 n_1 n_2 \ldots n_p k_2$
if $k_1 = M$ and $k_2 < M$, $C = k_1 n_1 n_2 \ldots n_p$
if $k_1 < M$ and $k_2 = M$, $C = n_1 n_2 \ldots n_p k_2$
if $k_1 < M$ and $k_2 < M$, $C = n_1 n_2 \ldots n_p$

Fig. A-1 Flow Chart of Algorithm to Determine Whether a Sequence of Chain Code Qualifies as a Straight Line (After Wu, 1982)

```
MAXLEN  [9]  = 2, 7
MAXLEN  [10] = 1, 7
MAXLEN  [11] = 5, 1
MAXLEN  [12] = 4, 1
MAXLEN  [13] = 3, 1
MAXLEN  [14] = 2, 1
MAXLEN  [15] = 1, 1.
```

Now we must search the MAXLEN array to find the longest segment left (not
marked USED). In this case, the first segment found would be the one
starting at element 3. This element is saved, along with the length and
direction of the line, as (start, len, dir):

LINE 3, 5, 5.

Then we mark the elements of this line segement as USED in the MAXLEN array:

```
MAXLEN  [0]  = 3, 3
MAXLEN  [1]  = 2, 3
MAXLEN  [2]  = 1, 3
MAXLEN  [3]  = 0, USED
MAXLEN  [4]  = 0, USED
MAXLEN  [5]  = 0, USED
MAXLEN  [6]  = 0, USED
MAXLEN  [7]  = 0, USED
MAXLEN  [8]  = 3, 7
MAXLEN  [9]  = 2, 7
MAXLEN  [10] = 1, 7
MAXLEN  [11] = 5, 1
MAXLEN  [12] = 4, 1
MAXLEN  [13] = 3, 1
MAXLEN  [14] = 2, 1
MAXLEN  [15] = 1, 1
```

and continue searching the list MAXLEN recursively until all elements are
marked USED.

The result for this example (sorted in order of starting element) would
be (start, length, direction):

LINE 0, 3, 3

LINE 3, 5, 5

LINE 8, 3, 7

LINE 11, 5, 1.

This line tells us the starting location, length, and direction of each line
segment in the chain code list.

Appendix B - Segment Matching for Feature Mapping

A detailed description of the technique for matching straight line segments is provided. In Fig. B-1 a second contour is quickly described for the purpose of matching with that in Fig. 9.

```
     0   1   2   3   4   5   6   7   8
  0  +---+---+---+---+---+---+---+---+---+
     |   |   |   |   |   |   |   |   |
  1  +---*---*---*---*---*---*---*---*
     |   |   |   |   |   |   |   |   |
  2  +---*---*---*---*---*---*---*---+
     |   |   |   |   |   |   |   |   |
  3  +---*---*---*---*---*---*---+---+
     |   |   |   |   |   |   |   |   |
  4  +---*---*---*---*---*---+---+---+
     |   |   |   |   |   |   |   |   |
  5  +---+---+---+---+---+---+---+---+
```
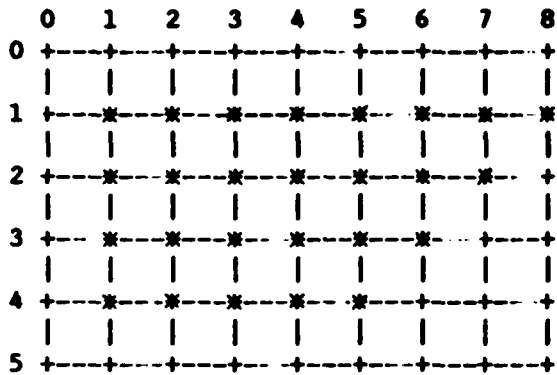
Fig. B-1 Region of Data with Contour Boundary Defined by the Chain Code (3, 3, 3, 5, 5, 5, 5, 6, 6, 6, 1, 1, 1, 1, 1, 1, 1), with Origin (1, 1) and Length 17

Applying the technique described in Appendix A to segment this new contour, we get values for (start, length, direction) of

LINE2 0, 3, 3
LINE2 3, 4, 5
LINE2 7, 3, 6
LINE2 10, 7, 1.

Of course, since a boundary is a continuous object, the starting location is basically arbitrary. In this case the upper left-most pixel is defined as the origin, but it could just as well have been the lower right-most. Therefore the code and associated data are treated not as a linear list, but in a circular fashion; e.g., a circular queue. Since the chain code is a directional code, the shape and orientation of the boundary are preserved no matter where the starting location of the code is designated to be.

97

There are several methods for comparing two such lists of line data as

```
LINE 0, 3, 3          LINE2 0, 3, 3
LINE 3, 5, 5          LINE2 3, 4, 5
LINE 8, 3, 7          LINE2 7, 3, 6
LINE 11, 5, 1         LINE2 10, 7, 1 .
```

Starting locations, line lengths, or directions can be compared. Consider the following match for the directional codes:

Segment Number	Line 1	Line 2
1	3	3
2	5	5
3	7	6
4	1	1

and, remembering that the list is circular, by examination we can see that we get the best (i.e., longest continuous) match between the two lists at segments (4, 4), (1, 1), and (2, 2).

For two large contours, which are broken up into closer to 20 line segments, the search is reiterative; i.e., the longest match is found, saved, and its elements marked as USED, the next longest match is found, etc., until no more matches can be made.

From this algorithm, we have a mapping between segments in the first feature and segments in the second feature. Each segment has several associated characteristics, including a segment length, orientation, starting code offset, and, for a given point in the segment, distance from some point of reference.

C. RAPID System Development

1. Introduction

RAPID is an acronym for the AFGL Remote Atmospheric Probing Information Display system. The main computer for the system is a VAX 11/750 with 450 mbyte fixed disk and 1600 bpi tape drive. Peripherals to the system include an Adage 3000 image processor, Summagraphics digitizing table, Dunn Instruments MicroColor digital camera, and HP7475 color pen plotter. The VAX is connected to the AFGL/LYR PE3242 via ETHERNET and to the AFGL/LYS VAX 11/750 via DECnet.

STX is responsible for maintenance of system software, data management, and development and management of general purpose applications software for the RAPID system. Its activities in these areas are summarized in the following sections.

2. VAX Software Installation

The LYR VAX 11/750 was upgraded to operating system VMS V4.4 and the FORTRAN compiler was upgraded to Version 4.5. Generally, the upgrades were transparent at the command level and consisted mainly of fixes from bugs found in the previous versions.

Two software packages, DECSlide and DECGraph, were installed. These new packages will be useful in creating slides, viewgraphs, and other demonstration materials. However, neither package can be used currently because both require terminals with REGIS graphics capability, which is available only on the DECMATE II that has not yet been connected to the VAX.

3. VAX Disk Reorganization

Thy LYR VAX disk was reorganized to allow faster and easier access to all data and programs located on the system. A stand-alone backup and restore was then performed on the VAX disk in order to compress the data and eliminate fragmentation, making disk I/O more efficient. All files are now categorized as DATA, ANALYSIS, DISPLAY, CONVERSION, or UTILITY files, as illustrated in Fig. 1.

```
                        +--RADAR-------+--ADAGE
                        |              +--VAX
                        |
                        +--SAT- ....---+--ADAGE
                        |              +--VAX
                        +--HELP
        +----ANALYSIS--+--MISC
        |               +--PROD--- ....+--ADAGE
        |               |              +--VAX
        |               +--RADAR
        |               |
        |               +--SAT----- .-+--LYS
        |               |             +--OLD
        |               +--HELP       +--UWSSEC
        +--- CONVERT---|
        |               +--PE--- .------SCRM
        |
        |               +--RADAR-- . +--LYR
        |               |            +--MOHR
        |               |            +--OTHER
        |               |
        |               +--SAT-- .----+--LYR
        |               |             +--LYS
        |               |             +--OTHER
        |               |             +--UWSSEC
        |               +--HELP
DUAO-+----DATA-- . .-+--MISC
        |               +--PROD--- . +--OVERLAY
        |               |            +--SNAPSHOT
        |               +--DEMO
        |
        |               +--RADAR
        |               +--SAT
        |               +--HELP
        |               +--PROD--- .-+--OLD-MCIDAS
        |               |
        +----DISPLAY-- +--PAINT-- .-+--EXE
        |               |            +--GEN
        |               |            +--UCODE
        |               |            +--UTIL
        |               |
        |               +--TOOLS-- ---INTERACTIVE
        |               +--HELP
        |               +--MISC
        +----UTIL---   +--IO-- .----+--BITPAD
                                     +--DISK
                                     +--OTHER
                                     +--PE
                                     +--PLOT
                                     +--TAPE
                                     +--TRILOG
                                     +--UCODEMEM
```

Fig. 1 Configuration of LYR VAX-11/750 Directory Structure for
         Locally Created Software and Data

100

4. Locally Developed Software

a. General Purpose Libraries

Several libraries were created and all resident software was categorized, documented, and placed in one of the common libraries. Object libraries now on the system are:

DISPLAY:[TOOLS]IK.OLB - locally-written software that performs various functions in the Adage 3000. Includes routines that set/get register values, load color tables, save/restore display memory to/from disk, set the crossbar switch, etc.

ANALYSIS:[PROD.VAX]ANALYZE ON VAX.OLB - locally-written software that performs data analysis in VAX memory. Includes routines that locate contours and extract boundaries, describe the contour boundary in terms of a Freeman chain code, find the relative maxima and minima or the center of area of a contour given its chain code, or return the coordinates of the point for a given code of the chain.

ANALYSIS:[PROD.ADAGE]ANALYZE ON ADAGE.OLB - locally-written software that performs data analysis using the Adage image processor. Includes routines to generate a contour silhouette or outline given its chain code, filter data for noise removal and smoothing, reduce or replicate displayed data, clear the display, subtract two images, calculate the histogram of a displayed image, etc. Many of the routines in this library are written in Icross, and run directly in the bitslice processor instead of on the VAX.

UTIL:[IO]IOLIB.OLB - locally-written software that performs various I/O functions between VAX and peripherals, including disk, tape, and image processor.

UTIL:[MISC]DRAWLIB - locally-written software that performs graphics primitive operations; e.g., line drawing, circle and

ellipse generation, character generators (three fonts available).
All are generated in integer or byte arrays, which can then be
displayed on the Adage or saved to disk as needed.

All software described above was fully documented, both in the source
code and separately in a general programmer's guide to using the routines.

b. Image Processing Calling Standard

A common calling standard was devised for all modules that access the
bitslice processor of the Adage. Modules that invoke Icross programs (which
run in the image processor) are written in a high-level language such as C
or FORTRAN and run on the VAX host processor.

The host module first checks a designated region of Adage scratchpad
memory to see whether the required Icross routine is already loaded into the
processor. If not, the routine is loaded, and the name of the routine is
written to that area of scratch. Any input parameters are written to a
predetermined location in scratchpad memory as well. Then the Adage program
counter (PC) is reset and the processor is started. The Icross routine
reads its parameter list from scratchpad, performs the requested functions,
and writes any output parameters to scratchpad. Once done, the routine sets
a flag for the host module to read, which signals that it has completed.
While the processor is running, the host module is in a loop checking for
this flag, and once the flag is set, the module stops the image processor,
reads the output parameters from the scratch area, and returns to its
calling program.

c. HP Plotter Software

Additional software was written for use with the Hewlett-Packard color
pen plotter acquired in 1986. This includes software to plot line graphs
and contour features. The software is generally for use with chain code
data and will plot features such as segments of chain code in a grid with
intervals along each axis marked and labeled. Such plots aid greatly in
analysis of data and also in the development of mapping techniques.

102

d. Demonstration Program

A RAPID demonstration program was written to illustrate the work being done on the RAPID system and some of the special techniques developed at the site. The demonstration program is menu-driven and provides a visual display on either of the Adage display monitors. The following features are available:

* A series of viewgraphs that gives a brief system overview (objective, approach, support, and applications)

* A sequence of time lapse images recorded during Hurricane Gloria that shows the hurricane's evolution through radar reflectivity and satellite visible data

* Several other viewgraphs, including a data pipeline schematic, an illustration of the layout of Adage memory, and a forecast processing flowchart

* An interactive demonstration of the contour location and following technique.

Also, special software was developed for generating viewgraphs in a choice of colors and character fonts on a 256x256 pixel display.

5. Data Management

a. Satellite/Radar Common Header Format

From discussions with AFGL personnel as to requirements for header and data storage of satellite and radar images, a standard image data format was designed. This format is intended for use in all future processing of LYR satellite and radar data.

Both radar and satellite images data files now consist of any number of sets of 256 byte image headers paired with variable size images. The reason for such a global standard format is to permit general purpose software to

be written to read/write/display all local data without regard to its type. The final RAPID Satellite/Radar Common Header Format is shown in Fig. 2.

A program was developed to convert satellite data files from the old standard LYR format to the revised standard. All existing data files were processed by this program, with the new data file headers reflecting the format changes. All programs that access these data files were also modified accordingly, so that the information could be ingested correctly.

b. Memory Mapping

ADAGE display memory was partitioned for future interfacing of satellite and radar data. There are several reasons for the selected mapping scheme (see Fig. 3). Since the RAPID system is supposed to allow simultaneous processing of radar and satellite data, a capability was needed to store data from both sensors in Adage display memory at one time, without the problem of disturbing or overwriting one another.

Satellite data are collected only once every 30 min and radar data once every 5-10 min. Thus there needed to be three to six times as many 'quadrants' reserved for radar data as for satellite data. Radar data is volumetric in nature. It was decided that three elevations would be sufficient to describe precipitation systems. These would be stored for each time interval, and the simplest, most logical method of doing this would be to store the three elevations in three different byteplanes of a single quadrant.

If 60 min of data were to be stored in memory, it would take three areas to store each type of satellite data. Thus, three visible satellite images will be stored in a single quadrant, in three different byteplanes; similarly with IR data - three time intervals in one quadrant in three byteplanes.

Ten quadrants reserved for radar images will permit storage of 1-2 h of data, depending on the frequency of collection. Radar data will be stored with a resolution of roughly 2 km; satellite data with a resolution of 4 km for IR and 2 km for visible. Therefore, to get a window of 512x512 km of data, we need quadrants of size 256x256 each for radar and visible satellite, but only 128x128 for IR.

Starting Byte	Length (bytes)	Mnemonic	Description
0	2	ITYPE	Image type; S/R/P/O
2	2	IOPT	Data type; VI/IR/RR/VR
4	2	DTYPE	Data type; IM/GR/PP/RH/CC
6	2	SENSOR	Sensor ID
8	2	SATID	Satellite ID
10	2	YEAR	YY; year of data
12	2	DAY	DD; julian day of data
14	2	HOURS	HH; hour of data
16	2	MINUTES	MM; minute of data
18	2	SECONDS	SS; second of data
20	2	ULL	upper left corner coordinate, line number
22	2	ULE	upper left corner coordinate, element number
24	2	NLINES	size of image in lines
26	2	NELES	number of elements per image line
28	2	ULATDEG	DDD; ° latitude of ULE
30	2	ULATMIN	MM; minutes latitude of ULE
32	2	ULATSEC	SS; seconds latitude of ULE
34	2	ULONDEG	DDD; ° longitude of ULL
36	2	ULONMIN	MM; minutes longitude of ULL
38	2	ULONSEC	SS; seconds longitude of ULL
40	2	LRES	line resolution, y-scale, km
42	2	ERRS	element resolution, x-scate, km
44	2	NUMSCALE	scale value numerator
46	2	DENOMSCALE	scale value denominator
48	2	SHIFT	linear shift factor
50	2	PRF	radar PRF factor
52	2	WAVELENGTH	radar wavelength (scaled)
54	2	CONSTANT	radar constant (scaled)
56	2	LEVEL	radar level
58	2	LATLOCDEG	sensor location. ° latitude
60	2	LATLOCMIN	sensor location, minutes latitude
62	2	LATLOCSEC	sensor location, seconds latitude
64	2	LONLOCDEG	sensor location, ° longitude
66	2	LONLOCMIN	sensor location, minutes longitude
68	2	LONLOCSEC	sensor location, seconds longitude
70	58	(reserved for future use)	
128	128	COMMENT	comments

Fig. 2   RAPID Common Data Header Format

(Total length of header is 256 bytes. Every entity is 2 bytes long and is either short integer or character data.)

With these factors in mind, it was decided that all data would be stored in the first page of memory, as shown in Fig. 3.

```
         0          256   384   512        768        1023
     0 +----------+-----+----+----------+------------+
       |          |     |    |          |            |
       |          |     |    |          |            |
       |    1     |  3  |    |    5     |     7      |
       |          |     |    |          |            |
       |          |     |    |          |            |
   256 +----------+-----+--------+----------+--------+
       |          |     |        |          |        |
       |          |     |        |          |        |
       |    2     |  4  |        |    6     |   8    |
       |          |     |        |          |        |
       |          |     |        |          |        |
   512 +----------+-----+--------+----------+--------+
       |          |     |        |                   |
       |          |     |        |                   |
       |    9     |  A  |        |                   |
       |          |     |        |                   |
   768 +--     ---+-----+----+   |       D           |
       |          |  B  | E  |   |                   |
   896 |    10    |-----+----|   |                   |
       |          |    C     |   |                   |
       |          |          |   |                   |
  1023 +----------+--------+------+------------+------+
```

Fig. 3 Map of Page 1 of Adage Display Memory Configuration;   Each Labeled Area is a Quadrant
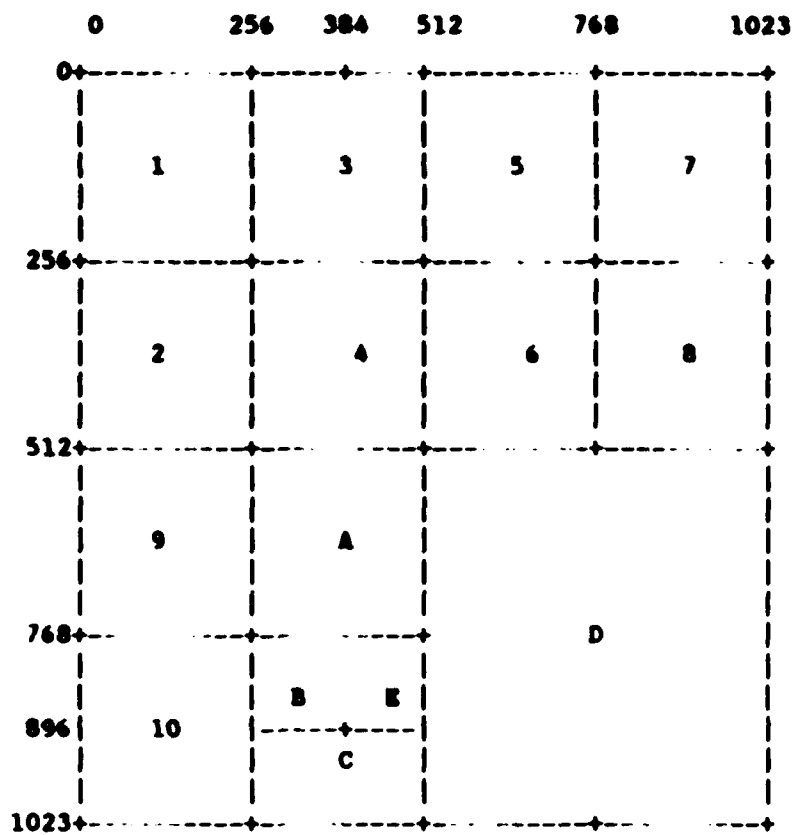
Storage in each of the quadrants is described as follows:

1-10 are the storage areas for ten 256x256 radar images, reflectivity or velocity. Each byteplane (0, 1, and 2) will store a different height for the time represented by its particular quadrant.

A is storage for three 256x256 visible satellite images, a different time scan being stored in each byteplane of the quadrant.

B is storage for three 128x128 IR satellite images, similar to A.

C contains all "file cabinet" information (see below).

D may be used for high resolution or large-scale data displays; e.g., as 512x512 km visible satellite data.

E is reserved for future use.

The second page of display memory is reserved for use as a general work area.

c. RAPID File Cabinet Organization

Since a large amount of data will be stored in memory simultaneously and will possibly be accessed by several separate programs, a method for keeping track of what and where data are presently stored in display memory had to be devised. The RAPID system file cabinet was developed to record in the Adage itself the type and location of all data currently stored in display memory, to serve as a directory that can be accessed by any program at any time. For each image stored in display memory there will be an entry in the file cabinet. The entry will be stored in the same byteplane as the image it describes; thus there will be a separate file cabinet for each of the three byteplanes available. Each entry will contain the information shown in Fig. 4.

Starting Byte	Mnemonic	Description
0-18	(same as in	RADAR/Satellite Data File Header)
20	LCORNER	upper left corner coordinate, line number relative to original image data array
22	BCORNER	upper left corner coordinate, element number relative to original image data array
24	LRANGE	size of displayed image in pixel lines
26	ERANGE	number of elements per displayed line
40	LRES	image resolution, y-length scale in km
42	ERES	image resolution, x-length scale in km
44	XWINDOW	element origin within display memory
46	YWINDOW	line origin within display memory
48	INUMBER	nth image number of this series

Fig. 4 Organization of RAPID File Cabinet

(Total length of each file cabinet entry is 256 bytes. Every entity is 2 bytes long and is either integer or character data.)

6. Analysis Software - SHOWSAT

Originally developed to display and process McIDAS satellite data, program SHOWSAT was modified to allow the user to manipulate the satellite images interactively. SHOWSAT was designed to be used as the main driver for the RAPID system program, which will control the concurrent display and analysis of satellite and radar data.

All display, processing, and analysis can be accessed through the main driver of this program. The program is completely menu-driven; options currently available are described below.

a. Data Selection

Data can be read from any data file storing data in the RAPID Standard Data File format. The data file being accessed can be changed at any time from the main program menu, so that both radar and satellite data can be displayed within the same session.

Images to be displayed can be selected in several different ways. One can display the next stored image or call up any desired image by specifying either its relative image number in the current data file or the time/data of the image data.

Depending on the type of data read from the file as well as what has already been stored in Adage display memory, the program will decide where in memory the image should be stored, and then place an entry with this information into the File Cabinet.

Data that have been previously stored in memory can be redisplayed. There are options to allow the user to display the last image of a given type (IR, VIS, REFL, VEL) retrieved from disk or to change the viewing window or byteplane to scan display memory for a particular image.

At any time, the entire memory or any portion thereof can be saved to a disk file and can also be restored for further processing.

b. Display

The overlay byteplane will contain various maps, grids, or other markers that can be displayed with the data as the user desires. Thus there is an option to turn a particular portion of the overlay plane on and off. This allows the flexibility to display, for example, either a map of New England or the latitude/longitude grid or both with an IR image.

Two standard color lookup tables were created that display the data either in pseudocolor or grayshades. Either color table can be loaded from the main menu of SHOWSAT. Colorbars have been generated and can be displayed to show the correlation between the colors of either lookup table and unit measurement (e.g., °C for IR images) for all data types. To enhance grayshade images visually, the color lookup table (rather than the image) can be manipulated by histogram shrinking or stretching techniques or black/white binary thresholding.

Finally, SHOWSAT supports viewable image enlargements by a zoom factor of 0-15 in both x- and y-directions.

c. Analysis

Approximations for cloud types and precipitation levels based on IR and visible satellite data can be calculated and displayed, with the different types/levels colorcoded, using software developed based on the Liljas (1982) classification scheme shown in Fig. 5.

Filtering, noise removal, and contour extraction can be accessed via a secondary menu. In addition to these features the menu will enable generation of contour plots, saving of the Freeman code for a given contour to disk, and mapping of one chain code to a second code.

7. University of Wisconsin/SSEC Data

A magnetic tape containing satellite data from 27 September 1985 (Hurricane Gloria) was obtained from the University of Wisconsin/Space Science and Engineering Center. The tape contained satellite imagery of the storm centered at Sudbury. However, since it was written in IBM format, the data had to be converted to a readable VAX/ASCII format. Once in ASCII
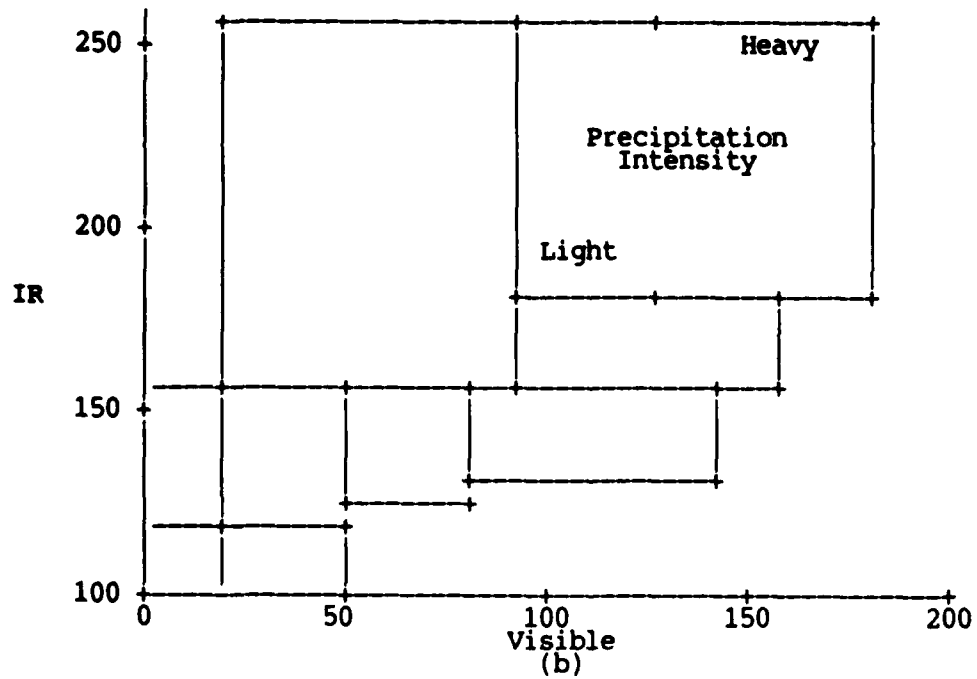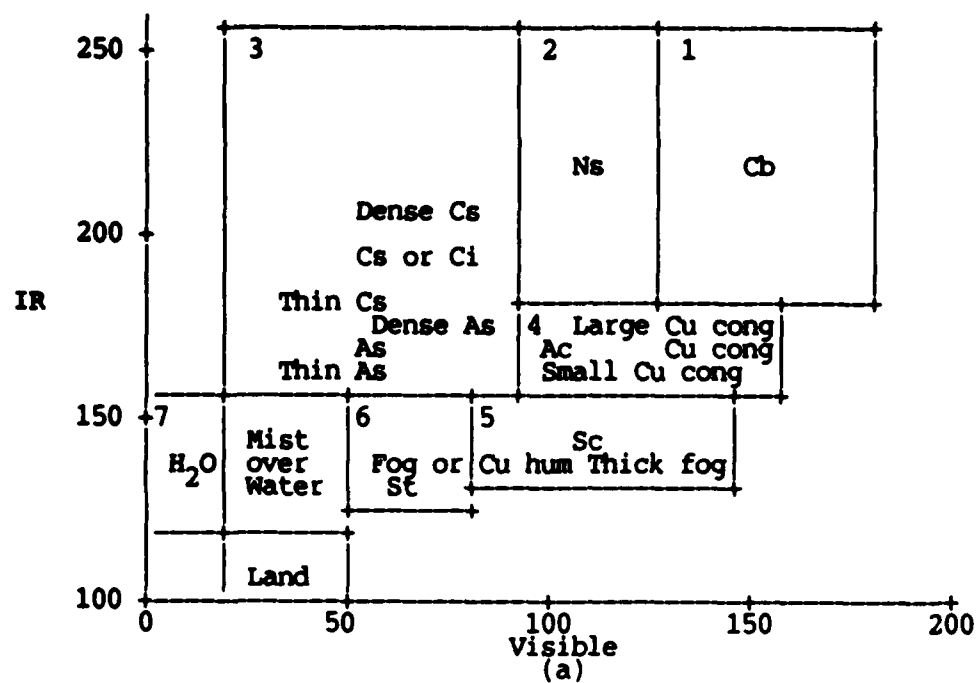
Fig. 5 Indications of Cloud Types and Precipitation Intensities Derived from VIS and IR Satellite Data

110

format, the tape was converted to a format standard to LYR. A program to process the data image-by-image and save it in the standard data format was developed.

8. Reference

Liljas, E., 1982: Automated techniques for the analysis of satellite cloud imagery. Nowcasting, K. A. Browning, ed., Academic Press, pp. 167-176.

D. Wind Shear Prediction

1. Introduction

A very important wind shear hazard for aviation operations is the microburst - a small, intense downdraft usually associated with convective storms. The vertical flow in these downdrafts is deflected by the earth's surface, resulting in a low-level divergent horizontal air flow. Where this divergent flow meets the enviromental flow a region of intense shear of the horizontal wind often results. If encountered by aircraft in air terminal approach or departure patterns, this combination of horizontal shear and strong vertical motion can be deadly.

Several observational programs have been designed specifically to study downburst (NIMROD, JAWS, CLAWS, and FLOWS). From these programs it has become quite obvious that Doppler weather radar is a valuable detection and possibly a forecast tool. Because of the magnitude of the resultant outflows, characteristic velocity couplets have been observed coincident with independent corroboration of downburst occurrence. Other potential forecast aids have been identified by Roberts and Wilson (1986): collocation of reflectivity maximum with downburst, descending reflectivity core, collapsing storm structure, organized convergence near and above cloud base, rotation, and reflectivity notch. However, many of these features are seen only occasionally or under special circumstances and not with any great consistency. The only truly consistent observation and the one that adapts most easily to an automated detection technique appears to be the divergent couplet seen in the Doppler velocity data.

An important observation from these studies is that downbursts are a fairly short-lived phenomenon, with the detected couplets lasting as little as 5 min and as long as tens of minutes, with the vast majority being in the 5 to 15 min range. Time scale is important for determining detectability and forecastability by the NEXRAD system in light of its anticipated 5 min data updates.

The goal of this effort is to develop a downburst nowcasting algorithm usable within the NEXRAD system. Based on current knowledge of downburst characteristics as seen in radar data, it is apparent that this algorithm must be based on the detection of the divergent (couplet) signature in the velocity fields.

2. Downburst Definition

Fujita (1981) was the first to define the scale of the low-level outflow from microbursts, the most severe of the downdraft phenomena, to be between 0.4 and 4.0 km. With that definition and a multitude of observations collected in the Joint Airport Weather Studies (JAWS) Project, Wilson et al. (1984) compiled a more complete definition in terms of radar observables; in particular, the velocity couplet. They found that the maximum velocity differences across the divergent center must be no less than 10 m s^{-1} and the initial distance between maximum approaching and receding centers must be no larger than 4 km in order to classify a particular couplet signature as a downburst. This translates to a minimum shear of 0.0025/s. MIT-Lincoln Laboratory (Merritt, 1986) uses a requirement of 8 m s^{-1} velocity difference across the downburst with a minimum separation of 1 km between peaks. Quite obviously there is probably no one set of universal thresholds and local fine tuning will most likely be required. Therefore the concern in algorithm development is the basic design and not in the specific thresholds to be applied.

3. Real Time Radar Application

The radar systems being deployed by NEXRAD will be collecting radial velocity and reflectivity factor data with resolutions of 250 m in range and 1 deg azimuth. Data will be collected in planes at constant elevation angle

such that much of the troposphere is observed in 5 min. Since downburst divergence signatures are seen only in the lowest ~.5 km of the atmosphere, only the lowest elevation scan is likely to be useful. This means that any algorithm used must utilize data only from one elevation scan and must be usable with updates only every 5 min. These temporal and spatial limitations on the data will severely hinder any algorithm performance over a broad region.

4. Proposed Downburst Detection Technique

As noted, the Doppler radar sees downbursts as velocity couplets. The shear of the radial velocities across these couplets is always positive; i.e., the velocities always increase with range. Of course noise, ground clutter, turbulence, etc. may make this statement somewhat less than accurate. Filtering of the data, however, usually minimizes these effects.

The algorithm as devised by STX procedes as outlined in Fig. 1. It is assumed that the data input are mean radial velocities and radar reflectivities organized along radials centered on the radar. These data are then averaged over a specified number of gates to remove "noise" effects. Velocity differences are then computed according to

$$\text{del } V(i) = V(i + N) - V(i - N).$$

If del V(i) is greater than zero its value is retained. Once all the shears are computed they are checked radially for contiguity. If the shear across the contiguous segment is not less than a threshold shear, that segment is retained for association in azimuth. Once all shear segments are compiled for a plane, they are checked for contiguity in azimuth. Segments must overlap in range by a prescribed amount in order for association into regions to occur. Regions are retained if there is at least one velocity difference across the couplet that is greater than 10 m s^{-1}, the NCAR definition.

Table 1 gives the threshold values used in this algorithm. These numbers are considered to be reasonable in light of previous studies. No attempt has been made to optimize these parameters.

113

```
|-----------------|
|  READ IN DATA   |
|_____|
         |
         |
|-----------------------------------|
|  AVERAGE VELOCITIES IN RANGE      |
|_____|
         |
         |
|-----------------|
|  COMPUTE SHEARS  |
|_____|
         |
         |
|-------------------------------------------|
|             DEFINE SHEAR VECTOR            |
|  APPLY LENGTH AND MAGNITUDE THRESHOLDS     |
|_____|
         |
         |
|-------------------------------------------|
|        ASSOCIATE VECTORS AZIMUTHALLY       |
|    APPLY AREA AND MAGNITUDE THRESHOLDS     |
|_____|
```
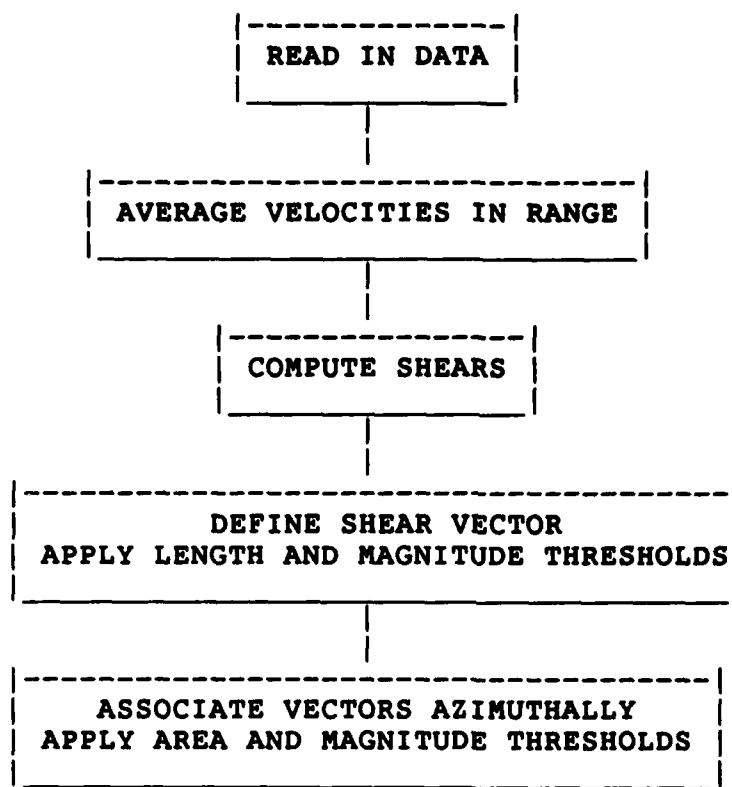
Fig. 1 Processing Procedure for Compiling Shear Regions Associated with Downbursts

114

Table 1. Acceptance Criteria for Downbursts

Segment	- 0.4 km ≤ Length ≤ 4.0 km
	- 10 m/s ≤ Velocity change across length
Downburst	- 5 ≤ Segments in a feature
	- 1.0 km ≤ Feature area
	- 10 m/s ≤ Velocity change across feature

5. Status of Work

The downburst algorithm has been applied to data collected by the 10 cm Doppler radar belonging to MIT-Lincoln Laboratory and located in Olive Branch, MI and to data collected in JAWS by the National Center for Atmospheric Research 5 cm Doppler located near Stapleton Airport, Denver. In all cases, the downburst was detected automatically with the algorithm with no false alarms. The downbursts were detected when first positively identified by eye and followed through their lifetimes. Examples of output are included in Figs. 2 and 3.

Of the downbursts in our data set, it was found that the downbursts did not persist long enough for one to determine a reliable track. However, because the downdrafts are dynamically tied to the convective storm, it would be reasonable to assume that any storm tracking algorithm would give a reasonable estimate of downburst motion.

6. NEXRAD Implementation

In the NEXRAD inventory there is a divergence algorithm (algorithm number NX-DR-03-024/10). Although it is designed to detect divergence at the top of convective storms, its basic design is similar to that needed for downburst detection. Basically, the algorithm looks for segments along radials in which the velocities are constantly increasing. These segments are then associated in azimuth to form divergence regions. Thresholds are applied to the magnitudes and lengths of the radial shear segments and to the area of the shear regions and the maximum shear within regions. If values do not pass the various thresholds they are rejected. As can be seen this is very much like the algorithm used in this study.
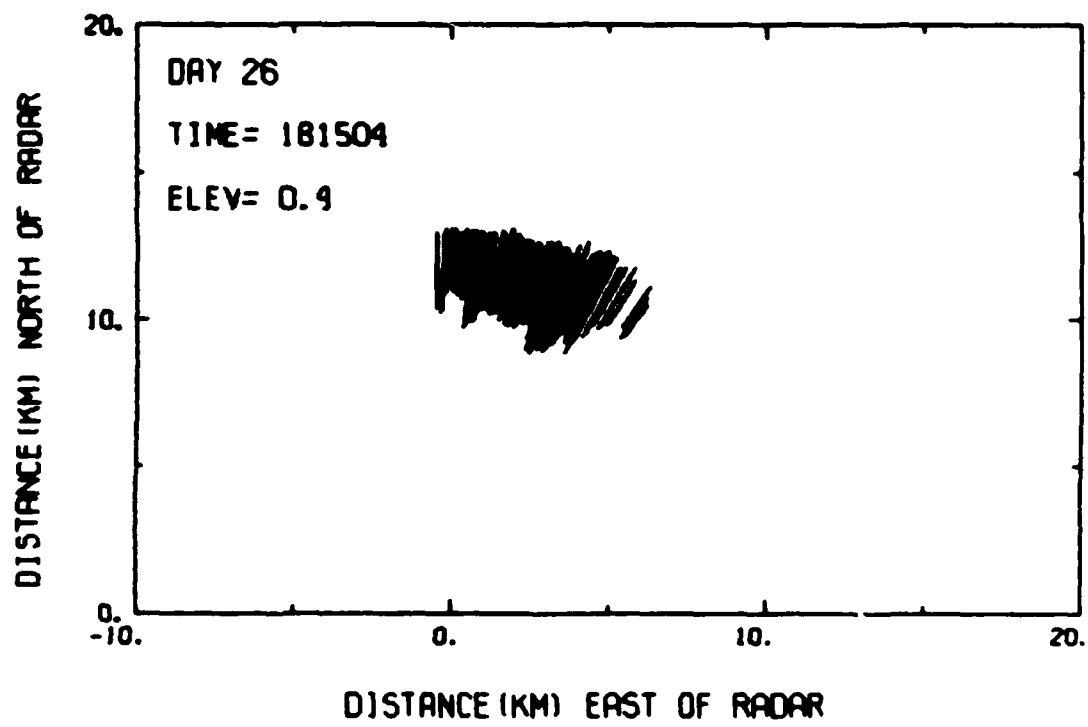
Fig. 2 Output for Downburst Detection Algorithm

(Data collected by MIT-Lincoln Laboratory at 1815 LST on 26 June 1985.
Doppler radar located at Olive Branch, MI.)

116
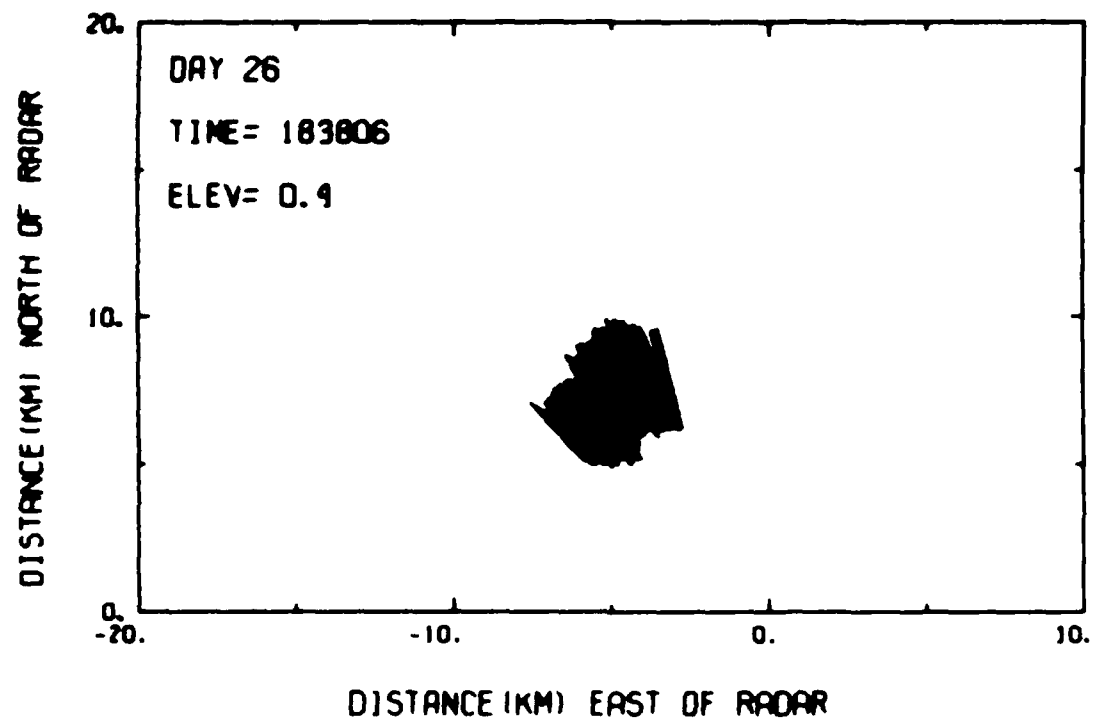
Fig. 3 Same as Fig. 2 but for Another Downburst at 1838 LST

Since the WEXRAD algorithm is already in existence, consideration should be given to its modification in terms of regions of application and thresholds for use as a downburst detection algorithm.

7. References

Fujita, T. T., 1981: Tornadoes and downbursts in the context of generalized planetary scales. *J. Atmos. Sci.*, 38, 1511-1534.

Merritt, M.W., 1986: *Interim Report on Microburst Surface Outflow Detection Algorithm*. MIT-Lincoln Laboratory, 10 pp.

Roberts, R. D., and J. W. Wilson, 1986: Nowcasting microburst events using single Doppler radar data. *Preprints*, 23rd Conference on Radar Meteorology, Snowmass, CO; AMS, Boston, 14-17.

Wilson, J. W., R. D. Roberts, C. Kessinger, and J. McCarthy, 1984: Microburst wind structure and evaluation of Doppler radar for airport wind shear detection. *J. Clim and Appl. Meteor.*, 23, 889-897.

E. Severe Storm Indicators

1. Tornado Intensity Estimation

a. Introduction

Mesocyclones are rotating regions often observed within thunderstorms associated with severe weather. These circulations produce characteristic signatures in Doppler radar data that are readily detectable by automatic techniques in terms of size, shear, and rotational velocity (Hennington and Burgess, 1981; Zrnic' et al., 1985; and Wieler, 1986). From Doppler radar observations it has been determined that roughly half of the observed mesocyclones have associated tornadoes (Burgess, 1976), with mesocyclone identification occurring an average of 20 minutes before tornado touchdown (Burgess et al., 1979). Thus the observation of a mesocyclone does not necessarily mean that a tornado exists or is likely to exist.

In an effort to improve the predictability of tornado occurrence, a method has been devised to predict which mesocyclones will be associated with tornados. It also gives an indication of the maximum tornado

118

intensity. The method is based upon the Excess Rotational Kinetic Energy
(ERKE) of the mesocyclone, a parameter first presented by Donaldson and
Desrochers (1985). ERKE represents the mesocyclonic rotation kinetic energy
in excess of that required for mesocyclonic identification, namely $ERKE = \rho \pi r^2 (V_r - S_m r)^2 / 4$. ρ is the air density at the observed height,
V_r is the rotational velocity of the vortex of radius r, and S_m is an
arbitrary shear threshold defining mesocyclonic rotation. S_m was selected
as 0.005/s for this study, after the value suggested by Donaldson (1970) and
later supported by Burgess (1976).

In previous work Donaldson and Desrochers (1985) examined the ERKE
associated with a single violent tornado-producing mesocyclone and found
ERKE offered warning potential. In this report we expand the study to ten
storms in order to generalize results. Half of these storms were tornadic,
approximating the distribution of tornadic and non-tornadic mesocyclones
seen in nature. This sample contains three categories of storms:
non-tornadic, strong tornado-producing (F2 - F3), and violent
tornado-producing (F4 - F5). None produced only weak (F0 - F1) tornadoes.

b. Standardizing the Analysis

To account for the varying resolution over which storms were seen,
vortex size and rotational velocity were corrected for radar resolution
according to the theoretical profiles of a Rankine combined vortex (Brown
and Lemon, 1976), making ERKE independent of range. Comparison among storms
was further facilitated by comparing all values of ERKE to that of a
Climatologically Mature Mesocyclone located in the lower troposphere
(Burgess et al., 1982). This is an average mesocyclone in its strongest
stage of development and is characterized by a diameter of 5.5 km and a
tangential velocity of 23.3 m s^{-1}, with a corresponding ERKE of 540
megajoules/m. This energy will be used as a new energy unit, namely 1 CMM.

c. Algorithm Considerations

Before discussing the investigation into ERKE we need to point out a
particular problem and its solution. A common complication to the
mesocyclone circulation was the observation of one or more vortices within

119

the mesocyclone after it entered its mature stage of development. We refer to these as "intraneous vortices." They are seen on scales ranging from 0.5 to 5 km in diameter. When they are large, automatic identification of the mesocyclone circulation sometimes becomes difficult.

The smaller intraneous vortices have been well documented as Tornadic Vortex Signatures (TVS) (Brown and Lemon, 1976; Brown et al., 1978). The definition of a TVS by these authors is resolution dependent and, although TVS size varies considerably, they are generally much smaller, usually less than 1 km in diameter, and have much smaller ERKE than a typical mature mesocyclone. For example, the F4 Binger tornado was one of the most intense ever observed by Doppler radar, but its associated TVS had a maximum ERKE magnitude of only 0.4 CMM.

In this study intraneous vortices were observed in nearly 200 quasi-horizontal antenna scans but only one-third satisfied the TVS criterion; namely, containing shears greater than 0.05/s in adjacent beams (Burgess et al., 1979). The remaining two-thirds had average shears of only 0.017/s and diameters of 2 to 5 km. About half of the latter group had ERKEs greater than those of their surrounding mesocyclones. One example of a large intraneous vortex is shown in Fig. 1. Here an intraneous vortex (indicated by A,B) 3.9 km in diameter is seen on the edge of the larger mesocyclone (about 8.5 km diameter indicated between A,C). It had ERKE of 1.1 CMM compared to 1.7 for the surrounding circulation. Although this intraneous vortex was quite large, it had vertical continuity with a TVS located at 1.5 km and coincided in time and space with a reported tornado. It is therefore thought to be part of the tornadic circulation.

Mesocyclone characteristics needed for ERKE, namely, size and rotational velocity, are byproducts of mesocyclone detection algorithms. These algorithms rely on a monotonic velocity change in order to detect a circulation. The intraneous vortex in Fig. 1 occupies a significant portion of the mesocyclone and disrupts this linearity needed for positive mesocyclone detection. Mesocyclone detection algorithms will therefore detect this intraneous vortex and will not see the surrounding mesocyclone. Because our existing algorithm becomes confused by the coexistence of mesocyclones and intraneous vortices, vortex size and rotational velocity were determined in this study through manual analysis. This allowed for the introduction of analysis modification to reduce this confusion and to
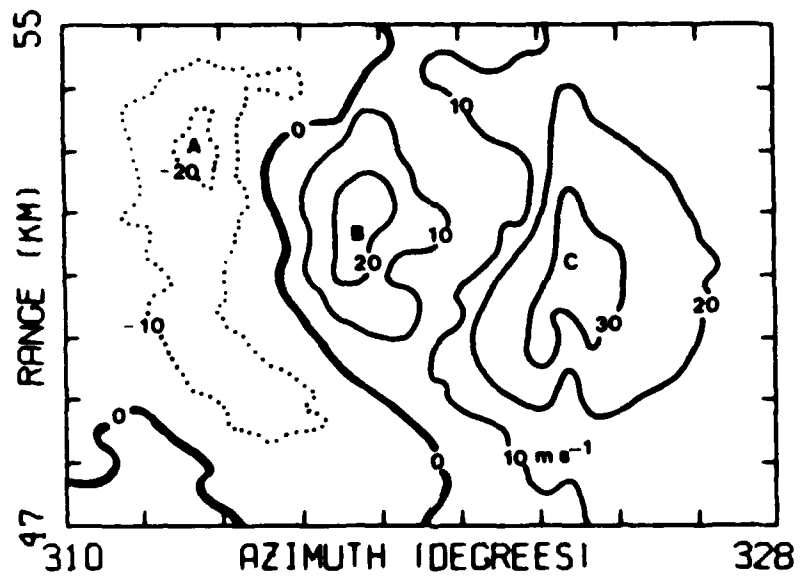
Fig. 1 Example of a Large Intraneous Vortex within a Mesocyclone

(Doppler data are from Piedmont, OK storm (30 April 1978) at 1802 and 2.9 km height.)

improve the delineation of parameter estimation. One such improvement was
the isolation of the rotational component in velocity couplets suggesting a
mix of divergence (or convergence) and vorticity.

The concept of ERKE can be applied to mesocyclones, intraneous
vortices, or some combination of these. Since automatic discrimination of
mesocyclones and intraneous vortices would be problematic for existing
algorithms, it was decided to adopt a simple scheme; namely, the detection
of monotonic velocity changes. This will automatically focus on intraneous
vortices when they exist and on mesocyclones otherwise. However, we
excluded those intraneous vortices seen as TVSs because generally their
small size did not obstruct significantly the monotonic velocity across the
mesocyclone.

d. Case Studies

It is instructive to examine the ERKE life cycle associated with the
non-tornadic, strong tornado-producing, and violent tornado-producing
categories of our data set. Although each storm displayed individual
qualities, distinct similarities exist within each storm classification. An
example from each classification is presented in Figs. 2-4 in the order
listed.

In the upper portion of each figure is plotted the maximum ERKE as a
function of the ending time of the volume scan. The lower portion displays
RRKE weighted mean height (h_g) for the detected circulation as a function
of time.

The Del City storm (Fig. 3) depicts characteristic evolution of our
tornadic mesocyclones. When the mesocyclone circulation was first
identified in the storm its RRKE magnitude was only a fraction of a CMM, and
h_g was above 10 km, somewhat higher than most other storms studied. As
the mesocyclone evolved, its RRKE increased to greater than 1 CMM and h_g
descended into the lower troposphere prior to tornado formation. As
observed in most of our other tornadic storms, RRKE then persisted above 1
CMM, a pattern not apparent in the non-tornadic mesocyclones. For example,
the Ada storm in Fig. 2 peaked in RRKE magnitude quickly when h_g was at
7 km. Then, as h_g descended, its ERKE stabilized at about 0.5 CMM.
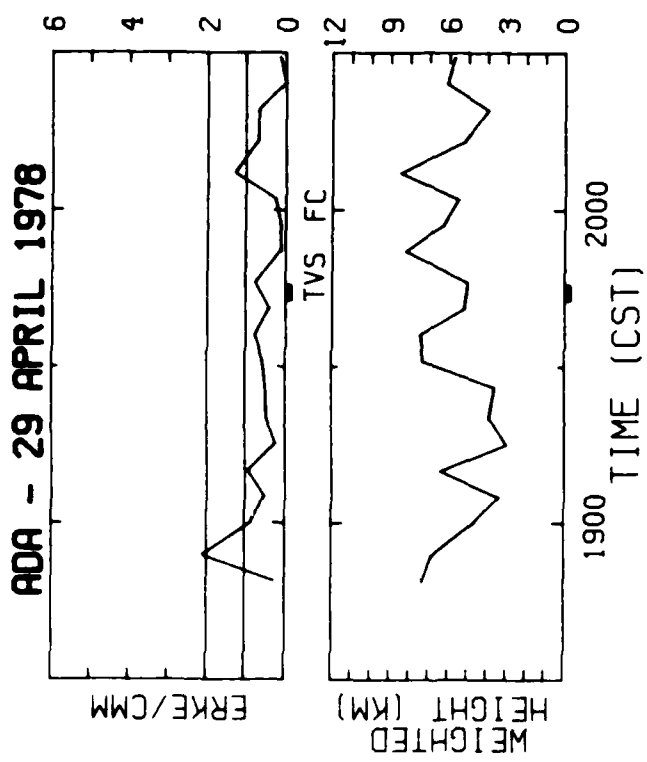
Fig. 2 Lifetime of Ada Storm in Terms of ERKE Magnitude (upper figure) and h$_E$ (lower figure)

(Tornado intensity is indicated by F1, F2, etc.; tornadic vortex signatures by TVS; funnel clouds by FC. Duration of these, if known, is indicated by heavy bar at bottom of figures.)
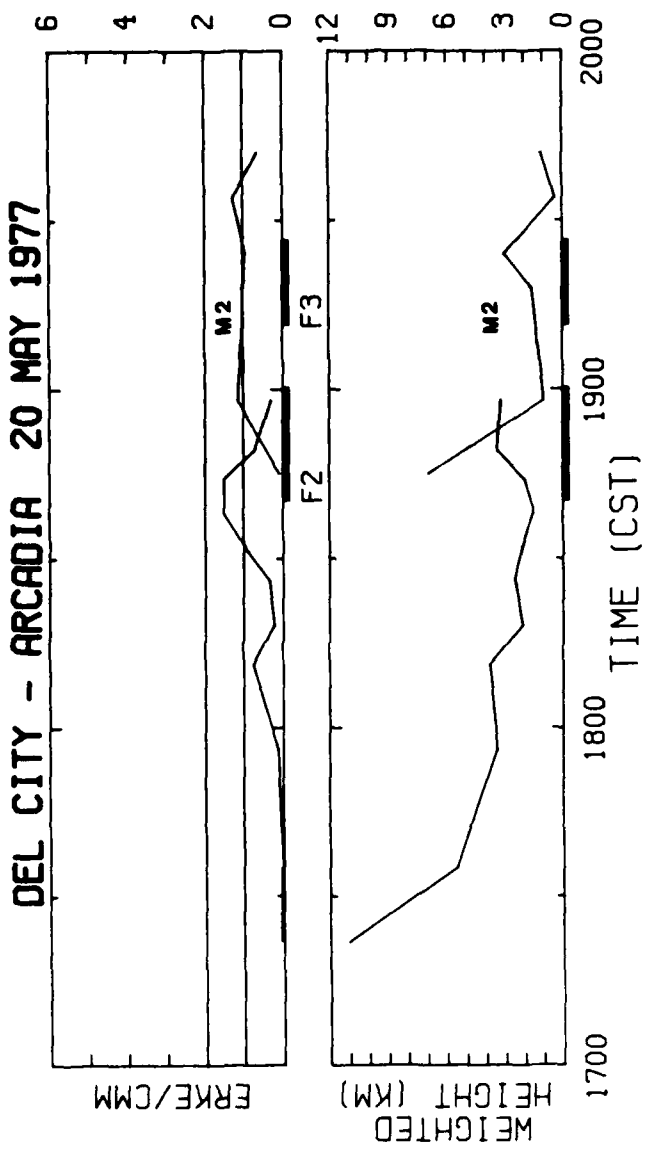
Fig. 3 Same as Fig. 2, except for Del City Storm
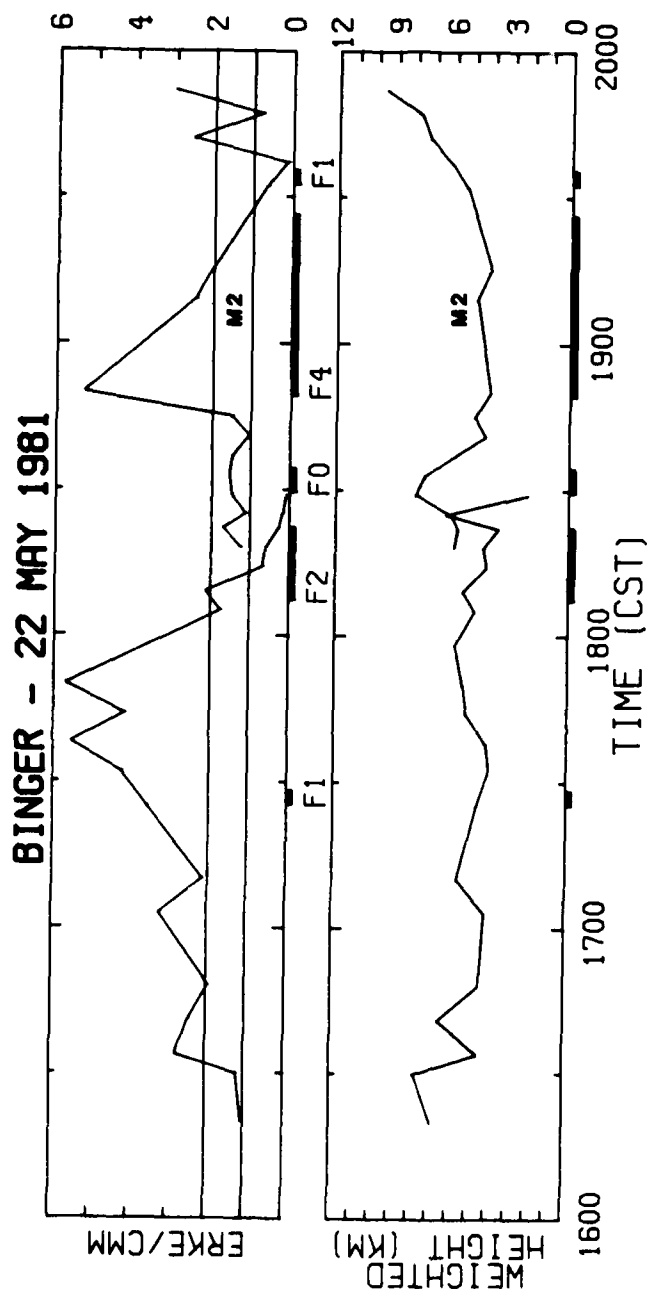
Fig. 4 Same as Fig. 2, except for Binger Storm

Two of the storms (Del City and Binger) produced more than one mesocyclone. The second of each is labeled as M2 in Figs. 3 and 4. In both storms the second mesocyclone had a shorter lifetime than the first, a characteristic noted by Burgess et al. (1982) for such multiple core mesocyclones, and both attained ERKE similar to the first. It is interesting that in both storms the most intense tornado formed in association with the second mesocyclone.

Comparison of ERKE among the tornadic storms suggests that it is somewhat proportional to the intensity of tornadoes produced. Consider for example that the maximum ERKE of the Binger storm (Fig. 4) was nearly four times that of Del City (Fig. 3). The Binger storm produced an F4 tornado in addition to a number of less intense ones, while Del City produced an F2 and an F3 tornado. ERKE magnitude prior to each tornado does not correspond well to the observed tornado intensity, however. This is readily apparent when comparing ERKE of the Binger storm with that of Del City; the very large ERKE prior to Binger's first F1 tornado, for example, was about twice the value attained during the entire Del City storm. ERKE does, however, seem related to a potential in tornado severity that is realized by the most intense tornado of a storm.

e. Technique and Results

From the above discussion a simple relationship follows for distinguishing tornadic from non-tornadic mesocyclones. Mesocyclones are predicted to be tornadic if satisfying the following criteria:
1) attainment of ERKE of at least 1 CMM at a height below 5 km; and
2) persistence of 1) for at least 5 min (two sample volume scans).
The height criterion here is not h_g discussed earlier but is the lowest height where ERKE equals or exceeds 1 CMM. This simplification results in the same forecast as for the weighted height but lead time is increased slightly because the necessary forecast criteria can be satisfied in less time than two radar volume scans. Analysis was performed on ten storms, with results summarized in Table 1. It can be seen that while the above criteria are arbitrary, they work very well in distinguishing mesocyclone type in nine out of ten cases. The Foster storm (19 May 1977) which produced two F2 tornadoes was the one failure, but reduction of the ERKE threshold to 0.7 CMM allows corrected classification of this storm.

126

Table 1. Data Set of Storms

Storm	tornadoes produced W	S	V	Correct tornado discrimination by ERKE 1 CM (any tornadoes)	2 CM (violent tornadoes)	Warning time (minutes) first tornado	most intense strong tornado	violent tornado
Binger	3	1	1	YES	YES	23	63	72
Piedmont	1	3	1	YES	YES	-8	13	20
Del City	0	2	0	YES	YES	-5	26	n.a.
Foster	1	2	0	NO	YES	--	--	n.a.
Fort Cobb	0	2	0	YES	YES	-3	20	n.a.
Ada	0	0	0	YES	YES	n.a.	n.a.	n.a.
Konawa	0	0	0	YES	YES	n.a.	n.a.	n.a.
Rush Springs	0	0	0	YES	YES	n.a.	n.a.	n.a.
Roosevelt	0	0	0	YES	YES	n.a.	n.a.	n.a.
Vanoss	0	0	0	YES	YES	n.a.	n.a.	n.a.

W = weak tornadoes (F0 - F1)
S = strong tornadoes (F2 - F3)
V = violent tornadoes (F4 - F5)

n.a. = not applicable

Increasing the ERKE threshold in criterion 1) to 2 CMM produced a predictor for tornadoes of violent intensity. This yielded correct forecasts for the two violent F4 tornadoes of the sample with no false alarms. The Piedmont and Binger storms were so very energetic and persistent that an incorrect forecast would have been difficult indeed. The same forecast would have resulted even if the ERKE threshold for violent tornadoes had been raised to 3 CMM.

In all of the storm cases, inclusion of intraneous vortices in the ERKE estimation did not improve tornado forecasts over those when only mesocyclones were considered. In a few cases they provided continuity and hence enhanced confidence in the forecast. A good example is the Fort Cobb storm (refer to Table 1). In this storm the mesocyclonic circulation decreased after the formation of the first tornado (F2) and for about 20 min there was no mesocyclonic ERKE. While in the other storms no tornadoes existed once the mesocyclonic shear fell below threshold, in the Fort Cobb case a second F2 tornado, larger than the first, was formed shortly after the re-detection of the mesocyclone. During the period when the mesocyclone was weak, the intraneous vortex had an ERKE about 1 CMM and substantiated the forecast for a strong tornado.

Operational forecasts of an event require some lead time if information is to be of any value. Using the criteria for mesocyclone discrimination we have determined the warning time for the first tornadoes, most intense non-violent tornadoes, and violent tornadoes of the storms. The results are given in Table 1. ERKE is generally not effective at warning for the first tornado of a storm. Fortunately, these are usually not the most intense of a storm. In three of the storms the first tornadoes were of F1 intensity and in the remaining two of F2 intensity. Warning time increases considerably for the most intense tornado of a storm, and is of remarkably long duration for the very large and violent Binger tornado.

f. Conclusion

ERKE works well as a discriminator of tornadic and non-tornadic mesocyclones and offers useful warning time for the most intense tornado of a storm. In our limited sample ERKE worked exceptionally well for predicting the occurrence of violent tornadoes. These storms were clearly

distinguished by RRKE from the remainder of the sample. This is fortunate because the F4 and F5 tornadoes, although rare, kill and injure more people than the more common strong or weak tornadoes.

2. Automated Mesocyclone Detection

Mesocyclones can be detected automatically if their velocity field can be recognized and isolated from extraneous data in the Doppler velocity field. A four-step process for this was designed by Hennington and Burgess (1981) consisting of:

1) Computation of azimuthal shear and organization of those contiguous shears of the same sign into runs referred to as Pattern Vectors (PV);
2) Synthesis of PVs from a single elevation scan into two-dimensional (2-D) features;
3) Vertical matching of 2-D features to form three-dimensional (3-D) features;
4) Classification of 3-D features (e.g., mesocyclone, elongated shear area, etc...).

This format was adopted by Wieler and Donaldson (1983) for a more comprehensive algorithm that combined both mesocyclone and TVS detection, designated the Mesocyclone Tornadic vortex Detection Algorithm (MTDA). Work on automatic mesocyclone detection was continued and efforts in 1986 were directed toward improvement of PV construction, classification of 3-D features, and implementation of an automated tornado intensity algorithm.

PV construction was found to be significantly deficient for mesocyclones. Investigation into the MTDA performance on the Piedmont, OK storm (29 April 1978) revealed that only a fraction of the possible pattern vectors was detected by the algorithm. This imposed limitations on the accuracy of 2-D and 3-D feature synthesis, and on the resulting classification of 3-D features.

The routine for PV construction is in itself simple. As the radar scans in the azimuthal direction a search is made at a constant range from the radar for a change in the sign of the azimuthally-oriented velocity gradient. A PV is completed and a new one is begun every time the velocity

gradient changes sign. A completed PV is retained for further use in the MTDA if it satisfies certain criteria for shear and velocity; namely, that the total shear and velocity difference across the PV is at least 0.002/s (Gerlach, 1985) and 15 m s^{-1}, respectively.

The MTDA operates as a controlled module of the Modular Radar Analysis Software (MRAS) system (Forsyth et al., 1981). Difficulties observed in PV construction result from MRAS time-saving procedures. MRAS was designed to pass Doppler data to the PV routine only when the signal strength is above a predefined threshold. Whenever the signal strength falls below threshold, PV analysis becomes dormant. As the algorithm was previously configured, PV construction then became faulty since there was no provision in MRAS for completing PVs at the point where the signal strength dropped off. Only when signal strength increased again above threshold, as the radar scanned and collected new data, could PVs be completed if shear of the opposite sign was encountered. If the sign of the PV velocity gradient coincided with that of the new data, the new data would be considered a continuation of the PV and the PV would not be completed until the velocity gradient changed sign. The result of this was a bogus PV that perhaps extended through hundreds of degrees of azimuth and had a length of hundreds of kilometers. Because of the potentially large size of these PVs their shear was generally much less than required for PV retention and were discarded. Also lost in this process were some potentially valuable data.

Low signal return is common within and adjacent to mesocyclones due to their location near flanks of severe thunderstorms, where one side of a mesocyclone (usually the south to southeast side) is often bounded by clear air. Detection of a mesocyclone will be particularly prone to the PV problem when the radar is scanning toward a mesocyclone through the clear air region.

Modifications were made to the algorithm to complete PVs when the signal drops below threshold. Also, this threshold-defining low signal return was reduced from 10 dBz to 2 dBz to allow continuation of a PV through a Bounded Weak Echo Region (BWER). These modifications resulted in a ten-fold increase in the number of identified PVs. Complete coverage of the core region of mesocyclones is now provided, which substantially improves the continuity of mesocyclone features with height and time.

Criteria for mesocyclone classification were changed to reduce false alarms and to increase mesocyclone detection. Previous criteria for

mesocyclone classification were too general. The maximum PV shear at any one elevation in any feature was required to be equal to or exceed 0.005/s and the 3-D feature to be somewhat circular in shape and at least as high as wide. In an effort to refine the criteria the following constraints were added: A 3-D feature must extend over a minimum of three elevations; total depth of the 3-D feature must be at least 5 km; and shear between velocity peaks must equal or exceed 0.005/s for two consecutive elevations. Testing of this modification on the Piedmont and Del City (20 May 1977) storms yielded extremely good results. The mesocyclones of these storms were nearly always identified. Only in one time period did the mesocyclone go undetected. This occurred for the first two volume scans of the Del City storm when the mesocyclone circulation was quite weak in terms of shear and poorly defined with height. The circulation was not sufficiently defined at that time to satisfy all of the criteria required for mesocyclone identification.

Modifications made to PV recognition and mesocyclone classification, along with improvements previously made, have resulted in a dependable tool for automatic mesocyclone detection. Estimates by the MTDA of mesocyclone size and velocity are now generally identical with those from manual analysis. ERKE estimation was incorporated into the algorithm with similarly positive results. For example, in the Piedmont and Del City storms the MTDA estimates of ERKE were generally within 0.2 to 0.5 CMM of those derived from manual analysis. Most differences are due to the smoothing of data within MRAS to approximately 1 deg of horizontal resolution to simulate that prescribed for NEXRAD. Smoothing tends, on average, to underestimate ERKE; to compensate, the threshold for non-violent tornadoes was reduced from 1.0 CMM to 0.8 CMM. No adjustment was needed in the ERKE threshold for violent tornadoes, however. With these thresholds, forecasts of tornado intensity in the Piedmont and Del City storms agree with those from manual analysis. These results strongly suggest that automatic tornado prediction is within reach.

3. References

    Brown, R. A., and L. R. Lemon, 1976: Single Doppler radar vortex recognition: Part II - Tornadic Vortex Signatures. Preprints, 17th Conference on Radar Meteorology, Seattle; AMS, Boston, 104-109.

Brown, R. A., L. R. Lemon, and D. W. Burgess, 1978: Tornado detection by pulsed Doppler radar. Mon. Wea. Rev., 106, 29-38.

Burgess, D. W., 1976: Single Doppler radar vortex recognition: Part I - Mesocyclone signatures. Preprints, 17th Conference on Radar Meteorology, Seattle; AMS, Boston, 97-103.

Burgess, D. W., and JDOP Staff, 1979: Final Report on the Joint Doppler Operational Project (JDOP) 1976-1978. NOAA Tech. Memo., ERL NSSL - 86, 84 pp.

Burgess, D. W., V. T. Wood, and R. A. Brown, 1982: Mesocyclone evolution statistics. Preprints, 12th Conference on Severe Local Storms, San Antonio; AMS, Boston, 422-424.

Donaldson, R. J., Jr., 1970: Vortex signature recognition by a Doppler radar. J. Appl. Meteorol., 9, 661-670.

Donaldson, R. J., Jr., and P. R. Desrochers, 1985: Doppler radar estimates of the Rotational Kinetic Energy of mesocyclones. Preprints, 14th Conference on Severe Local Storms, Indianapolis; AMS, Boston, 52-55.

Forsyth, D. E., C. Bjerkaas, and P. Petrocchi, 1981: Modular radar analysis software system (MRAS). Preprints, 20th Conference on Radar Meteorology, Boston; AMS, Boston, 696-699.

Gerlach, A. M., ed., 1985: Objective Analysis and Prediction Techniques - 1985. AFGL-TR-86-0002, Contract F19628-82-C 0023, SASC Technologies, Inc., ADA169746.

Hennington, L. D., and D. W. Burgess, 1981: Automatic recognition of mesocyclones from single Doppler radar data. Preprints, 20th Conference on Radar Meteorology, Boston; AMS, Boston 704-706.

Wieler, J. G., and R. J. Donaldson, Jr., 1983: Mesocyclone detection and classification algorithm. Preprints, 13th Conference on Severe Local Storms, Tulsa; AMS, Boston, 3-6.

Wieler, J. G., 1986: Real-time automated detection of mesocyclones and tornadic vortex signatures. J. Atmos. Oceanic Technol., 3, 98-113.

Zrnic', D. S., D. W. Burgess, and L. Hennington, 1985: Automatic detection of mesocyclonic shear with Doppler radar. J. Atmos. Oceanic Technol., 4, 425-438.

V. SATELLITE METEOROLOGY

A. AFGL Interactive Meteorological System Development

1. Introduction

The AFGL Interactive Meteorological System (AIMS) has been under development for several years. STX scientists and software engineers have been directly involved in the development effort, working with AFGL in-house scientists since the beginning of the project (Gerlach, 1985, 1984). AIMS has evolved into a system of distributed processors, each functionally unique and linked by a local area network. Fig. 1 is a schematic representation of the current system configuration. AIMS consists of three general purpose computers--VAX 11/750, SEL 32/27, and microVAX II; two image processing workstations built around Adage frame buffers; a GOES mode AAA receive subsystem; and various input and graphics display devices. The system is connected to the AFGL main computing center and to the AFGL remote radar site (Sudbury, MA) by external network links and is tied to the Laboratory-wide broadband network for terminal communications between offices. For a more complete system overview, see Gustafson et al., 1987.

During 1986 STX was responsible for system development in three major areas:

    1) Database and database management design and implementation;

    2) GOES mode AAA ingest;

    3) Automatic acquisition of meteorological observation reports.

Work performed in these areas is described in the following sections.

2. Database Management

The system-wide database management (DBM) function is performed on the VAX 11/750 node. Information describing data files located anywhere on the network is maintained and processed here. As described in Gerlach (1985, pp. 187-191) the AIMS DBM is made up of three layers: interface layer, data dictionary layer, and I/O layer. Data file descriptor information is maintained within the data dictionary layer by a commercial database package modified to meet the specific requirements of AIMS. File descriptors are
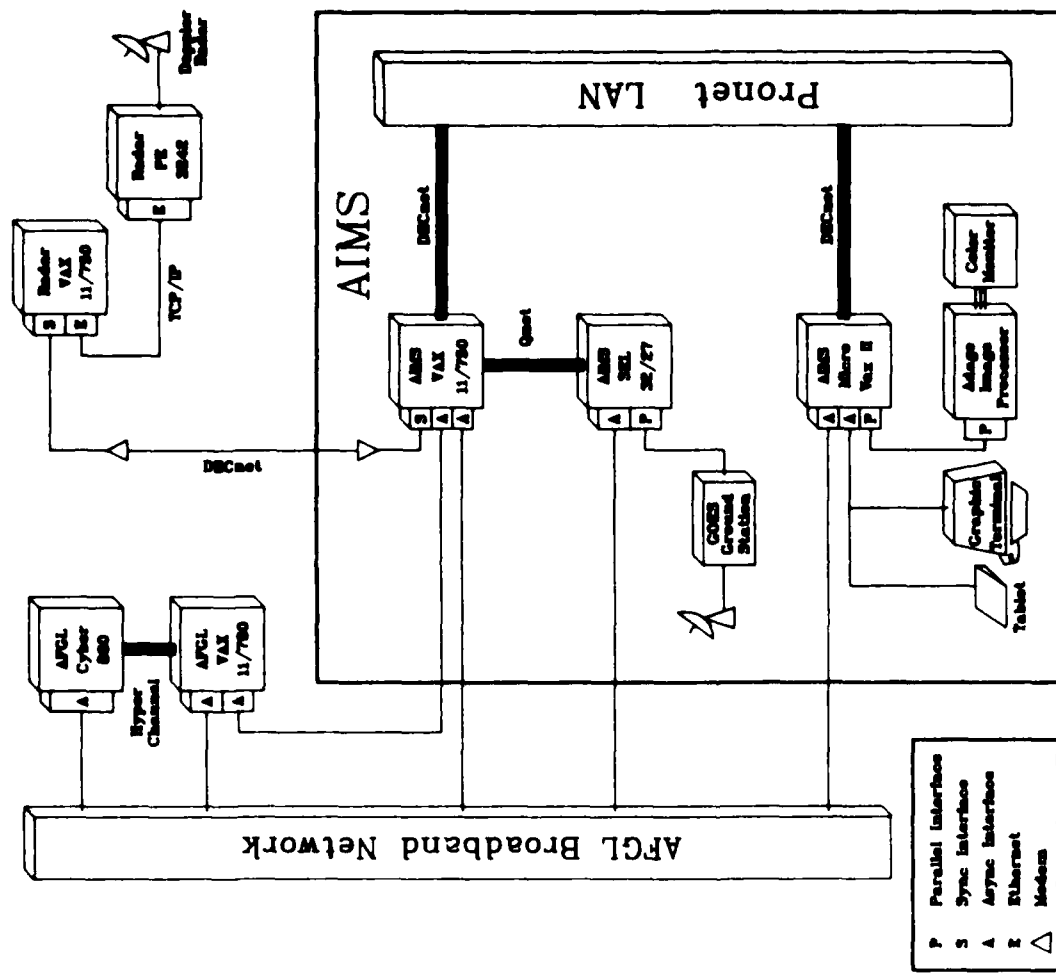
Fig. 1 Schematic Representation of AFGL Interactive Meteorological System

stored in a hierarchy of data dictionary files. Each file contains information on a particular aspect of the data file and pointers to other dictionary files containing ancillary information. When the DBM processes a data query, control flows down the dictionary hierarchy and related files are processed as necessary.

To make the dictionary processing as fast as possible the entire data dictionary layer was placed in a separate, detached process that is always active on the system. Processes external to this layer communicate via an interprocess communication method known as mailboxes. Mailboxes are analogous to postal mailboxes in that messages can be deposited and picked up at any time; the two processes do not have to be synchronized. Multiple messages are placed in a mailbox queue; the receiving process is notified automatically each time a new message is deposited. In the data dictionary application only a single mailbox is used for communications routed into the data dictionary layer. Incoming requests are queued in the order they are received, insuring that multiple queries are processed in order. Information returned by the dictionary layer is passed back through a separate mailbox created for each external process. This procedure eliminates bottlenecks at the input mailbox and insures that the requested information is routed directly to the requesting process. When an external process terminates, the return mailbox is automatically deleted. When no requests are pending, the data dictionary process drops into a hibernation state where it remains defined to the system but does not use any system resources. It remains in hibernation until notified by the operating system that a new request has been deposited in the input mailbox. This method insures that each data request is processed in an orderly way and that no extra overhead is incurred in constantly activating and deactivating the data dictionary process.

All details of communicating with the data dictionary layer are hidden from the user or applications program by the utility layer. Data requests are made through utility interface routines; all resulting mailbox communications and data dictionary transactions are performed automatically. The user simply calls the appropriate utility routine and the data are returned in a common block.

The DBM is built around the data dictionary files. Each file is organized so that it contains information on one aspect of the actual data.

The data dictionary organization can be illustrated through an example. Tables 1(a)-1(g) contain listings of the data dictionary entries for a class of polar orbiting satellite data, a single AVHRR channel. The dictionary hierarchy is illustrated in Fig. 2. All search operations begin at the top of the hierarchy in the data TYPE dictionary (Table 1(a)). The TYPE dictionary contains information about the data file structures and pointers to the SOURCE dictionary (Table 1(b)) which describes where the data came from, and to the type-specific dictionaries in the next layer of the hierarchy. Even if no specific type of data is specified in the request, the TYPE dictionary is searched to find the pointers to all the type specific dictionaries. In this example the POLAR dictionary for polar orbiting satellite data (Table 1c) is the type-specific dictionary. While the TYPE dictionary contains information generic to all data of a particular type, the POLAR dictionary is specific to a single data file. Information contained at this level includes entries that are common to most data types (e.g., valid time, location, and extent) as well as entries that are specific to the particular class of data (e.g., satellite ID, sensor information, orbital parameters). Continuing down the hierarchy there are dictionaries that contain descriptions of ancillary or related data files. In this example there are four such dictionaires: the SENSOR dictionary contains information on the specific sensor channel, the EPHEM dictionary points to a file containing navigation parameters, the LATLON dictionary points to a file of latitude--longitude values that correspond to individual pixels in the AVHRR data file, and the ZENANG dictionary points to a file of solar zenith angle values.

Each dictionary in the hierarchy is sorted on the most common search parameter(s) in the list. This allows use of an ordered or binary search algorithm when searching the dictionary for a specific entry. However, since this restricts fast searches to only one main parameter (or key) and possibly one or two sub-parameters, a technique was developed to expand this capability to any parameter in the dictionary. The technique requires a separate two-dimensional file known as a key file for every search parameter in the list. Key files contain only two fields, the search parameter list in sorted order and the corresponding record numbers pointing to the dictionary file. When a query is processed on a parameter contained in a key file, it is the key file, not the full dictionary file, that is

Table 1. Sample Data Dictionaries for Tiros AVHRR

ITEM	DESCRIPTION	SIZE	TYPE
1	type index code	2	B
2	source index code	2	B
3	record length (bytes)	4	B
4	file size (blocks)	4	B
5	descriptor	4	C
6	default directory	8	C
7	data dictionary pointer	8	C
8	data type name	32	C

TABLE 1a. TYPE data dictionary

ITEM	DESCRIPTION	SIZE	TYPE
1	source index code	2	B
2	source name	30	C

TABLE 1b. SOURCE data dictionary

ITEM	DESCRIPTION	SIZE	TYPE
1	year day	4	B
2	z time (ms)	4	B
3	type index code	2	B
4	begin latitude	4	B
5	begin longitude	4	B
6	number of elements	2	B
7	number of lines	2	B
8	scan interval	2	B
9	pixel resolution	2	B
10	satellite ID	2	B
11	sensor channel code	2	B
12	orbital period	4	B
13	ascending node cross time	4	B
14	ascending node longitude	2	B
15	EPHEM file code	2	B
16	LATLON file code	2	B
17	ZENANG file code	2	B
18	creation date	4	B
19	data format flag	1	B
20	number of coeficients/line	1	B
21	calibration file rec-len	2	B
22	calibration file name	16	C
23	satellite/sensor name	16	C
24	data file name	32	C

TABLE 1c. POLAR data dictionary

ITEM	DESCRIPTION	SIZE	TYPE
1	sensor channel code	2	B
2	satellite ID	2	B
3	wavelength/frequency	4	F
4	minimum wavelength	4	F
5	maximum wavelength	4	F
6	response fn record number	2	B
7	response fn intervals	2	B
8	sensor name	12	C

TABLE 1d. SENSOR data dictionary

ITEM	DESCRIPTION	SIZE	TYPE
1	EPHEM file code	2	B
2	EPHEM file rec-len	2	B
3	year day	4	B
4	z time (ms)	4	B
5	satellite ID	2	B
6	TYPE code	2	B
7	EPHEM file name	16	C

TABLE 1e. EPHEM data dictionary

ITEM	DESCRIPTION	SIZE	TYPE
1	LATLON file code	2	B
2	LATLON file rec-len	2	B
3	scans/record	2	B
4	number of records	2	B
5	cross scan interval	2	B
6	along scan interval	2	B
7	backup descriptor	4	C
8	LATLON file name	16	C

TABLE 1f. LATLON data dictionary

ITEM	DESCRIPTION	SIZE	TYPE
1	ZENANG file code	2	B
2	ZENANG rec-len	2	B
3	scans/rec	2	B
4	number of records	2	B
5	cross scan interval	2	B
6	along scan interval	2	B
7	backup descriptor	4	C
8	ZENANG file name	16	C

TABLE 1g. ZENANG data dictionary

Fig. 2 Data Dictionary Hierarchy

searched. Once the correct entry is located in the key file, the corresponding record number points to the location of the full entry in the dictionary file. This technique generates the extra overhead of maintaining the key files along with the root dictionary; however, it is still much more efficient than doing unordered (sequential) searches on the root.

On research systems like AIMS, the DBM must be designed to be expandable both in scope and in content. Additional data are constantly being added to the system; also, new data types may be brought in from the outside or produced directly on the system. The data dictionary structure on the AIMS attempts to meet expansion requirements in two ways. First, through the use of type-specific data dictionaries such as the POLAR dictionary. These dictionaries, while designed for a specific type of data, are still general enough to handle different types of data that are of the same class. For example, the POLAR dictionary will handle AVHRR data as illustrated above and will equally well handle imagery type data (as opposed to sounder data) from any of the polar orbiting weather satellites, such as DMSP, TIROS, NIMBUS, or even LANDSAT. Second, the entire dictionary structure can be expanded to include a totally new class of data. The expansion procedure is well defined and will not disrupt the existing database. In outline, expansion is performed in three steps:

1) A new data structure is defined to store the data physically on disk. The only restriction on the structure is that all records be of fixed length; packing is up to the user.

2) A type specific dictionary is created from a default template and added to the DBM. Any ancillary files that might be required are added to the third level of the hierarchy.

3) The new data type is added to the TYPE dictionary along with the file structure (defined in step 1 above).

Once a new data type has been added to the DBM, applications can immediately access the data. Required file access information as well as data descriptor information is contained in the dictionary files. The default template used to generate the type-specific dictionary (step 2 above) insures that the first items in the list always contain basic time and location information (see for example Table 1(c), items 1-9). By adhering to the above expansion procedure, generic user-driven processing programs like contour, plot, or image display are able to operate on new

139

data types with either minor or no modifications. Some applications may
need to be recompiled in order to add a new data type to an internal
validation list or to increase buffer sizes, but in general this should not
be necessary.

3. GOES Mode AAA Ingest

The existing AFGL GOES mode A ground station is being replaced with new
hardware and software to support the new operational VISSR Atmospheric
Sounder (VAS) communications format known as mode AAA scheduled for
transmission in early 1987. The SEL 32/27 minicomputer has been identified
as the processing facility responsible for ingest, storage, and transmission
of mode AAA data. The SEL consists of a CPU, 1 mbyte (MB) of memory,
input/output processor, one 160 and two 340 MB disk drives, 800/1600 bpi
magnetic tape drive, line printer, operator's console, and support for six
terminals. Also included is a Gould model 9130 High Speed Device (HSD) to
interface the ground station electronics and the SEL for 32-bit parallel
transfers of mode AAA data. AFGL personnel acquired and installed ground
station electronics consisting of an Aydin Monitor Systems model 1050
receive subsystem and an Integral Systems model 8402 down-link interface
(DLI). The DLI converts the serial GOES bus output from the receive
subsystem to the 32-bit parallel format compatible with the HSD.

a. Mode AAA Requirements

AFGL requirements for mode AAA data specify support for the two
sub-modes of VAS operations. The first is the Multispectral Imaging (MSI)
mode that will provide simultaneous imagery in the visible at 1 km
resolution, one IR channel from the small detector at 8 km, and two
(possibly three) other IR channels from the large detectors at 16 km
resolution. The second sub-mode, known as the Dwell Sounding (DS) mode,
will provide radiometric information sufficient to construct temperature and
moisture profiles of the atmosphere. Through selection of different
detector/filter wheel combinations, 12 channels will be provided; seven in
selected CO_2 absorption bands between 4.3 and 15 μm, three in H_2O
absorption bands between 6.7 and 12 μm, and two window channels at 3.7 and
11 μm.

The data ingest procedure will collect nearly all data from the two large IR detectors and a subset of the broadcast from the small IR detector and visible data. This subset will provide coverage for all of North and Central America, parts of South America, and surrounding ocean. Exact coverage will depend on the satellite selected. Fig. 3 illustrates the approximate geographic extent of data to be collected for visible and IR channels as viewed from GOES-6. Table 2 shows the volume of data stratified by channel planned for routine collection every half-hour (IR only at night) under the MSI mode. During daylight hours visible data account for nearly 94 percent of all imagery data ingested during a single collection period. A four-hour online rotating archive of full resolution data from all channels is planned to provide a temporally continuous set of imagery data that will not be initially available with the McIDAS Sony Cassette Archive System.

Data routinely ingested and stored on the 32/27 will be available to users either at the user's request or specified automatically as part of the ingest/store/transmit sequence to eliminate user intervention. Requests will normally define some subset of stored data and may require preprocessing (e.g., degraded resolution).

b. Software Systems Specification

Prior to actual software development, specification of the required developmental tasks had to be accomplished. To this end the following initial task outline was generated, based on the above stated requirements:

1) Applications-Related Software

    a) System main loop
    b) FORTRAN-callable system services
    c) Applications job initialization
    d) I/O subsystem

2) Data Ingest

    a) Automated scheduling of real time ingest sequence

Fig. 3 Full Disk Visible Image with Overlay Showing Approximate Geographical Extent of VAS MSI Data by Channel

(View is from GOES-6.)

Table 2. VAS (MSI) Data Storage per Collection Period

Channel	Detector Resolution (km)	No. of Lines	Line Length (elements)	Memory Storage/ Element (bytes)	Disk Storage (MB)	Percent Relative Volume
Visible*	1	7680	7680	1	59.0	93.8
IR 1	8	1152	1152	2	2.7	4.3
IR 2/3	16	768	768	2	1.2	1.9

*Daytime only

143

b) Override of automated sequence

c) Image/sounding definition

d) Ingest of navigation parameters

e) Ingest of imagery/sounding data

3) Data Storage

   a) Database design

   b) Database management

4) Data Transmission

   a) Sectorize and/or average imagery data

   b) Communication network manager

   c) Data transmission routine

5) Hardware-Related Software

   a) HSD handler

   b) HSD/DLI diagnostic software

6) Terminal Communications

   a) Terminal handler

   b) Command line interpreter

7) Error Handler

8) Auto-Recovery

c. Determination of Operating System Characteristics

Given this articulation of software systems development into discretely defined components, a determination of required Operating System (O/S) features was made. It was concluded that it must be a real time operating system, equipped to handle the asynchronous collection and dissemination of

data and commands. It must accommodate multitasking to encourage the modular approach to program design and to allow concurrent processing of overlapping tasks. It must allow synchronized task processing and intertask communication through system service requests, since the various tasks comprising an ingest/store/transmit sequence must execute in an orderly manner and require the sharing of common data. Finally, the operating system must be flexible enough to accommodate unanticipated system design changes or expansion. Gould's Mapped Program Executive (MPX-32) was judged to meet all these requirements and was therefore incorporated into AIMS.

d. Software Development

Of the eight development tasks enumerated above, three have been completed, as follows.

1'. Applications-Related Software

The system main loop has three functions. First, it is responsible for job loading; that is, loading a job from secondary storage, initiating execution, and providing an environment for the job to retrieve input parameters either entered at the keyboard or specified in software. Secondly, it supports and simplifies interjob communication. Jobs that activate other jobs specify an array containing the name of the program to execute along with any input parameters to be passed. In this way, applications need not be concerned with creating and maintaining complicated data structures that would be required to accomplish the same function using system services. This simplifies program design and assures consistency of format for a keyboard-entered command and a software-coded command. Finally, the system main loop monitors the scheduled satellite data ingest sequence and works in unison with the scheduler to execute in an orderly manner the programs that comprise an ingest sequence.

The system main loop handles these three functions continuously through a software "endless loop" design in which the same code executes in a cyclic manner. Each function is broken down into logical steps with one step executed for each pass through the loop. Progression from one step to the next is managed with state tables. The main loop was coded in Gould CSD

145

Assembly to maximize speed of execution, minimize memory requirements for resident task space, and to take advantage of the extended repertoire of system services available for this language.

Before any applications programs could be written, FORTRAN-callable system service subroutines had to be developed to provide the link between the system main loop and the application. Subroutine IQ was developed to retrieve input parameters originally specified when the calling program was activated, either from the keyboard or from another program. Subroutine SQ was developed to provide the calling program with a simple procedure to activate another program and optionally pass input parameters.

Since all applications jobs require these subroutines, they were incorporated into a module containing the entry and exit points for all applications jobs. The entry point or prologue activates the applications program as a subroutine. The exit point or epilogue makes a standard exit call to the operating system. The epilogue also reports completion status for programs that comprise a macro chain.

A primary subset of routines that collectively define a record-directed input/output subsystem will be incorporated as part of the database management system. The subsystem provides applications access to an I/O module that can more fully exploit services of the MPX-32 Input Output Control System (IOCS) than standard FORTRAN and simplifies the activation call by reducing the number of calling arguments. The I/O subsystem has been designed to execute in the real time environment and supports synchronous/asynchronous unbuffered I/O, block addressability within disk files, file generation and deletion, and interface routines to assign, open, close, and de-assign files. Programs running under MPX-32 and performing I/O will each contain a file access lookup table (FALT) that is used by the subsystem to monitor connected file status, thus reducing operating system dependence and simplifying I/O requests. The I/O subsystem is accessed by routines coded in either FORTRAN or assembly and the object code exists in subroutine library format to facilitate the catalog process with applications software that requires its use.

2´. Terminal Communications Software

Interactive program execution will be necessary during the debug and test phase (and probably on an operational basis) for control over programs

that comprise the ingest/store/transmit sequence, to maintain the online
database, and to monitor system performance. However, it is not desirable
that every interactive program developed be responsible for retrieving and
formatting input parameters because these functions add unnecessary
duplication of effort to program development. Consequently, a terminal
handler and associated command line interpreter were developed.

The terminal handler supports real time, asynchronous I/O between a
user terminal on the 32/27 and interactive programs. At the user level the
terminal handler executes as a utility. Once activated by entering the
utility name it prompts the user for input, accepts a repertoire of
commands, and terminates with a standard exit command. The handler combines
command language features native to the Gould and McIDAS. Gould features
include command name abbreviation, parameter passing, and a choice of
delimiters in constructing a command. From McIDAS the two-letter command
structure has been implemented to provide the user with the environment for
rapid command entry and to reduce program activation latency. The
two-letter command is especially useful when time constraints are imposed on
operations. The terminal handler supports use of the break key for options
to abort an executing program, issue a hold request, or resume execution of
a program in hold. In association with the handler, a terminal output
subroutine was developed. Subroutine TQ provides a standard interface
between programs and the terminal handler for output of ASCII messages.

Once input is complete, the terminal handler passes the ASCII command
line to a command line interpreter. The interpreter executes as an
applications job to validate the command name and decode any parameters that
may follow, converting ASCII decimal characters to equivalent binary.
Finally, the interpreter activates the application job identified by command
name via the system service routine SQ.

3´. Hardware Related Software

Foundation software to execute device functions on the HSD/DLI was
developed. Subroutine HSDSTART, a FORTRAN-callable assembly routine, resets
the DLI for normal mode of operation and initiates mode AAA block read
transfers from the DLI to HSD to Gould memory. Subroutine HSDSTOP resets
the DLI to terminate I/O. I/O performed at this level is device-dependent,

147

utilizing the execute channel program system service to communicate instructions between CPU and HSD via I/O command lists (IOCL). IOCL's are developed to refer to either logical or physical addresses in memory. Although faster to code, logical IOCL's must be converted to physical IOCL's to satisfy HSD requirements. Considering the real time constraints of ingesting satellite data, physical IOCL's were chosen to eliminate the overhead generated by the operating system in performing the conversion. Errors stemming from HSD and/or DLI transactions are posted on the operator's console for notification and operator intervention.

Using this software, an interactive program was developed to ingest from one to twelve unmodified mode AAA blocks and store the blocks in predefined files for later examination. Currently, the program is being used to validate the mode AAA format as received from GOES-6 and also to validate data formatting performed by the DLI.

e. System Configuration

The MPX-32 operating system was configured to satisfy requirements of an interactive minicomputer-based satellite ingest system. The system clock was changed so that software wait states can be specified to fractions of a second. This capability is used by the system main loop to maximize throughput when handling multiple requests. To exploit true full duplex operations for improved terminal response, dual channel mode capability was added on the 8-line asynchronous controller so that I/O is routed through separate subchannels. This eliminates subchannel contention normally present when I/O is directed through the same subchannel as in single channel mode. The HSD was jumpered, installed, and configured with the generic device driver provided by Gould. Finally, a static global memory partition was configured to provide physically contiguous memory to be used for buffering the satellite data and also for location of IOCL's.

4. Automatic Acquisition of Meteorological Observation Reports

The capability to receive, decode, and archive meteorological reports automatically has been developed for AIMS. Hourly surface reports for North America, global synoptic reports, ship and buoy reports, and upper air

measurements are disseminated by the National Weather Service over a
subscription telephone line known as the WB604 service. Raw reports are
received by the VAX 11/750 through an RS-232 communications port. A
dispatch routine manages data and control flow to various decoder routines.
Decoders extract specific parameters from the raw reports and format the
collected data into a predefined archive structure. The reformatted data
are then stored in a rotating disk file such that the individual reports can
be accessed randomly.

a. Acquisition Subsystem Overview

The WB604 data acquisition subsystem consists of three components (Fig.
4) and will accommodate as many decoders as real time constraints will
permit. The components consist of two independent, detached processes and
an interactive inquire utility. The detached processes, a driver and a
dispatcher, run continuously, receiving and distributing data coming in over
the WB604 line. The utility program is used to control the two detached
processes.

The interactive inquire utility provides an interface between the users
and the driver and dispatcher detached processes. The following functions
are supported:

    1) Starting/restarting/shutting down the driver and dispatch processes;

    2) Querying and resetting internal status counters;

    3) Enabling different modes used when debugging the decoders;

    4) Modifying the configuration database.

The inquire utility has a user interface that follows the operating
system command language protocol. This makes the utility operate as though
it were a native command within the system command language. The inquire
function is used by both the system manager and general users to communicate
with and control the driver and dispatch processes. Since these are
detached processes, there is no other way to communicate with them.

The dispatcher process resides logically between the driver and the
decoders. The dispatcher has four primary functions:

    1) Receiving the raw data records from the driver;

    2) Interrogating the data catalog number to determine the data type;

    3) Routing the data and invoking the correct decoder routine;

    4) Handling queries from the inquire utility.
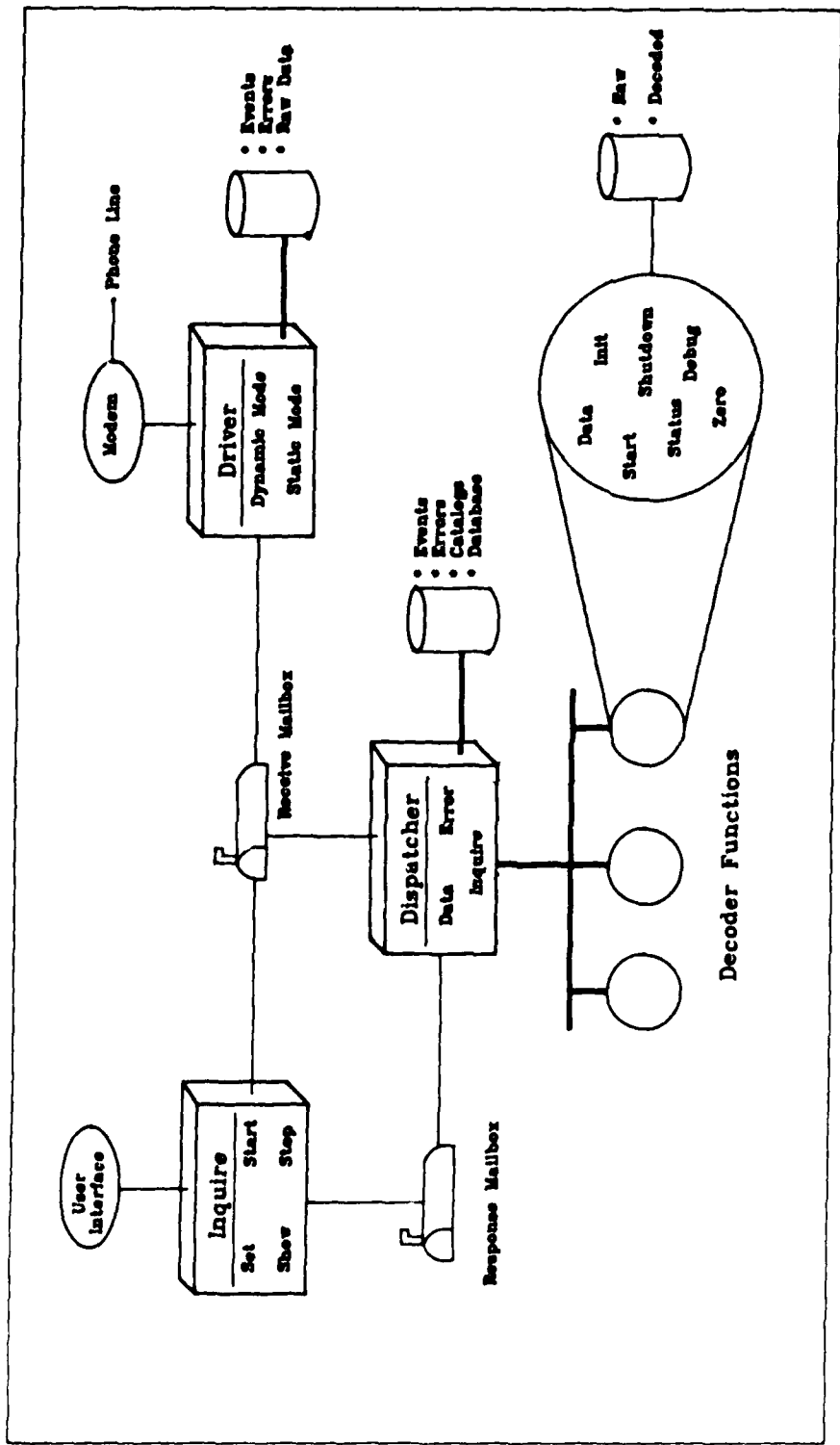
Fig. 4 Meteorological Acquisition Subsystem

Raw data are received one record at a time from the driver via a communications mailbox. The dispatcher will wait until a record has been completely processed by a decoder before the next record is accepted. Included at the beginning of each series of reports is a catalog number that refers to the type of data contained in the subsequent reports. The catalog number is checked against a validation list and the data are routed to either the appropriate decoder or, if not on the list, ignored. The validation list can be dynamically modified through the inquire utility so that decoders can be added or removed at any time. For debugging procedures the raw reports can also be routed to a separate data file for later examination. Each decoder maintains statistics on the number of reports handled, the number of reports successfully decoded, error conditions, etc. The inquire utility is used to generate a report of these statistics by instructing the dispatcher to query the specified decoders.

The driver process receives the data from the WB604 line via an asynchronous communications port and passes each record on to the dispatcher over the mailbox link. It checks for transmission errors and validates the data. Error statistics are also passed to the dispatcher process.

b. Surface Report Decoder

The WB604 line transmits surface reports from over 1200 stations in the U.S. and Canada every hour. Hourly reports consist of temperature, dewpoint temperature, surface pressure reduced to sea level, altimeter setting, visibility, weather, and cloud cover for up to four layers. In addition to the hourly reports, reports of accumulated values are received on a 3-hourly basis for pressure change and tendency, precipitation amounts, and snow cover. Six-hour maximum and minimum temperatures and 12-hour freezing level data are also transmitted. A surface decoder has been written to strip out these parameters and store them in two different data structures, one for the hourly data and the second for the accumulated reports. Tables 3(a) and 3(b) give the formats for the hourly and accumulated structures respectively. Each of these structures is stored in a separate rotating file that contains the most recent 168 hours (one week) of data. The files are set up such that each report is indexed on valid time and station identifier.

151

Table 3(a). Data Structure for Hourly Surface Weather Reports

Parameter description	Size	Range
Time offset from hour	6	(+/-) 30 min
Pressure	10	950.0-1049.9 mb
Visibility	8	0, 1/16-23/4, 3-50
Temperature	8	(+/-) 127 F
Dew point temperature	8	(+/-) 127 F
Cloud Layer 1-2		
height	8	0-25500 ft
opacity	1	
cover	2	X, SCT, BKN, OVC
Cloud Layer 3-4		
height	9	0-51100 ft.
opacity	1	
cover	2	SCT, BKN, OVC
Clouds obscured	1	
Clouds missing	1	
Weather		
TORNADO	1	
FUNNEL CLOUD	1	
WATERSPOUT	1	
T, RW, L, ZR,		
ZL, IP, IPW, S,	3 each	(+/-/--)
SW, SP, SG, IC		
A, F, GF, BS,		
BN, BD, IF,	1 each	
H, K, D, BY		
Liquid precip.	1	
Frozen precip.	1	
Altimeter setting	10	29.50-30.49 in Hg
Wind		
direction	6	0-36
speed	7	0-127 kts
missing flag	1	
gust	8	0-255 kts

Table 3(b). Data Structure for Accumulated Surface Weather Reports

Parameter description	Size	Range
3 hr. pressure change	8	0-25.6 mb
3 hr. pressure tendency	4	0-9
3/6 hr. precip. amount	11	0-20.45 in
Missing precip. flag	1	
Cloud Layer 1-4		
type	4	
amount	4	1-10
Snow depth	8	0-255 in
Max and min temperature	8	(+/-) 127 F
Freezing level	8	0-25500 ft
24 hr. precip. amount	12	0-40.95 in
Missing snow depth	1	
Missing max/min temp.	1	
Missing freezing lvl.	1	
Missing total precip.	1	

A separate file is maintained that contains a list of all the reporting station identifiers and their locations plus the index value used to locate entries in the rotating report files. To access data in the report files the record number of the specified report must first be calculated. This is done by searching the station file for the specified station ID, obtaining the index value, and then computing the relative address in the report file. Report files are set up for direct (or random) access so that once its address is known, a report can be extracted directly. The station file is sorted on the station ID's so that a binary search algorithm can be used to locate any specific ID, which makes the search process very fast. A separate station file is maintained so that stations can be added or removed from the list without affecting the report files. The only constraint imposed on modifications to the station file is that the sorted order of the station ID's must be maintained.

Applications programs have been written to access the report data in several different ways. For any specified time the data can be accessed by station, by state or province, by predefined regions, or by latitude-longitude bounds. Fig. 5(a) is a sample listing of reports from stations in Massachusetts for a specified time, 1200 GMT, 29 October 1986. Reports for single stations can also be accessed for any time interval contained in the rotating file. Fig. 5(b) is a sample of reports from Boston for the 48-hour period 1200 GMT to 1200 GMT on 27-29 October 1986, with the reports sampled every three hours. Applications programs that graphically display the data (e.g., contour maps or plots over a geographic area) need to access all the data within specified latitude/longitude bounds. Access routines have been written that locate all the stations within the bounds and return the requested parameters. For each method of accessing the data, a separate station file is maintained that is sorted on the search parameter. Specifically there are separate files sorted on individual stations names, states and provinces, regions, and latitude/longitude. Each of these sorted files contains index values that point back to the same 168-hour report file, so while many of the small sorted files exist, only a single report file is required to support all the access methods used on the system.

154

```
                    29-OCT-1986 12:00Z
ID  HH   T   TD   PRE    WIND    VIS   WX   LYR1 LYR2 LYR3 LYR4 dPR  PTT  TXN SNO
ACK 12  49  48  1022.7*  2806    10         CLR
AYE 12  39  34  1022.2   0000     4FH       250S
BAF 12   M   M  1021.3*  0000    3/4F  -X   250S
BED 12  38  38  1021.7*  0000     3FH       CLR
BOS 12  48  43  1022.0   2411     M    M                     0.5       46
BVY 12   M   M  1022.0*  0000     8         CLR
CEF 12  35  31  1022.1   0000   11/2F       001S 250S        0.0
EWB 12  39  37  1022.3*  0000     6F        CLR
FMH 12  41  37  1022.6   0000     6FH       CLR              0.3
HYA 12  45  39  1023.7*  2705     8         CLR
MVY 12  45  41  1021.0*  2708    10         CLR
NZW 12  39  38  1021.8   1801   21/2F       CLR              0.3       39
ORH 12   M   M    M       M       M    M                     0.0
OWD 12  39   M  1022.0*  0000     5F        CLR
```

Fig. 5(a)   Surface Observation for Massachusetts at 1200 GMT, 29 October 1986

```
              27-OCT-1986 12:00Z TO 29-OCT-1986 12:00Z
ID  HH   T   TD   PRE    WIND    VIS   WX   LYR1 LYR2 LYR3 LYR4 dPR  PTT  TXN SNO
BOS 12  49  49  1015.1   0312     M    M                     0.2 0.13  47
BOS 15  no report
BOS 18  no report
BOS 21  51  50  1010.7   3508     5F        005B 0080       -0.8
BOS 00  50  49  1011.2   3606     5F        006B 0110       -0.5       52
BOS 03  50  48  1011.4   3307     4F        007O            0.2
BOS 06  50  49  1010.8   2308     4F        004B 007O       -0.5       52
BOS 09  51  50  1011.0   2411     4F        003O            0.2
BOS 12  52  50  1011.2   2510     5F        008B 014O       0.2        50
BOS 15  57  51  1012.5   2810     5F        050B 065O       5.5
BOS 18  61  51  1012.5   2714    12         022S 050O
BOS 21  63  50  1014.4   3211    15         030S 050S       1.9
BOS 00  59  50  1017.4   3011    10         035S            3.0        65
BOS 03  55  46  1019.8   3010    10         CLR             2.4
BOS 06  51  46  1021.0   2908    10         CLR             1.2        65
BOS 09  49  44  1021.5   2610     8         CLR             0.5
BOS 12  48  43  1022.0   2411     M    M                     0.5       46
```

Fig 5(b)   Surface Observations for Boston over the 48-hour Period 1200 GMT - 1200 GMT, 27-29 October 1986, Sampled Every Three Hours

5. Summary

The AFGL Interactive Meteorological System has been defined and implementation is well under way. STX has been responsible for implementing three major subsystems during 1986: database manager, GOES mode AAA ingest capability, and automatic acquisition of WB604 meteorological reports.

The database manager is a centralized system residing on the VAX 11/750. It consists of three layers of software: utility layer, data dictionary layer, and I/O layer. The data dictionary layer is a hierarchical structure of data dictionary files each of which contains information on data files located anywhere on the system. The DBM maintains the data dictionary files and associated key files and performs searches on the dictionary files in response to data queries from users. A commercial database management package is used to handle the data dictionary layer of the management system.

Development of an interactive minicomputer-based GOES mode AAA ingest system has been undertaken. Definition of required tasks and identification of an appropriate operating system have been completed. A software environment to facilitate interactive program development and use has been designed and developed. Mode AAA data are currently being ingested and validated.

A receive and command structure has been developed to handle meteorological data arriving over the WB604 data line. A driver process handles ingest of data into the system and then passes the data off, one record at a time, to a dispatcher process. The dispatcher validates the data and invokes an appropriate decoder routine. Decoders strip out desired parameters from the data stream and reformat them into an archive structure. User interaction with the driver or dispatcher is accomplished through an interactive inquire utility.

6. Reference

Gustafson, G., D. Roberts, C. Ivaldi, R. Schechter, T. Kleespies, K. Hardy, R. D'Entremont, G. Felde, R. Lynch, 1987: The AFGL Interactive Meteorological System. Preprints, Third International Conference on Interactive Information and Processing Systems for Meteorology, Oceanography, and Hydrology, New Orleans; AMS, Boston, 151-154.

B. Microprocessor-Based Satellite Data Ingest System

1. Introduction

Under a contractual agreement between the National Oceanic and Atmospheric Administration and AFGL, a redundant data path in the AFGL GOES mode A ground station has been made available to a consortium of users known as the Northeast Area Remote Sensing System (NEARSS). Included in the agreement is a requirement to develop a central processing facility to ingest, store, and transmit over a dedicated communications line subsets of the GOES imagery transmission. To satisfy this requirement an Intel 8086-based microprocessor with fixed disk mass storage was purchased and assembled. AFGL personnel developed software to handle configuration of the central processor. STX software engineers participated in various phases of the software system specification and development.

This report summarizes the concluding efforts to configure the final system for sustained unattended operation. Also, a brief description of the NEARSS operational schedule is provided.

2. System Configuration

Configuration of the final RAM-based system was completed using the Interactive Configuration Utility. Individual tasks were grouped according to the function they perform as a multi-tasking unit. Three groups or subsystems were identified. The network communications subsystem includes the network manager, receive interrupt handler and task, transmit interrupt handler and task, and USART initialization task. The ingest/store/transmit subsystem contains the scheduler, clock task, ingest interrupt handler and task, and protocol assembler task. The I/O subsystem contains the FORTRAN-86 and PLM-86 callable links to the iRMX86 Basic I/O System. Under iRMX86 these subsystems are known as first-level jobs and were configured to execute in unique environments. As required by the operating system, initialization tasks were developed for each subsystem. These tasks define the tasks to be synchronously or asynchronously initialized under a first-level job.

An empirical technique was employed to determine optimal size values for task stack, job memory pool, and I/O cache buffers. The technique utilizes the iRMX86 Debugger to monitor these and other parameters during system operation and record events in which system components use their peak demand of the stated resources. Maximum values for each parameter were set during configuration and adjusted to reflect lower thresholds if previous settings were not detected. The debugger was run as part of the system for ten days and optimal values determined for each parameter. The values were increased by 10 percent and then specified during the final system configuration.

3. Operations

Since October 1985, the microprocessor-based satellite ingest system developed at AFGL has been providing NEARSS with near real time GOES mode A satellite data. NEARSS receives half-hourly collocated visible (daytime only) and infrared imagery along with image documentation and orbit/attitude information required for precise earth locating of imagery. Images have a resolution of nearly 8 km per picture element and a size of 512x512 pixels or approximately 0.25 MB of 8-bit data. The standard broadcast for NEARSS is transmitted in approximately 9 min at 9600 baud.

C. McIDAS Operation and Maintenance

STX has been responsible for day to day operations support of the AFGL McIDAS. Routine activities included maintenance of the Sony satellite archive, GOES navigation ingest and quality control, scheduling use of terminal time, and maintaining and updating the surface and upper air data archive. Scheduling of real time GOES imagery ingest and production of data save tapes and hardcopy imagery were provided as required by project scientists. The condition of McIDAS software was monitored to ensure system integrity. System software saves were made and system regenerations from save tapes were performed when software or hardware failures warranted such action.

Equipment recently added to the McIDAS includes a GOES Mode AAA Receiver Subsystem model 1050 and a Down-Link Interface model 8402. These

components are required because down-link transmission from the Synchronous Meteorological Satellite (SMS) is scheduled to change in 1987 from standard mode A format to a new AAA format.

The GOES Mode AAA Receiver Subsystem, built by Aydin Monitor Systems, is a PSK demodulator, bit synchronizer, and frame synchronizer all in one chassis. This unit will receive a 67.1 mHz signal from the antenna receiver and will produce the following signals which are sent to the DLI (Down-Link Interface):

        Frame Code
        VISSR Information Start
        End of Block
        Serial Data
        Data Clock
        ID 1
        ID 2
        ID 3
        ID 4
        ID 8
        Header Start
        Information Start
        Error Check Start
        Word End.

The Down-Link Interface built by Integral Systems will pack the incoming AAA serial formatted data into 32-bit parallel words and transfer them to the SEL computer via a High Speed Data Interface.

Excessive head and drum wear over the past several years required that modifications be made to the Sony Archive System VO-2800 recorders. The excessive wear was traced to the way in which the operating time of each recorder was controlled by a timer applying AC power to the unit. Timers were required because of the many hours that data were being collected after normal hours of operation and on weekends. When the unit's AC power was turned off, the video tape would be left around the drum which would continue to rotate since its power came from the Record Electronic Drawers.

To eliminate this problem a modification was built into the recorders to eject the tape automatically whenever the tape counter reaches 900. Thus, when the AC power is terminated by the timer, the tape cassettes have been removed from the recorder.

McIDAS operators' Terminal 22 was moved from Room C242 to the
Meteorological Chart Room, C234, where it is used by forecasters to bring in
additional information to aid in weather analyses and briefings.

The Adage Video monitors (Conrac model 7211) were modified with a
low/high resolution switch. This modification enables the operator to
change monitor resolution without requiring removal of the monitor cover and
changing a series of jumpers.

The following major items of equipment required maintenance during
1986. The end item is listed, followed by the component(s) repaired or
replaced to bring the equipment back to operating condition.

a. Conrac Video Monitor model 7211
   Resistor R20 (100 kΩ)

b. McIDAS Video Rack 3
   Power/Mate power supply model UMI-30G

c. Harris 80 MB disk
   Low voltage power supply, disk controller, and channel board

d. MDS-800 Development System
   1702A EPROM (Bootstrap program prom)

e. Sony Archive System Recorders model VO-2800
   New heads and upper drum assemblies

f. EMR Bit Synchronizer model 350
   Transistor Q1 (2N 5771), R2 (1.8 kΩ), and R3 (100 Ω)

g. Textronix Spectrum Analyzer model 7L13
   Repairs made by Tektronix, Inc.

h. Sony Archive System Record Electronic Drawer 1
   ± 12 volt power supply

i. Terminal 21 Conrac Video Monitor
   Capacitor C9

j. Myriad/XK Integrated Circuit Tester
   Repairs made by Hy-Tronix Instruments, Inc.

k. Sony Archive System Record Electronic Drawer 2
   IC AH1 (74LS123)

l. Sony Player VP-2000
   Midway pulley assembly

m. Leonessa Signal Processor model 140B
   IC 8(7490) on board 1453

n. Adage System 2

Blower fan in +5 volt power supply

o. EMR Frame Synchronizer model 56A-B5885A

Capacitor C1 (7200 µf, 20v)

p. MicroVAX II System Disk

Blower fan assembly

q. Digital Video Storage System for Terminal 21

IC BC 030 (74LS 669) on DVSS Board

VI. CLIMATOLOGY

A. Cloud Cover Realizations

1. Cloud Cover Simulation

a. Introduction

Cloud cover simulation models have been developed at AFGL using single-point probabilities of cloud amounts, cumulative probability distributions of threshold cloud amounts along lines or over areas as derived by Gringorten (1979), and a stochastic processing technique known as the Boehm Sawtooth Wave (BSW) Model (Boehm et al., 1985). These models are used to simulate the impact of cloud cover on the selection of sites for ground-based laser (GBL) systems.

This report discusses the generation of additional cloud statistics for cloud simulation model developments, current status of cloud simulation models at AFGL, and an initial cloud simulation model validation procedure. Also, presented are updated descriptions of support for research efforts on cloud morphologies as derived from satellite digital data and expansion of a rainfall rate database used for compiling rain rate recurrence statistics.

b. Specifications

AFGL specifications guiding development of the cloud simulators are to:

o   Modify software originally designed for deriving spatial cloud cover correlation decay from conventional data sources, to define the parameter scale distance for the joint probability of a cloud-free line of sight at two stations simultaneously;

o   Implement onto AFGL computers (Cyber 180/860 and VAX 11/780) all USAFETAC cloud simulation software for testing and validation purposes;

o   Derive spatial and temporal correlation functions from sunshine data to compare with similar functions derived using the cloud simulation models, for model validation.

Additional specifications supporting other cloud studies are to:

o   Develop software for research on determining probable cloud-free or
    cloudy intervals of cumulus clouds as derived from digitized
    satellite imagery;

o   Process rain rate data to provide statistics of rain rate
    recurrences over selected sites.

c. Cloud Statistics

The data processing configuration for providing cloud cover statistics
from ground-based conventional observations originally described in Gerlach
(1985) was modified to provide, among other cloud statistics, the parameter
scale distance from the joint probability of a cloud-free line of sight at
two stations simultaneously. The modified configuration is depicted in
Fig. 1, shaded portions of which represent the updated sequences.

This and subsequent data flow figures show how data sources combine
with developed software to produce end results. The diagrams show data
sources at the left, followed by the data transfer software developed to
format, compress, and transfer data to permanent files for interactive
processing. Names of permanent files are directed to the scientific
applications software developed to accomplish what is briefly described at
the right of each diagram. The backup tape numbers and tape labels (TN)
also shown record where all data for each project are kept for permanent
retention. Details of the updated data flow in Fig. 1 are discussed below.

Several additional stations reporting weather in DATSAV format from
other parts of the globe were acquired to provide a more robust statistical
data sample. Program COT2 was modified (COT 3) to derive a relation between
sky cover probabilities and line of sight (LOS) probabilities to compute the
parameter scale distance for the joint probability of a cloud-free line of
sight (PCFLOS) at two stations simultaneously. As specified by AFGL, steps
to achieve these computations using DATSAV data are as follows:

With frequency distributions of sky cover categorized in eighths, for
each designated station i for January and July stored in the form
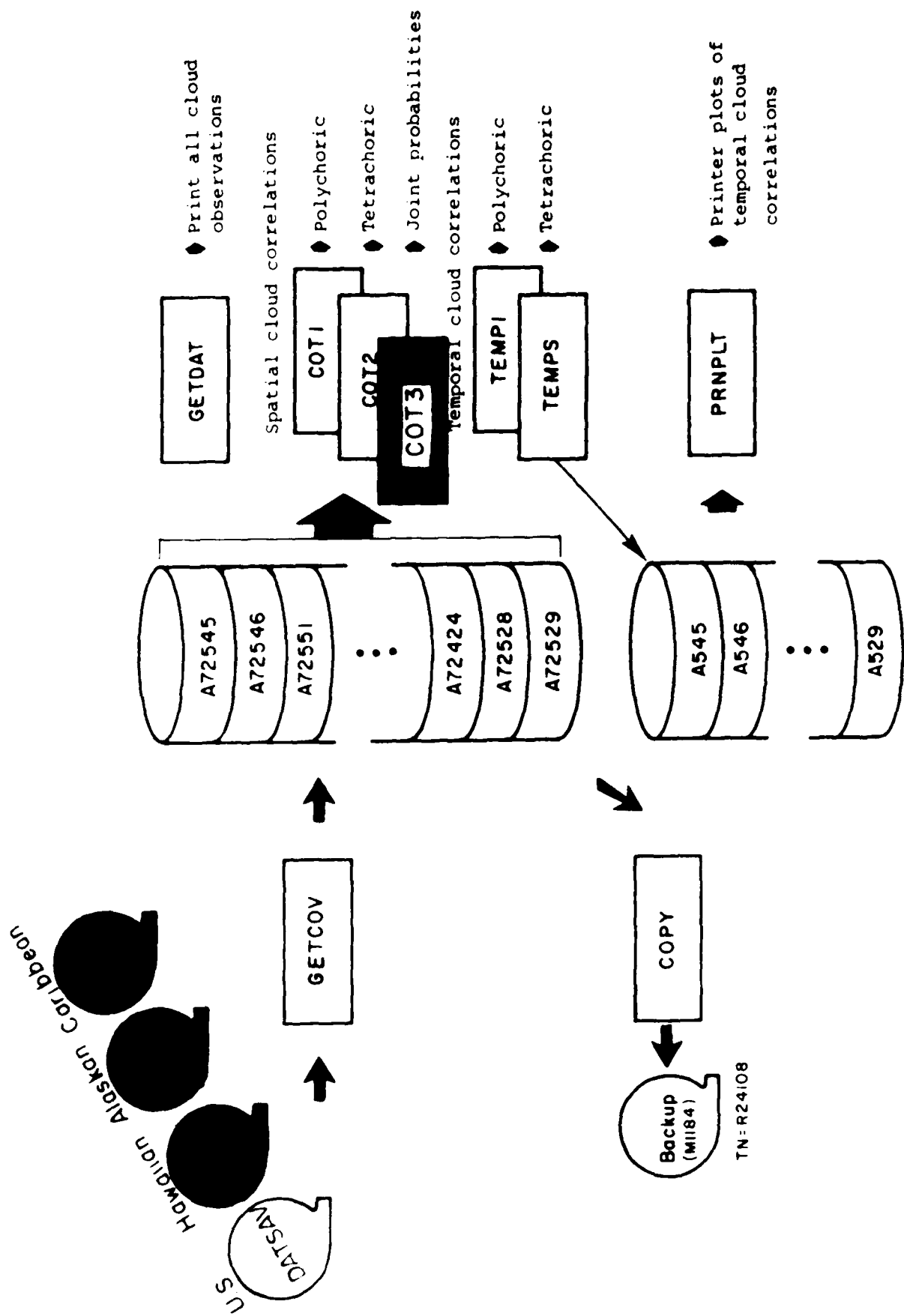
Fig. 1 Updated Processing Configuration for Producing Cloud Cover Statistics from Ground-Based Observations

$$P_i(F) \text{ for } F = 0(1)8,$$

compute partly cloudy skies $P(\bar{C})$, as

$$P(\bar{C}_i) = \sum_{F=0}^{4} P_i(F)$$

and cloudy skies $P(C)$, as

$$P(C_i) = \sum_{F=5}^{8} P_i(F) \; .$$

Then compute probability of cloud-free (CF) and partly cloudy ($\bar{C}$) skies using

$$P(CF_i, \bar{C}_i) = \sum_{F=0}^{4} P_i(F)\left(\frac{8 - F}{8}\right)$$

and cloud-free and cloudy (C) skies by

$$P(CF_i, C_i) = \sum_{F=5}^{7} P_i(F)\left(\frac{8-F}{8}\right).$$

Then compute probability of cloud-free line of sight (PCFLOS) as

$$PCFLOS = P(CF_i, \bar{C}_i) + P(CF_i, C_i).$$

Compute probability of cloud-free skies given partly cloudy skies by

$$P(CF_i | \bar{C}_i) = \frac{P(CF_i, \bar{C}_i)}{P(\bar{C}_i)}$$

and probability of cloud-free skies given cloudy skies as

$$P(CF_i | C_i) = \frac{P(CF_i, C_i)}{P(C_i)} \; .$$

With each pair of stations (i and j), find distance s' in nautical miles
using

$$s' \text{ (nm)} = 60 \cos^{-1}[\cos(90-LA_i)\cos(90-LA_j) + \sin(90-LA_i)\sin(90-LA_j)\cos(LO_j-LO_i)]$$

where

LA_i and LO_i = latitude and longitude of station 1
LA_j and LO_j = latitude and longitude of station 2.

Survey each station pair to give estimates of the probabilities of each combination so that

$$a = P(\bar{C}_i, \bar{C}_j) = \frac{N(\bar{C}_i, \bar{C}_j)}{N},$$

where

N is total number of pairs

$$b = P(\bar{C}_i, C_j)$$
$$c = P(C_i, \bar{C}_j)$$
$$d = P(C_i, C_j).$$

Note that $a + b + c + d = 1.0$.

Then find tetrachoric correlation estimates, $\rho_{i,j \ (SKY)}$, for sky cover using the approximation formula

$$\rho_{i,j \ (SKY)} = \sin \left[\frac{\pi}{2} \ \frac{\sqrt{ad} - \sqrt{bc}}{\sqrt{ad} + \sqrt{bc}} \right] = RHO_{s(SKY)} \ .$$

This leads to

$$s = \frac{3 - \sqrt{1 + 8\rho_{i,j(SKY)}}}{4} \ .$$

which is used to find

$$\Lambda = \frac{s'}{s} (nm).$$

Then sky cover scale distance ($r_{i,j \ (SKY)}$), also known as the sawtooth 3D scale distance, is given by the expression

$$r_{i,j \ (SKY)} = \frac{\Lambda}{256} (nm) \text{ or } 1.852 \ \frac{\Lambda}{256} (km).$$

Moreover, with each pair of stations (i,j), find line of sight (LOS) joint probabilities

$$\begin{bmatrix} t & u \\ v & w \end{bmatrix}$$

where

$$t = P(CF_i, CF_j) = \left[P(CF_i|\bar{C}_i), P(CF_i|C_i) \right]_{STA_i} \begin{pmatrix} a & b \\ c & d \end{pmatrix} \begin{bmatrix} P(CF_j|\bar{C}_j) \\ P(CF_j|C_j) \end{bmatrix}_{STA_j}$$

$u = PCFLOS_i - t$

$v = PCFLOS_j - t$

$w = 1 - t - u - v$.

Then find tetrachoric correlation between cloud-free lines of sight (CFLOS) at two stations using again the approximation formula

$$\rho_{i,j(CF)} = \sin\left[\frac{\pi}{2} \quad \frac{\sqrt{tw} - \sqrt{uv}}{\sqrt{tw} + \sqrt{uv}} \right] = RHO_{L(LOS)}.$$

This leads to

$$s = \frac{3 - \sqrt{1 - 8\rho_{i,j(CF)}}}{4} .$$

which is used to find

$$\Lambda = \frac{s'}{s} \quad (nm).$$

Finally, LOS scale distance $r_{i,j(CF)}$ is given by the expression

$$r_{i,j(CF)} = \frac{\Lambda}{256} \quad (nm) = 1.852 \frac{\Lambda}{256} \quad (km).$$

As shown in the notation, partly cloudy skies ($\bar{C}$) were the result of setting all conventional cloud cover observations less than or equal to four eighths into one category; cloudy skies (C) were the result of setting sky covers greater than four eighths into a second category. (Obscurations were excluded from the analysis.) Results of these computations were hand-plotted for all site combinations in a particular region; i.e., U.S. Midwest, Hawaii, Alaska, etc. Typical results are plotted in Fig. 2 showing $RHO_{s(SKY)}$ between sky covers at two stations vs. separation distance (s') on the left and correlation $RHO_{L(LOS)}$ vs. s' on the right, for midwest stations in January. Spatial sky cover correlation decay derived from these computations provided standards for the derivation of other weighting functions used to compute similar realizations introduced into the Boehm sawtooth cloud simulation technique. Boehm et al. (1986)

167
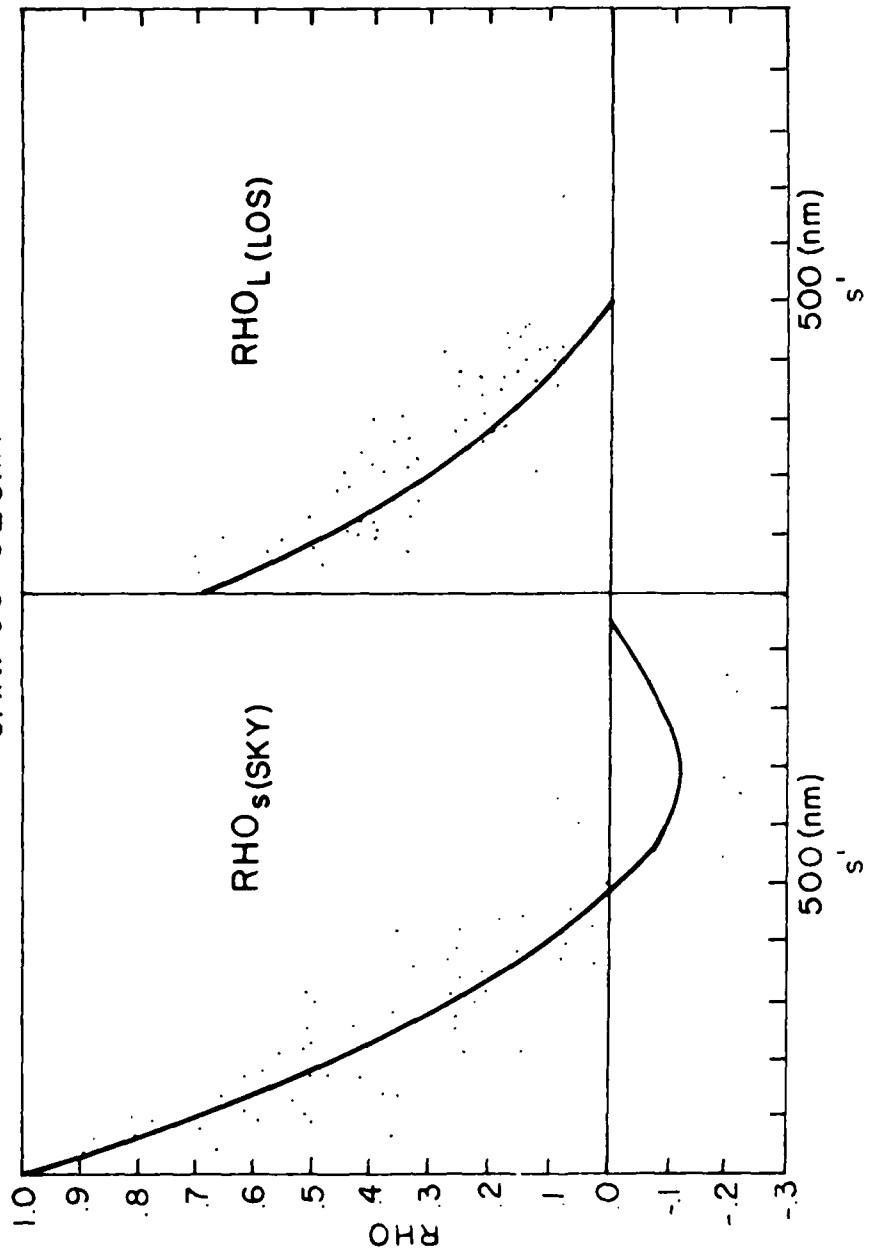
Fig. 2 For Midwest Stations in January 00-02 GMT: (left) Correlation $RHO_s(SKY)$ between Sky Covers at Two Stations vs. Separation s'; (right) Correlation $RHO_L(LOS)$ vs. s

discuss in more detail the algorithms defined for combining spatial and
temporal cloud cover decay functions with sawtooth models to simulate cloud
cover.

d. Cloud Simulation Software

This section discusses cloud simulation software currently residing on
AFGL computers.

The cloud simulation software was developed mainly by Harms (1986).
Two simulators were designed to provide realizations of cloud-free lines of
sight (CFLOS4D) and cloud-free arcs of sight (CFARC) for multiple stations
correlated in time and space. ("4D" means four dimensions; i.e., x, y, and
z spatial dimensions and one time dimension.) The geometry peculiar to
these two models is portrayed in Fig. 3. Cloud-free lines of sight are
lines unobstructed by clouds that may, for example, extend from a
ground-based laser (GBL) to a geostationary satellite relay mirror to a
target. Cloud-free arcs are arcs unobstructed by clouds that may extend
from a GBL to an <u>orbiting</u> relay mirror to a target. Both programs produce
downtime statistics for systems of one to multiple sites. They are
therefore highly important to the Air Force in selecting sites for optimum
ground-based laser operations. STX was responsible for implementing the
cloud simulation software onto AFGL computers for model testing and
verification purposes. Fig. 4 shows the current configuration of software
available at AFGL for performing cloud simulations. A detailed description
of program operation can be found in Harms (1986). Each of the programs is
briefly described below.

Meaningful cloud cover simulation requires adequate definition of sky
cover climatology stratified by region, season, and time of day. Burger's
<u>World Atlas of Total Sky Cover</u> (Burger, 1985) is specifically designed for
this purpose. It contains mid-seasonal mean sky cover and scale distance
parameters in contoured form over the world for four time periods of the
day. Program FOURIER has been designed to interpolate hand-extracted
values from the atlas into hourly values for input to the simulation
.

will compute mean sky cover and scale distance parameters
models given sky cover data from other climatological

169
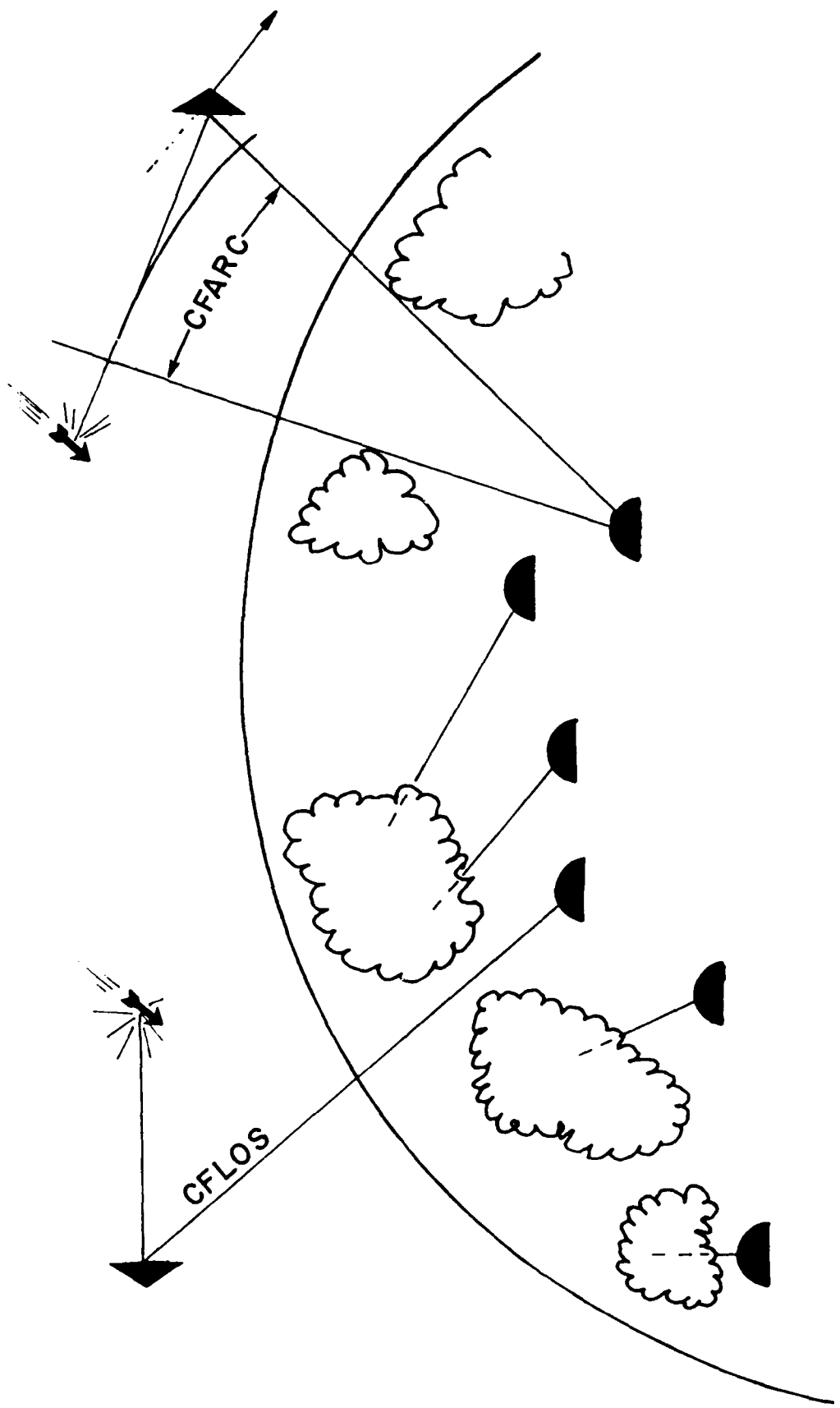
Fig. 3 Cloud-free Line of Sight (CFLOS) to Geostationary Satellite and Cloud-free Arcs of Sight (CFARC) to Orbiting Satellite

CFLTS (CFLOS Mapping)

Downtime statistics
Geostationary relay
mirror

Downtime statistics
Orbiting relay mirror

CFLOS4D
(586)

CFARC
(586)

Parameters
Site times
Site locations
Mean sky cover
and
Scale distance
Parameters
Site locations

FOURIER

SDIS

Backup

TN = OSQ256

SKY COVER
ATLAS

Mean sky cover,
Scale distance,
Options

Climo.
data

Mean sky cover,
Variances,
Options

Fig. 4 AFGL Cloud Cover Simulation Software Configuration

171

archives. For example, given cloud cover frequencies in Airways form (i.e., Clr, Sct, Bkn, and OVC) or in octas or means and variances from tables or other sources, hourly scale distances and mean sky covers are computed and stored for model input. Option flags can be set prior to program execution to inform the program concerning the form of the data.

Program CFLOS4D, version 586, (month 5, year 1986) simulates cloud-free lines of sight and produces downtime statistics for GBL systems for one to multiple sites. The line of sight is viewed from the site to a geostationary satellite relay mirror. Parameter input to this program consists of geostationary satellite longitude, random number primer, and number of times and years each simulation is to run. Since stochastic processes require many iterations to provide valid statistical results, as many as 20 years of 1 min simulated observations is not an unusual input request to this model. Site names, times, and locations are separate input variables residing on independent data files. Typical output from the program showing downtime duration statistics computed for sites KYUM, KLSV, KCPR, KHMN, and PHNL is shown in Table 1, where:

KYUM - Yuma, AZ   = Station 1

KLSV - Nellis AFB, NV   = Station 2

KCPR - Casper, WY   = Station 3

KHMN - Holloman AFB, NM = Station 4

PHNL - Honolulu, HI   = Station 5.

Program CFARC, version 586, simulates cloud-free lines of arc to an orbiting satellite relay mirror to produce downtime statistics for GBL systems for one to multiple sites. Parameter input to this program is the same as that described for CFLOS4D except satellite inclination, height, and revolution parameters are additional input requirements used to define orbital elements peculiar to a variety of satellites. Latitude-longitude coordinates of selected sites and their names are input through separate files. Output from this program is similar in structure to that shown for program CFLOS4D.

172

Table 1. CFLOS4D Output Example

DOWNTIME DURATION STATISTICS FOR 1 TO 5 SITES
FOR A 1 - YEAR RUN, RUN NO.   1

Station No.	1	2	3	4	5
Duration (min)					
1 - 5	2424	2146	1843	1410	602
6 - 30	2155	1682	1149	830	273
31 - 180	511	381	197	132	24
181 - 360	88	59	10	5	0
361 - 720	38	14	2	2	0
721 - 1440	5	0	0	0	0

1 SITE(S) WAS DOWN WITH A CLOUDY LINE-OF-SIGHT FOR 21.64 PERCENT OF TOTAL

2 SITE(S) WAS DOWN WITH A CLOUDY LINE-OF-SIGHT FOR 14.02 PERCENT OF TOTAL

3 SITE(S) WAS DOWN WITH A CLOUDY LINE-OF-SIGHT FOR 6.47 PERCENT OF TOTAL

4 SITE(S) WAS DOWN WITH A CLOUDY LINE-OF-SIGHT FOR 4.53 PERCENT OF TOTAL

5 SITE(S) WAS DOWN WITH A CLOUDY LINE-OF-SIGHT FOR 1.06 PERCENT OF TOTAL

Program CFLTS is a modified version of CFLOS4D put together for special testing purposes. For example, mean sky covers and scale distances from Columbia, MO over a short time period in the summer were input to this version to compare results with studies made using whole sky camera cloudiness. Further modifications to this version were also initiated to investigate the model's usefulness in mapping clouds over extended areas. Procedures and results of this areal cloud simulation exercise are explained next.

Preliminary areal cloud mapping results were produced by first defining a 30 nm x 30 nm area typical of an observer's sky dome area, that could be stored in a computer as 120 pixels by 120 scan lines. The center of the area was chosen to be located near Hawaii at 22°N, 160°W. The sky cover climatology for this location according to Burger's sky cover atlas for July between 18-20 LST can be generated with a mean sky cover value of 0.5 and a scale distance of .55 km. Inserting these two parameters into Burger's formula for deriving cloud cover frequencies produced a rather dampened bell-shaped distribution typical of the sky cover climatology for this area. Then a portion of the model code that simulates cloudy lines of sight on moving targets was activated, so that whenever the simulator obstructed a pixel (target) with a cloud, the pixel was saturated (black); otherwise it was left blank (white). Spanning the entire area in this manner for a fixed time period of 1 min for 24 min produced pictorial cloud frames like those shown in Fig. 5. Although clouds in this figure exhibit rather straight line geometric shapes, it is thought that simply increasing the number of short waves in the original model will cause the clouds to appear more fragmented and therefore more realistic.

e. Model Validation

This section describes a validation procedure conducted to compare model results with observed periods of sunshine. Various methods have been used by several investigators for validating the AFGL cloud models. STX has been working with AFGL to derive spatial and temporal correlation functions of sunshine data supplied by NOAA to compare with similar functions used in the models. The tape data consist of 1-min observations of sunshine coded 0 when the sun is shining and 1 when the sun is not shining. Strings of
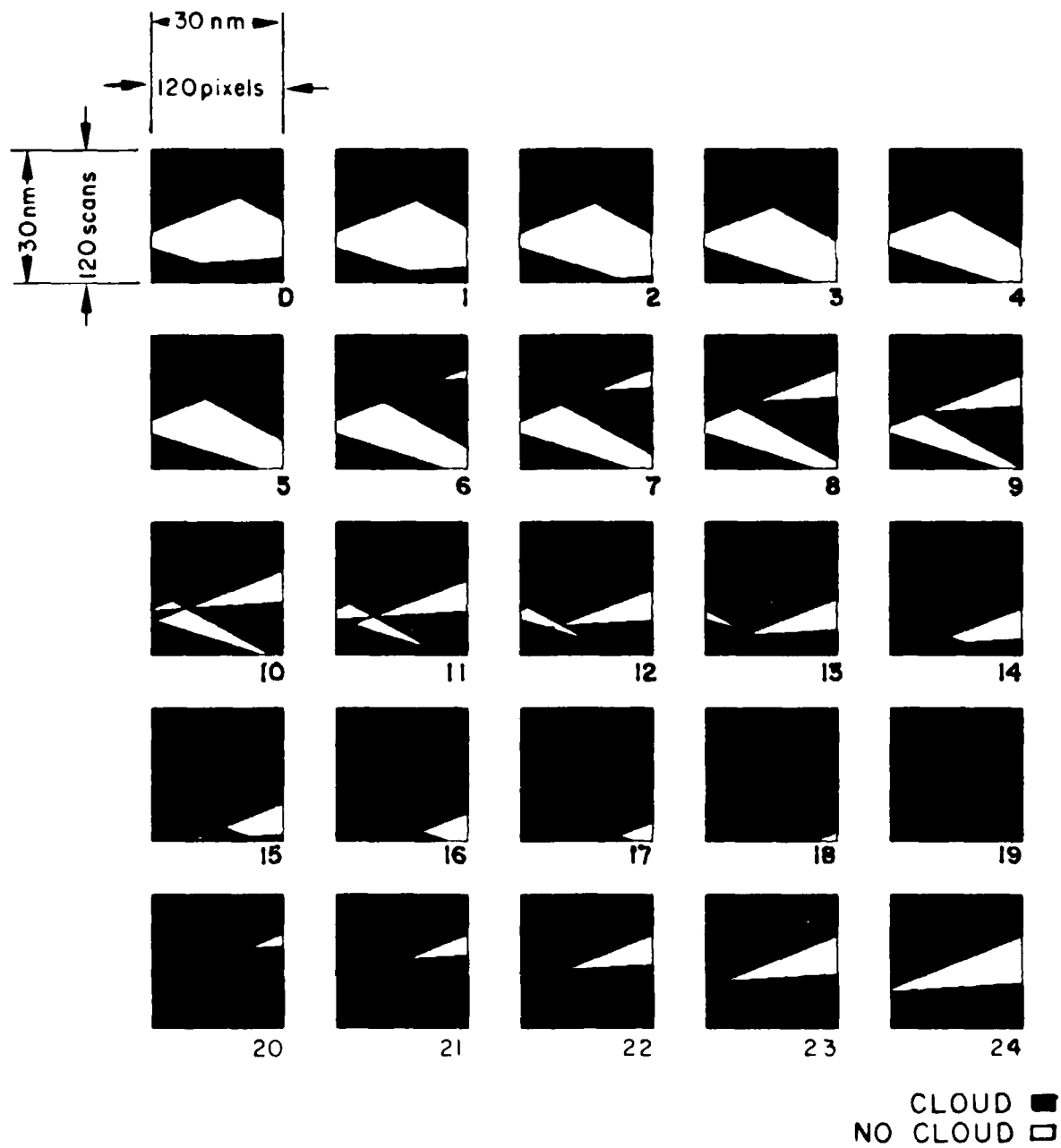
Fig. 5 One-minute Frames of Simulated Areal Cloud Cover over Hawaii

(Typical July case 1800-2000 LST. Mean cloud cover is 0.5 and scale
distance is 0.55 km.)

nines are used to distinguish periods of missing data. The data are for six stations in the southwestern U.S. for January and July between 0900 and 1300 MST. Site names and their yearly periods of record are:

Site Names	Yearly Period of Record
Flagstaff, AZ	1976-1977, 1979-1980
Tucson, AZ	1976-1980
Albuquerque, NM	1936-1940, 1977-1980
Roswell, NM	1976-1980
El Paso, TX	1976-1980
Santa Fe, NM	1936-1940.

The software configuration designed to process the sunshine data for model validation is depicted in Fig. 6.

As shown there, the sunshine data on tape are processed first by a formatting program called READSN to formulate the data onto disk file for interactive processing. Program COT4 was written to compute and output spatial sunshine correlation decay functions between all combination pairs of stations. Program TEMP3 computes temporal sunshine correlation decay at each individual station for each minute of observation between 9 and 13 MST (240 min). Initially, both programs utilized algorithm AS87 (Martinson and Hamdan, 1975; Beardwood, 1977) to estimate these correlations. However, the 1-min data sampling rate proved to be too highly correlated for the algorithm to handle. Therefore, new code was generated in both programs to compute more trustworthy results of correlation using the bivariate normal distribution function. The temporal sunshine correlations for each individual station were saved on separate files for further processing. For example, the file called R176 contained all 1-min sunshine correlations from Roswell, NM; EL76 for El Paso, TX, etc. Because of the high data sampling rate of 1 min per sample, these temporal correlations were of particular interest to the validation procedure. Several steps are discussed next that describe how these temporal sunshine correlations were compared with simulated temporal cloud cover correlations for model validation.
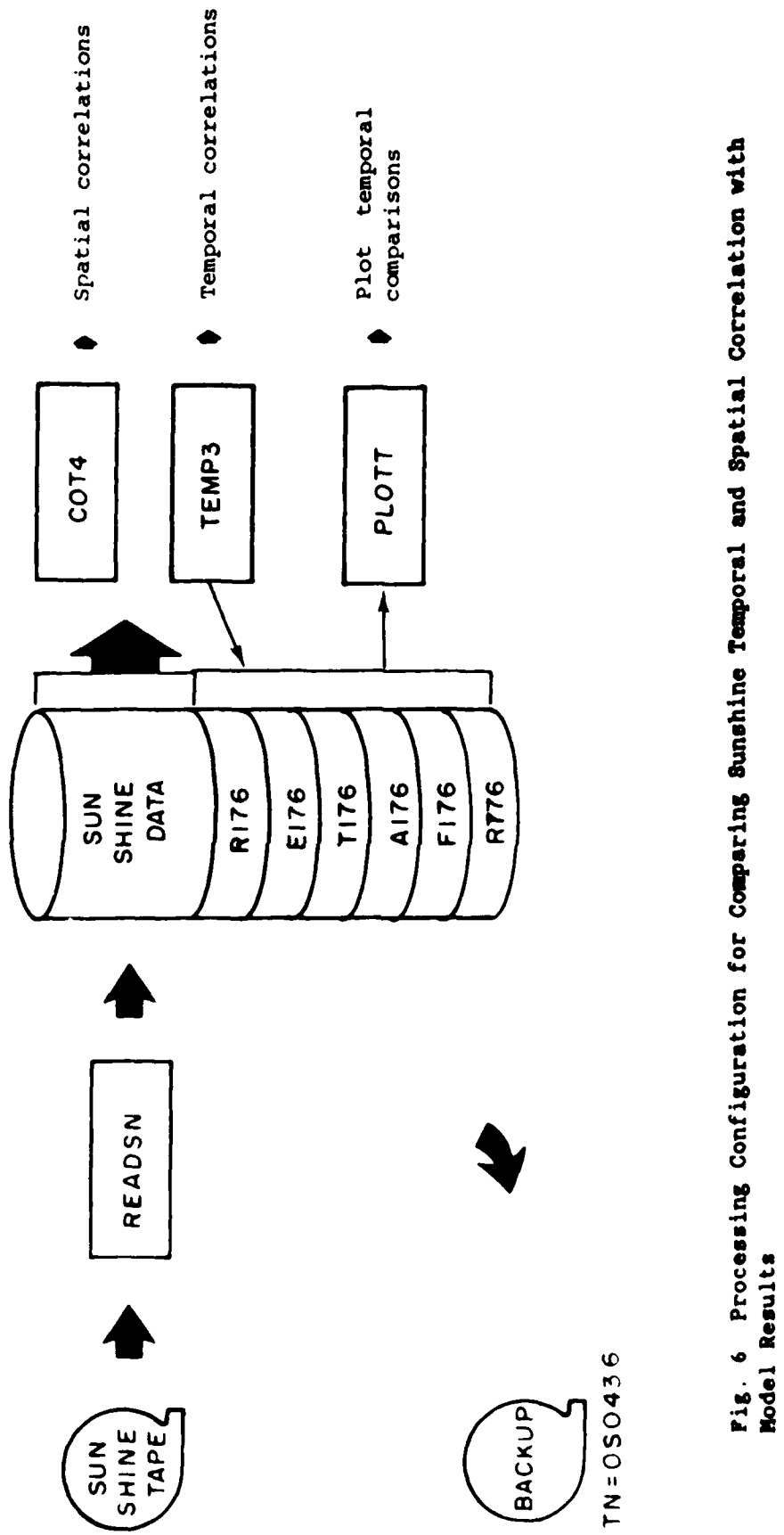
Fig. 6 Processing Configuration for Comparing Sunshine Temporal and Spatial Correlation with Model Results

Program PLOTT was designed to input the stored temporal sunshine
correlations (COR) to compare with simulated temporal cloud cover
correlations (ρ) stochastically generated by the models. For this
comparison, we first define the equation used in the model for computing ρ
to be

$$\rho_{\delta T} = w^2 e^{-\frac{\delta T}{T_s}} + (1 - w^2) e^{-\frac{\delta T}{T_e}} \qquad (1)$$

where

T_s = short relaxation time, taken to be constant at .31 hours

T_e = long relaxation time, taken to be constant at 13 hours

w^2 = a weighting function, given by

$$w^2 = \frac{1.0}{10.25(r_\delta)^{1.4}}$$

where

r_δ = scale distance (km) for given station, month, and hourly
        period; referred to as line-of-sight (LOS) scale distance.

Values of r_δ were hand-computed for each given station for January
and July between 0900 and 1300 MST. When input to PLOTT these values were
used with a reduced version of Eq. (1) in the form

$$\rho_{\delta T} = w^2 (.94766)^{\delta T} + (1 - w^2)(.998719)^{\delta T}$$

to compute temporal cloud cover decay given δT in min. Root mean square
errors between the simulated temporal cloud cover correlations and the
stored temporal sunshine correlations were then computed using

$$RMSE = \sqrt{\frac{1}{239} \sum (\rho_{\delta T} - COR_{\delta T})^2}.$$

Typical results showed rather good agreement between model predictions
and observed sunshine correlations Fig. 7 is an example of the results
plotted out by program PLOTT ior El Paso, TX. The larger error between
model results and sunshine observations at δT greater than about 230 min
is caused by an insufficient number of samples to be statistically valid.

2. Cloud-Free/Cloudy Intervals from Satellite Data

Satellite imagery of the earth's atmosphere in digital form provides an
interesting data source for investigating certain statistics of cloud
populations. Several software packages have been assembled by STX to
process satellite digital data for exploratory cloud research. The
configuration in Fig. 8, from Gerlach (1985), depicts software developed to
process various cloud phenomena from LANDSAT digital tapes and digitized
space shuttle photographs. Shaded portions of this figure show updated
software and newly acquired digital imagery of space shuttle photographs.
The three new cumulus cloud scenes are located in the vicinity of Cape
Canaveral, FL (CCD), Baja California (BCS), and Puerto Rico (PRV).
Techniques for defining cloud/no cloud (CNC) thresholds described in Gerlach
(1985) were used to distinguish clouds in these images from the earth
background. These thresholds are necessary for input to all subsequent
software for accurate cloud detection.

Program IMAGE, originally used to display CNC scenes, was modified to
optimize the image display operation. The new version makes use of a color
graphics terminal (Tektronix 4115) with hardcopy capability to produce
images of digital data interactively. Fig. 9 shows a typical computerized
CNC image of cumulus clouds over Baja California (BCS). Products of this
nature are used to study methods for determining cloud-free or cloudy
intervals as detected from low orbiting earth viewing satellites.

A nomogram has been developed (Snow and Willand, 1986) for use with
tropical and sub tropical cumulus cloud structures to specify the
probability of clear or cloudy intervals of cumuliform cloud fields of any
length as long as the two parameters cloud cover C and recurrence interval L
are known. These parameters were determined from the CNC files but could be
specified in real time given a scanning radiometer of sufficient resolution
onboard a meteorological satellite. In order to determine the sample size

179
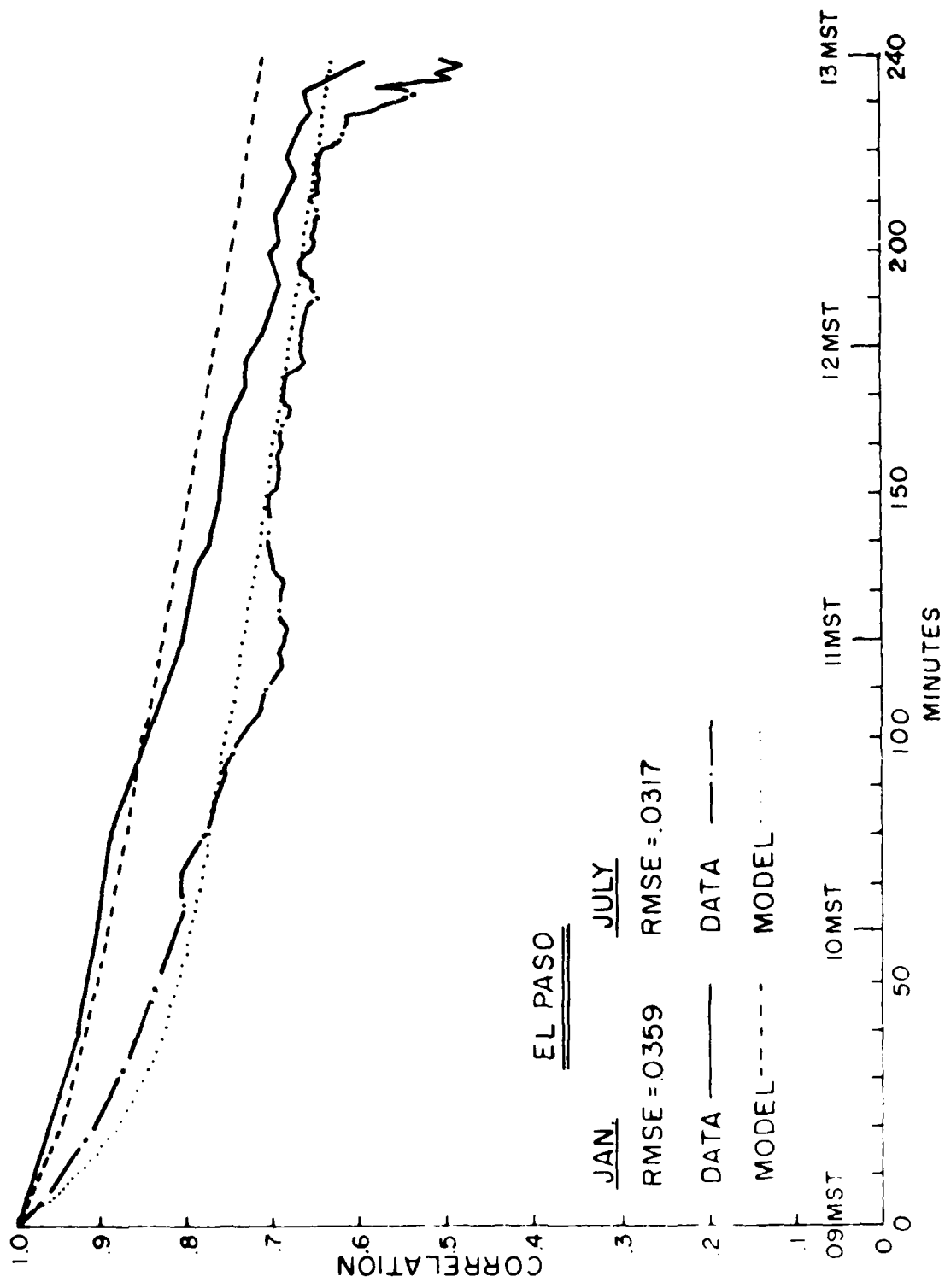
Fig. 7 Comparison of Temporal Sunshine Correlation Decay with Model Results for El Paso
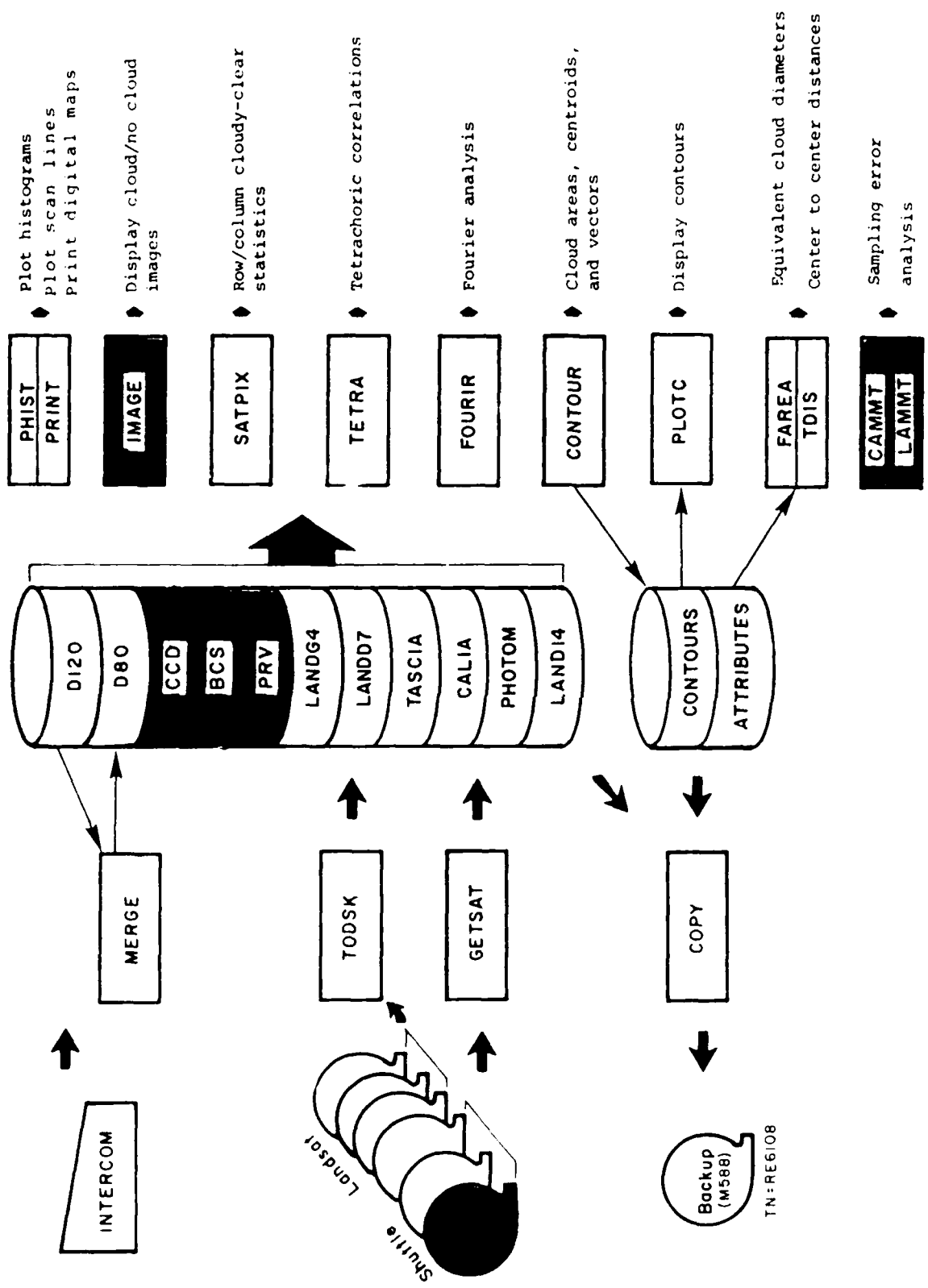
Fig. 8 Updated Configuration for Processing Digitized Cloud Images

0   5   10   15   20   25   30 KM

BCS

CLOUD ☐
NO CLOUD ■
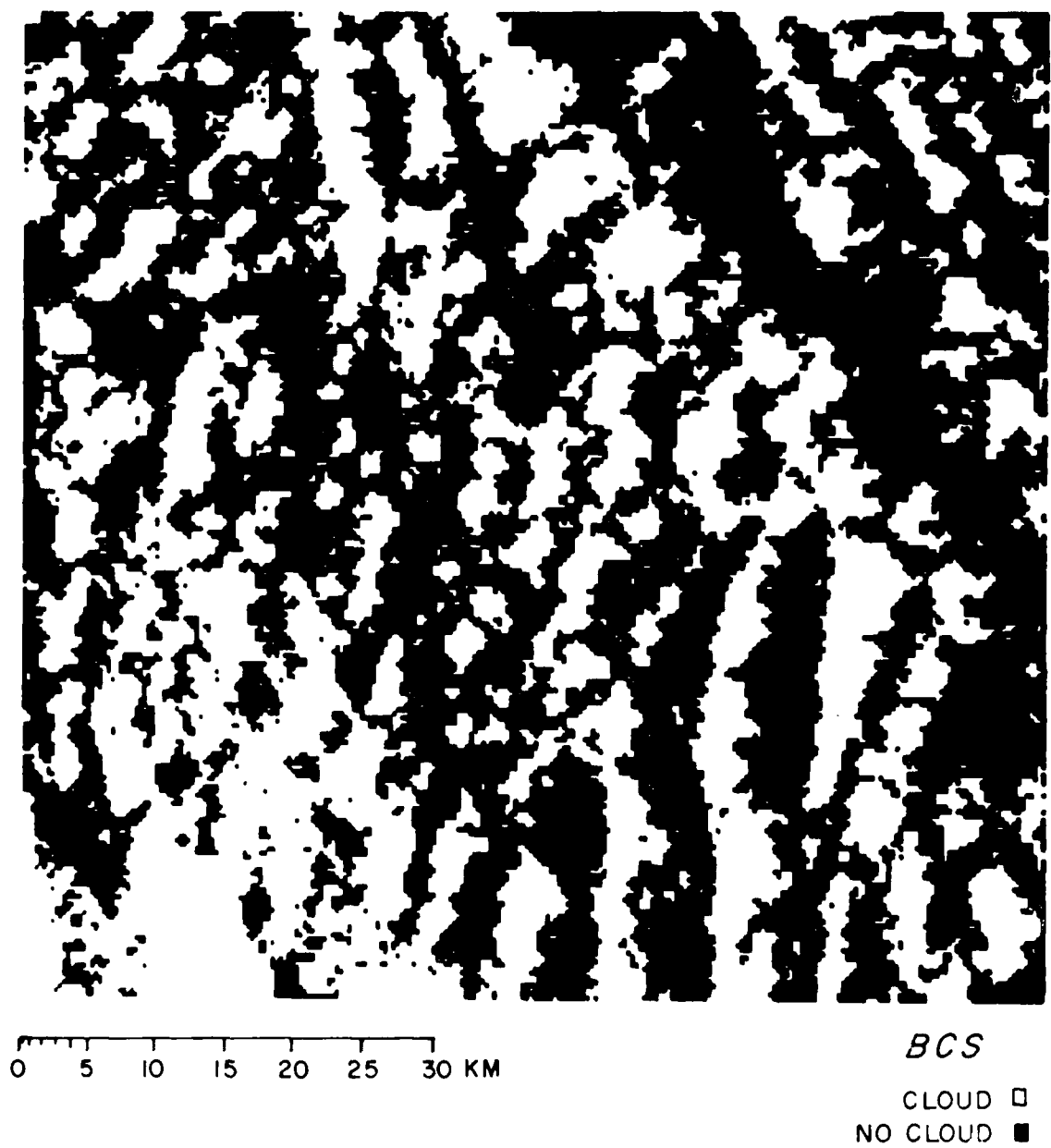
Fig. 9 Computerized CNC Space Shuttle Scene over Baja California (BCS
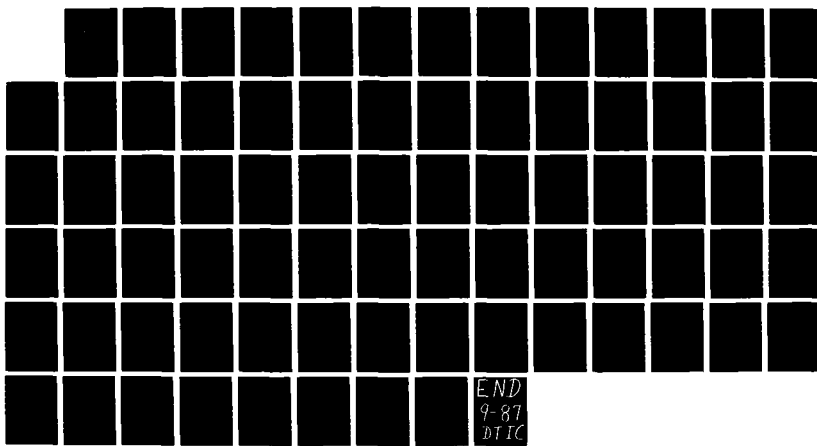
END
9-87
DTIC
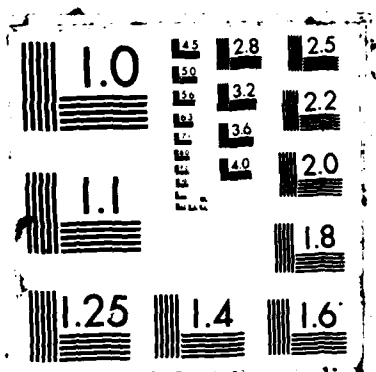
needed to specify the two required parameters C and L, two sampling error programs, CAMMT and LAMMT, were developed. These programs utilize the CMC digitalized imagery similar to that shown in Fig. 9. By varying the size of the sample used to calculate C and L from 10 to 400 pixels, the RMSE of cloud cover (S_C) and cloudy plus cloud-free intervals (S_L) as a function of sample size were determined and are shown in Fig. 10 for four space shuttle digitized photographs. Three of these cases (CCD, BCS, and NDR) show that a sample size of approximately one hundred or so adjacent pixels is necessary before stable estimates of C or L can be obtained. On the other hand, PRV shows that sample size of more than 200 pixels is necessary before reliable parameters are determined. This difference is caused by the fact that the clouds in the PRV scene were stratified and not the small cumulus type found in the other three scenes.

Many more samples of digital satellite imagery are required to verify these results and to extend them to clouds in the polar or sub-polar regions.

3. Rainfall Rate Database Update

A joint effort between AFGL and the National Weather Records Center in Asheville, NC has been underway to expand the data sample of an existing rain rate database used to compile rain rate recurrence statistics. These rainfall observations have been processed by STX to derive rainfall rate recurrence statistics stratified by season for rainfall rate duration times of 5 and 10 min with rates that exceed 0.1, .25, .5, .75, 1.0, and 2.54 mm min^{-1}. The configuration of software developed for processing rainfall data from Urbana, IL described in Gerlach (1985) has been utilized to process rain rate recurrence statistics for these additional sites:

Freiburg, West Germany

Boston, MA

Key West, FL

Denver, CO

Seattle, WA

Omaha, NE

Grand Junction, CO

Yuma, AZ.

183
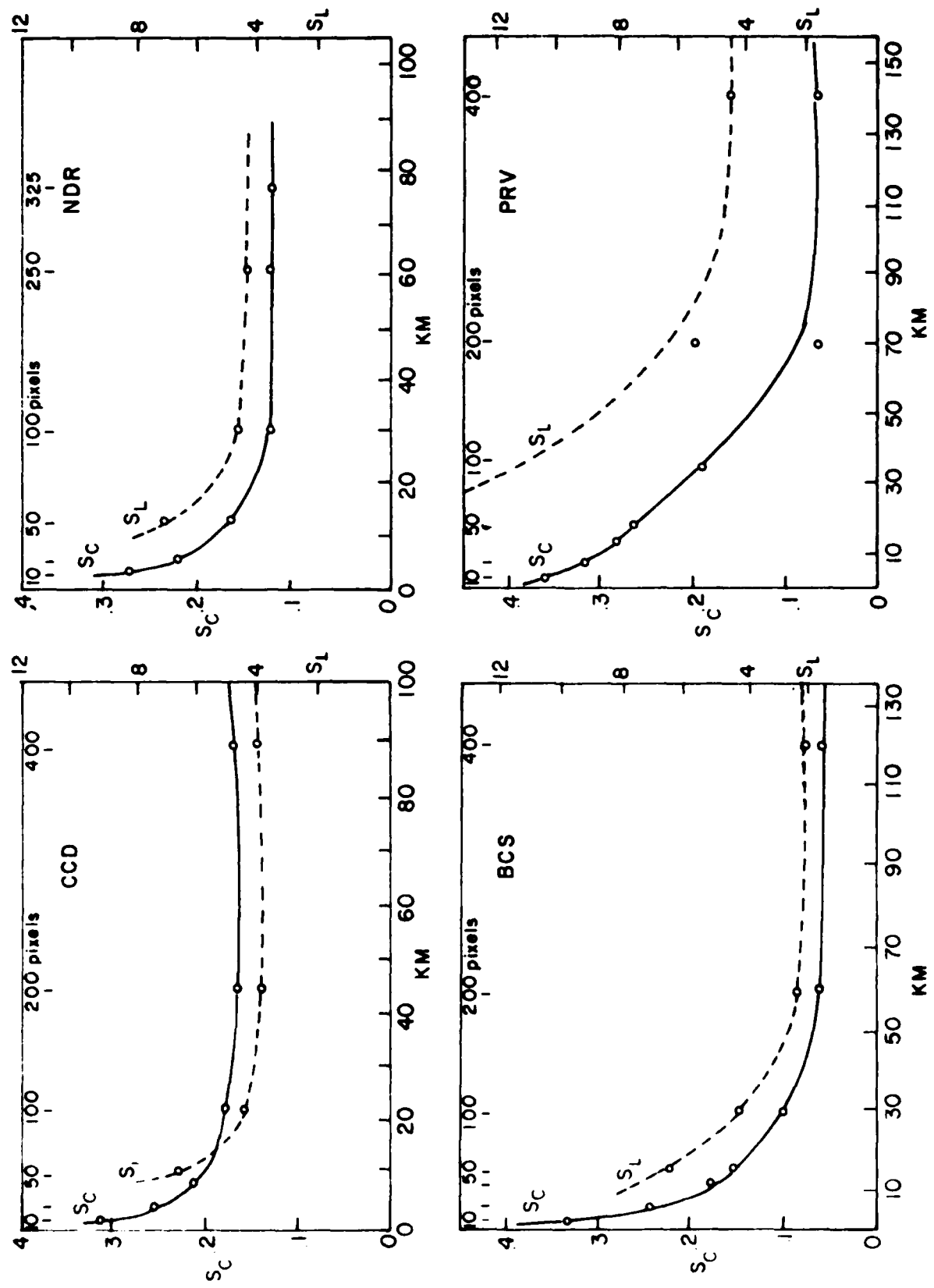
Fig. 10 Sampling Error Analysis from Digitized Space Shuttle Photographs

The Germany data samples were for 1-min intervals observed over a three-year period from January 1978 through December 1980. All additional rainfall rate measurements from U. S. sites were 1-min samples collected from January 1970 through December 1979.

4. References

Beardwood, J. E., 1977: A remark on algorithm AS87: Calculation of polychoric estimate of correlation in contingency tables. _Applied Statistics_, 26, 121.

Boehm, A. R., C. F. Burger, and I. I. Gringorten, 1985: AFGL cloud simulation research: the sawtooth model, sky cover distributions, and cloud-free arcs. _Presentations at the Third Tri-Service Clouds Modeling Workshop_, Air Force Geophysics Laboratory, Hanscom AFB, MA.

Burger, C. F., 1985: _World Atlas of Total Sky Cover_. AFGL-TR-85-0198, Air Force Geophysics Laboratory, Hanscom AFB, MA, ADA170474.

Gringorten, I. I., 1979: Probability models of weather conditions occupying a line or an area. _J. Appl. Meteorol._, 18, 957-977.

Harms, D. E., 1986: _Cloud-Free Line-of-Sight (CFLOS) Simulator for Beam Weapons_. Environmental Technical Applications Center, Air Weather Service, Scott AFB, IL.

Martinson, E. D., and W. A. Hamdan, 1975: Algorithm AS87: Calculation of polychoric estimate of correlation in contingency tables. _Applied Statistics_, 24, 272-278.

Snow, J. W., and J. H. Willand, 1986: Computing clear-interval probabilities for cloud scenes photographed from the space shuttle. _Presentations at the Fourth Tri-Service Clouds Modeling Workshop_, Air Force Geophysics Laboratory, Hanscom AFB, MA.

PART TWO

I. NUMERICAL WEATHER PREDICTION

A. Background

In 1981 STX was called upon to assist the Air Force Geophysics
Laboratory in achieving its goal to improve the numerical forecasting of
atmospheric moisture, especially with regard to cloud formation. The effort
was necessary because, although numerical weather prediction (NWP) had made
significant strides since its inception, the forecasting of water in any
form in the atmosphere was still quite inaccurate. The importance of
moisture as a predictant is obvious. In fact, most of one's conception of
what constitutes "weather" involves moisture in one of its states. Yet it
has remained elusive to forecasters because of several factors, not the
least of which is the difficulty in obtaining an accurate measurement of its
dispersion in the atmosphere. Water vapor is, all in all, only a trace
constituent of the atmosphere. Obtaining a quantitative assessment of its
three-dimensional distribution is dependent on a variety of unreliable
instruments designed to measure one or another moisture parameter. Even
when the measurements are accurate, there is still a need to analyze them in
a manner suitable for NWP. This analysis must take into account the
structure and scaling of moisture as depicted by the model doing the
forecasting. These may differ from the scales and dynamic structures of
other variables such as wind velocities and temperatures. Once properly
analyzed, the model must also predict with precision the physical and
dynamical processes that affect moisture. In the case of moisture, the
physics can be quite complex, taking into account changes of state and the
physical processes that effect them.

AFGL's efforts in improving moisture forecasting have been in
developing a global spectral model (GSM) to experiment and test various
improvements and innovations in the field of numerical prediction. This was
a fundamental change in AFGL's orientation of research, which had previously
focused on improving various aspects of numerical forecasting but without
invoking specific numerical models. Conditions that allowed this change of

direction were governed by developments in computational capabilities at AFGL, and indeed throughout the scientific world. Whereas in previous years only large institutions with plentiful resources were able to undertake the development and execution of numerical models, the revolution in computer technology in recent years led to a proliferation of numerical models among smaller institutions.

In support of AFGL's activity in numerical model development, STX was asked first to develop an objective analysis and initialization scheme and, second, to construct a flexible, regional model that would work in tandem with the GSM, yet would allow concentration in certain geographic areas with greater resolution than available with the GSM. These tasks were undertaken by STX and have resulted in completion of an objective analysis procedure and a regional model with a selection of numerical options.

B. Objective Analysis and Initialization

Because numerical models require initial conditions, an analysis of observations is necessary for numerical forecasts. The main task of the analyzer is to represent an array of variables on a given mesh of grid points by operating on a set of dispersed observations made by a variety of instruments. If the task is to be performed manually, the analyst has to use his personal judgment as to which observations to accept and how to weight their impact on various grid points. Upon completion of his analysis, the gridded data may still be unsuitable for a given forecast model because of the sampling size and distribution of the observations vs. the scales of the model. The process of adjusting the data to the scales of the model is known as initialization and is an important part in the preparation of data for forecasting.

Research performed by STX took two different tracks in formulating an objective analysis procedure. The first built upon the experience of the National Meteorological Center (NMC) by adapting its optimum interpolation (OI) method to the AFGL model. This led to the AFGL Statistical Analysis Program (ASAP), which eventually included updates in the handling of moisture. The other track led to a more theoretical investigation of the possibilities of combining the analysis procedure with the initialization

187

process. This could be accomplished by fitting the observations directly to normal mode functions that define the linearized state of the model. Although some intriguing results were found from the latter study, no practical application was formulated at the time of its completion.

1. ASAP

The OI procedures of the ASAP code are based on the NMC procedures outlined by Bergman (1979) and updated by Dey and Morone (1985). In fact, the initial procedure was almost completely a copy of Bergman's methods, but modifications were necessary in order to bring the analysis procedure in line with the AFGL model and make it compatible with the AFGL computer system. The moisture analysis was updated as well, in order to further AFGL's goal of better moisture forecasts.

The ASAP procedure is based on the updating of first-guess values of winds, temperatures, humidity, and surface pressure by analyzing residuals, i.e., differences between first-guess values and observations. The analysis is performed at each grid point where a 6 h forecast is used as the first guess. Forecasts are also interpolated to the observation sites to obtain residuals. The residuals are then evaluated as to their worth by taking into consideration various factors including their distance from the grid point, the instrument supplying the observation, the expected deviation from the forecast, etc. Certain residuals are discarded because of unreliability or because they exceed certain error checks or because they do not correlate well with other observations in the area. Those that are retained are given weights that are computed from statistical considerations and the resulting consummate residual added to the first guess to give an optimum grid value. Winds and temperatures are related through geostrophy over much of the globe and are, therefore, cross-correlated so that corrections to each of them are made through observations of the other. Moisture, however, is analyzed univariately and can only use moisture observations for updating.

Despite the straightforward appearance of the procedure, several experiments had to be conducted in order to arrive at the final product. Bergman (1979) himself admits that there are shortcomings to his method and

some of these problems cropped up in the development of ASAP. For instance, ASAP does its analysis on the σ-layers where the first-guess values are normally found. On the other hand, it took several iterations to determine that the analyzed values should not be vertically interpolated to new pressure surfaces, once the surface pressure had been updated. In the end the surface pressure analysis had to be discarded because of economy and an interpolation (extrapolation) scheme substituted to derive updated surface pressure values. That decision did not impact the forecast much, however, because the initialization procedure destroyed most of the changes calculated during the surface pressure analysis. Many other adjustments had to be made to the procedure in order to allow proper economy while maintaining sufficient accuracy.

The moisture analysis upgraded WMC's conventional analysis by allowing more types of observations into the analysis. WMC's sources of humidity measurements in the upper air come from rawinsondes, aircraft measurements, and satellite observations. ASAP allowed for humidity information inferred from surface humidity and cloud analyses (3DNeph). Experiments held out little promise for humidities inferred only from surface measurements but did indicate that cloud analyses are of some benefit.

The ASAP package as furnished by STX seems to provide an analysis comparable to those of other organizations. Comparisons with FGGE III-A analyses showed that ASAP produced heights that were closer to observed heights but wind velocities that were further from observed winds than FGGE III-A. Humidity analyses did show marked improvement, but they seemed to have little effect on forecasts of moisture. The AFGL GSM, like most global models, seems to ignore initial distribution of humidity, quickly substituting a favored state, as pointed out by Smagorinsky et al. (1970). To overcome this shortcoming, an upgrading of model physics and dynamical structure is required.

2. Fitting Functions

After an objective analysis has been performed, gridded data must still be prepared for a model by initialization. This rule applies as well to

ASAP, where, it was noted, initialization made a separate surface pressure analysis superfluous. Initialization balances the fields of mass and motion so as to avoid initial high-frequency waves that can produce unwanted computational modes in the forecast. Objective analysis does not normally take into consideration the model structure when trying to determine the values at the grid points. It is therefore necessary to readjust the values so that the surface pressure and σ-layer heights are in balance with the winds at the outset. But it seems, then, that the two processes can at times be at odds with each other. STX looked into the possibility of combining objective analysis and initialization so that what was transferred to the grid points contained information relevant only to the scales of the model.

The development of the method proceeded through several stages. First, the idea of fitting randomly dispersed observations to a set of analytic functions was tested in one dimension. Baer and Tribia (1976) had carried out a similar study. Their study and STX's study concluded that distribution of data, rather than quantity of data, was the more important factor in providing an accurate fit. With that in mind, an attempt was made to fashion a set of functions that could best serve the purpose of streamlining the combined objective analysis/initialization package. The first choice was a set of Hough functions, which are the normal modes of the linearized shallow water equations, because these were used by NMC to serve as a mechanism for initialization during the early 1970's (Cooley, 1974). NMC, after performing an objective analysis, projected the gridded data onto Hough functions, which are frequency dependent, and eliminated the high frequency modes. STX attempted to circumvent the two-step procedure by fitting the observations directly to the Hough functions. Only the largest-scale (external) modes were used for the study. It was soon recognized that the fitting method itself was a major issue that had to be faced before developing the full procedure.

When dealing with gridded data, the orthogonality of the Hough functions could be exploited, and appropriate coefficients for the functions could be obtained readily. But when the data are randomly distributed, the Hough functions (vectors, in the finite sense) are no longer orthogonal, and

190

it is not clear how best to represent the data in terms of expansions of these Hough vectors. The most straightforward method is a least-squares fit, which indeed was attempted. But this fit was found to be very sensitive to distributions, uneconomical, and inherently ill-conditioned. When the fitting was changed to account only for residuals and the resultant fits added to first-guess values at the grid points, the results improved somewhat but the fitting procedure was still too sensitive to distribution. A better and more economical method of fitting was found by initiating what Holmström (1963) termed a "finality" procedure, where sequential contributions from previous Hough vectors are subtracted from the current one, akin to what one does, by analogy, in long division. This procedure is well-conditioned but depends significantly on the ordering of the vectors. One would hope that the low frequency vectors contribute the most and should thus appear first, but there is no assurance that this is always the case. In any event, the procedure worked well under limited testing with high quality observational data.

As a further demonstration, STX attempted to carry out a similar experiment with the model's normal modes, which are currently used for initialization at NMC as proposed by Ballish (1980). But a new element was inserted to help draw the analyzed values even closer to the large scale. After the analysis, the gridded data were initialized by Ballish's method to remove any remaining high frequency tendencies. Then the data were reintroduced as a first guess and the procedure begun anew. It was hoped that after a few iterations, the data would converge to the meteorologically significant "slow" mode, i.e., the large scale structure defined by the model. This idea was first proposed by Williamson and Daley (1983) in the context of an OI procedure.

Thus an experiment was conducted, where a 12 h forecast was produced by the GSM to serve as an initial guess field. The spectral fields were connected to gridded data and to first-guess values at observation sites to obtain the residuals. The residuals at the observation sites were projected onto eight vertical modes from the model's normal mode structure. The projected residuals were then fit to the horizontal mode functions by Holmström's finality method. The normal mode functions were then expanded

191

at the grid points to give the analyzed residuals which were added to the first-guess field. A normal mode initialization was performed on the field and the resulting updated field substituted for the first-guess for the next iteration. The procedure, however, did not converge and the departure from the observations increased at each iteration. Even worse, the first-guess values were closer to the observations than the final analysis, rendering the analysis nearly useless. Although several areas for improvement were defined, the study was ended in order to allow for concentration on ASAP and the development of a regional model.

C. Regional Model Development

Once the studies on objective analysis and initialization were completed, STX was asked to formulate a limited-area model that could be run in conjunction with the GSM to forecast weather phenomena, especially moisture-related phenomena, in concentrated geographical areas. The model was also to be flexible and modular, allowing its user to choose from among several temporal and horizontal differencing schemes and physical parameterizations.

STX began to fashion its relocatable limited-area model (RLAM) by translating a generalized set of equations to code. These are the basic equations of motion, thermodynamics, continuity, and moisture processes in finite difference form but with flexible treatment of the differencing scheme, time-stepping, and physical parameterizations. A pre-processor was developed that defines the domain, initial conditions, and location-dependent temporal constants. It always defines the domain as a rectangle drawn on some projection. There are four possible projections: mercator, Lambert, polar stereographic, and latitude-longitude. The first three are conformal and only one map factor is necessary. The last requires a latitudinal and longitudinal map factor. Thus, the generalized equations in the model contain two map factors which are set equal to each other in the conformal mappings. The initial conditions are derived from the GSM or any spectral field by expanding the variables (wind velocities, temperature, moisture,

and surface pressure) at the appropriate grid points. The expansion is streamlined by converting the spectral coefficients to coefficients of polynomials in sine of latitude and expanding the polynomials at the grid points. The variables may all be expanded at the same points, or, in the case of staggered grids, different variables may be defined on different grids. In the model, all equations are in terms of a staggered grid, with unstaggered grids a special case of staggering.

Once the initial field and its companion time-independent variables are defined, the model begins its forecast. The objective of designing a modular construction was based on the necessity of conducting various experiments with the model as a research vehicle. In the past, it was common practice to contrast various physical parameterizations by repeating forecasts while changing parameters. It was felt that both the numerics and the physical parameterizations should be subject to various options in a well-designed set of model experiments. The model was therefore built with its selections to facilitate numerical experiments. To this end, the model has been developed to where it will allow second-order, fourth-order, or fourth-order compact horizontal differencing; Brown and Campana (1978), leap-frog, or semi-implicit time stepping; and low- or high-order diffusion and smoothing. The physical processes were modeled after those found in NMC's quasi-Lagrangian nested grid model (QNGM) as described by Mathur (1983). The processes included dry and moist convection and boundary layer fluxes. Provision has been made to allow substitutions with other physical parameterizations, if desired.

To act as a baseline for comparison, the QNGM was obtained and adjusted to run on the AFGL computer system. Provisions were made to take initial conditions from the RLAM and use them for the QNGM and vice versa. Inter-comparisons could thus be made between the two models. It was found that small domains, though beneficial when working with limited computer facilities, produced unrealistic results with the QNGM, because the QNGM used an extensive boundary region where it heavily damped all variables. In small domains with about 500 grid points, most of the domain was taken up by boundary points and could not be realistically compared with the RLAM forecasts. Expanding the domain and/or increasing the number of grid points helped substantially in the comparison of the two models.

Results from several tests of the RLAM showed that its numerical options did not function well under all combinations. For certain horizontal differencing schemes, only certain types of smoothing or diffusion allowed the model to remain stable for the duration of the forecast (mostly 24 h). The fourth-order compact scheme in particular retained stability only when accompanied by high-order smoothing at each time step. This, in turn, oversmoothed the field and made it depart significantly from the GSM and other RLAM forecasts. It would be advantageous to discover a set of circumstances for which all combinations would remain stable. Experiments could then be performed to assess the differences between forecasts made with particular combinations. Yet, despite this drawback, the RLAM has shown itself to be an efficient vehicle for numerical experimentation in local regions. It would be of value, in fact, if elements of ASAP were introduced to improve the initial depiction of moisture and to see whether any improvements in moisture forecasts result.

D. References

Baer, F., and J. J. Tribia, 1976: Spectral fidelity of gappy data. Tellus, 28, 215-227.

Ballish, B. A., 1980: Initialization, Theory, and Application to the NMC Spectral Model. Ph.D. Thesis, University of Maryland, 151 pp.

Bergman, K. H., 1979: Multivariate analysis of temperatures and winds using optimum interpolation. Mon. Wea. Rev., 107, 1423-1444.

Brown, J. A., Jr., and K. A. Campana, 1978: An economical time-differencing scheme for numerical weather prediction. Mon. Wea. Rev., 106, 1125-1136.

Cooley, D. S., 1974: A Description of the Flattery Global Analysis Method-No. 1. Tech. Proc. Bull. No. 105, NWS-NOAA, 9 pp. [Available from National Meteorological Center, World Weather Building, Camp Springs, MD 20233.]

Dey, C. H., and L. L. Morone, 1985: Evolution of the National Meteorological Center global data assimilation system: January 1982-December 1983. Mon Wea. Rev., 113, 304-318.

Holmström, J., 1963: On a method for parametric representation of the state of the atmosphere. Tellus, 15, 127-149.

Mathur, M. B., 1983: A quasi-Lagrangian regional model designed for operational weather prediction. _Mon. Wea. Rev._, 111, 2087-2098.

Smagorinsky, J., K. Miyakoda, and R. F. Strickler, 1970: The relative importance of variables in initial conditions for dynamic weather prediction. _Tellus_, 22, 141-157.

Williamson, D. L., and R. Daley, 1983: A unified analysis-initialization technique. _Mon. Wea. Rev._, 111, 1517-1536.

B. SASC Technologies, Inc. Bibliography

Halberstam, I. M., 1981: _An Investigation of Three Methods for Spectral Representation of Randomly Distributed Data_. AFGL-TR-81-0234, Contract No. F19628-81-C-0039, Systems and Applied Sciences Corporation, ADA111854.

Norquist, D. C., and C. Johnson, 1982: _Spectral Characteristics of the Global Moisture Distribution and Their Importance in Objective Analysis of Moisture for NWP Models_. AFGL-TR-82-0190, Contract No. F19628-82 C 0023, Systems and Applied Sciences Corporation, ADA120397.

Halberstam, I. M., and S.-L. Tung, 1983: Objective analysis using orthogonalized discrete Hough function vectors. _Preprints_, Sixth Conference on Numerical Weather Prediction, Omaha; AMS, Boston, 171-174.

Halberstam, I. M., C. Johnson, D. C. Norquist, and S.-L. Tung, 1984: _Two Methods of Global Data Assimilation_. AFGL-TR-84-0260, Contract No. F19628-82-C-0023, Systems and Applied Sciences Corporation,ADA155981.

Halberstam, I. M., and S.-L. Tung, 1984: Objective analysis using Hough vectors evaluated at irregularly spaced locations. _Mon. Wea. Rev._, 112, 1804-1817.

Halberstam, I. M., 1984: Data assimilation, in Summary of workshop on global NWP cloud modeling. _Bull. Am. Meteor. Soc._, 65, 709-710.

Norquist, D. C., 1984: _Users Guide for Optimum Interpolation Model of Global Data Assimilation_. AFGL-TR-84-0290, Contract No. F19628-82-C 0023, Systems and Applied Sciences Corporation, ADA155929.

Tung, S.-L., 1985: _Users Guide for Normal Mode Objective Analysis of Global Data Assimilation_. AFGL-TR-85-0042, Contract No. F19628-82-C-0023, Systems and Applied Sciences Corporation, ADA160373.

Halberstam, T. M., and S.-L. Tung, 1985: Normal mode functions as fitting functions for FGGE observations in an objective analysis procedure. Preprints, Seventh Conference on Numerical Weather Prediction, Montreal; AMS, Boston, 483-485.

Halberstam, I. M., 1985: Polynomials as a substitute for Legendre functions in spectral models. Submitted to Mon. Wea. Rev.

Tung, S.-L., I. M. Halberstam, and C. Johnson, 1986: Towards the development of an improved modular limited-area model. PSMP Report Series, No. 19, WMO/TD-NO. 114.

Tung, S.-L., I. M. Halberstam, and C. Johnson, 1986: Development of an improved modular relocatable limited area model. Submitted to the Special Volume of the Journal of the Meteorological Society of Japan.

Norquist, D. C., 1986: Alternative forms of humidity information in global data assimilation. Submitted to Mon. Wea. Rev.

Norquist, D. C., 1986: Alternative Forms of Moisture Information in 4-D Data Assimilation. AFGL-TR-86-0194, Contract No. F19628-82-C-0023, SASC Technologies, Inc. ADA179792

II. MESOSCALE FORECASTING

A. Introduction

To meet requirements for accurate and timely reporting of airfield weather conditions, the Air Weather Service (AWS) initiated a plan to modernize its base level weather support for the 1980's. The plan was implemented through a program known as the Automated Weather Distribution System (AWDS). AWDS was designed to replace the manual, labor-intensive weather support function with one in which environmental data and products would be acquired, stored, displayed, analyzed, and forecast through modernized computer and dedicated communication systems. Once fully implemented, AWDS would provide support to base weather stations worldwide and to deployed Air Force and Army tactical units.

The shift in focus of AWDS from a primarily human to a computer-oriented environment raised concern over the potential of saturating the user (meteorologist) with more information than could be handled efficiently. This concern was rooted in communication advancements that have made meteorological data from a number of sources routinely available on computer systems and advancements in interactive graphics display systems that facilitate a seemingly endless number of ways data can be plotted, displayed, analyzed, and manipulated. This potential is realized more fully on an operational basis when a forecaster is faced with a complicated weather scenario that requires preparation or updating of short-range terminal forecasts for one or more locations.

With this concern in mind, a research and development study was undertaken at AFGL between 1982 and 1984 to examine the potential benefits and/or problems introduced with computer-driven interactive graphics and video display systems in the preparation and monitoring of short-range terminal forecasts. STX focused on research into the kinds of data, displays, and capabilities applicable to the AWDS scenario and on a broader scale to interactive weather forecasting facilities in general. The work effort was considerable, culminating in a number of so-called Mesoscale Forecasting Experiments (MFE) conducted between 1982 and 1984. These experiments were designed to assess: 1) the value of certain mesoscale objective plot, analysis, and forecast assistance procedures in the

197

preparation of short-range terminal forecasts; 2) the value of certain remotely sensed data in short-range terminal forecasting; 3) the relative difficulty in formulating certain forecasts (elements) using an interactive graphics system; and 4) the performance of forecasters, in weather episodes exhibiting substantial mesoscale variability, in generating both numerical (deterministic) and probabilistic terminal forecasts using an interactive graphics system.

This retrospect describes STX research against the above objectives. In addition, a related study that evolved from this research is included for completeness.

B. Man-computer Interactive Data Access System (McIDAS)

The basic resource for technique development in mesoscale forecasting at AFGL was the Man-computer Interactive Data Access System (McIDAS), similar in hardware and software to the one developed at the University of Wisconsin. The AFGL McIDAS consisted of a mode A geosynchronous satellite ground station, Harris 6024/5 minicomputer, Idetik digital video storage system, Suomi/Sony cassette archive, and two workstations each consisting of an alphanumeric terminal and a video/graphics display monitor. The AFGL McIDAS was well suited to simulate aspects of an interactive minicomputer-based system envisioned for AWDS because it had access to most of the data that would be available through AWDS and because of its interactive graphics and video display capabilities. Conventional observational data were routinely ingested from the FAA WB604 data line and then decoded and archived for later use. Geosynchronous satellite information consisting of visible (daytime only) and infrared image data and ephemeris data was available in real time normally every half-hour. Automated plotting and contoured analysis of conventional surface and upper air data was performed using McIDAS graphics capability. On each terminal an electronic cursor controlled by joysticks permitted interactive data retrieval and graphics modification. Once loaded onto the system, satellite imagery was available for precise geographical and political gridding, enhancement and contouring, sequencing to form animated time series loops for cloud tracking or translation purposes, and as a base for overlays of conventional data to form integrated displays.

C. Mesoscale Forecasting Experiment (MFE)

The procedure established to assess aspects of interactive systems,
data sources, and weather-user effectiveness was to conduct a forecast test
experiment addressing a particular set of short-range terminal forecasting
requirements using research meteorologists. Two Mesoscale Forecasting
Experiments (MFE) were established; the first was conducted in the summer of
1982, the second in the summer of 1983. Results of the 1982 and 1983 tests
were reported in Chisholm and Jackson (1984); an initial assessment based on
the 1982 MFE was reported earlier in Chisholm et al. (1983).

In order to conduct the tests most efficiently, episodes used in the
forecast sessions were chosen from cyclogenesis and cold front cases
archived during the 1981-1982 and 1982-1983 winter and early spring storm
seasons in the Northeast U.S. The episodes typically displayed rapidly
changing weather conditions, such as significant wind shifts, changes in
cloud cover, alterations in ceiling height, and onset (or termination) of
precipitation. Such short time scale variabilities constituted the most
rigorous bases for evaluating the sensitivity and practicality of newly
developed and existing mesoscale forecasting methods.

The MFE tests were conducted so that the time available for forecast
preparation was constrained to real time limits. The forecasters had a
singular task and objective: to prepare terminal forecasts for two locations
using as many of the resources available to them through McIDAS, for the
purpose of evaluating new and standard products and data sources. One
forecast experiment was conducted each week (typically in two 40-hr periods
per forecaster, with three forecasters working as a team to evaluate the
weather situation but independently preparing their forecasts). At the
conclusion of each case, each forecaster completed evaluation forms in which
the products used and forecast aspects of the case were assessed. These
forms represented the basis for a critique of the experiments in light of
the purposes stated in the Introduction.

Forecasters were required to predict (on an hourly cycle) wind speed
and direction, total cloud amount, ceiling height and 6-hr precipitation
amount for periods of 1, 2, 4 and n hours ahead. The period n was chosen at
each forecast time to verify at the nearest MOS valid forecast period. This

was done so that MOS could be used as an additional forecaster for certain parameters and as guidance for the other participating forecasters. Forecasts for two airfield locations were required for each case; the specific locations were predicated on the availability of FOUS bulletins containing MOS, LFM-II guidance, and 3-D trajectory forecasts that were made available for guidance purposes. Logan International Airport (BOS), being the closest candidate location to AFGL, was forecast in each of the cases used in the test. The second location varied among airports in Connecticut, New York, and Rhode Island depending on factors related to the episode being tested.

For wind speed and direction, a numerical forecast was prepared. With each of the other forecast variables, both categorical and probability forecasts were prepared. Forecasts were entered through the computer-based forecast entry and verification procedure known as the Mesoscale Forecast Facility (MFF). This was a menu-driven interactive package designed to accept individual forecasts through the use of formatted interrogation/response messages via the McIDAS keyboard/alphanumeric CRT terminal interface. After each case, the numerical, categorical, and probability forecasts were verified with the MFF, and accumulated statistics were summarized and made available to forecasters for review. The error statistics calculated were mean absolute error and RMSE for numerical and categorical forecasts, and the p-score, cumulative p-score, and Heidke skill score vs. persistence for probability forecasts. The method of comparison for the study was persistence, measured directly and in sample (unconditional) climatology form.

D. Mesoscale Forecasting - Technique Development

As stated earlier, STX focused on research into the kinds of data, displays, and capabilities that should be supplied to interactive facilities. The research effort produced a number of products that were evaluated over the course of both MFE test periods. They included a fine-scale analysis routine using a five-pass Barnes method with approximately 55 km grid spacing for surface data gridding and contouring, and two data handling procedures displaying surface observations in a time series format. These products were designed to enhance the resolution of small-scale features. Also a number of existing software packages developed

as terminal forecast aids were incorporated on McIDAS for evaluation. These included a cold front decision assistance procedure and the Generalized Exponential Markov (GEM) short-range forecast technique. The McIDAS database was expanded by inclusion of additional sources such as NWS FOUS bulletins, Manually Digitized Radar (MDR), and ship and buoy reports. Routines to analyze and display these data were also developed and evaluated.

A number of products were developed after the MFE tests and thus could not be assessed as to their value. However, they remain important as candidates for planned future tests and are mentioned for historical completeness. They included an objective analysis technique that advects one and two hour old data and analyzes them using a time- and space-weighting method; a routine to display vertical profiles of vertical velocity, vorticity, and divergence using the kinematic approach; and the modification of existing surface and upper air analysis routines to include wet bulb temperature and wet bulb potential temperature, used to help identify and forecast frontal zones.

1. Objective Analysis Techniques

Objective analysis routines for the AFGL McIDAS were developed at the Space Science and Engineering Center of the University of Wisconsin. They employed a technique proposed by Cressman simplified for implementation on a minicomputer. Although the method could be quickly executed on a computer, it tended to smooth out small-scale variations in the data field. Two factors contributed to this tendency: coarse grid spacing and the use of only one iteration or pass by the interpolation routine through the observed data. To reduce smoothing and thereby retain small-scale variation, a new analysis routine was developed to address both of these factors.

Increasing the grid point density, and therefore the resolution of features within it, was accomplished by modifying the grid generating algorithm to allow for smaller grid lengths. On McIDAS, all grids were pseudo-mercator and grid lengths were defined in terms of degrees of latitude. The existing analysis routine, capable of generating grids with grid lengths no smaller than one degree of latitude, was replaced by a routine capable of producing grids with grid lengths as small as one-tenth of a degree.

To exploit this denser grid, a more exhaustive interpolation technique was needed. The method proposed by Barnes was chosen to take advantage of the superior weighting function contained in it. Implementation of the technique included five passes through the data, in which the scan radius was reduced by 20 percent for each pass after the second. Reducing the scan radius had the effect of increasing, with each successive pass, the weight or influence of observations in close proximity to any given grid point, thus maximizing details on a scale approximately a unit grid length. As in the Cressman technique a zero-value initial field was used and the first pass was constrained to include a minimum of four observations in estimating the grid point value. The remaining four passes constituted a successive approximation technique based on the rough field average calculated in the first pass to achieve the final grid point values.

Implementation of finer scale grids and the five-pass Barnes space-weighting interpolation routine was accomplished through development of software on McIDAS. This program was evaluated during the 1982 and 1983 MFEs and found to be one of the most useful products, primarily in forecasting wind speed and direction.

Objective analysis over coastal regions with McIDAS was subject to inconsistencies due primarily to the lack of observational data over coastal waters. To alleviate the problem, software was developed and implemented on McIDAS to routinely decode and store ship and buoy weather observations transmitted over the WB604 data line. Reported data included temperature, dew point, sea surface temperature, pressure, wind speed and direction, and total cloud amount. These data are reported four times daily at 0, 6, 12 and 18 GMT with the text transmitted one and one-half to two hours after observation time. With this new data source to enrich geographically the existing network of surface observation stations, objective analysis routines could include ship and buoy data if the observation time made it appropriate to do so. Thus, development and movement of discontinuities in weather patterns in coastal regions could be detected and monitored as long as adequate maritime data were available.

2. Terminal Forecast Aids

To enhance the utility of the AFGL McIDAS as a terminal forecast facility, several available software packages were implemented and subsequently evaluated during the two MFEs.

A cold front forecast decision assistance procedure developed at AFGL was coded and added to the MFE. A series of menu "pages" directed the forecaster in the use of existing analysis and display programs to locate accurately a front, identify significant weather occurrences, and trace frontal development and movement. Subsequent pages provided forecast guidance based on the data collected. In the experiments of 1982 and 1983, the cold front decision assistance procedure was generally considered to be too time consuming for those forecasters familiar with the interactive capabilities of McIDAS. However, the potential benefit of such a procedure to forecast operations support was recognized in that the procedure could be used to train forecasters unfamiliar with a particular region or in the use of interactive systems.

The Generalized Exponential Markov (GEM) short-range forecast technique developed at the Techniques Development Laboratory (TDL) of the NWS was modified for use on McIDAS. The GEM technique is a fundamental statistical weather forecasting procedure developed by Miller who defines GEM as "a statistical technique for predicting the probability distribution of local surface weather elements hour by hour. It uses only the current local surface weather conditions as predictors. From these probability distributions categorical predictions are made for each surface weather element." For its use in the MFEs, GEM was adapted to generate wind, cloud cover, and ceiling height forecasts which were verified at 1, 2, 4, and 6-hr intervals coincident with MFE verification procedures.

Three factors had to be recognized regarding the application of GEM to the MFE tests. First, GEM is founded on a Markov assumption (that is, the future state is completely determined by the present state and is independent of the way in which the present state has developed). Second, it uses multivariate linear regression equations that were developed from continous observational samples that spanned a 12-year period at a number of locations and thus are climatologically and statistically sound. Third, in the MFE test, it was applied to cases that represented "heavy weather" and

203

did not therefore reflect the characteristics of the full sample from which the GEM statistical operators were developed. It was felt, however, that applying it to demonstrate the general performance of GEM vs. persistence was proper and appropriate.

GEM was incorporated into McIDAS following the 1982 MFE. Thus output from GEM was not available during the experiment. However, the output was available to forecasters as objective terminal forecast guidance during the 1983 MFE and was evaluated concurrently with forecaster results and persistence for a 10-case sample. Results compiled over the course of the two experiments showed that although it yielded skill relative to persistence probability, in general GEM yielded higher RMSE scores than did persistence in its numerical form. Its guidance value was deemed to be minimal in "heavy weather" episodes characteristic of both MFEs.

In 1985, the Eastern Space and Missile Center weather facility requested an evaluation of the GEM technique for possible use as short-range forecast guidance for launch operations at the Kennedy Space Center (KSC). Patrick Air Force Base, FL (COF) was chosen as the location to test GEM since it was the closest station to KSC that routinely reported the weather elements necessary for application of the GEM forecast technique and subsequent verification.

The available hourly observations at COF for July and December 1983 comprised the database used to evaluate GEM. Data taken from 12 GMT through 03 GMT were used to generate GEM forecasts 1, 2, 4, and 6 hr later. For this application GEM generated deterministic surface wind vector forecasts and probability forecasts of cloud cover and ceiling height in the "standard" MOS categories. Conversion from probability to categorical forecasts was based on a simple maximum probability approach. The cloud cover and ceiling probabilities and categorical forecasts and the deterministic wind vector forecasts were verified against observed conditions 1, 2, 4, and 6 hr after forecast times. As in the MFEs, the measures of skill used in the evaluation were RMSE for the deterministic forecasts and the p-score for the probability forecasts. RMSE scores were provided for persistence and the Heidke (or percent improvement) score of GEM relative to persistence was also provided.

Results were similar to those found in the MFE test; that is, differences between GEM and persistence were generally too small to be

statistically significant. Where differences did exist, persistence yielded smaller RMSE scores although with the exception of summertime ceiling height, GEM probability forecasts scored better than persistence probability. For purposes of the study, the results were inconclusive.

A forecast guidance technique to derive cloud cover and precipitation amounts was developed and implemented on McIDAS. The technique represented a combination of methods developed independently in earlier studies. The first calculated a two-dimensional backward trajectory on a single level (700 mb, for example) from objectively analyzed rawinsonde winds. Utilizing a user-specified time range for the trajectory, forecast values interpolated from an objectively analyzed grid and translated to the forecast location could be generated at each hourly trajectory location and then displayed. Any weather element suitable for gridding could be forecast in this manner. The second method estimated cloud cover category and 1-hr precipitation amount from collocated GOES visible and infrared imagery for an area designated by the electronic cursor. The algorithms were developed from a sample of non-convective storms in the fall and early winter of 1980 and applied generalized techniques to normalize for sun angle. By combining these two methods, one could utilize a calculated trajectory to specify six one-hourly upstream locations at which to apply the cloud cover category and 1-hr precipitation estimation technique. The six one-hourly estimates of precipitation amount could then be combined to produce a 6-hr quantitative precipitation forecast (QPF).

In both 1982 and 1983 MFE tests, the product combining these two methods was evaluated for use as well as the 2-D trajectory forecast guidance model without satellite imagery. The combined product was found to be useful in 6-hr quantitative precipitation forecasting, while the 2-D trajectory forecast guidance model provided quantitative guidance on overall timing, hour to hour changes, and development aspects of a particular weather system. Obviously, the further the forecast time was removed from 00/12 GMT (the time of rawinsonde observations) the less reliable this guidance became. One shortcoming in the effective use of this guidance technique was attributed to evolving wind fields that diminished the representativeness of the trajectories. With the combined product, its use was restricted to daytime and even then to the central 75-80 percent of the daylight regime due to the sensitivity of the algorithms to solar angle

variations. Nevertheless, as rated by participating forecasters, the combined product remained as one of the four most useful over the course of both experiments.

3. Time Series Displays

In 1982, two new observation plot routines designed to enhance the depiction of mesoscale detail in emerging weather situations were developed.

The first was a station model time series display that allowed the user to select up to six weather stations and a time corresponding to the end of the series. The surface station model consisted of a predefined number of meteorological elements whose positions remained fixed relative to the model. The parameters included temperature, dewpoint, surface pressure, present weather, cloud cover, and wind speed and direction in symbolic station model format. With proper selection of stations, the plotting model could aid in locating and tracking (hour to hour) synoptic and mesoscale features such as dry lines, lake or sea breezes, and areas of precipitation.

Results of the 1982 MFE showed that the station model time series display was the most useful of the set evaluated for two reasons. First was the ease of specifying the stations to be included and tailoring the display to the current weather situation. Second was the wealth of basic information it provided in a format that facilitated extensive subjective interpretation in tracking one or more weather elements and identifying their spatial extent. Specific application of this product included using the display to resolve the location and movement of inland covergence zones, frontal boundaries, and isallobaric centers which in turn were factored into terminal wind forecasts. It was also used to attempt to reconcile precipitation characteristics to define geographical distribution of precipitation when satellite and/or radar data were not available and hourly observations of precipitation intensity were inconsistent. It was also the most widely used non-satellite product for tracking cloud amount conditions.

The second observation plotting routine developed was a time series line/bar graph display. The line graph format was available for plotting temperature, dewpoint, surface pressure, or wind speed and could accommodate up to 24 hours of data and up to six stations on any one display. The bar

graph format was designed to depict ceiling height and cloud cover, accommodating observations for up to six stations at one time or up to six observations at one station. Multiple cloud layers could be displayed and cloud cover categories were represented with a simple line coding scheme.

The time series line graph display was found to be of some limited value in forecasting wind speed but its potential could not be fully explored due to the forecasting problem addressed during the experiments. On the other hand, the time series bar graph display was heavily relied upon in trying to arrive at ceiling height forecasts.

4. Forecast Guidance Displays

As an interactive aid to formulating short-range forecasts, software was developed to analyze and contour United States Forecast (FOUS) bulletins. These forecasts are derived from output of the Limited Area Fine Mesh Model (LFM-II) run by the National Meteorological Center (NMC). FOUS forecasts are received through the WB604 data line from the 00 GMT and 12 GMT runs of the LFM. Three types of FOUS bulletins (FOUS 12, FOUS 50-57, FOUS 60-78) were routinely decoded and stored in McIDAS. Up to eight forecast periods were stored for each of the three bulletins, the oldest being overwritten by the most recent forecast.

The software developed collected the individual station forecasts decoded by McIDAS and produced an analysis of the forecast data using existing interpolation and contouring software. A two-pass Barnes technique was used to interpolate the data to grid points using a scan radius of one and one-half grid lengths.

FOUS 12 forecasts are based on the regression equations relating the predictand to variables output from the LFM. Model Output Statistics (MOS) forecasts from 67 stations were decoded and made available for analysis. Station distribution for this bulletin is not ideal; certain areas of the U.S. have very dense coverage while other areas have large gaps between forecast stations. This shortcoming had to be considered when MOS analysis was examined. The other FOUS bulletins do not suffer this shortcoming. MOS parameters that could be contoured included 6-hr probability of precipitation, 12-hr probability of precipitation, probability of

thunderstorms, categorical forecasts of snow amount and cloud amount, ceiling heights, visibility, and forecasts of temperature, dewpoint, streamlines, and wind speed.

LFM guidance forecasts (FOUS 60-78) were available from 89 stations in the continental U.S., adjacent coastal waters, and eastern Canada. Forecasts of model layer relative humidities, vertical velocity, lifted index, 1000-500 mb thickness, boundary layer wind speed and streamlines, boundary layer temperature, sea level pressure, and 6-hr accumulated precipitation amounts were available for contouring. The analyses could be displayed for initial time and consecutive 6-hr forecast intervals through 48 hours.

Trajectory forecasts (FOUS 50-57) contain 24-hr forecasts of temperature and dewpoint at 700 mb, 850 mb (except for stations whose elevation is above 850 mb), and the surface, along with a prediction of George's K Index. Three-dimensional positions (latitude, longitude, parcel pressure) are also given at six-hour intervals starting with the predicted parcel origin point at initial time and terminating at the forecast station 24 hours later. In all, 73 stations well distributed around the continental U.S. were available in the FOUS 50-57 bulletins.

The advantages of software developed on McIDAS to analyze and contour FOUS bulletins over the facsimile charts sent by NMC included the ability to analyze forecast parameters at more frequent time intervals, to contour parameters not analyzed by NMC, and to be completely flexible in overlaying different types of parameters. The software was also viewed as a limited backup to the facsimile maps if chart transmission was interrupted.

In addition, a routine was written to plot the predicted trajectory positions available from FOUS 50-57 bulletins. One of the problems forecasters faced in using trajectory forecasts was the difficulty in visualizing the path air parcels were predicted to follow. To alleviate the problem, a graphical representation of the trajectories was developed in which the 6-hourly positions were connected by line segments, solid lines indicating rising motion and dashed lines sinking motion for all applicable trajectories. For a given station the three trajectory forecasts could be displayed on the same map background in order to view the three-dimensional motions at the different levels. Forecasts of parcel pressure would be shown color coded for each of the 6-hourly predicted positions and arrows

208

would indicate the direction of the trajectory as well as the location of
the terminal point for that 6-hr period. Other parameters could be overlaid
on the predicted trajectory to enhance forecast guidance.

The capability to analyze and contour FOUS bulletins was made available
between the 1982 and 1983 experiments. Consequently, its use as a forecast
guidance product was evaluated during the second experiment only. Analyses
of LFM output were used minimally although sometimes it was beneficial
guidance for storm development, movement, and position for the later
forecast periods (4 and n-hr). LFM-based precipitation guidance (FOUS LFM
Guidance and FOUS 12 MOS) provided valuable assistance on the precipitation
potential of a storm system, guidance which forecasters could adjust to
information on actual storm tracking and intensity. The 6-hr QPF FOUS
guidance was found to be more useful than guidance for other forecast
variables. The surface and boundary layer wind vector forecasts presented
in the FOUS bulletins (FOUS 12 MOS and FOUS 60's) were found to provide
useful guidance, especially for the 4 and n-hr forecast intervals. 3-D
trajectory guidance (FOUS 50's) was of limited value due to lack of
timeliness and/or horizontal resolution.

E. An Error Analysis of LFM Forecasts Using FOUS 60-78 Bulletins

With experience gained from the adaptation of FOUS bulletins to a
product evaluated as objective terminal forecast guidance, an independent
study evolved whose purpose was to identify systematic errors in the LFM-II
and to investigate what might be best defined as model bias. Chief
motivation for the study was the continuing need to evaluate short-range
forecast guidance in the preparation of terminal forecasts of wind,
precipitation, ceiling height, and total cloud amount. In broader terms the
results could serve the dual purpose of alerting forecasters to consistent
and systematic model errors and at the same time provide some indication as
to the areas where model physics and procedures might be improved.

Beginning in 1983, McIDAS was used to collect FOUS 60-78 bulletins from
89 stations received twice daily for valid model run times of 00 GMT and 12
GMT. Initially the parameters chosen for error analysis in this study
included mean relative humidity, sea level pressure, 1000-500 mb thickness,

209

boundary layer temperature, and the boundary layer wind in vector form (the boundary layer is defined as the bottom 50 mb of the model atmosphere in the LFM-II). Forecast values for each parameter at each station were obtained from the appropriate location in the FOUS 60-78 bulletin. Verification values were obtained from the initial conditions in the relevant successive FOUS 60-78 bulletins that were derived from the model initial analysis. Parameter forecast errors were accumulated at each of the 89 locations by simply subtracting the verification value from a parameter forecast value. Because verification values were available on a 12-hr cycle, only the 12, 24, 36, and 48 hour forecast errors were analyzed. This procedure was applied to forecasts beginning on 23 November 1982 through 31 March 1983. By calculating the forecast errors in the manner described, a positive number would indicate an overforecast (i.e., the forecast was too warm, too wet, pressure too high, etc.) while a negative number indicated an underforecast (too cold, too dry, pressure too low).

Errors at each of the 89 stations were further stratified into error sums from 00 GMT model runs and 12 GMT model runs. This stratification was selected to examine the sensitivity of the error fields to diurnal variations. For computational simplicity, the analyses required that all variables being evaluated at all 89 FOUS stations be available for the pertinent forecast and verification periods. Any data that were missing from a forecast or verification series eliminated the entire set.

Results from the 1982-1983 winter season showed that indeed there were systematic errors in the model for all parameters considered. Sea level pressure was, on average, forecast too low east of the Rockies and too high west of the Rockies, particularly in the Southwest. The magnitude of the errors increased with forecast length. The pressure error was reflected in the boundary layer wind forecasts with the tendency to forecast too much of a northerly component in the nation's mid-section. Bias for forecasts of 1000-500 mb thickness was relatively small and not strictly related to forecast length. The model was too high (warm) in the central U.S. and too low (cold) west of the Rockies. Model relative humidity was generally forecast higher than observed in the northern Rockies and drier than observed along the Gulf Coast, especially around Florida.

The bias for boundary layer temperature and for boundary layer relative

humidity (and to a lesser degree 1000-500 mb thickness) appeared to be composed of two components, one of which varied diurnally, the other which grew with forecast length. In general, the model was too warm along the Gulf Coast and too cold in the vicinity of the Great Lakes.

In 1984, the study continued with data collected from 1983-1984 cool season (1 October 1983 to 30 April 1984). As in the original study, individual forecast errors for the period of examination were summed and average errors computed using the same methodology as described above. In general, the systematic errors found in LFM-II forecasts for 1983-1984 were very similar to the errors found in the 1982-1983 study. Differences that did exist between the two seasons were generally the magnitude of the errors and not geographical location. The average errors from 1983-1984 were also stratified by month (12 GMT forecasts only) to see if error patterns change coherently over the course of the cool season; however, few coherent trends could be found for most of the variables, although many showed their maximum errors in December.

The similarity of the bias patterns for the two seasons examined suggested that it might be possible to develop a forecast correction technique. The goal of the technique, using the identified error characteristics, was to adjust the model forecasts with the objective of reducing the forecast errors. The technique was devised using 12 GMT forecasts from the 1983-1984 cool season to test the feasibility of the concept.

The technique employed was based on a dynamic error adjustment procedure in which a correction factor was generated for each station, variable, and forecast interval, based on the 10 most recent model runs to determine an average error. The modification procedure was then simply to subtract the correction factor from the variable's forecast value. An objective measure of the value of the modification technique was performed by comparing map average RMSE and standard deviations before and after the correction. Results of applying the correction technique were mixed. Some forecasts were degraded while others (particularly the boundary layer variables) showed a noticeable improvement at some forecast intervals.

The FOUS guidance error study continued into 1985 and 1986 with data collected from 1 October 1984 through 30 November 1985. This phase of the

211

study differed in some respects from previous work in that lower
tropospheric relative humidity was included as an additional parameter in
the error analysis. Also, the analysis was broadened to include forecasts
from the warm season in order to determine if the error patterns changed
significantly over the course of a year. This was accomplished by
stratifying the data into seasonal error sums with the seasons arbitrarily
defined as follows: winter from December 1984-February 1985, spring from
March 1985-May 1985, summer from June 1985-August 1985, and fall from
September 1985-November 1985.

Results from this phase of the study were once again similar to
previous data collected for analysis. Sea level pressure showed a strong
tendency to be underforecast in the central U.S. and overforecast in the
western part of the nation. The magnitude of the errors found for all
seasons in 1984-1985 seemed in general to be smaller than that found in
previous years examined. This was attributed at least in part to
differences in the overall weather patterns that existed during each of the
seasons examined. Summertime errors in general were smaller than the errors
found in other seasons. This was not surprising since pressure patterns are
usually much weaker in summer.

1000-500 mb thickness errors which were small in winter were larger in
each of the other seasons. In general, thickness was overforecast in the
central U.S. and underforecast in the western third of the nation,
particularly in the Rockies. The diurnal variation in the thickness error
pattern (i.e., larger negative errors for forecasts that verified at 00 GMT
and larger positive for forecasts that verified at 12 GMT) was surmised as a
reflection of the noted diurnal variation found for boundary layer
parameters, specifically boundary layer temperature. When one considers
that thickness is a measure of the average virtual temperature of an air
column, a tendency for large negative boundary layer temperature errors
should be reflected as a larger negative thickness error, other factors
being equal.

The Rockies appeared to be a favored location for the strongest biases
for many of the variables examined. In the case of 1000-500 mb thickness it
was thought that this might reflect a problem with the manner in which
station pressures are reduced to 1000 mb. Since in general there was a

212

significant negative bias in this region (except in winter) it appeared that the mean temperature being applied for the reduction to 1000 mb may have been on the average too low.

Mean relative humidity was generally forecast too moist in the Rockies. This pattern was also found for boundary layer relative humidity and even more pronounced for lower tropospheric relative humidity. This observation was thought as possibly linked to the improper treatment of the moisture and temperature structure associated with reducing the model atmosphere to sea level in mountainous terrain. In the analysis all three humidity parameters exhibited a tendency to be underforecast in the vicinity of the Gulf of Mexico. Seasonally, the worst dry bias was for boundary layer relative humidity in summer. It appeared that evaporation from the Gulf of Mexico may not have been adequately parameterized. The fact that the dry bias was largest in summer and fall may have had something to do with the higher water temperatures found at those times of the year, i e., the actual evaporation rate may have been larger than the one incorporated into the model.

Boundary layer temperature was overforecast for all seasons around the Gulf of Mexico, especially over the Florida peninsula. This may have been due to improper sensible heat transfer between the warm Gulf of Mexico and the overlying model boundary layer. The cold bias found in the Great Lakes in winter evolved into a moderate sized warm bias in summer. One explanation was that the model atmosphere was not gaining enough sensible heat from the relatively warmer Great Lakes in winter and gained too much sensible heat during the summer when the waters were relatively cooler than the surrounding land.

Finally, the diurnal variations seen during previous phases of this study were also seen for all seasons during this phase of the study. As described in Schechter (1984) this may have been attributable to the way the LFM parameterizes longwave radiational cooling, i e , treating the longwave radiational cooling rate as a constant

In conclusion, a large number of LFM forecasts for various parameters were analyzed for systematic errors using the FOUS 60 78 bulletins Analysis results have shown that the LFM II has some bias in all of the forecast parameters that were examined in the study. The error patterns varied both diurnally and seasonally. Examining these analyzed error fields

and their seasonal and diurnal variations, it was possible to infer
potential causes for some of the biases. Not surprisingly, some of the
causes of the model bias seem to be connected with boundary layer
parameterizations and model terrain considerations. The identification and
diagnosis of model biases may help in improving future physical
parameterizations.

F. References

Smith, E. A., 1975: The McIDAS System. IEEE Trans. Geosci. Elec.,
GE-13, 123-136.

Chisholm, D. A., and A. J. Jackson, 1984: An Assessment of Interactive
Graphics Processing in Short-Range Terminal Weather Forecasting.
AFGL-TR-84-0029, Air Force Geophysics Laboratory, Hanscom AFB, MA, ADA142706.

Chisholm, D. A., A. J. Jackson, N. E. Niedzielski, R. Schechter, and
C. F Ivaldi, 1983: The Use of Interactive Graphics Processing in
Short-Range Terminal Forecasting: An Initial Assessment. AFGL-TR-83-0093,
Air Force Geophysics Laboratory, Hanscom AFB, MA, ADA137165.

Gerlach, A. M., ed., 1980: Computer-Based Weather Research.
AFGL-TR-80-0069, Contract No. F19628-79-C-0033, Systems and Applied Sciences
Corporation, 49-73, ADA094020.

Cressman, G. P., 1959: An operational objective analysis system. Mon.
Wea. Rev., 87, 367-371.

Barnes, S. L., 1964: A technique for maximizing details in numerical
weather map analysis. J. Appl. Meteor., 3, 396-409.

Miller, R. G., 1981: GEM: A Statistical Weather Forecasting Procedure.
NOAA TR-NWS-28.

Wash, C. H., and T. M. Whittaker, 1980: Subsynoptic analysis and
forecasting with an interactive computer system. Bull. Am. Meteor. Soc.,
61, 1584-1591.

Muench, H. S., 1981: Short-Range Forecasting of Cloudiness and
Precipitation Through Extrapolation of GOES Imagery. AFGL-TR-81-0218, Air
Force Geophysics Laboratory, Hanscom, AFB, MA, 13-17, ADA108678.

Keegan, T. J., 1978: Variation in Ground Brightness Over Northeastern
United States As Sensed by GOES Satellites. AFGL-TR-78-0290, Air Force
Geophysics Laboratory, Hanscom AFB, MA, 12, ADA068085.

214

Schechter, R., 1986: An error analysis of LFM forecasts using the FOUS 60-78 bulletins. _Preprints_, Eleventh Conference on Weather Forecasting and Analysis, Kansas City, MO; AMS, Boston, 67-71.

Schechter, R. 1984: An error analysis of LFM-II forecasts during the 1982-1983 winter season. _Bull. Am. Meteor Soc._, _65_, 1073-1080.

III. BOUNDARY LAYER METEOROLOGY

A. Introduction

Throughout the contract STX has developed and implemented software for a variety of research investigations of meteorological phenomena in the planetary boundary layer. In some instances the research data were derived from the AFGL Weather Test Facility (WTF) located at Otis Air National Guard Base near Falmouth, MA. The WTF provides instrumented towers and ground sites both for gathering weather data automatically and for testing newly developed and newly acquired weather sensors. STX has been responsible for maintenance and operation of the WTF.

The data retrieval system at Otis, called the Modular Automated Weather System (MAWS), collects one-minute mean weather data from various instruments, converts them to digitized form, and stores them on magnetic tape at the WTF; for some years data were also transmitted to AFGL over telephone long lines. Data are archived from sensors that sample wind speed and direction, temperature, dewpoint, visibility, precipitation, and cloud height. STX has provided a data processing program, MAWSE, to unpack the archived data and transform them into meteorological units in a format convenient for study. STX has supplied pen plots and printed displays to facilitate data analysis. Data have been prepared using statistical methods such as regression, time series, spectral analysis, and cross correlation; plots showing scatter and lines of best fit have been also provided. Editing programs have regularly been written to overcome noise and system-induced spurious data points to produce "clean" data for study.

.

B. Slant Wind Shear

Since wind distribution in the lowest layers of the atmosphere is an extremely important factor in aircraft operations, Brown (1982) studied the capability of surface wind sets located along a runway near touchdown and take off points, together with wind towers offset from the runway, to specify true slant wind speed along the aircraft flight path. He used data collected over the previous five years at the WTF. STX established the project database from the MAWS one-minute mean weather values. These

printouts were used to locate appropriate wind shear episodes for study. Selected episodes were extracted from the master file via computer software and stored on permanent disk file for further interactive processing. A quality review of the data was then initiated to edit out faulty data caused by sensor or transmission malfunctions.

With the database established, additional software was developed for computing and tabulating various types of wind shear statistics. For instance, data populations, means, standard deviations, variances, biases, correlation coefficients, root mean square errors, standard errors of estimates, covariances, and best fit linear equation coefficients of averaged wind shear speeds and directions were computed. Probability values for wind shear detection, false alarm ratios, critical success indices, and wind shear detection statistics over different time lag intervals were also determined. These statistics were the basis for research on using offset tower wind sets together with surface winds to specify the wind shear over the approach or takeoff zone of an airfield.

In 1983 STX was involved in a follow-up study of slant wind shear. The objective was to evaluate the relative effectiveness of two statistically-based approaches using offset tower data in predicting slant wind shear at intervals of 0, 5, 10, 15, 30, and 60 minutes. The two approaches examined were extrapolation techniques and screening regression determined equations. STX developed the software, using the data ensemble from the previous year. The screening regression equations developed in the study were judged to be superior overall to the extrapolation technique in predicting slant wind shear speeds (Brown 1983).

C. Weather Instrumentation Testing

Several prototype nephelometers developed under the Battlefield Weather Observation and Forecast System (BWOFS) program were tested at the WTF. STX software converted nephelometer analog outputs into extinction coefficients and visibilities to compare with standard visibility sensors (transmissometers). This conversion was added to the MAWSE program. During the testing it was found that the transmissometer readings drifted erratically. STX wrote software for the MAWSE program to recalibrate the transmissometer readings and applied the correction to the succeeding data,

217

thus providing a more reliable basis for comparison between the nephelometer and the transmissometers.

D. Fog Microphysics

In addition to evaluating weather instruments, STX was involved in producing software for fog microphysics studies using WTF generated data. To investigate fog prediction and prediction of visibility during fog episodes, spectrometer probes that measured the size distribution of fog droplets were installed at the WTF and also at Hanscom AFB. A 1982 fog field program saw additional probes added at Nobska Light in Woods Hole, MA. Data from these probes were collected, averaged, and categorized through the MAWSE program. Further software was devised to demonstrate relationships among fog droplet concentration, mean and median volume diameters, liquid water content, extinction coefficients, and mean terminal velocity. The scatter diagrams of the five-minute averages of liquid water content compared with average extinction coefficient were found to be logarithmic and the best fit of these two parameters was shown to lie along an exponential curve. Curvilinear relationship was shown to exist between liquid water content and droplet terminal velocity. By employing the variance of the errors of estimate based on the least-squares polynomial rather than the least-squares line, STX software produced a regression index that successfully described the relationship of the two parameters.

A two-dimensional fog model obtained from the Navy was revised and modified and both versions were tested on six advective fog case studies. Plots were provided to illustrate the capabilities of the revised version and to point out strengths and weaknesses in the basic approach of the model's physics.

E. Atmospheric Attenuation Effects

STX supported a study initiated to investigate probability prediction methods for estimating the performance of electro-optical remote sensing systems. Transmission data from ground-based remote instruments operating at infrared (8-12μ), visible (3-5μ), and laser (1.08μ) wavelengths

218

were made available in digital form for investigating their usefulness for tactical decision aids during snowfall conditions. The data were obtained during the SNOW-ONE-A (Aitken, 1982) field program at Camp Ethan Allen, VT.

Software was developed to categorize these transmissions in units of DB/km and to distribute the frequencies of their durations in time intervals of one minute through 45 minutes or more. Also, software was designed to provide power spectrum analyses and autocorrelations of the transmission data quantities over several time periods. A library of algorithms and computer codes known as EOSAEL (Duncan, 1979) was implemented to assist in describing atmospheric effects on E-O sensors.

Many cumulative probability-duration relations of transmission during given snowfall conditions were portrayed. Dyer (1984) demonstrated that probability duration curves for systems operating at known band widths within certain snowfall conditions can be approximated using a Markov chain.

F. Refractive Index Study

Over the past several years, the Air Force Electronic Systems Division and Mitre Corporation have been investigating the performance of a tactical tropospheric scatter radio link during different seasons and at various geographic locations. AFGL has conducted atmospheric research to enhance understanding and interpretation of test results. Troposcatter radio propagation is based on scattering of electromagnetic energy from refractive discontinuities existing in turbulence in the lower atmosphere. Energy cascades from large to smaller and smaller eddies until dissipated in the molecular range. This results in an energy to wavelength relationship in the inertial subrange which can be defined completely by a constant, the refractive index structure function $C_N 2$.

Turbulence data were recorded onto magnetic tape through an AFGL developed data retrieval system (TURBO) from aircraft-mounted refractometers flown over various parts of the United States and other parts of the world. STX developed software to process these data tapes, separating out refractivity from temperature, pressure, and signal voltages and displaying representative samples of each. $C_N 2$ was derived by two different methods and shown for periods of level flight and separately for spiraling down

219

periods. Turbulence profiles were constructed for each of the several field tests undertaken by AFGL.

A new TURBO system was introduced in 1985 requiring STX to learn and alter resident C language software. The sampled refractometer data were input to Cyber programs that converted the voltages to frequencies. The spectra obtained had to be corrected to remove filter characteristics of the refractometer used to prewhiten the data. Three separate methods were used to restore spectra in computer programs written to handle data acquired by different refractometers flown over Korea, Arizona, Florida, and Chatham, MA.

Most data reduction was done on the Cyber mainframe but analysis routines available only on the VAX dictated transfer of reduced data to that computer for statistical evaluation and plotting.

G. Chemical Dispersion and Windflow Modeling

At the direction of the Air Force Scientific Advisory Board, AFGL has been conducting research seeking to improve the mathematical models used to predict dispersion of chemicals in the atmosphere following space shuttle launches or possible chemical spills.

Since 1983, STX has adapted three models to operate in the AFGL computer environment, made extensive changes in the software and peripheral programs, provided appropriately formatted data, run tests, and aided in the evaluation of results. The three models selected for in-depth examination were the Shell Development Co. SPILL, the NASA REEDM, and the Army Atmospheric Sciences Laboratory (ASL) model used to predict surface layer windflow.

SPILL is one of the most complete Gaussian plume dispersion models in existence. It is an unsteady state model representing the evaporation of a chemical spill and the atmospheric dispersion of vapors. The model software when acquired was incompatible with AFGL host computers and was lacking a vital part. STX rewrote the code to run locally and reconstructed the missing routines. The model remains an active part of the AFGL effort and is available for use as a standard for further model development.

The NASA REEDM is used to assess the environmental impact of space shuttle launches at Cape Kennedy, FL. It was planned to be used with

appropriate changes to reflect fallout and terrain differences to predict the consequences of space shuttle launches at Vandenberg AFB, CA. STX reconstructed the model on the AFGL mainframe computer and replaced the model's plotting routines with ones capable of running on in-house systems. Four test runs were successfully achieved.

In 1984 emphasis shifted to a newly acquired ASL model which subsequently has undergone significant changes at AFGL and has emerged as a working surface layer windflow model which, when combined with a Gaussian puff diffusion model, will produce for the Air Weather Service a prediction system for toxic chemical spill transport over complex terrain.

Terrain data for Ft. Polk, LA, Vandenberg AFB, CA and Ft. Devens, MA were acquired and tailored by STX for input to the windflow model. Data errors were detected and corrected and an appropriate database was constructed for each location to insure proper testing with the model. Vegetation data were added to the Ft. Polk testing, with estimated roughness substituted for vegetation in the other two test site cases. Thorough testing took place using both Ft. Polk and Vandenberg data and results were published. STX discussed Vandenberg testing and results at a windflow model workshop attended by representatives of the three military services and NASA.

A prototype version of the model was tested in support of Army Special Forces operations at Ft. Devens. The model was run on the Air Force Weather Detachment Z-100 microcomputer at Ft. Devens using current weather observations or terminal forecasts as input. Field personnel were trained to use the model by STX. Subsequent operational testing under actual field conditions showed that the model software and utility plotting programs were easily utilized. Results demonstrated that the model can be used to generate wind climatologies for remote deployment areas. Vertical wind speed profile prediction can improve the accuracy of low-level wind forecasts used to support paradrop operations.

H. References

Aitken, G. W., ed., 1982: SNOW-ONE-A Data Report. Special Report 82-8, U. S. Army Cold Regions Research and Engineering Laboratory, Hanover, NH.

Brown, H. A., 1982: Analysis and Specification of Slant Wind Shear. AFGL-TR-82-0366, Air Force Geophysics Laboratory, Hanscom AFB, MA, ADA125883.

Brown, H. A., 1983: <u>Prediction of Slant Wind Shear With an Offset Tower Observation System.</u> AFGL-TR-83-0308, Air Force Geophysics Laboratory, Hanscom AFB, MA, ADA142676.

Dyer, R. M., 1984: <u>A Probabilistic Model for Predicting the Duration of Levels of Electromagnetic Transmission in Falling Snow</u>. AFGL-TR-84-0047, Air Force Geophysics Laboratory, Hanscom AFB, MA, ADA143318.

Duncan, L. D. <u>et al</u>., 1979: <u>The Electro-Optical Systems Atmospheric Effects Library</u>, Vol. I: <u>Technical Documentation</u>. ASL-TR-0047, U.S. Army Atmospheric Sciences Laboratory, White Sands Missile Range, NM.

Lanicci, J. M., J. M. Ward, and R. E. Wallace, 1986: Operational evaluation of a prototype surface windflow model for use as a tactical weather support tool. Presented at Electro-Optical Systems Atmospheric Effects Library and Tactical Weather Intelligence Conference, New Mexico University, Las Cruces, NM.

IV. RADAR METEOROLOGY

A. Introduction

Over the last five years the STX radar meteorology research program has been directed toward development and improvement of algorithms for NEXRAD, the next-generation weather radar. STX has concentrated on automated detection and short-term warning of severe weather hazards at the ground and in the lowest few kilometers above the ground, with the ultimate aim of significant reduction in casualties and property loss by destructive weather phenomena. Contributions have ranged from origination, development, and testing of new techniques, to writing software for creation of algorithms, to adaptive modification of existing algorithms.

The severe weather hazards addressed in these studies have included mesocyclones, wind shear, icing, turbulence, and high winds associated with hurricanes and intense extra-tropical cyclones. The prediction of motion of such disturbances related to convective storms has also been investigated. Mesocyclones, which are rotating regions located within some intense and well-organized thunderstorms, are the parent circulations of the great majority of tornadoes and all of the violent ones. About half of all radar-detectable mesocyclones have produced one or more tornadoes, and over 90 percent of mesocyclones have produced some form of severe weather manifestation at the ground, so their investigation is crucial for improvement of warnings of severe storms as well as of tornadoes. Events related to wind shear, for example, microbursts and gust fronts, may also cause wind damage at the ground; however, the principal interest in these phenomena is their extreme danger to aircraft during takeoff and final approach. Heavy icing and severe turbulence are also hazardous to aircraft in flight. The studies of these threats to flight safety have been directed toward their more reliable and timely detection by radar, so that pilots may effectively take evasive action.

B. Severe Storm Indicators

Over the lifetime of the contract, investigations of severe storm indicators have centered on the mesocyclone. These studies have included a

search for a mesocyclone precursor through rotational and convergent inter-storm motions, and a search for a predictor of tornado occurrence and intensity in the rotational kinetic energy development of the parent mesocyclone. Also, an algorithm has been developed for automated identification of mesocyclones from single-Doppler radar data. This algorithm has the capability to detect tornadic vortex signatures, which trace the circulation of tornadoes when there is sufficient resolution of the radar beam across the diameter of the tornado.

The relative motions among distinct echo cells of emerging convective storms have been investigated by Donaldson and Snapp (1983) for their usefulness as a precursor of mesocyclone development. This approach was supported by the reasonable expectation that one of the pre-conditions for mesocyclone development is a wind field displaying significant values of convergence and cyclonic vorticity in the low-altitude environment surrounding a storm during its early stages of growth. Furthermore, small echo cells could serve as imperfect but revealing tracers of the environmental wind field prior to mesocyclone development. Accordingly, the relative motions of pairs of distinctive echoes were studied in two storms that later developed mesocyclones and two that did not. Convergence was inferred by the approach toward one another of the two echoes in an echo pair, and vorticity was inferred by rotation of the axis joining the echo pair. Mean magnitudes of inferred cyclonic vorticity in the eventually mesocyclonic storms were more than an order of magnitude greater than in the storms that did not develop mesocyclones. Warning times were also significant: In one mesocyclonic storm, unusually intense vorticity was traced by rotation of an echo-pair axis 45 min before the mesocyclone appeared. The echo pairs indicated strong convergence only in the storm in which tornadoes were spawned by a mesocyclone.

These studies, conducted manually and to some degree subjectively, were time-consuming and obviously not suitable for operational application. They did, however, indicate that relative echo motions during the first hour of a storm's lifetime may predict the probability of subsequent development of a mesocyclone. Accordingly, Harris and Petrocchi (1984) developed a reflectivity peak detection algorithm so that small echoes could be identified automatically and their relative motions monitored in real time.

The large number and short lifetimes of the reflectivity peaks compromised the reliability of automated tracking results. However, the rate of change with time of the number of cells and the average reflectivity mass within the cells did provide an early indicator of the eventual evolution toward a supercell storm 15 to 20 min before a mesocyclone was detected.

An algorithm for automated detection of mesocyclones in real time was developed and successfully tested by Wieler (1986), following guidelines proposed by Wieler and Donaldson (1983). The MTDA, or Mesocyclone-Tornado Detection Algorithm, is very versatile: It will identify large mesocyclones up to 10 km in diameter, as well as tornadic vortex signatures that are an order of magnitude smaller. It also can handle both cyclonic and anti-cyclonic circulations. This feature was built into the algorithm because a small fraction of tornadoes and an occasional mesocyclone do rotate anticyclonically. After identification of a circulation, the algorithm computes its horizontal and vertical extent, temporal persistence, average shear, momentum, and rotational kinetic energy. The algorithm also compensates for cross-beam degradation of resolution with range, which is especially important for reliable identification and classification of small features such as tornadic vortex signatures. Many small, weak, and ephemeral perturbations in Doppler velocity characterize natural wind fields; these perturbations are initially discarded by requiring all velocity differences in an azimuthal scan at a particular range to exceed resolution-dependent thresholds of magnitude and shear. No significant atmospheric vortices are eliminated by these thresholds. The MTDA can also identify and measure divergence (or convergence) on the scale of the mesocyclone. This is an important capability, because in many mesocyclones the vorticity is co-existent with convergence near the ground and with divergent outflow at the top of the circulation.

Further improvements in the MTDA have been made by Desrochers, after he discovered that the algorithm was mishandling areas of velocity change in weak reflectivity. This problem needed correction, because in many supercell storms weak echo regions are coincident with mesocyclones. With these improvements, the algorithm now works well in regions of weak as well as strong reflectivity.

The MTDA provides information on the radius and maximum rotational

velocity of mesocyclone cores as a function of height and time. This
information can be used for quantitative classification of mesocyclone
intensity in an effort to predict the occurrence of tornadoes and their
destructive power. Donaldson and Desrochers (1985) discovered that
rotational kinetic energy of the mesocyclone core is the most reliable
predictor of tornadoes. They also found that shear must be combined with
energy, in order to eliminate a high rate of false alarms from large and
weakly rotating mesocyclones near threshold shear that never produce
tornadoes. Consequently, they devised a parameter called ERKE (Excess
Rotational Kinetic Energy), which is the rotational kinetic energy of a
mesocyclone core calculated from its radius and its rotational velocity in
excess of the value required to maintain threshold mesocyclonic shear. Thus
the large and weakly rotating mesocyclones will have appropriately small
values of ERKE. In one tornadic mesocyclone, ERKE attained unusually large
values 20 min before touchdown of a violent maxi-tornado.

Desrochers et al. (1986) expanded the study of ERKE to a sample of ten
mesocyclonic storms. Half of these storms were tornadic, approximating the
distribution seen in nature. Two of the tornadic storms produced
maxi-tornadoes of violent intensity (F4 and F5). The predictor of tornado
occurrence was a value of ERKE at least as large as the climatological mean
of all mesocyclones in the mature stage, penetrating below a height of 5 km
and persisting there for at least 5 min. Although these classification
criteria are tentative, pending the analysis of a much larger sample, they
correctly predicted whether or not a tornado occurred in nine storms out of
ten. The predictor for a violent F4 or F5 tornado was identical to that for
any tornado, but with ERKE exceeding twice the climatological mean. This
predictor was correct for all storms. The first tornado in a storm, usually
of weak F1 intensity, generally occurred a few minutes before the tornado
occurrence predictor verified. However, positive warning times of 13 to 63
min were attained for the most intense non-violent tornado in a storm, of
strongly damaging intensity F2 and F3. The two violent tornadoes, which
were predicted perfectly, also occurred after adequate warning times of 20
min for one storm and an amazing 72 min for the other. This excellent
predictability of ERKE for the violent F4 and F5 tornadoes is indeed
fortunate, because this class of tornadoes, despite its rarity, kills and
injures many more people than the more common strong or weak tornadoes.

C. Wind Shear Related Hazards

Aircraft are particularly susceptible to accidents during terminal
approach and takeoff procedures because of their proximity to the ground.
Several crashes have occurred when aircraft experienced alterations in lift
upon encountering substantial environmental wind shear. These wind changes
tend to be associated with convective storm outflow, seabreeze fronts, and
synoptic fronts. Detection of the location of these features in real time
could provide valuable guidance to air traffic controllers and pilots. With
this information they would be able to alter their flight procedures to
prevent mishaps. During the past five years STX has conducted considerable
research directed toward determining the detectability by Doppler radar of
these low-level shear phenomena and developing and testing automated
detection techniques where appropriate.

The primary effort has been on the detection of the outflow from
convective storms since this appears to be the primary source for air
crashes. Fujita (1985) has documented several cases where commercial
aircraft have crashed on takeoff or final approach due to encounters with
thunderstorm outflow. These outflows are the product of the downdrafts that
occur within all convective storms. Downdrafts deflected by the ground
produce a perturbation on the horizontal flow. Some storms produce only
weak downdrafts and hence only weak outflows which are less likely to prove
hazardous. However, a great many storms produce strong downdrafts that
Fujita (1985) calls downbursts. He defines a downburst as any strong
downdraft that produces damaging winds at or near the ground. He separates
downbursts into two categories: microbursts (horizontal extent less than 4
km across) and macrobursts (greater than 4 km). A microburst is attributed
to a single intense downdraft. On the other hand, the macroburst is more
likely the product of a number of less intense downdrafts that accumulate
cold air beneath the storm. This causes a pressure gradient force directed
outward from the dome of cold air with the strongest force usually toward
the inflow region. This force pushes the cold air from beneath the storm,
inducing gusty winds especially near the region where the outflow interacts
with the inflow. The boundary between these two flow regimes is called a
gust front. In future discussion, reference to the macroburst phenomenon

227

will be in terms of its gust front because it is this portion of the macroburst that is the primary hazard for aircraft.

A great many microbursts and gust fronts kick up enough debris, have enough precipitation, or have sufficient refractive index gradients for detection by microwave Doppler radar. In an effort to provide guidance to the forecaster, STX has explored a variety of techniques for automatic detection of microbursts and gust fronts. In 1981 more was known about the radar characteristics of gust fronts than downbursts, because gust fronts had been studied extensively, especially in Oklahoma (Bensch and McCarthy, 1978; Goff, 1976). With this backlog of knowledge and a number of readily available cases from the JDOP program, efforts were directed toward detection of gust fronts. First, a correlation technique developed by Smythe and Zrnic´ (1983) for determining motions within storms was investigated to see if gust fronts were observable in the resultant motion fields. Two problems were encountered in the use of this technique. First, gust fronts usually have only a narrow region that yields radar returns, too small to allow the correlation technique to produce enough motion vectors for reliable gust front discrimination. Second, this technique determines motions of patterns of reflectivity or velocity and these may have very little relationship to the air motion. In fact, a comparison of the correlation-derived motion fields with those derived from multiple Doppler analyses showed discrepencies in direction as high as 180 deg. Consequently this technique was discarded.

A common observation of gust fronts from the NSSL studies was the presence of gradients of the radial velocity. We then decided to look at techniques for the estimation of these gradients in real time. In the NEXRAD inventory there are algorithms to determine regions of shear in range and azimuth individually. It is unfortunate that individually they do not depict the gust front completely and there appears to be no easy way of combining their products. The approach adopted by STX was to compute both gradients and place them on a rectangular grid for combination into a single two-dimensional gradient of the radial velocity. Using this technique and placing a threshold on the gradient magnitudes, it was found that gust fronts were readily discernible throughout most of their length. The gradient computation scheme used in this analysis has become the Combined

228

Shear Algorithm in the NEXRAD library of Category 1 algorithms, that is, those to be implemented in the prototype radar system. Some efforts were directed towards automatically extracting the gust fronts from the gradient data in terms of a line or contour and in tracking and forecasting their motions. While it was found to be possible to characterize the gust front with either a line or a contour, the evolution of the detected feature was great enough that the use of simple techniques was found not to be applicable to the high degree of evolution of the patterns in the gradient data and these efforts were abandoned.

By 1985, considerable knowledge of the nature of microbursts had been compiled (e.g., Fujita, 1985; Wakimoto, 1985) and it was apparent that we might well be able to detect microbursts automatically with Doppler radar. Microbursts produce very distinctive divergent signatures in the radial velocity fields at the very lowest elevation angles. An algorithm, discussed elsewhere in this report, was developed to detect this divergent signature and was found to be quite successful on the limited data set available. A similar algorithm was developed independently at the MIT-Lincoln Laboratory (Merritt, 1986), with equally promising results.

Downburst and seabreeze fronts are not always observable by microwave radar but it is thought that Doppler lidar might more easily detect these clear air features. An effort was initiated to assist the Air Force in developing a Doppler lidar program. Studies were initiated to explore the capabilities of Doppler lidar as a detector of clear-air phenomena, and it was found, in fact, that the CO_2 system clearly had considerable potential. Once the Air Force acquired the lidar STX assisted in its assembly and testing.

D. Position Tracking and Forecasting

To this point discussion has been focused primarily on detection of weather phenomena and not on determination of future locations, a necessary ingredient in any forecast. To tackle this problem, one needs first to look at the present and past locations of the phenomenon being analysed. There are different perspectives that can be taken here. One could focus on the cell concept. One definition of cells might be those regions that have

reflectivity values above some threshold value. This is the approach developed by AFGL for its automated cell identification and subsequently adopted by NEXRAD as one of its primary algorithms. One could also define cells as simply peaks in the reflectivity fields where there is some threshold on the magnitude of the peaks relative to the surroundings. This has the advantage of being able to follow cells from their inception and to provide much more structural information for complex storm systems. Crane (1979) introduced this concept as a potential tracking tool. STX examined its application to real time processing and to the appraisal of changes in the internal structure of storms. In a study early in this contract (Wieler et al., 1982), Crane's definitions of peaks (regions where reflectivities are 3 dB above background) were found to be inadequate because more peaks were found than could be reliably correlated in time, thus making the peaks of little use as an analysis tool. As part of the attempt of automation in the relative storm motion study discussed earlier it was decided to revisit this technique of cell identification. Larger peaks (6 dB above background) were sought. While these could be tracked visually through pattern recognition considerations, simple automated techniques did not appear to be possible, because of the large numbers and close proximity of the detected cells.

Another approach to storm tracking is to attempt to follow a region as defined by a contour and to monitor the shape and position of the region. STX pursued this approach in its contributions to the AFGL efforts to nowcasting cloud-free lines of sight, of which there has been considerable discussion elsewhere in this report. Suffice it to say that with contour definitions utilizing the Freeman chain code there appears to be considerable promise for this technique as a real time tool. To date efforts have been directed towards development of a software system environment in which implementation and evaluation of analysis techniques is relatively easy. A few selected techniques have been evaluated.

Besides developing and evaluating techniques for potential utilization in NEXRAD, STX has also implemented algorithms developed elsewhere. One such algorithm is the icing algorithm that was developed at McGill University. Aircraft icing is most often caused by small (less than 60 microns in diameter) supercooled liquid water droplets, too small to be

detected by radar. However, there is reason to expect icing encounters when supercooled rain drops are present. Normally when ice particles fall from their region of generation through the 0° C level they melt and produce a "bright band" in the radar reflectivity measurements. Since supercooled water and ice particles are not likely to co-exist, from the presence of a bright band one can deduce that there is no super-cooled liquid water. Conversely, the absence of a bright band within a precipitation region that extends above and below the 0° level might well indicate the presence of super-cooled liquid water and the absence of ice particles. This is the basis of the McGill technique and the algorithm developed there. The automated algorithm has been implemented but remains to be corroborated with coincident radar and aircraft data.

As a continuation of a previous effort by STX and a further effort by AFGL in assessing the utility of the variance of the Doppler spectrum as an estimator of aircraft turbulence, an automated algorithm was encoded into the AFGL real time processing package. This software and its accompanying graphics software have been debugged and tested.

E. Synoptic-Scale Wind Anomalies

Hurricane Belle (1976) was the first tropical storm observed by Doppler radar. The maximum and minimum locations of Doppler velocity were not opposite in this hurricane; Donaldson et al. (1978) explained this deviation as an effect of curvature of the wind field. However, this explanation was incomplete. Donaldson and Harris (1984) reconsidered the Doppler velocity patterns observed in synoptic-scale wind field anomalies produced by intense cyclones like hurricanes and concluded that crosswind shear as well as curvature contributes to the deviation from opposition of the Doppler velocity extrema. Recently they derived a formal expression for the Doppler velocity pattern, given by a radar scanning in azimuth at constant range and elevation angle, of all four first-order spatial derivatives of the wind field. These derivatives are curvature, diffluence, crosswind shear, and downwind shear. An original approach was used to model diffluence, in order to preserve streamline integrity, by postulating a virtual (but fictitious) streamline apex at a fixed distance upwind from the radar for diffluence or

231

downwind for confluence. The inverse problem was solved for recovery from the Doppler velocity pattern of downwind shear, diffluence, and the sum of curvature and crosswind shear, as well as wind speed.

Donaldson and Ruggiero (1986) applied these results to an analysis of Hurricane Gloria (1985). Their most important finding revealed pronounced decay after landfall of both circulation and maximum wind speed around the eye region nearly three hours before confirmation by more direct radar measurements. Negative downwind shears, owing to frictional loss over rough ground, were also measured, and largely compensated by persistently positive diffluence. This type of diagnosis, utilizing wind field derivatives recovered from the pattern of scanned Doppler velocities, offers great promise for remote and early assessment of the trend in intensity of hurricanes and severe extra-tropical cyclones.

F. Other Activities

Throughout the five years of this contract STX scientists have been active in terms of participation and attendence at formal and informal technical meetings. Thirteen presentations have been made at such technical conferences as the 21st, 22nd, and 23rd Conferences on Radar Meteorology, 12th, 13th and 14th Conferences on Severe Local Storms, 16th Conference on Hurricanes and Tropical Meteorology, NEXRAD Doppler Radar Symposium/Workshop (1982), and a URSI Commission F meeting (1985). In addition, less formal presentations were made concerning shear detection to the FAA and in the orientation session for the Boston Area NEXRAD experiment. Ralph J. Donaldson, Jr. had the distinct honor of being elected Fellow of the American Meteorology Society, of being chosen to co-chair a special AMS Radar Meteorology Symposium/Workshop, and to teach a course on radar meteorology interpretation to National Weather Service personnel. He was also called upon to participate in an experiment by PROFS to evaluate its products.

G. References

Bensch, R. R., and J. McCarthy, 1978: Low-level cloud features and airflow of an Oklahoma hailstorm. Mon. Wea. Rev., 106, 566-571.

232

Crane, R. K., 1979: Automated cell detection and tracking. IEEE Trans. Geoscience Elec., GE-17, 250-262.

Desrochers, P. R., R. J. Donaldson, Jr., and D. W. Burgess, 1986: Mesoscylone rotational kinetic energy as a descriminator for tornadic and non-tornadic types. Preprints, 23rd Conference on Radar Meteorology, Snowmass, CO; AMS, Boston, 1-4.

Donaldson, R. J., Jr., and P. R. Desrochers, 1985: Doppler radar estimates of the rotational kinetic energy of mesocyclones. Preprints, 14th Conference on Severe Local Storms, Indianapolis; AMS, Boston, 52-55.

Donaldson, R. J., Jr., and F. I. Harris, 1984: Detection of wind field curvature and wind speed gradients by a single Doppler radar. Preprints, 22nd Conference on Radar Meteorology, Zurich, AMS, Boston, 514-519.

Donaldson, R. J., Jr., and M. R. Snapp, 1983: Interstorm motion as a mesoscylone precursor. Preprints, 21st Conference on Radar Meteorology, Edmonton; AMS, Boston, 7-10.

Donaldson, R. J., Jr., M. J. Kraus, and R. J. Boucher, 1978: Doppler velocities in rain bands of Hurricane Belle. Preprints, 18th Conference on Radar Meteorology, Atlanta; AMS, Boston, 181-184.

Donaldson, R. J., Jr., and F. H. Ruggiero, 1986: Wind field derivatives in Hurricane Gloria estimated by Doppler radar. Preprints, 23rd Conference on Radar Meteorology, Snowmass, CO; AMS, Boston, JP236-JP239.

Fujita, T. T., 1985: The Downburst. Satellite and Mesoscale Research Project (SMRP) Research Paper #120, University of Chicago, Chicago, IL, 122 pp.

Goff, R. C., 1976: Vertical structure of thunderstorm outflows. Mon. Wea. Rev., 104, 1429-1440.

Harris, F. I., and P. Petrocchi, 1984: Automated Cell Detection as a Mesoscylone Precursor Tool. AFGL-TR-84-0266, Air Force Geophysics Laboratory, Hanscom AFB, MA, ADA154952.

Merritt, M. W., 1986: Interim Report on Microburst Surface Outflow Detection Algorithm. MIT-Lincoln Laboratory, 10 pp.

Smythe, G. R., and D. S. Zrnic', 1983: Correlation analysis of Doppler radar data and retrieval of the horizontal wind. J. Clim. Appl. Meteor., 22, 297-311.

Wakimoto, R., 1985: Forecasting dry microburst activity over the high plains. Mon. Wea. Rev., 113, 1131-1143.

Wieler, J. G., 1986: Real-time automated detection of mesocyclone and tornado vortex signatures. _J. Atmos. Oceanic Tech._, 3, 98-113.

Wieler, J. G., and R. J. Donaldson, Jr., 1983: Mesocyclone detection and classification algorithm. _Preprints_, 13th Conference on Severe Local Storms, Tulsa; AMS, Boston, 58-61.

Wieler, J. G., F. I. Harris, and M. R. Snapp, 1982: _An Evaluation of an Automatic Cell Detection and Tracking Algorithm_. AFGL-TR-82-0386, Air Force Geophysics Laboratory, Hanscom AFB, MA, ADA126263.

H.   SASC Technologies, Inc. Bibliography

1981

Bohne, A. R., 1981: Estimation of turbulence severity in precipitation environments by radar. _Preprints_, 20th Conference on Radar Meteorology, Boston; AMS, Boston, 446-453.

1982

Bohne, A. R., 1982: Radar detection of turbulence in precipitation environments. _J. Atmos. Sci._, 39, 1819-1837.

Donaldson, R. J., Jr., and D. W. Burgess, 1982: Results of the Joint Doppler Operational Project. _Proceedings_, NEXRAD Doppler Radar Symposium/Workshop, U. of Oklahoma, 102-123.

Donaldson, R. J., Jr., D. E. Forsyth, and C. L. Bjerkas, 1982: Exploration of inter-storm motion as an indicator of meso-β circulation. _Preprints_, 12th Conference on Severe Local Storms, San Antonio; AMS, Boston, 419-421.

Moroz, E. Y., J. I. Metcalf, and F. I. Harris, 1982: _System and Atmospheric Effects on Measurement_. AFGL Tech. Memo. No. 64, Air Force Geophysics Laboratory, Hanscom AFB, MA.

Wieler, J. G., F. I. Harris, and M. R. Snapp, 1982: _An Evaluation of an Automatic Cell Detection and Tracking Algorithm_. AFGL-TR-82-0386, Air Force Geophysics Laboratory, Hanscom AFB, MA, ADA126263.

1983

Donaldson, R. J. Jr., and M. R. Snapp, 1983: Interstorm motion as a mesocyclone precursor. Preprints, 21st Conference on Radar Meteorology, Edmonton, AMS, Boston, 7-10.

Moroz, E. Y., S. B. Alejandro, and F. I. Harris, 1983: Systems Integration and Test Plan for the AFGL CO_2 Lidar Doppler Wind Measuring System. AFGL Tech. Memo. No. 85, Air Force Geophysics Laboratory, Hanscom AFB, MA.

Smythe, G. R., 1983: Sub-storm scale motions as determined from single-Doppler and non-Doppler radar data. Preprints, 13th Conference on Severe Local Storms, Tulsa; AMS, Boston, 109-112.

Smythe, G. R., and D. S. Zrnic', 1983: Correlation analysis of Doppler radar data and retrieval of the horizontal wind. J. Clim. Appl. Meteor., 22, 297-311.

Wieler, J. G., and R. J. Donaldson, Jr., 1983: Mesocyclone detection and classification algorithm. Preprints, 13th Conference on Severe Local Storms, Tulsa; AMS, Boston, 58-61.

1984

Donaldson, R. J., Jr., and F. I. Harris, 1984: Detection of wind field curvature and wind speed gradients by a single Doppler radar. Preprints, 22nd Conference on Radar Meteorology, Zurich; AMS, Boston, 514-519.

Harris, F. I., and P. Petrocchi, 1984: Automated Cell Detection as a Mesocyclone Precursor Tool. AFGL-TR-84-0266, Air Force Geophysics Laboratory, Hanscom AFB, MA, ADA154952.

Smythe, G. R., and F. I. Harris, 1984: Sub-cloud Layer Motions from Doppler Radar Data using Correlation Techniques. AFGL-TR-84-0272, Contract No. F19628-82-C-0023, Systems and Applied Sciences Corporation, ADA156477.

Wieler, J. G., 1984: Real-time Automated Detection of Mesocyclone and Tornado Vortex Signatures. AFGL-TR-84-0282, Contract No. F19628-82-C-0023, Systems and Applied Sciences Corporation, ADA154968.

1985

Bohne, A. R., and F. I. Harris, 1985: Short Term Forecasting of Cloud and Precipitation Along Communication Paths. AFGL-TR-85-0343, Air Force Geophysics Laboratory, Hanscom AFB, MA, ADA169744.

Donaldson, R. J. Jr., and P. R. Desrochers, 1985: Doppler radar estimates of the rotational kinetic energy of mesocyclones. Preprints, 14th Conference on Severe Local Storms, Indianapolis; AMS, Boston, 52-55.

Donaldson, R. J., Jr., and D. E. Donaldson, 1985: Tornado viewing in Corfu, Greece. Bull. Amer. Meteor. Soc., 66, 845-846.

Harris, F. I., K. M. Glover, and G. R. Smythe, 1985: Gust front detection and prediction. Preprints, 14th Conference on Severe Local Storms, Indianapolis; AMS, Boston, 342-345.

Harris, F. I., K. M. Glover, and G. R. Smythe, 1985: Shear zone delineation with Doppler radar data. Abstracts, Commission F Meeting, URSI, Washington, 71.

Harris, F. I., and P. J. Petrocchi, 1985: Cellular characteristics as a severe storm indicator. Abstracts, Commission F Meeting, URSI, Washington, 66.

Leary, C. A., and P. R. Desrochers, 1985: Interactions between cellular and stratiform precipitation in a tropical mesoscale convection system. Preprints, 16th Conference on Hurricanes and Tropical Meteorology, Houston; AMS, Boston, 168-169.

1986

Bohne, A. R., R. Boucher, F. I. Harris, and D. R. Egerton, 1986: The evolution of hurricane Gloria during passage over New England. Preprints, 23rd Conference on Radar Meteorology, Snowmass, CO; AMS, Boston, JP240-JP243.

Bohne, A. R., F. I. Harris, D. R. Egerton, and F. H. Ruggiero, 1986: Hardware and Software Requirements for the RAPID Data Processing and Display System. AFGL Tech. Memo. (In press)

Desrochers, P. R., R. J. Donaldson, Jr., and D. W. Burgess, 1986: Mesocyclone rotational kinetic energy as a discriminator for tornadic and non-tornadic types. Preprints, 23rd Conference on Radar Meteorology, Snowmass, CO; AMS, Boston, 1-4.

236

Donaldson, R. J., Jr., and F. H. Ruggiero, 1986: Wind field derivatives in hurricane Gloria estimated by Doppler radar. _Preprints_, 23rd Conference on Radar Meteorology, Snowmass, CO; AMS, Boston, JP236-JP239.

Sadoski, P. A., and D. R. Egerton, 1986: _Remote Atmospheric Probing Information Display (RAPID) System._ AFGL Tech. Memo. (In press)

Wieler, J. G., 1986: Real-time Automatic Detection of Mesocyclones and Tornadic Vortex Signatures. _J. Atmos. Oceanic Tech._, _3_, 98-113.

V. SATELLITE METEOROLOGY

A. Introduction

At the beginning of the contract period, research in satellite
meteorology at AFGL was based on the capabilities of the Man-computer
Interactive Data Access System (McIDAS) that had been purchased by AFGL from
the University of Wisconsin. Extremely advanced for its time, this system
had the capability to receive, store, manipulate, and display meteorological
satellite and observational data in a user-friendly interactive
environment. With these capabilities it was to become the primary analysis
tool for work in satellite meteorology at AFGL. Unfortunately, while McIDAS
had these advanced capabilities it was by no means a simple task to use
them. When received from Wisconsin, the McIDAS was limited to receiving and
viewing GOES images and associated functions. When it became desirable to
expand the usefulness of McIDAS to include new techniques or new data it
quickly became apparent that the documentation received with the system was
wholly inadequate to understand, much less modify, the McIDAS. For this
reason STX became significantly involved in the understanding and expansion
of McIDAS capabilities.

The initial task in understanding the McIDAS was to document the
existing software. Working closely with AFGL in-house scientists, STX
software engineers began the painstaking task of walking through the source
code for the various routines and figuring out what functions they performed
and what other routines they interfaced with. While this task was difficult
enough, it was further complicated by the fact that the Wisconsin software
normally contained no comments, had obviously been written in a hurry, often
contained obsolete code or even outright errors, and tended to follow no
programming convention known to man. Add to this the fact that due to the
limited amount of mass storage on the system (i.e., a single 80 mbyte disk)
all source code had to be maintained on punched cards and had to be
interpreted one deck at a time in order to produce even a listing of a
program, and one can get some idea of the magnitude of the job. However, if
the McIDAS was to be of any use beyond the limited functions that it had
arrived with, the task was a very necessary one.

The result of the documentation effort was six volumes produced jointly by the STX and AFGL staffs. Five of these described the individual routines contained in the five main program libraries that made up McIDAS and the sixth described all the various data structures that were used on the system. With these manuals it became possible for a scientist and an applications programmer, working together, to begin to do serious work utilizing the true capabilities of McIDAS. Three separate research projects grew out of these early efforts to understand how to use the McIDAS. They were a study of the then new Visible Infrared Spin Scan Radiometer (VISSR) Atmospheric Sounder (VAS) flying on the GOES-4 satellite; a feasibility study comparing radar reflectivity values to GOES visible and infrared imagery to determine if there was a relationship between moderate to deep convective systems sensed by radar and cold/bright scenes detected by satellite; and an experimental cloud analysis program designed to validate and improve the operational cloud analysis algorithm being used at the Air Force Global Weather Central (GWC) in its 3DNEPH program. STX meteorologists and applications programmers worked together with AFGL personnel on all three of these projects throughout the full term of each.

Early work digging through the McIDAS software would eventually lead to STX leadership on two other large projects begun later in the contract period. The first resulted from a joint agreement between AFGL and NOAA that called for AFGL to provide GOES mode A VISSR data to a consortium of users that was to be known as the Northeast Area Remote Sensing System (NEARSS). This was initially viewed as providing a redundant data path from the McIDAS GOES ground station to NEARSS with some associated command and control functions performed through a separate microprocessor based system. What it finally became will be described later. The second project became the replacement of the McIDAS itself. With the development of new bigger, faster, and cheaper processors than McIDAS and the requirement to handle more varied and larger data sets in an integrated environment, the decision was made to replace the McIDAS at approximately the halfway point in the contract period. Due largely to the background obtained working with the McIDAS, STX personnel were to perform a key function in what was initially called the McIDAS upgrade and later became the AFGL Interactive Meteorological System (AIMS).

239

B. Evaluation of VAS Radiance Measurements

One of the first research projects undertaken on the McIDAS was a
quantitative evaluation of the measurements from the VAS instrument on
GOES-4. The objective of this study was to determine if VAS radiance
measurements compared favorably with equivalent radiance values computed
from radiosonde temperature measurements made over a dense radiosonde
network in north Texas. The first part of the project required that the VAS
data be added to the McIDAS in such a way that the data handling
capabilities of the system could be brought to bear on the problem. This
required that a new database management structure be developed to handle the
sounder data. Once this was accomplished all the relevant applications
software had to be modified to recognize the new data type. When this was
done the VAS data could be treated by the McIDAS in exactly the same manner
as the GOES VISSR data. That is, it could be displayed on a McIDAS
workstation, navigated, overlaid with map boundaries, overlaid with contour
analysis of different parameters (such as contours of constant level
temperatures from the radiosonde network), or overlaid with plots of station
locations or data values. The VAS images could be stored and archived in
the same manner as VISSR images and hardcopies could be made. In short the
researchers had all the tools they needed to complete their initial study of
the data.

It was important to recognize that there are fundamental differences
between the way the VAS instrument senses the atmosphere and the way a
radiosonde does. The VAS makes a near instantaneous measurement of a
radiance value integrated over a column with a horizontal cross-section
equal to the resolution of the sensor for the particular channel being
sensed. A radiosonde makes a point measurement of temperature at scattered
discrete points as it ascends and drifts with the wind. It was not
therefore expected that the VAS and radiosonde would show exact agreement;
however, for validation of the VAS instrument the comparison values should
be comparable. A statistical comparison of the VAS and radiosonde data was
conducted on a large number of cases selected using the interactive
capabilities of McIDAS. From this comparison it was discovered that a 10 to
30 percent positive bias existed in the VAS data. Examination of the

equations used to convert from IR count values to radiance and from radiance
to brightness temperature revealed that if certain constants were modified
the resultant radiance and temperature values showed a much better agreement
with the radiosonde data. This information was communicated to the Space
Science and Engineering Center at the University of Wisconsin, the
organization responsible for producing the conversion equations, and a new
set of constants was generated. The updated results showed a marked
improvement in the comparison results.

C. Comparison of Satellite and Radar Estimates of Precipitation Rate

At about the same time as the VAS experiment, a combined AFGL/STX study
was conducted to determine the feasibility of using a quantitative method
for estimating rainfall intensity in regions of moderate to deep convection
(M/DC) from satellite derived visible and infrared imagery. Ground truth
for this study was provided by manually digitized radar (MDR) digital video
integrator processor (DVIP) levels which can be related to rain rate by an
empirical Z/R relationship. The motivation for this study was the need to
provide some information on precipitation bearing systems on a theater-scale
area in the absence of any direct measurements. The McIDAS was again
selected as the most suitable environment on which to perform this study.

The initial phase of the study was to select cases of moderate to deep
convection and then collect the data for each case. The sources of data
were to be GOES visible and infrared images, and the associated MDR
reports. At that time MDR data could be received at the McIDAS via the
WB604 data line; however, it was not being decoded or archived.
Consequently an MDR decoder was written and integrated into the McIDAS
traffic handler routine that controlled the data flow from the WB604 line.
Once the MDR decoder was operating correctly, the selection of the case
studies was begun. The selection process required the interactive
interpretation of satellite data along with overlaid MDR data in order to
find cases of M/DC. The MDR data had first to be converted from the polar
stereographic projection that it has been generated in, to a
latitude/longitude grid projection so that the McIDAS earth location
software could be used to warp the MDR data to match the projection of the

241

satellite image. This gave the user the capability not only to display the
MDR grid data but also to extract the data value from a grid point selected
on the screen. After these new capabilities were in place, interactive case
selection could proceed. Accumulation of the satellite and MDR data for
each case was performed automatically by the McIDAS. A total set of 66
hours of M/DC data collected over the continental U.S. was selected from the
three summer months of 1982.

After initial case selection, the second phase of the study was
undertaken, to determine if satellite data could be used to discriminate
rainfall intensity in regions of M/DC. From the 66 hours of data selected
in phase 1, 4094 individual cases were selected as being representative of
the general population. In order to insure that the selected cases did not
have an anomalous distribution of DVIP levels, a chi-square test for
independence was performed between the selected sample and the entire set of
national grid data. The chi-square test showed that the M/DC set was in
fact representative of the larger set and that sample size had minimal
influence on the distribution of DVIP levels.

The analysis technique to be tested consisted of comparing the relative
brightness of collocated visible and infrared pixels and determining the
probability that the corresponding DVIP level would exceed a given level.
Frequency distributions were generated for categories of area-averaged
visible and infrared satellite data contained in the previously collected
case. to determine the probability of detecting no-rain (DVIP = 0) and rain
(DVIP > 0) conditions for each VIS - IR pair. Exceedence probabilities
stratified by each DVIP level over 0 were then computed for each VIS - IR
pair.

Results of the second phase analysis showed that non-zero DVIP levels
were contained in a relatively small subset of the combined brightness and
IR values. To reduce the sensitivity of the study to non--rain areas in the
selected cases, the visible and IR data were combined into a new set of
categories that covered only the rain regions. Frequency distributions for
the new categories were then computed. Results of the combined data showed
that for cloud top temperatures colder than -15° C and reflectance values in
excess of 85 percent, the visible and infrared data were sensitive to
changes in DVIP level. Probability distributions were computed for the

range of values above these cutoffs that could be useful for determining rainfall rates in the absence of any data except passive geosynchronous satellite imagery.

The study also tried to determine if any useful information could be obtained from the infrared data alone. It was found that only for extremely well developed systems, where cloud top temperatures were below -45° C, did the IR data show any sensitivity to DVIP level change.

D. Automated Cloud Analysis

The third major study undertaken on the McIDAS involved the Air Force operational cloud analysis model known as 3DNEPH. This model was used to produce a global analysis of cloud extent and location on a three-hourly basis for use in Air Force operational and experimental programs. The satellite meteorology group at AFGL had been tasked to investigate the satellite processor portion of the nephanalysis model and to improve both the accuracy and sharpness of the analysis. STX again worked closely with AFGL scientists on this project. The approach that was decided on was to implement a research and development version of the operational model on the McIDAS and using that as a baseline to investigate areas where the model could be improved. This version of the model became known as the RDNEPH and was based on the satellite processor algorithm from the 3DNEPH.

The satellite processor used the DMSP OLS as the primary data source and, when that was not available, it used data from the NOAA/TIROS-N AVHRR sensor. Since the sensor channels on the OLS were broad compared to the AVHRR, the two visible and two thermal IR channels were combined so as to appear more like the OLS. Several other data types were used in conjunction with the satellite data in the cloud algorithm; these included surface or skin temperature, background brightness, and upper air temperature profiles. GWC was the only practical source for all global data used in the neph experiments since it routinely archived all the data necessary to produce the nephanalysis. However, while using GWC was convenient and even necessary in order to get all the data, it caused a difficult database management problem due to the vastly different architectures of the GWC Univac computers and the McIDAS Harris computer. As was the case in the

projects described above, the first task in starting up the neph project was to build a new database management structure on the McIDAS for the GWC data.

One aspect of the GWC data that greatly facilitated the management task was that all data at GWC were mapped to a common map projection; namely, a polar stereographic projection true at 60 deg latitude. Data that were mapped to this projection were given a mesh designation based on the resolution of the data. The grid mesh was based on a whole mesh grid that had a nominal resolution of 200 nautical miles (nm). Finer resolution data could be stored in quarter, eighth, or sixty-fourth mesh grids that were subsets of the base whole mesh grid. By maintaining this convention on the McIDAS data manager the entire conversion operation was simplified. The McIDAS already had a grid database based on a regular latitude/longitude grid system. By patterning the neph grid database structure after the latitude/longitude structure, the integration of new data types into the McIDAS scheme became straightforward.

Once the neph data were in the system, it was a relatively simple exercise to write a series of applications programs to perform the common interactive data operations such as plot, contour, display images, and hardcopy. The next major task was to write the RDNEPH program itself. The analysis algorithm used a thresholding technique to make the cloud/no cloud determination. Data are analyzed for each eighth-mesh grid box (i.e., 25 nm resolution) resulting in an 8x8 pixel array for each analysis point. A frequency distribution histogram is computed for each box, peaks in the histogram are combined to produce four or less clusters, and each cluster is subjected to a threshold to determine if it is cloud. The IR threshold is based on the background surface temperature as derived from shelter height measurements and forecast model output. The visible data threshold is based on the background brightness database compiled from satellite measurements of clear scenes. In both cases the algorithm looks for clusters of pixels that are colder (IR) or brighter (VIS) than the background. Once a cloud has been identified, the cloud top brightness temperature is compared to the upper air temperature database to determine the cloud top height.

In order to determine how accurate the cloud analyses were, and to provide a means of quality control on the program itself, a new display was generated. This display was a synthesized image depicting the automated

244

interpretation of the cloud field. The image was generated by taking the representative grayshade from each cluster that was used in the thresholding operation and storing that grayshade value in a new image file known as the RGS. By replacing each IR or VIS pixel in an original image with the corresponding RGS value, the new synthetic image was formed. The RGS images proved very useful in evaluating the analysis algorithm results. Since they were based on the original data, regions in the RGS image that were analyzed as cloud looked almost identical to the original image. Regions that were interpreted as cloud-free were assigned an arbitrary (black) grayshade that was typically displayed as green for a clear land surface or blue for a clear water surface.

The AFGL study revealed several areas where the analysis algorithm broke down. The worst situation was for low stratus or fog over cold ocean surfaces. Due to the low thermal contrast between the cloud and the background surface, the threshold was just not sensitive enough to detect the clouds. Contributing to this problem was the fact that the infrared data had a resolution of only about 1.5° C whereas the surface temperature database had a resolution of 0.1° C. This often resulted in a checkerboard pattern in the RGS image in regions of these low clouds due to slight variations in the surface database. Recommendations were made to GWC to include more dynamic range in the IR data at the warm end of the spectrum where these ambiguities between a cool surface and warm cloud were most likely to occur. A second problem area in the automated analysis was along coastlines. It was discovered that often in completely clear situations, a line of low cloud would be analyzed right off the coastline. After some investigation it was learned that the low resolution of the surface temperature database was causing these anomalous clouds to appear. The problem was that in coastline grid boxes, the entire box was assigned the temperature value of the land portion of the box. In regions of large thermal contrast between the land and water surfaces (e.g., coastal New England in early summer), the cold water was being interpreted as cloud because the threshold value was based on a warm land surface.

The second issue that was to be addressed in the cloud analysis study was that of sharpness. For tactical applications, it is desirable for a cloud analysis to be as binary as possible (i.e., no partially cloud filled

analysis grid boxes). To determine whether improving accuracy adversely affected the analysis sharpness a new data set was generated. Through the use of run-time processing options, the RDNEPH program could be tuned to produce an optimal analysis for any situation. By computing a measure of sharpness known as the 20-20 score for a series of analyses produced using different run-time options, it was possible to quantify this relationship. The results showed that for different analysis options the resulting sharpness was always extremely high; that is, the 20-20 score was always in excess of 0.89 (where 1.00 is binary) and the variation was only a few percent. Thus it seemed reasonable to drop the sharpness issue from the need to improve accuracy.

Another issue that appeared to affect the accuracy of the analysis had to do with an apparent trend to over-analyze cloud at the edge of the satellite scan boundary. There were two possible causes for this: First, a geometric effect caused by the fact that the sensor tended to look more at the sides of cloud at the high scan angles; and second, atmospheric attenuation effects enhanced by the long pathlength through the atmosphere at the high angles. To quantify just how severe this problem was a large amount of raw brightness temperature values was accumulated and categorized by the satellite viewing angle. Plots of average brightness temperature vs. viewing angle showed a strong negative bias of about 7° C over land and 8° C over water at angles out to 65 deg from subpoint. Further investigation showed that a correction was applied to the data at GWC to account for that effect. This study showed that this correction was insufficient to remove the bias from the raw data; however, it was still not clear whether the error was carried through to the analysis produced from that data. To determine the effect of the scan angle bias on the cloud analysis, a second study was initiated to perform a similar test on the analysis itself. Unfortunately a much smaller sample set had to be used for this study due to computer problems. Nevertheless, the results gave some indication of how the error was carried through. The cloud analysis over land backgrounds did not appear to have any scan angle bias associated with the cloud amount product, but the analysis over water displayed a bias of 20 to 25 percent out to 65 deg. Due to the small sample size it was only possible to speculate as to why no bias appeared in the over land sample. The

conclusion was that clouds over land during the summer (when this sample was taken) had a large enough thermal contrast over the warm background that a 7° C bias was not enough to affect the threshold cutoff. Recommendations were made to GWC to apply the bias correction directly to the brightness temperatures used in the cloud threshold decision rather than a coarse correction to the raw grayshade data as was currently being done.

B. Northeast Area Remote Sensing System (NEARSS)

In 1983 work began on a project for the newly created NEARSS consortium. AFGL contracted with NOAA to provide GOES mode A VISSR data from the AFGL ground station to NEARSS for use by the research community within the association. The original specification called for a redundant data path to be established from the AFGL GOES ground link to a separate microcomputer-based storage and distribution system. Three tasks were identified: ingest, storage, and transmission to the users. The ingest function required that capabilities be established to schedule (with operator override), sectorize, and receive imagery and navigation data, all without user intervention. Limited data storage requirements would allow users to access recent GOES images in the event an image was missed when it first came in. Data transmission was to be over a dedicated serial network with the AFGL node performing network management functions.

AFGL purchased computer hardware for the project with the intention of doing system integration in-house. Because of this decision computer components were purchased at the board, and sometimes even the chip, level. This would eventually lead to a great deal of wasted and duplicated effort on the part of STX software engineers who were doing the integrating because the capabilities and connectivity requirements of the individual components were not always completely understood when they were purchased. After over two years of continuous effort, an integrated system based on a Intel 86/30 single board computer (SBC) with associated mass storage and communications subsystems was produced. This system used the iRMX86 real time operating system with a full blown development environment including an editor and debugger.

Once the system integration was complete, software development was able to proceed. A system originally developed for McIDAS known as the Offline Data Ingest System (ODIS) is used for scheduling and sectorizing the data as it is received from the satellite and performing data conversion from 6 (for the visible data) and 9 bits (for the IR data) to 8-bit bytes. From there the data are handled by the ingest software on the Intel system. Ingest software can handle various size sectors and different resolution images. Navigational parameters are automatically stripped out of the data stream with each image and stored locally by the database manager. Data are transmitted according to a pre-established schedule to the Massachusetts Institute of Technology (MIT) where the images can be viewed on a monitor and where they are made available to the rest of the NEARSS community.

The NEARSS microcomputer-based satellite ingest and distribution system has been running operationally since October 1985. Every half hour it automatically generates a 512x512 8-bit visible and infrared 8 km resolution image of the eastern U.S. and Canada during the day, and an IR image only at night. As soon as it is received from the satellite, each image is transmitted to MIT, requiring approximately 9 minutes to transmit both a visible and an infrared image over the 9600 bps transmission line. The NEARSS transmission protocol includes provisions for the imagery, navigational parameters, and error checking. It was originally designed to handle messages between the NEARSS users as well; however, that capability is not being used. Thus NEARSS is provided with full GOES mode A coverage in near real time on a continous basis.

F. AFGL Interactive Meteorological System (AIMS)

As research in satellite meteorology at AFGL become more varied, and as data from more and more different sensors were required, the McIDAS became overloaded and was unable to perform all of the functions required of it. In addition the development environment on the system had become archaic and unresponsive by the standards of the day. A plan was formulated in AFGL to replace the CPU of the McIDAS with a newer and more powerful processor. To this end a Gould SEL 32/27 minicomputer was purchased by the Laboratory with

the intention of simply transferring all the McIDAS functions over to the
new machine. However, after further thought it was concluded that a single
minicomputer would not be sufficient to handle all the tasks that the users
wanted to perform and that a more powerful solution was needed. At this
point STX personnel became actively involved in the upgrade project and the
formulation of a solution.

It was decided that the only way to find a solution to the upgrade
problem was first to be sure that the requirements were completely
understood. To do this, STX with AFGL in-house support began working on a
requirements statement. The requirements came from existing McIDAS
functions that were to be carried over, capabilities that users wanted but
that McIDAS was unable to provide, and speculation as to what future
requirements would be. Seven functional areas were identified that the new
system would have to address:

1) data ingest, both satellite and other types

2) data storage and retrieval

3) generation of output products

4) interactive display and objective analysis

5) applications development

6) system maintenance

7) system architecture and distribution of data and products.

At this point a fundamental decision was made to go with a system of
distributed processors rather than a single CPU. There were several reasons
for this. First, in order to handle all the identified and projected
functions, any single CPU would have to be very large and therefore too
expensive. Next, no matter how large the processor was, it was inevitable
that at some point the needs would outgrow the capabilities. Also, in an
interactive environment it is desirable to be able to isolate the individual
users so that one person's heavy system use will not impact the response
time of other users. A distributed system seemed to be a solution for all
these problems since it could always be expanded by simply adding another
processor; individual minicomputers and microcomputers were becoming less
expensive while at the same time becoming more powerful; and by providing

249

separate CPU's for interactive workstations, each user was isolated from the effects of others.

The down side to this decision was that by using a distributed system, the system design became considerably more complicated. To get a grip on this system design problem, STX contracted for a design study by Technology Systems Inc. (TSI), a company with considerable experience in this area. STX, AFGL, and TSI conducted a long series of weekly meetings in which system requirements were carefully specified and a system design evolved. The result was a plan for a distributed system, linked by a local area network (LAN), that could be expanded virtually without limits and that would meet all the specified system requirements. The design called for a layered system, where each layer was one function the system had to provide. Layers were organized in a hierarchical structure such that the lower layers were most machine (computer) dependent and the top layers were where the users interacted. Six layers were identified, with each layer built upon the one just below it. The layers from top to bottom were:

1) user interface
2) applications programs
3) database management
4) network communications
5) computer interface
6) physical link.

The next problem was how to implement the design. A three phase implementation plan was developed in which each phase would be completed before work on the next phase began. In phase 1 the main processors would be identified and procured and a common development environment would be built for each computer. A VAX 11/750 was selected as the system host, batch processing node, database manager (DBM), and network bridge to systems outside the LAN. The SEL 32/27 became the GOES ground station processor and local archive node. A microVAX II was chosen as the host processor for the user workstations. There were to be two workstations built around Adage display systems. The common development environment consisted of utility routines to compile, link, perform library management, and access tape data. All utilities on each machine would be operated in an identical

250

manner so that a programmer had to learn only one convention to be able to
work on all machines. Other development tools that were developed included
parsing algorithms, a console manager, and terminal input routines.

Phase 2 of the implementation plan called for three tasks to be
performed concurrently with different teams working on each one. First was
the database management (DBM) function. Database management on a
distributed system can be complex due to the requirement to manage files on
all linked processors in a consistent manner and to make the information
describing the files available to all users regardless of which machine they
are operating on. The method selected for the AIMS is known as a star
configuration, so named because there is only one central data dictionary
(at the center of the star) for all data files located anywhere on the
system. A data dictionary is a series of specialized files that contain
information describing the contents of data files that are located
elsewhere. Redundant backup dictionaries are maintained on each node for
use in the event of a network failure. The second task performed under
phase 2 was the specification and installation of the local area network.
While it is highly desirable to have only one LAN topology connecting the
entire system, at the time this task was performed there was no single
network available within the prevailing cost constraints that could
interconnect all three of the different processors that made up the AIMS.
The best solution that could be found was to select two different links that
both ran under the same protocol, DECnet. A point to point link was
established between the VAX 11/750 and the SEL 32/27 and a token passing
ring network was set up between the VAX and microVAX. The VAX acts as a
gateway between the two different links. The third task was to establish a
standard for the user interface that would be followed for each
application. It was decided that at least two methods would be used so that
users would have a choice depending on how much help they need from the
computer in entering the commands. The first method assumes that the user
is familiar with the command and simply wants to enter it with the fewest
possible keystrokes. This uses the command language that is provided under
the VMS operating system and consists of a single command name to invoke a
program followed by qualifiers and parameters. By specifying different
qualifiers the user can customize the command to meet his particular needs.

Minimal prompting is provided by this method. The second method is menu directed input. In this case the user is led step by step through all the different command options and is presented with a list of all possible choices at each decision point along the way. This method is very helpful for users who have little or no familiarization with a particular command; however, it is very time consuming.

Phase 3 of the implementation plan is the transfer of applications from the McIDAS to the AIMS and the development of new programs. This process was on-going for the last six months of the contract and STX has been responsible for a number of new programs. A WB604 data line ingest capability was developed for automatic ingest of meteorological reports from the National Weather Service (NWS). Building on the ingest routine, a decoder program for interpreting surface reports as they come in over the data line was added. A series of programs was written to bring in, format, store, and display GWC data used in the AFGL nephanalysis program. Considerable progress has been made toward developing a GOES mode AAA data ingest capability. As part of the mode AAA task STX developed a terminal handler to interpret commands on the SEL; a FORTRAN callable I/O subsystem for unbuffered, asynchronous disk I/O; a device driver for receiving raw data from the downlink interface unit; and a documentation line interpreter to display on a CRT screen information on each line as it is received from the satellite.

G. Summary

During the five year lifetime of the contract, STX participated and in some cases provided a leadership role in most of the major projects undertaken by the Satellite Meteorology branch at AFGL. The cumulative work that was produced is significant. The VAS study was a pioneering effort in an emerging technology that located a very serious error in the brightness temperature equations. The satellite/MDR experiment showed promise for estimating rainfall rate, at least over a large (battlefield) area, by relying solely on passive satellite measurements. The nephanalysis experimental program produced results in a number of areas: locating sources of error in the existing operational algorithm; making recommendations for improving the analysis algorithm; quantifying the scan

252

angle bias that exists in the raw visible and IR data and specifying how
these biases affect the resulting cloud analysis. The NEARSS program,
although plagued by hardware problems in its early years, resulted in an
operational system that has operated perfectly, without operator
intervention, for over a year. At this point AIMS is considered to be a
functional system that has the basic capabilities needed to operate on its
own. Phase 3 development will continue for as long as the system continues
to operate. Because of its modular design and distributed architecture it
can be reasonably expected that the useful lifetime of the system will
exceed the 10+ years of its predecessor, the McIDAS.

VI. CLIMATOLOGY

A. Introduction

STX involvement in AFGL research in climatology began in 1984. Initial
activities related to the revision of Military Standard 210, which was
established by the U.S. Government to provide engineers with temperature and
density extremes of the earth's atmosphere for flight vehicle design.
Later, emphasis shifted to research on cloud cover climatology and its
usefulness in developing cloud cover simulation models.

B. Military Standard 210 Revision

Prior to 1984 Military Standard 210 provided statistically derived
global extremes of the vertical atmosphere as envelopes of one and ten
percent cold/warm temperatures and high/low densities for worst month and
location at each altitude. Values at various levels on these envelope
curves provided unrealistic values compared to structures of realistic
atmospheres. A study was therefore undertaken by AFGL to determine
consistent vertical profiles of temperature and density that would occur
with one and ten percent extremes at specified altitudes.

A huge amount of upper air radiosonde and rocketsonde data from various
stations around the world was acquired to derive monthly statistics of
temperatures and densities at the 5, 10, 20, 30, and 40 km levels. STX was
tasked to process this large upper air data ensemble to determine individual
profiles for stations and months containing the most extreme values only.
Out of thousands of possible cases, a graphical cumulative probability
scheme was derived that allowed for rapid identification of the most extreme
cases of temperature and density profiles. Temperature and lapse rate data
from these extreme profiles were then extracted and used as input to a
program developed to compute final hydrostatically consistent profiles from
the surface to 80 km. Final revision of Mil Std 210 as a result of this
work can be found in Kantor and Tattelman (1984).

C. Cloud Cover Climatology

In mid-1984 STX began its participation in AFGL research on global cloud cover climatology. Conventional hourly weather observations of sky cover taken over many locations in the world were utilized in developing global cloud cover statistics. Also, spatial and temporal decay of cloud cover conditionality was investigated to improve definition of cloud behavior in the development of computerized cloud cover simulation software. Shapes of spatial (and temporal) autocorrelation functions of the cloud cover decay over several regions of the world as derived from conventional hourly observations were fairly well defined through the efforts of STX programming. It remained to be seen how spatial cloud cover decay would behave using satellite cloud scenes to derive similar spatial autocorrelation functions. Consequently, multispectral LANDSAT digital data were acquired for investigation of spatial cloud cover decay as derived from satellite data.

With the availability of LANDSAT data, considerable software had to be developed to handle a variety of satellite data manipulations. For example, a single LANDSAT scene consists of more than 6×10^6 pixels. STX therefore designed a system whereby selected smaller portions of these images could be extracted and stored on permanent file for interactive processing. Software was then devised to display these subsections in pictorial form using the McIDAS imaging system. Later, this display package was modified to display the images interactively using a color graphics terminal with hardcopy capability. Contour analyses, histograms, and scanline extraction techniques were automated to assist in defining cloud/no cloud (CNC) threshold values unique to each satellite cloud scene to distinguish clouds from the earth background. These CNC threshold techniques were quite adequate since cloud scene selection was confined only to those over water and not over ice, snow, or areas of sunglint, etc. Additional software was written to separate cloudy pixels from non-cloudy pixels of a satellite cloud scene in a manner so that tetrachoric correlation decay of spatial cloud cover decay could be addressed for an entire scene. The spatial autocorrelation function derived from these satellite cloud images exhibited a much faster rate of decay of cloud cover

with distance than those using conventional data. Fourier transforms of these cloud scenes were also provided. Population density functions of cloudy and clear pixels were computed to investigate recurrence interval statistics over typical cumulus cloud fields. Distributions of equivalent diameter sizes of cumulus clouds were also studied.

Selected areas of cloud scenes photographed on space shuttle missions were extracted at AFGL and digitized for computer processing. The software developed to process LANDSAT cloud images was put to use to perform the same types of cloud analysis on space shuttle scenes, thus adding additional important information to the study.

Results of the studies of cloud cover as derived from satellite data were presented at the Third Tri-Service Clouds Modeling Workshop (Snow, 1985).

While processing satellite data for cloud research, STX supported another study that made use of LANDSAT multispectral digital data. Good quality digital images of portions of LANDSAT cloud scenes were produced for estimating cloud cover amount within defined grid squares. Then from the digital values making up each scene, thresholds were determined by computer methods that gave percent cloud cover the same as by human visual observations. Brightnesses integrated over 0.5, 0.75, 1.5 and 3 nm were then compared with corresponding subjective estimates of cloud cover. Results were portrayed as scatter plots with computed linear regression coefficients and curves. Final results were presented at the Fourth Tri-Service Clouds Modeling Workshop by Hawkins (1986).

In 1985 AFGL was developing software for simulating cloud-free lines of sight to a geostationary satellite relay mirror and cloud-free arcs to an orbiting satellite relay mirror. The objective was to produce downtime statistics for ground-based laser (GBL) systems of one to multiple sites. The AFGL cloud cover simulation models were being developed using an algorithm by Gringorten (1979) that extends, from single-point probabilities of cloud amount, the cumulative probability distributions for threshold cloud amounts over surrounding areas or along particular lines of varying scale. Horizontal fields were generated stochastically with the Boehm (1985) Sawtooth Wave (BSW) Model. The World Atlas of Total Sky Cover by Burger (1985) was also an important contribution to the model development

for deriving sky cover distributions over various parts of the world.

STX was involved with processing many conventional cloud amount observations to portray spatial and temporal cloud cover decay typical over several areas of the world. In processing these cloud decay statistics cloud amount observations less than or equal to four-eighths were categorized as partly cloudy skies and those greater than four-eighths were categorized as cloudy skies. Using these dichotomously defined cloud groups greatly reduced computer processing time and to some extent allowed conventional cloud cover decay to be derived in the same manner as that used on satellite data. Cloud cover decay was critical to the derivation of other weighting functions used to compute similar cloud realizations that were initiated into the BSW cloud simulation technique.

During this same period AFGL acquired several data tapes containing ten years of one-minute rainfall rates over several stations in the U.S. and West Germany. STX processed these data to derive rainfall rate recurrence statistics for duration times greater or equal to five and ten minutes with rainfall rates that exceed or equal .1, .25, .5, .75, 1.0, and 2.54 mm min^{-1}. These statistics were displayed in graphical normal probability vs. logarithmic grid form. Later this software was modified to display the rainfall recurrence statistics in histogram form. These rainfall statistics will be useful in modeling attenuation of satellite communication systems.

D. References

Boehm, A. R., C. F. Burger, and I. I. Gringorten, 1985: AFGL cloud simulation research: the sawtooth model, sky cover distributions, and cloud-free arcs. In Presentations at the Third Tri-Service Clouds Modeling Workshop, Air Force Geophysics Laboratory, Hanscom AFB, MA.

Burger, C. F., 1985: World Atlas of Total Sky Cover. AFGL-TR-85-0198, Air Force Geophysics Laboratory, Hanscom AFB, MA, ADA170474.

Gringorten, I. I., 1979: Probability models of weather conditions occupying a line or an area. Journ. App. Meteor., 18, 957-977.

Hawkins, R. S., 1986: Cumulus cloud cover from meteorological satellites. In Presentations at the Fourth Tri-Service Clouds Modeling Workshop, Air Force Geophysics Laboratory, Hanscom AFB, MA.

Kantor, A. J., and P. Tattelman, 1984: Profiles of Temperature and Density Based on 1- and 10- Percent Extremes in the Stratosphere and Troposphere. AFGL-TR-84-0336, Air Force Geophysics Laboratory, Hanscom AFB, MA, ADA160552.

Snow, J. W., K. Tomlinson, and J. H. Willand, 1985: Distributions of clear and cloudy intervals, spatial correlations from space shuttle cloud photographs. In Presentations at the Third Tri-Service Clouds Modeling Workshop. Air Force Geophysics Laboratory, Hanscom AFB, MA.

END

9-87

DTIC